

Modelling of intertidal floodplains for enhanced
estuarine transport and decay of faecal indicator
organisms from a diffuse source



A thesis submitted to Cardiff University in candidature
for the degree of Doctor of Philosophy

1st October 2019

Amyrhul Abu Bakar

Hydro-environmental Research Centre
School of Engineering, Cardiff University, Cardiff CF24 3AA, U.K.

Abstract

The noncompliance of microbiological quality to the standards of the EU Water Framework Directive at shellfish harvesting waters in the UK has become a serious threat to human health. The infected filter-feeding shellfish by enteric bacteria or viruses from these waters is major to the spreading of foodborne diseases as humans consumed them raw or undercooked. Although the quality of effluents from the wastewater treatment works has been improved significantly, diffuse source of pathogens from urban and agricultural settings remained as the reason to the microbiological noncompliance. The exploitation of natural wetlands along with poor management practices at catchments delivered the overloading of faecal contaminants from sources into the receiving water.

In this study, a developed hydro-environmental model is novel in contributing to the understanding of the microbial behaviour on the implicit response to the complex estuarine environment from the perspective of their morphological characteristics. Besides, the extended modelling domain at intertidal floodplains is novel in contributing to the representation of the tidal creek connectivity with the sub-mesh scale design based on the hydrological characteristic of the complex floodplain topography. Furthermore, the modelled of FIO transport and decay from intertidal marshlands is novel in contributing to the inclusion of the diffuse source with the integration to the release-kinetic model and based on an active source at the wetting and drying boundary.

The hydrodynamic calibration at several sites resulted in an optimum Manning's n of 0.025. The successful integration between the bathymetric and topographic data at intertidal floodplains resulted in a significant improvement for the tidal circulation within the study area. The sensitivity analysis on the diffusive transport has suggested the decrease in the tracer diffusivity with the increase in the mesh resolution, with the concentration gradient has increased with the decrease of the former parameter. The sensitivity analysis on the bottom roughness has suggested the increase in the tracer retention at floodplains with the increase in the roughness during low tides, with the concentration in subtidal channels was less sensitive to the roughness changes during high tides. The sensitivity analysis on the microbial kinetic has suggested that MS2 coliphage experienced the biphasic decay in the estuarine environment, with the T_{90} value ranged at 1 hour and from 50 to 125 hours for the first and second components decay respectively. The sensitivity analysis on the FIOs transport from the diffuse

source has suggested the increase in the spreading area and the flush-out mass with the decrease in τ , with the earlier release resulted in the higher FIOs concentration at shellfish harvesting waters for the case of the conservative mass and vice versa for the case of the decay. The FIOs distribution has indicated that shellfishes near tidal creeks of the adjacent marshland were highly exposed to the faecal contamination as compared at the far-field sites.

Keywords: Hydrodynamic modelling, intertidal floodplains, pollutant transport, microbial tracer, biphasic decay, faecal indicator organisms, diffuse source, release kinetic, shellfish contamination

Acknowledgement

There are a great number of individuals and organizations that have contributed to the completion of this PhD thesis. In particular, I would like to thank my research supervisors, Dr Reza Ahmadian and Professor Roger A. Falconer for their initial ideas, continued support and constructive criticism throughout my research activity at Cardiff University. I would also like to thank the official sponsor, Majlis Amanah Rakyat (Malaysia) for the financial support through the scheme of postgraduate sponsorship besides the Food Standard Agency (UK) for the research studentship.

I would like to thank the Environment Agency and Natural Resources Wales and the team from the Centre for Research into Environment and Health (CREH) of Aberystwyth University and the City and County of Swansea for the data provided under the Interreg 4A Smart Coasts and Sustainable Communities Project. I would also like to thank the user community of the TELEMAC Modelling System and its managing consortium for the modelling guidance through the model application and development. In addition, I would like to thank the Advanced Research Computing at Cardiff (ARCCA) for the supercomputing facility and technical support offered throughout the research period.

I would like to thank the staff at the office of Postgraduate Research for their continued assistance in the management of this research. I would also like to thank research fellows at the Hydro-environmental Research Centre in particular, those who have shared their insight towards the improvement of knowledge. My parents, wife, son, sibling and in-laws are those who deserve the most appreciation upon this achievement. I thank them for their unconditional support throughout my PhD journey.

Table of contents

Abstract.....	i
Acknowledgement	iii
Table of contents.....	iv
List of figures.....	ix
List of tables.....	xvii
List of acronyms	xviii
List of publications	xxii
Chapter 1: Introduction	1
1.1 Motivation.....	1
1.2 Water quality standard	2
1.3 Loughor Estuary.....	3
1.4 Water quality monitoring and modelling.....	5
1.5 Research objectives.....	7
1.6 Thesis organisation	8
Chapter 2: Literature review	10
2.1 Introduction.....	10
2.2 Review of SEBC modelling studies.....	10
2.2.1 Hydrodynamic modelling	10
2.2.2 Water quality modelling	12
2.3 Overview of mesh sizing criteria	13
2.3.1 A-priori criteria	13
2.3.2 A-posteriori criteria.....	17
2.3.3 Mesh discretisation at floodplains	20
2.3.3.1 Significance horizontal length scales.....	20
2.3.3.2 Topographically significant points	21
2.3.3.3 Features incorporation into mesh discretization	26

2.3.3.4 Sub-grid-scale parameterization	26
2.4 Overview of floodplain roughness parameterisation	28
2.4.1 USDA Soil Conservation Service and related methods.....	29
2.4.2 Vegetation drag model.....	30
2.4.3 Floodplain roughness parametrisation	30
2.5 Review on bacteriophage as a microbial tracer	34
2.5.1 Environmental stress.....	36
2.5.2 Biphasic decay modelling.....	38
2.5.3 GASP mechanism and agent-based modelling.....	39
2.6 Overview of diffuse source release kinetics	41
2.6.1 Parametric release kinetic models.....	43
2.7 Summary	48
Chapter 3: Hydrodynamic model development	49
3.1 Introduction.....	49
3.2 Free surface hydrodynamics	49
3.2.1 Definition of domain.....	50
3.2.2 Free surface Navier–Stokes equations	51
3.3 Model setup.....	60
3.4 Hydrodynamic calibration	63
3.5 Summary	73
Chapter 4: Intertidal floodplains extension.....	75
4.1 Introduction.....	75
4.2 DEM data processing.....	76
4.2.1 Bare earth	76
4.2.2 Horizontal and vertical datums conversion.....	80
4.2.3 Land-water boundary mask.....	81
4.2.4 Filling gaps in the intertidal data	88

4.3 Intertidal domain extension.....	93
4.3.1 Outer boundary	94
4.3.2 Domain decomposition	96
4.3.3 Mesh resolution function	98
4.3.4 Tidal creeks network extraction.....	100
4.3.5 Unstructured mesh-nodes placement	105
4.4 Bottom roughness parameterization	113
4.5 Catchments delineation.....	116
4.5.1 Streams discharge estimation.....	117
4.6 Summary	120
Chapter 5: Transport and persistence of microbial tracers	121
5.1 Introduction.....	121
5.2 Microbial tracer release experiment.....	121
5.2.1 Microbiological and environmental data analyses.....	124
5.3 Hydrodynamic modelling process	128
5.3.1 Hydrodynamic at intertidal floodplains	128
5.3.2 Hydrodynamic at release and sampling sites	135
5.4 Tracer transport and decay modelling processes	139
5.4.1 Transport calibration.....	140
5.4.2 Decay calibration	146
5.5 Summary	154
Chapter 6: Transport and decay of FIOs from a diffuse source.....	156
6.1 Introduction.....	156
6.2 Materials and methods	156
6.2.1 Study area.....	156
6.2.2 Loading deposition of FIOs	160
6.2.3 Release-kinetic of FIO	162

6.2.4 Transport and decay of FIO	164
6.2.5 Shellfish exposure to FIOs.....	167
6.2.6 Statistical analyses	168
6.3 Results and discussion	170
6.3.1 Hydrodynamic validation.....	170
6.3.2 FIOs loading deposition.....	170
6.3.3 FIOs release modelling	171
6.3.4 FIO transport and decay.....	185
6.3.5 FIO exposure to shellfish.....	193
6.4 Summary	203
Chapter 7: Conclusion and recommendations	204
7.1 Conclusion	204
7.1.1 Development and calibration of a hydrodynamic model for the SEBC waterbody	204
7.1.2 Extension of the modelling domain at intertidal floodplains of the Loughor Estuary	205
7.1.3 Modelling the transport and persistence of microbial tracers in the estuarine environment	206
7.1.4 Modelling the transport and decay of FIOs from intertidal marshlands as the diffuse source	208
7.2 Recommendations.....	209
References.....	211
Appendix A.....	230
A.1 Shellfish Water Directive (SWD) compliance studies at Loughor Estuary.....	230
Appendix B.....	234
B.1 Stream flows boundary condition	234
Appendix C.....	236
C.1 Lidar composite.....	236

C.2 DEM data processing	237
C.3 Streams discharge estimation	241
Appendix D.....	244
D.1 Microbial tracer release experiment.....	244
D.2 Environmental data analysis	248
D.3 Sensitivity analysis on the transport of salinity	250
D.4 Hydrodynamic validation at Swansea Bay	255
Appendix E	256
E.1 Spatial distribution analyses of FIO and its exposure to shellfish.....	256
E.2 Lumped statistics of temporal FIOs concentration at shellfish beds.....	258

List of figures

Figure 1.1: Overview of the sites of interest for the area of Loughor Estuary, i.e. Pembrey and Rhossili designated sampling points (DSPs) and Burry Inlet (BI) North and BI South – shaded areas show designated shellfish waters (DSWs), and the potential sources of FIOs, e.g. wastewater treatment works (WwTWs), combined sewer overflows (CSOs), shellfish processing plants (SPPs) and Llanrhidian Marsh. The dashed line is the extended boundary of the modelling domain.	4
Figure 2.1: Study area, showing one- and two-dimensional boundaries (Yang <i>et al.</i> 2008)...	12
Figure 2.2: Illustration of the anisotropic mesh refinement strategy for an idealised bathymetric profile (Legrand <i>et al.</i> 2007).....	16
Figure 2.3: (a) Existing mesh of the SAB and (b) inset shows coast details (Bacopoulos <i>et al.</i> 2011).	18
Figure 2.4: A sample model variogram showing range, nugget, sill (Bates <i>et al.</i> 2003).....	21
Figure 2.5: Sample of correct building raster, generated grid sample, and error of two different sample grids. (a) Actual data. (b) Sample of generated grid. (c) Error of grid without considering edge point when generating grid. (d) Error of grid considering edge point (Tsubaki and Fujita 2010).	23
Figure 2.6: An example of variable grid sizing (Noh <i>et al.</i> 2018).....	24
Figure 2.7: An example of a subgrid Delaunay triangulation developed for a single finite element from the mesh. The element contains 219 individual x, y, z-points obtained from laser altimeter survey from which a triangulation consisting of 439 smaller triangles can be calculated (Bates and Hervouet 1999).	27
Figure 2.8: Generation of DEMs with additional topographic information. (A) Reference DEM, (DEM ^{ref}); (B) DEM with additional topographic content of ± 25 cm (DEM ^{±25cm}) (Casas <i>et al.</i> 2010).	28
Figure 2.9: Particle tracers for the marsh with channel width of 5 m for (a) moderately rough marsh surface with Manning’s n = 0.07; and (b) very rough marsh surface with n = 0.5 (Lawrence <i>et al.</i> 2004).	33
Figure 2.10: Illustration of energy model (Martin <i>et al.</i> 1998).....	38
Figure 2.11: Conceptual model of the E. coli adaptive mutation using agent-based modelling (Bucci <i>et al.</i> 2012).....	40

Figure 2.12: General model of biphasic decay and three mechanistic submodels (Brouwer *et al.* 2017). Solid lines are a transfer of pathogens, and the dashed lines indicate the measurement.41

Figure 2.13: Differences in shapes of release curves simulated with three release models: exponential, Bradford-Schijven (B-S), and Vadas-Kleinman-Sharpley (VKS) (Blaustein, Pachepsky, Shelton, *et al.* 2015).44

Figure 2.14: Cumulative amounts of bacteria and Cl⁻ released () as a function of time since initial release (top row) and rainfall depth since initial release (bottom row) (Blaustein, Pachepsky, Hill, *et al.* 2015).45

Figure 2.15: Relationship between parameters in the two-parametric BS model and irrigation rate (Guber *et al.* 2006). A linear regression equation is explaining that relationships were $y = ax + b$, where a is irrigation rate (cm h⁻¹) similar to Equation 2.17.46

Figure 3.1: Domain of calculation.50

Figure 3.2: Modelling domain of the Severn Estuary and Bristol Channel (SEBC) with the interpolated bottom elevation relatives to Ordnance Datum Newlyn (ODN), ‘bare earth’ DEM based on Lidar surveys at South West Wales with the overlaid 10 m contour at floodplains, imposed tidal boundary at seaward and hydrodynamic validation sites.62

Figure 3.3: Comparisons of calibrated water levels to measured data at Ilfracombe (a), Mumbles (b), Hinkley Point (c) and Newport (d).65

Figure 3.4: Comparisons of the calibrated tidal current for velocity (a), direction (b), and speeds in x- (c) and y-directions (d) to measured data at site 1179P.67

Figure 3.5: Comparisons of the calibrated tidal current for velocity (a), direction (b), and speeds in x- (c) and y-directions (d) to measured data at site 1179R.69

Figure 3.6: General circulation patterns at phases of low tide (a), flood tide (b), high tide (c) and ebb tide (d) during a spring tidal cycle in the Severn Estuary and Bristol Channel. Details of island’s wake (e) during high tide.73

Figure 4.1: Topography of the ‘bare earth’ DEMs for Carmarthen Bay, Loughor Estuary and Swansea Bay, with the overlaid contour line of zero-meter elevation is shown in red. The scale is shown on the top right of the figure.77

Figure 4.2: Overlaid contour lines of -2 m (light blue), -1 m (dark blue), 0 m (red), 1 m (dark green) and 2 m (light green) on the DEMs at Carmarthen Bay (a), Loughor Estuary (b) and Swansea Bay (c) that highlighting the convex spots between drying intertidal areas and the water surface.80

Figure 4.3: Land-water boundary mask overlaid on the DEMs at Carmarthen Bay (a), Loughor Estuary (b) and Swansea Bay (c) with the contour lines as guidance in defining the extension of the intertidal areas.....	84
Figure 4.4: ‘Land extracted’ DEMs at Carmarthen Bay (a), Loughor Estuary (b) and Swansea Bay (c) with the elimination of water surface at the maximum extension of drying intertidal areas.	87
Figure 4.5: The gridded depth-averaged data of the hydro-environmental model by Liang <i>et al.</i> (2013). Dry cells are shown in the yellow background (i.e. elevation set to zero) that surrounded by wet cells.	88
Figure 4.6: The bottom elevation of the Liang <i>et al.</i> (2013) model with its contour lines, overlying with contours of the DEMs, a gap-fill polygon at the intertidal area, and the cross-sectional lines.....	90
Figure 4.7: Plots of bottom elevation profiles comparing between datasets of Liang <i>et al.</i> (2013) model and the DEMs along Sections 1 (a), 2 (b), 3 (c) and 4 (d), as shown in Figure 4.6.....	93
Figure 4.8: The flowchart of procedures for the unstructured mesh generation with the bottom elevation assignment (a) and the friction zones assignment to the unstructured mesh (b).....	95
Figure 4.9: The outer boundary extension of the modelling domain with the benchmark of the mean high water spring (MHWS) tidal levels over Carmarthen Bay, Loughor Estuary and Swansea Bay.	96
Figure 4.10: The domain decomposition at Loughor Estuary with four segments for the assignment of mesh resolution functions.....	97
Figure 4.11: Mesh resolution functions (y-axis) for the unstructured mesh triangulation based on the bottom elevation (x-axis).	99
Figure 4.12: The mesh resolution that ranges from 20 m to 100 m at higher and lower bottom elevations respectively, following the order of segments TM1-D, TM2a-D & TM2b-D, TM3-D and TM4-D.....	100
Figure 4.13: The profile view of a sink before and after the iterative filling to the z-limit. The z-limit is the maximum difference specified between the depth of a sink and the pour point for the filling allowance. The pour point is the boundary cell of the lowest elevation within the contributing area of a sink.....	102
Figure 4.14: The eight valid output directions based on the D8 flow model. The elevation dataset is in green highlight with the decent values in bold. The calculation of the steepest descent allows for the greater distance to diagonal neighbours with a factor of (Freeman 1991). The steepest descent is southwards in this example.	102

Figure 4.15: Flowchart of processing the depression-less DEM for extracting tidal creek and river networks (Poggio and Soille 2012).	103
Figure 4.16: The overlaying tidal creeks feature of TCN on the segment with the resolution function of TM12a2b-D.	104
Figure 4.17: Vertex redistribution of the tidal creeks feature based on the mesh resolution function as TCN-D.	105
Figure 4.18: Stage 1 of the unstructured mesh triangulation for segment MNP1.	106
Figure 4.19: Stage 2 of the unstructured mesh triangulation for segment MNP2.	107
Figure 4.20: Stage 3 of the unstructured mesh triangulation for segment MNP3.	108
Figure 4.21: The unstructured mesh of TMW2.	109
Figure 4.22: Stage 4 of the unstructured mesh triangulation for segment MNP4. The red cell is the area of floodplain under investigation.	109
Figure 4.23: High-resolution image of the meshing structure along the TCN at the floodplain of investigation.	110
Figure 4.24: Interpolated bottom elevation to the mesh-nodes of vertical features and floodplains. TCN-B and CPW1-B are three-dimensional polylines for tidal creek networks and crowns of training walls respectively. Cells a, b and c represent areas of marshland, tidal flat and intertidal channel.	111
Figure 4.25: Three-dimensional views of mesh geometries at the marshland (a), tidal flat (b) and intertidal channel (c) based on Figure 4.22. Views from the North with the horizontal-to-vertical plot at 1:10 scale.	113
Figure 4.26: The assigned friction of different sub-domains (i.e. Zone 1 for the subtidal channel, Zone 2 for the intertidal channel, Zone 3 for the tidal flat and Zone 4 for the marshland) to the mesh-nodes at the study area of Loughor Estuary.	115
Figure 4.27: The stream networks and catchment boundaries that being delineated to 25 sub-catchments discharging into the Loughor Estuary (● location of gauging station, ⊕ locations of stream outlets).	117
Figure 4.28: The flow-duration percentiles at 10 percent interval that were plotted as the linear single regressions (LSRs) against the catchment areas of 18 gauging station at South West Wales.	119
Figure 5.1: Locations of the release and sampling sites for microbial tracers in and around the Loughor Estuary.	123
Figure 5.2: Plaques on the agar overlay in Petri dishes.	125

Figure 5.3: The observed solar radiations from the Blackpill meteorological station during the three-days sampling period, consist of extra-terrestrial, global, UVA, and UVB radiations.	126
Figure 5.4: Estimated ranges of T90(dark) and T90(light) based on the environmental data measured at five sampling sites.	128
Figure 5.5: Validation of water levels at Burry Port for five days (a) and details of one day (b) between refined and unrefined domains with scenarios of variable bottom roughness.	129
Figure 5.6: Validation of water levels at Llanelli for five days (a) and details of one day (b) with scenarios of variable bottom roughness.	130
Figure 5.7: Validation of water levels at Lliw for five days (a) and details of one day (b) with scenarios of variable bottom roughness.	131
Figure 5.8: Predicted current velocities at site 1076H between refined and unrefined domains with scenarios of variable bottom roughness.	132
Figure 5.9: General circulation patterns at phases of low tide (a), flood tide (b), high tide (c) and ebb tide (d) during a spring tidal cycle in Loughor Estuary.	134
Figure 5.10: Modelled water level, current velocity and direction at the tracer release site of a) Great Pill, b) Morlais River, c) Loughor Bridge and d) Afon Lliedi.	137
Figure 5.11: Modelled water level, current velocity and direction at the tracer sampling site of a) Rhossili DSP, b) Broughton, c) Loughor Boat Club, d) Burry Port and e) Pembrey DSP.	139
Figure 5.12: Effects of different grid resolutions on the dispersion transport of MS2 coliphage at the molecular diffusivity of $1 \times 10^{-10} \text{ m}^2/\text{s}$	142
Figure 5.13: Calibration results of the estuarine longitudinal dispersion as compared to the measured data at Loughor Boat Club (a) and Burry Port Harbour (b).	143
Figure 5.14: Transport fields of microbial tracers after 18 hours of release for a range of multi-zones for bottom friction.	145
Figure 5.15: Calibration results of the advection transport with varied bottom roughness at multi-zones as compared to the measured data at Loughor Boat Club (a) and Burry Port Harbour (b).	146
Figure 5.16: Results of simple first order decay calibration for a range of constant T ₉₀ values compared to measured data at Loughor Boat Club (a) and Burry Port Harbour (b).	148
Figure 5.17: Results of day-night time decay calibration for a constant night T ₉₀ of 60 hours and a range of day T ₉₀ values of 2.5 – 20 hours compared to measured data at Loughor Boat Club (a) and Burry Port Harbour (b).	150
Figure 5.18: Typical two-stage bacterial decay mass balance.	151

Figure 5.19: Results of the transported microbial tracer after considering the two-stage decay processes with a $T_{90(1)}$ value of 1 hour and $T_{90(2)}$ values ranging from 50 to 125 hours at Loughor Boat Club (a) and Burry Port Harbour (b).	153
Figure 6.1: Locations of shellfish beds for cockle (i.e. site 1-50, ■) and mussel (i.e. site 51-60, ■), grazing area of the Llanrhidian Marsh (i.e. green area) and modelling observation points (i.e. site 1-91, ■) within the area of Loughor Estuary. Hydrodynamic observations at Burry Port and site 1076H, and water quality monitoring at Pembrey DSP and Broughton.....	157
Figure 6.2: Hygiene survey results of faecal coliform (FC) and E. coli for March 2012 that represented from 60 sampling stations, including 50 cockle beds and ten mussel beds (Youell <i>et al.</i> 2013a; Youell <i>et al.</i> 2013b).	159
Figure 6.3: Hygiene survey results of faecal coliform (FC) and E. coli for October 2012 that represented from 60 sampling stations, including 50 cockle beds and ten mussel beds (Youell <i>et al.</i> 2013a; Youell <i>et al.</i> 2013b).	160
Figure 6.4: The Manning's values used at the friction sub-domains of Loughor Estuary based on Bakar <i>et al.</i> (2017) as compared to the values from the literature.....	166
Figure 6.5: Time series of the FIOs loading deposition () at different releasing depths based on the B-S and IF release models.	171
Figure 6.6: The time series of the fitting parameter () at different releasing depths based on the B-S release-kinetic model.	172
Figure 6.7: The time series of the FIOs release coefficient () at different releasing depths based on the B-S release-kinetic model.....	173
Figure 6.8: The time series of the flooding discharge rate () at different releasing depths based on the B-S and IF release models.	174
Figure 6.9: The time series of the FIOs release concentration () at different releasing depths based on the B-S and IF release models.	175
Figure 6.10: Percentage of total FIO released at different releasing depths based on the B-S and IF release models. The black-solid line indicates the designed release at the node with $\alpha = 0.1$	176
Figure 6.11: Percentage of FIO mass lost at different releasing depths based on the B-S and IF release models.....	177
Figure 6.12: The time series of the FIOs mass balance at different releasing depths based on the B-S and IF release models.	178

Figure 6.13: The time series of the FIOs release mass at different releasing depths based on the B-S and IF release models.	180
Figure 6.14: The time series of the FIOs mass lost with the conservative mass at different releasing depths based on the B-S and IF release models.	182
Figure 6.15: The time series of the FIOs mass balance with the conservative mass at different releasing depths based on the B-S and IF release models.	184
Figure 6.16: Concentration gradients of the FIO transport as a conservative mass across the Loughor Estuary at HW -3 hours referred at Burry Port (i.e. 284.25-284.75 JD from 01/01/2014), that released at different based on the B-S release-kinetic model. .	187
Figure 6.17: Box plots at 3 of the FIO concentrations distribution as a conservative mass at top 10 impacted shellfish beds, that released at different based on the B-S release-kinetic model.....	188
Figure 6.18: Time series of the FIO concentrations at shellfish bed no. 15, as a conservative mass and at different based on the B-S release-kinetic model.	189
Figure 6.19: Concentration gradients of the FIO transport with constant decay ($T_{90} = 14.9$ hours) across the Loughor Estuary at HW -3 hours referred at Burry Port (i.e. 284.25-284.75 JD from 01/01/2014), that released at different based on the B-S release-kinetic model.....	191
Figure 6.20: Box plots at 3 of the FIO concentrations distribution with constant decay ($T_{90} = 14.9$ hours) at top 10 impacted shellfish beds, that released at different based on the B-S release-kinetic model.	192
Figure 6.21: Time series of the FIO concentrations at shellfish bed no. 15, with constant decay ($T_{90} = 14.9$ hours) and at different based on the B-S release-kinetic model.	193
Figure 6.22: Exposure time of FIO to shellfish at HW -3 hours referred at Burry Port (i.e. 284-284.5 JD from 01/01/2014), that released as a conservative mass at different based on the B-S release-kinetic model.	195
Figure 6.23: Exposure severity of FIO to shellfish at HW -3 hours referred at Burry Port (i.e. 284-284.5 JD from 01/01/2014), that released as a conservative mass at different based on the B-S release-kinetic model.....	197
Figure 6.24: Exposure time of FIO to shellfish at HW -3 hours referred at Burry Port (i.e. 284-284.5 JD from 01/01/2014), that released with constant decay ($T_{90} = 14.9$ hours) at different based on the B-S release-kinetic model.....	199

Figure 6.25: Exposure severity of FIO to shellfish at HW -3 hours referred at Burry Port (i.e. 284-284.5 JD from 01/01/2014), that released with constant decay ($T_{90} = 14.9$ hours) at different based on the B-S release-kinetic model.201

List of tables

Table 1.1: Burry Inlet (BI) North and BI South shellfish flesh compliance with guideline standard, 2001-2011 (Youell <i>et al.</i> 2013a; Youell <i>et al.</i> 2013b).	5
Table 4.1: Scenarios of the variable bottom roughness at different friction zones of Loughor Estuary.	116
Table 4.2: The developed LSR equations for each flow-duration percentile based on the areas of gauging catchments.	119
Table 5.1: Details of the released microbial tracers at locations along the Loughor Estuary.	124
Table 5.2: The parameter values for the two-stage bacterial decay model.....	152
Table 6.1: The values of the fitting parameter () at different releasing depths with different releasing times.	172
Table 6.2: The values of the FIOs release coefficient () at different releasing depths with different releasing times.....	173
Table 6.3: The values of the FIOs release concentration () at different releasing depths with different releasing times.....	175
Table 6.4: The values of the FIOs mass balance from the IF release model with the releasing depth equal or greater than 1×10^{-1} m that levelled at different tidal cycles with different mass increments.	178
Table 6.5: The result of the statistical analyses for the FIOs mass balance at the test node.	179
Table 6.6: The result of the statistical analyses for the FIOs release rate at the grazing marshland during the first tidal cycle.	180
Table 6.7: The result of the statistical analyses for the FIOs release rate at the grazing marshland during the second-to-fourth tidal cycles.	181
Table 6.8: The result of the statistical analysis for the FIOs mass lost with the conservative mass at the grazing marshland during the second-to-fourth tidal cycles.	183
Table 6.9: The result of the statistical analyses for the FIOs mass balance with the conservative mass at the grazing marshland.	184

List of acronyms

ARCCA	Advanced Research Computing at Cardiff
ADCIRC	Advance Circulation Model
AMETC	Automated Method for Extracting Tidal Creeks
AIC	Akaike Information Criterion
ASCII	American Standard Code for Information Interchange
ABM	Agent-based Model
BI	Burry Inlet
B-S	Bradford-Schijven
BODC	British Oceanographic Data Centre
BNG	British National Grid
BST	British Summer Time
CREH	Centre for Research into Environment and Health
CSO	Combined Sewer Overflow
CD	Complex derivatives
C-CAP	Coastal Change Analysis Program
DEM	Digital Elevation Model
DSW	Designated Shellfish Water
DSP	Designated sampling point
DH	Drop heuristic
DTM	Digital Terrain Model
D8	Eight-direction
DRM	Digital roughness model
DEB	Dynamic energy budget
DCWW	Dŵr Cymru Welsh Water
DSM	Digital Surface Model
EAW	Environment Agency Wales
EU	European Union
ENT	Enterococci
EC	E. coli
FC	Faecal coliform
FIO	Faecal indicator organism
FIB	Faecal indicator bacteria

GASP	Growth advantage in stationary phase
GSI	Groundwater stream interactions
GW	Groundwater
GMF	Gaussian-matched filtering
GETM	General Estuarine Transport Model
HW	High water
H_{release}	Depth releasing threshold
HT	Hierarchy transform
HLIP	High-level image processing
IF	Instantaneous flushing
IQR	Inter-quartile range
JD	Julian date
LTEA	Localised truncation error analysis
LiDAR	Light detection and ranging
LULC	Land use and land cover
LAT	Lowest astronomical tide
LB	Loughor Bridge
LSR	Linear single regression
m-ABM	Mutation Agent-based Model
MPI	Message Passing Interface
MSAL	Mississippi and Alabama floodplains
MFD	Multiple flow direction
MNA	Median neighbourhood analysis
ME	Model efficiencies
ME	Mean error
MAE	Mean absolute error
MST	Microbial source tracking
MHWS	Mean high water spring
NSF	Node spacing function
NLCD	National Land Cover Database
NAOC	Natural Assimilable Organic Carbon
NRW	Natural river water
OCTM	Optimal-curvature threshold method
OETM	Optimal-elevation threshold method

OC	Organic carbon
ODN	Ordnance Datum Newlyn
OSGB	Ordnance Survey National Grid
OS	Ogmore-by-Sea
PCR	Polymerase chain reaction
PBS	Phosphate buffer solution
P	Phosphorus
PD	Pontardulais
RFF	Reason for failure
RWT	Rhodamine WT
rpoS	RNA polymerase, sigma S
RMSE	Root mean square error
RE	Relative error
RRE	Relative RMS error
SEBC	Severn Estuary and Bristol Channel
SWD	Shellfish Water Directive
SSSI	Site of Specific Scientific Interest
SAB	South Atlantic Bight
SAC	Special area of conservation
SPA	Special protection area
SW	Surface water
SGW	Synthetic groundwater
STW	Sewage treatment work
T ₉₀	Time for FIO mass to decrease by 90%
TMDL	Total maximum daily load
TAT	Two-stage adaptive thresholding
TPR	True positive rate
TS	Transient storage
TC	Total coliform
TCN	Tidal creek network
UK	United Kingdom
USDA	United State Department of Agriculture
USA	United State of America
UTM	Universal Transverse Mercator

UVA	Ultraviolet A
UVB	Ultraviolet B
VBNC	Viable but not culturable
VIP	Very important point
VKS	Vadas-Kleinman-Sharpley
WFD	Water framework directive
WwTW	Wastewater treatment work
WT	Wild type

List of publications

Peer-reviewed journals

Bakar, A.A., Ahmadian, R. and Falconer, R.A. (2017). Modelling the transport and decay processes of microbial tracers in a macro-tidal estuary. *Water Research* **123**:802–824.

Conference proceedings

Bakar, A.A., Ahmadian, R. and Falconer, R.A. (2019). The representation of tidal creek connectivity for a complex floodplain topography. *Proceedings of the 38th IAHR World Congress* (submitted).

Bakar, A.A., Ahmadian, R. and Falconer, R.A. (2018). Microbial tracer transport as particles with biphasic-decay. *Proceedings of the 5th IAHR Europe Congress*:171–172.

Bakar, A.A., Ahmadian, R. and Falconer, R.A. (2017). Diffuse bacteria loading from intertidal marshland and impacts to adjacent estuarine water quality. *Proceedings of the 37th IAHR World Congress*:3563–3570.

King, J., Ahmadian, R., Bakar, A.A. and Falconer, R.A. (2017). Modelling the impact of microbial sources on water quality: a study on the designated sampling point in Swansea Bay, UK. *Proceedings of the 37th IAHR World Congress*:2729–2736.

Bakar, A.A., Ahmadian, R. and Falconer, R.A. (2016). Modelling the transport and decay of microbial tracers in a macro-tidal estuary. *Proceedings of the 4th IAHR Europe Congress*:76.

Chapter 1: Introduction

1.1 Motivation

Estuaries are highly productive and dynamic ecosystems at the transition between river and marine environments. These ecosystems are crucial to sustaining numerous socioeconomic activities. Among them are to provide food and habitat for fish and shellfish, areas for recreation and tourism, besides hosting other services (Malham *et al.* 2014). These ecosystems however are increasingly exposed to environmental pressures as human populations are concentrated in coastal areas (Perkins *et al.* 2016). Point and diffuse inputs of pollutants from wastewater treatment works, combined sewer overflows, urban and agricultural runoff (Almeida and Soares 2012), all can have significant impacts on these ecologically and economically important areas.

Globally, 3 billion people in 2009 are relying on fish and other seafood products in supplying approximately 20% of their animal protein intake (Food and Agriculture Organization 2012). This demand is expected to increase as the shellfish products are more widely recognised as a relatively cheap and nutritious source of food (Clements *et al.* 2015). Shellfish products for commercially produces are extensively cultivated parallel with the demand. The shellfish cultivation waters, besides experiencing dynamic alterations on their indigenous microbial community due to nutrient level rises from sewage, also potentially contaminated by bacterial (Riou *et al.* 2007) and viral pathogens (Lees 2000). It is especially true with the increase in flow during storm events that lead to the release of untreated sewage into the sea from treatment facilities that exceed their capacity (Lessard and Beck 1990).

The consumption of faecal contaminated seafood from the harvesting areas being a risk to public health (Bettencourt *et al.* 2013), as they are transferring pathogenic microorganisms into the human food chain when traditionally consumed either raw or lightly cooked (Potasman *et al.* 2002). The overall global burden of human diseases caused by sewage pollution to coastal waters has been estimated at 4 million lost person-years annually (Winterbourn *et al.* 2016). A wide range of bacterial, protozoan and viral pathogens have been responsible for waterborne (Leclerc *et al.* 2002) and shellfish-borne illness (Rippey 1994). Typhoid fever, bacterial illness of the oysters associated sewage-contaminated, was the massive outbreak in the USA at the beginning of the 20th century (Malham *et al.* 2014). The protozoan transmission via seafood is

rare – one oyster-associated giardiasis outbreak reported (Iwamoto *et al.* 2010). Norovirus, besides leading water-borne viral outbreaks, also responsible for 83.7% shellfish-borne outbreaks (Malham *et al.* 2014).

Efforts to effectively manage and preserve the quality of water are less strenuous and less expansive with the application of numerical models. In this context, a balance between all phenomena involve at coastal and catchment scales is required for predicting impacts of FIO fluxes on the water and shellfish quality (Bougeard *et al.* 2011). However, the existing coastal models only consider the physical factors of dilution and dispersion with few references were available on the pathogen mortality (Kashefipour *et al.* 2006). Short-term impacts and the subsequent recovery time of viral water contaminations were less considered though large faecal microorganism loadings were observed at tributaries (Riou *et al.* 2007). For the bacterial contamination of cultured shellfish, very few studies contextualised the evidence of environmental influences on FIO contamination with the shellfish hygiene in growing waters (Campos *et al.* 2013) and none of the modelling approaches has fully accounted the bivalve's physiological response to the changing environmental conditions (Dabrowski *et al.* 2014).

In the current study, a hydro-environmental model was developed to understand the process experienced by the faecal indicator organisms (FIOs) in the estuarine environment. The modelling domain was extended and refined at intertidal floodplains to understand its influence on the transport process of FIO. The transport and dispersal of FIO cannot be modelled accurately in the tidal creek-marsh system if without detailed representation of the floodplain topography. In the estuary, the process experienced by the FIO of microbial tracer was evaluated with the consideration of the hostile environment. The microbial tracer was reported as experiencing environmental stress before persisting to the marine environment. At the intertidal floodplains, the FIO loading was released into the waterbody as a diffuse source with the consideration of its potential impacts to water quality at shellfish harvesting waters.

1.2 Water quality standard

The suitability of shellfish harvesting areas is directly related to the quality of waterbodies where the shellfish are growing (Almeida and Soares 2012). The impairment of water quality in these highly productive coastal systems can have significant impacts on social and economic

activities. This is especially true with catchments that incorporates blue flag beaches and shellfish waters (Perkins *et al.* 2016).

The primary water quality standards in nearshore marine and estuarine waters are defined concerning microbiological parameters, which indicate pollution by faecal wastes from human and animal sources. The coliform bacteria specifically *E. coli* (Clements *et al.* 2015), is the principal compliance parameters in current standards for shellfish waters and shellfish flesh, defined in the Shellfish Water Directive and the Shellfish Hygiene Directive respectively. The latter directive is now replaced by Regulation (EC) No. 854/2004 (Stapleton *et al.* 2011).

Designated shellfish harvesting areas throughout Europe are subjected to a range of regulations designed to maintain a high quality of shellfish for human consumption (Kay *et al.* 2008). The hygiene regulations based on (EC) No. 853/2004 (CEU 2004a) and (EC) No. 854/2004 (CEU 2004b) yield classifications of bivalve mollusc harvesting areas (Almeida and Soares 2012) based on the *E. coli* concentration measured in shellfish flesh and intervalvular fluid, as i) Class A ≤ 230 counts/100 g in all samples, ii) Class B $\leq 4,600$ counts/100 g in 90% of samples, iii) Class C $\leq 46,000$ counts/100 g in all samples (Bettencourt *et al.* 2013). These classification grades assigned to an individual shellfish bed impacts both consumers and shellfish industry, i.e. post-harvest treatment required for shellfish products at different gradings, could promote either a change in management practice or temporary closure of harvesting areas (Clements *et al.* 2015).

Codified Shellfish Waters Directive (2006/113/EC) (CEU 2000) specifies a guideline standard of less than 300 FC/100 ml in the shellfish flesh and intervalvular liquid in 75% of samples (Kay *et al.* 2008). This directive was repealed in 2013 by the EU Water Framework Directive (WFD) (2000/60/EC). The WFD provides similar levels of protection as given by the repealed directive. Higher microbial standards (i.e. *E. coli* and intestinal enterococci) for water quality, in particular for bathing water is required (Malham *et al.* 2014).

1.3 Loughor Estuary

The Loughor Estuary is a macro-tidal waterbody that located at the north-eastern side of the Bristol Channel, U.K. (see Figure 1.1). This estuary has a spring tidal range that reaches the maximum of 7.5 m at Burry Port. With the shallow bottom of sand and muds, this estuary is

mostly dried during low tides and formed an essential site for shellfish harvesting waters. There are two Designated Shellfish Waters (DSWs) namely Burry Inlet (BI) North and BI South. The former is located at the north of the tidal channel between Llanelli and Burry Port while the latter is at the northern edge of the Llanrhidian Marsh. These inlets are subjected to a number of designations (i.e. protection of natural ecosystems) which include a Site of Specific Scientific Interest (SSSI), Special Area of Conservation (SAC), Special Protection Area (SPA), a Ramsar Site and a National Nature Reserve (Youell *et al.* 2013a; Youell *et al.* 2013b). From these areas also present several bivalve mollusc species, including the commercially important species of common edible cockles and mussels.

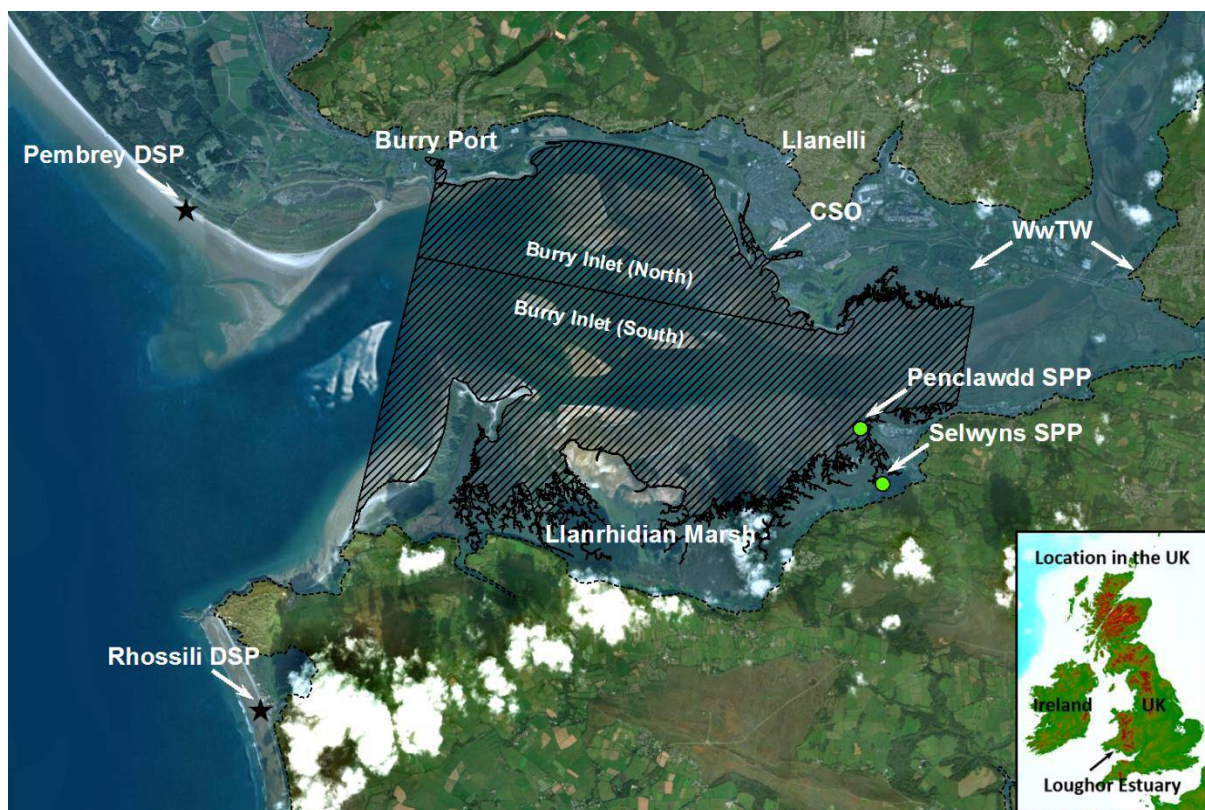


Figure 1.1: Overview of the sites of interest for the area of Loughor Estuary, i.e. Pembrey and Rhossili designated sampling points (DSPs) and Burry Inlet (BI) North and BI South – shaded areas show designated shellfish waters (DSWs), and the potential sources of FIOs, e.g. wastewater treatment works (WwTWs), combined sewer overflows (CSOs), shellfish processing plants (SPPs) and Llanrhidian Marsh. The dashed line is the extended boundary of the modelling domain.

The upstream catchments of this macro-tidal estuary are dominated by rural and agricultural activities, besides large development areas at Llanelli and Burry Port that associated with

important urban and industrial activities. Llanrhidian Marsh at the southern edge of the estuary which floods during high tides was historically used as a grazing area. This marshland with other agricultural tributaries in the upper catchments is identified among the potential sources of diffuse bacterial pollution that contribute to the waterbody. Besides, the primary sources of bacteria that enter this waterbody among others are from the treated and untreated effluents through wastewater treatment works (WwTWs), combined sewer overflows (CSOs) (Kay *et al.* 2008), the industrial flow from shellfish processing plants (SPPs) and the raw flushing bacteria from urban runoff through the streams (Kay *et al.* 2005). Readers are referred to Tables A1.1 and A1.2 in the Appendix for the reasons for failure (RFF) based on the Shellfish Water Directive (SWD) compliance studies (Youell *et al.* 2013a; Youell *et al.* 2013b).

Based on the SWD compliance studies (Youell *et al.* 2013a; Youell *et al.* 2013b), 24 out of the 26 DSWs in Wales complied with the mandatory standard in 2010, while the compliance with the guideline standard is lower than is deemed acceptable, with only 6 of the 26 DSWs (23 %) in 2010. From 11 out of the 26 DSWs that are located in South West Area, 10 of them failed to meet the guideline standard in 2011/2012, with all 11 DSWs failing in 2010/2011. These designated shellfish waters include BI North and BI South, which have failed to achieve the standard of shellfish flesh guideline compliance for all years between 2001 and 2011 for the BI North and only met the guideline compliance three times between 2001 and 2011 for the BI South, as shown in Table 1.1. It is revealing that no distinct pattern of compliance for these DSWs, and with low confidence in any of the improving trend.

Table 1.1: Burry Inlet (BI) North and BI South shellfish flesh compliance with guideline standard, 2001-2011 (Youell *et al.* 2013a; Youell *et al.* 2013b).

Shellfish water	Shellfish flesh compliance with guideline standard										
	2001	2002	2003	2004	2005	2006	2007	2008	2009	2010	2011
BI North	NC	NC	NC	NC	NC	NC	NC	NC	NC	NC	NC
BI South	NC	C	C	NC	NC	NC	NC	NC	NC	NC	C

where C represents comply, and NC represents not comply.

1.4 Water quality monitoring and modelling

Current procedures of microbiological water quality monitoring are based on the concept of faecal indicator organism (FIO), where the concentration of this indicator group is assumed to correlate with that of the major pathogen (Hipsey *et al.* 2008), hence the risk of illnesses (De Brauwere *et al.* 2014). High-frequency monitoring campaigns in more areas with the emergence of historical measurement time-series provide an increasing wealth of complex water quality datasets. It is, however, unfeasible to experimentally monitor the FIO levels at high spatiotemporal resolutions, i.e. not possible for analysing datasets for primary pollution sources and their location, nor for assessing consequences of observed single high *E. coli* concentration at one spot to neighbouring beaches or in the next day event, in bathing beaches context (Schernewski *et al.* 2012). Numerical water quality models are therefore necessary to exploit these datasets.

The use of numerical models in simulating microbiological water quality is increasingly widespread since they can highlight dominant processes controlling organism dynamics, besides can be used to fill knowledge gaps and test management scenarios (Hipsey *et al.* 2008). The real-time prediction of FIO concentrations at recreational compliance points has been achieved using two principal approaches (World Health Organization 2003): i) a statistical (i.e. black-box) model based on relationships of multiple predictor variables which used background conditions for the calibration, and ii) a mechanistic model based on nearshore hydrodynamics that linked to water quality processes (Falconer *et al.* 1998). The black-box model indeed has the advantage over the mechanistic regarding its efficiency for predicting the short-term operational in highly uncertain systems (Francy 2009). This model, however, does not enable an in-depth understanding of the systems as it does not include causal relationships (De Brauwere *et al.* 2014).

The faecal bacteria concentrations in mechanistic models are predicted based on a fundamental principle of mass balance. The mathematical equations expressing their mass should be conserved considering the influence of source/sink into the system, the reaction within the system and transport through the system (Shoemaker *et al.* 1997). These models require the identification and understanding of the primary controlling mechanisms and knowing how to describe these mechanisms mathematically and quantitatively. The parameters involved in the equations describing the faecal bacteria fate in aquatic systems represent interpretable physical, chemical or biological quantities, like mortality rate and settling velocity (De Brauwere *et al.* 2014). These parameters can be made dependent on meteorological, bathymetric, physical,

chemical and biological conditions to consider the environmental variability. The parameter's value can be assigned based on experimental experiences or by fitting the model to available observations.

Faecal bacteria in natural surface waters are generally assumed to come exclusively from external sources due to the hostile aquatic environment (De Brauwere *et al.* 2014). The multiple and variable faecal bacteria sources make the source identification and quantification cumbersome but necessary for the mechanistic modelling study. Faecal bacteria probably enter the model domain implicitly if it does not include the whole drainage network. In that case, the model boundaries can act as real sources, with high-resolution time series concentrations are required for modelling the correct extreme-short-term events (Bougeard *et al.* 2011). Alternatively, the upstream boundary conditions can be obtained from a catchment model that consider all streams and rivers in a watershed (Jamieson *et al.* 2004). This model often includes detailed descriptions of processes and sources on land, in soil and in groundwater, which extensively reviewed by (Bradford *et al.* 2013).

Faecal bacteria are subjected to biotic and abiotic processes that influencing their abundance once they entered natural aquatic environments. The decay rate of faecal bacteria in a model is based on measurements from culture-based methods, that based on batch and field experiments which generally does not include VBNC cells. The decay of faecal bacteria in natural waters is based on experimental data usually follows first-order kinetics. Models of faecal bacteria are considered either as a constant decay that simplifies the modelling approach (Wilkinson *et al.* 1995; Steets and Holden 2003; Shen *et al.* 2006), or as a dynamic decay that depends on biotic and abiotic factors (Hipsey *et al.* 2008), i.e. light intensity, temperature, salinity, nutrients and grazing. Biphasic decreases in *E. coli* concentrations are also reported (Easton *et al.* 2005; Hellweger and Masopust 2008; Hellweger and Bucci 2009; Bucci *et al.* 2011; Bucci *et al.* 2012) with an initial rapid first-order decay followed by a slower decay rate.

1.5 Research objectives

This research aims to improve the understanding of the processes experienced by the faecal indicator organisms (FIOs) that being transported in the estuarine environment from different

sources and impacts to water quality at the sites of interest. In order to achieve this aim, four research objectives were drawn based on the main research question¹ as follows:

- Objective 1: The development and calibration of a hydrodynamic model for the Severn Estuary and Bristol Channel (SEBC) for the understanding of the tidal circulation patterns at different regions during different tidal phases. The accurate current circulation is the key to model the correct transport process in this waterbody as the tidal current is the main vector here that drive the FIO mass.
- Objective 2: The extension of the modelling domain at intertidal floodplains of the Loughor Estuary for the understanding of its influence on the transport process and retention of FIO within this region. The accurate representation of floodplains with its features is the key to model the correct transport process as this effort is an improvement to the hydraulic conductivity in the tidal-creek marsh system.
- Objective 3: The modelling of transport and persistence of microbial tracers in the estuarine environment for the evaluation of the transport process and the behaviour of this tracer in response to the hostile environment. Modelling these processes correctly with the best understanding is the engineering significance to assist the WwTW managers for optimising the plant performance.
- Objective 4: The modelling of transport and decay of FIO from intertidal marshlands as the diffuse source for the evaluation of its potential impacts to water quality at shellfish harvesting waters. The realistic exchange of FIO loadings is the key to model the correct transport process as the actual mass transfer at space and time determines the accurate water quality status within the waterbody.

1.6 Thesis organisation

This thesis was organised into seven chapters. Chapter 1 is an introduction to the thesis. Chapter 2 is a review of the literature for this research. Chapter 3 is about the development and

¹ What processes are experienced by the FIOs that being transported in the estuarine environment?

calibration of a hydrodynamic model for the SEBC. Chapter 4 is about the extension of the modelling domain at intertidal floodplains of the Loughor Estuary. Chapter 5 is about modelling the transport and persistence of microbial tracers in the estuarine environment. Chapter 6 is about modelling the transport and decay of FIO from intertidal marshlands as the diffuse source. Chapter 7 is the conclusion to the thesis based on research findings and recommendations for future research.

Chapter 2: Literature review

2.1 Introduction

This chapter reviews the literature on the related topics for providing understanding along with conducting the research in order to achieve the objectives drawn in Chapter 1.

This chapter is organised as follows: Section 2.2 provided a review of modelling studies for hydrodynamic and water quality at the Severn Estuary and Bristol Channel (SEBC). Section 2.3 provided an overview of the mesh sizing criteria for the unstructured mesh discretisation, including at the open oceans and low-lying areas. Section 2.4 provided an overview of the floodplain roughness evaluation methodologies and their parameterisation strategies in the numerical models. Section 2.5 provided a review on the bacteriophage as a microbial tracer in the hydraulic environment, including their response to the exposure and the modelling strategies. Section 2.6 provided an overview of the release kinetics of faecal indicator organisms (FIOs) from the diffuse source at the land-water boundary. Section 2.7 summarised the chapter.

2.2 Review of SEBC modelling studies

The Severn Estuary and Bristol Channel is an ideal site for a development of tidal renewable projects as it has the second highest tidal ranges in the world, peaking over 14 and 7 m during spring and neap tides respectively near Avonmouth. The estuary located at 240 km west of London, spans South Wales from the South West of England. The estuary including the Bristol Channel is approximately 200 km in length, with a weir located at Gloucester defines the tidal limit at the estuary's head. The estuary has a large intertidal mudflat area and during spring tides, tidal currents are in excess of 2 m/s. Estimated of large suspended sediment level in the estuary at 30 and 4 Mt during spring and neap tides respectively, causing low light penetration and dissolved oxygen concentration in the water column. There is limited aquatic life in the estuary as it has a harsh estuarine regime. The estuary is however protected under the European and international legislative directives due to its unique characteristics.

2.2.1 Hydrodynamic modelling

Several numerical models have been developed and refined to study hydrodynamic processes in the Bristol Channel and Severn Estuary. Uncles (1981) used a 2D depth-averaged hydrodynamic model to predict M2 tide processes and distribution of tidal stress on the seabed in Bristol Channel and Severn Estuary. Uncles (1984) then predicted co-phase and co-amplitude lines for M2 surface elevation and derived estimates tidal energy flux across typical sections according to observed currents data of 1975 to 1977. Evans *et al.* (1990) calibrated 2D depth-averaged hydrodynamic model of Bristol Channel, and investigated effects on water quality and other parameters with the construction of Severn Barrage. Barber and Scott (2000) used a 2D model depth-adapted grid in simulating tidal propagation process at upstream of Avonmouth and used the curvilinear non-orthogonal coordinate system to accurately represent complex estuary shape. Amin and Flather (1995) dynamically linked three 2D models of Bristol Channel with different grid resolutions to a 1D model of River Severn, indicated linked numerical models and harmonic analysis provide identical predictive accuracy. Harris *et al.* (2004) applied 2D depth-integrated, curvilinear boundary-fitted coordinate model to predict tidal currents and sediment transport processes in Bristol Channel, indicated closer agreement between predicted and measured results. Owen (1980) and Stephens (1986) used 3D numerical models to predict tidal elevations and currents in Bristol Channel. Falconer *et al.* (2009) used a 2D total variation diminishing (TVD) finite volume methods of triangular mesh model to evaluate tidal processes and tidal energy in the Severn Estuary on the proposed Severn Barrage and other tidal power options, found that the Severn Barrage potentially reduce the tidal current to cause a changing of the biodiversity system in the estuary, besides reducing flood risk at the upstream of the barrage. Xia *et al.* (2010a) then refined the model to study hydrodynamic impacts and flood inundation extent to the construction of proposed three tidal power projects, with the model particularly suited the flow through barrage and lagoon structures, besides producing a high level numerical accuracy of simulation by adopting procedure of treating wet and dry fronts in solving 2D shallow water equation. Xia *et al.* (2010b) then found the velocity field would become more complex at the barrage area, with the maximum water level at upstream of the barrage would decrease by 0.5 – 1.5 m to reduce flood risk along the estuary.

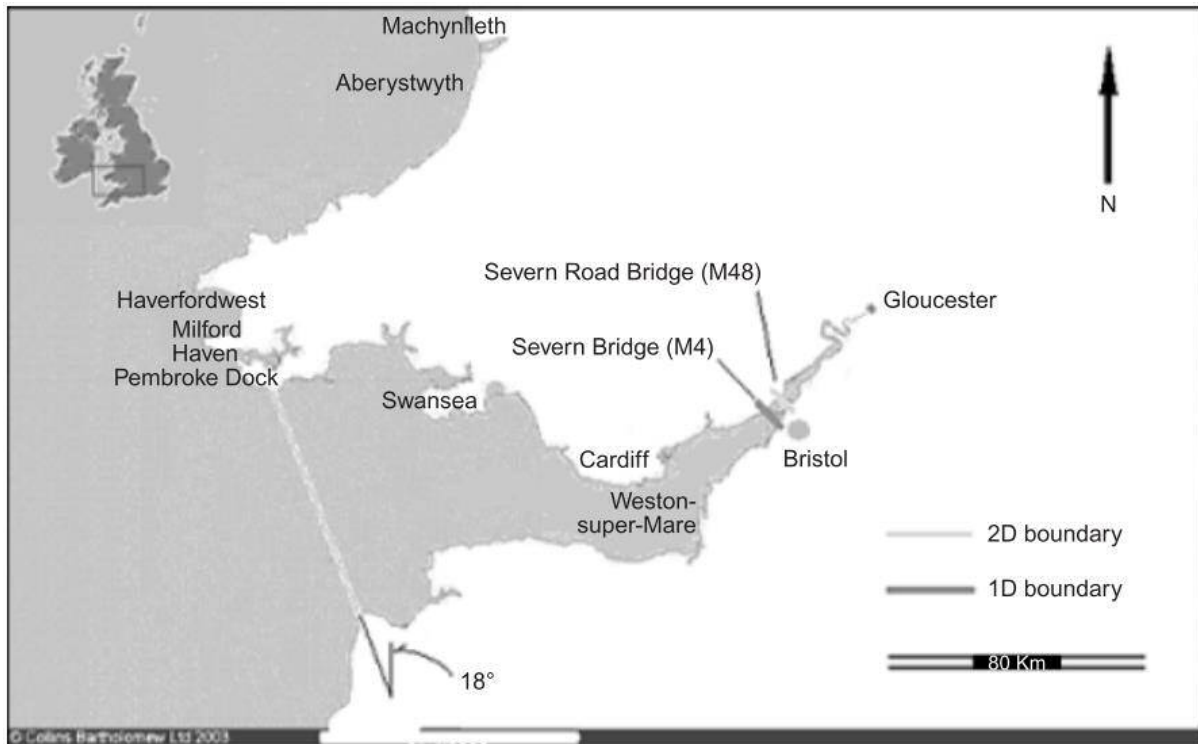


Figure 2.1: Study area, showing one- and two-dimensional boundaries (Yang *et al.* 2008).

2.2.2 Water quality modelling

Several numerical models have been developed and refined to study water quality processes in the Bristol Channel and Severn Estuary. Yang *et al.* (2008) developed a model representing bacteria enterococci disappearance rate due to suspended sediment deposition and increase rate due to bed sediment resuspension, with the resuspension process has shown an increase impacts to the enterococci population level particularly at shallow water sites. Murdoch *et al.* (2010) used a coupled 1D and 2D hydrodynamic-water quality model to compute the advection and dispersion of metal contaminants in the Severn Estuary, with the results showed the sediments potentially act as a sink to mercury and chromium but not to cooper and arsenic as their low partition coefficient make them appear more geochemically in the dissolved phase. Ahmadian *et al.* (2010) used modified numerical models of Divast and Faster to investigate the far-field impacts of the proposed barrage in the Bristol Channel and Severn Estuary, with the linked model gives a good agreement to the limited hydrodynamic data for calibration and validation in predicting suspended sediment and faecal bacteria concentration at selected sites along the estuary. Gao *et al.* (2011) used a combined 1D and 2D numerical models to investigate the impacts of suspended sediment fluxes on the bacteria transport processes in the Severn Estuary, with the bed bacteria concentration plays an important role in governing the concentration of

the overlay water column, especially during conditions of significant sediment transport activity.

Previous review in early 1970 about the Severn Estuary and Bristol Channel (NERC, 1972; Water Pollution Research Laboratory, 1972; Welsh Office, 1974) concludes that knowledge about water, sediments, and biota were lack to provide basis in assessing pollution impacts and maintaining natural resources for planning the economic expansion (Glover, 1984). The Severn Estuary and Bristol Channel is a vulnerable ecosystem to pollution as it bounded by a large urban population, large major industrial area, regions of the most active tourist centre, besides passing catchments of heavily farm areas. This area is very attractive to industries as it has a large capacity to disperse and assimilate pollutants loading (Energy, 1981a). Some issues about water quality impairment at upstream were reported, but the Bristol Channel as a whole system is still considered safe from contamination to their aquatic ecosystems (Owens, 1984; Humphrey et al., 1980).

2.3 Overview of mesh sizing criteria

Mesh sizing criteria is broadly divided into a-priori and a-posteriori (Mazzolari *et al.* 2015). A-priori mesh sizing criteria justifies the mesh size depending solely on the experience, while a-posteriori mesh sizing criteria justifies the mesh size depending on the empirical evidence besides the experience.

2.3.1 A-priori criteria

A-priori mesh sizing criteria used for ocean and coastal areas are the wavelength to grid side ratio (Luettich and Westerink 1995), the topographic length scale (Hannah and Wright 1995; Legrand *et al.* 2007), the maximum bathymetric gradient (Bilgili *et al.* 2006), the coastline resolution (Blain *et al.* 1998; Greenberg *et al.* 2007), and the spatial gradient of input forcing function (Blain *et al.* 1998; Araújo *et al.* 2011).

Legrand et al. (2007) demonstrated the ability of anisotropic unstructured meshes to adequately address the challenge of simulating the hydrodynamics occurring in the Northwestern European continental shelf, the continental slope and the neighbouring ocean. For evaluating

the parameters of two target element size function () and the privileged direction () in a mesh refinement strategy, authors considered some aspects of tidal propagation physics and a numerical accuracy constraint related to the pressure gradient in regions of the seabed that exhibits steep slopes. The metric tensor was built following the steps of i) setting the privileged direction () along the direction normal to the bathymetry gradient, ii) evaluating the speed of external gravity waves in the domain of interest (i.e. a first estimate of size target), and iii) estimating the size target of . The mesh refinement strategy was able to resolve the continental shelf, the shelf break and the seamounts.

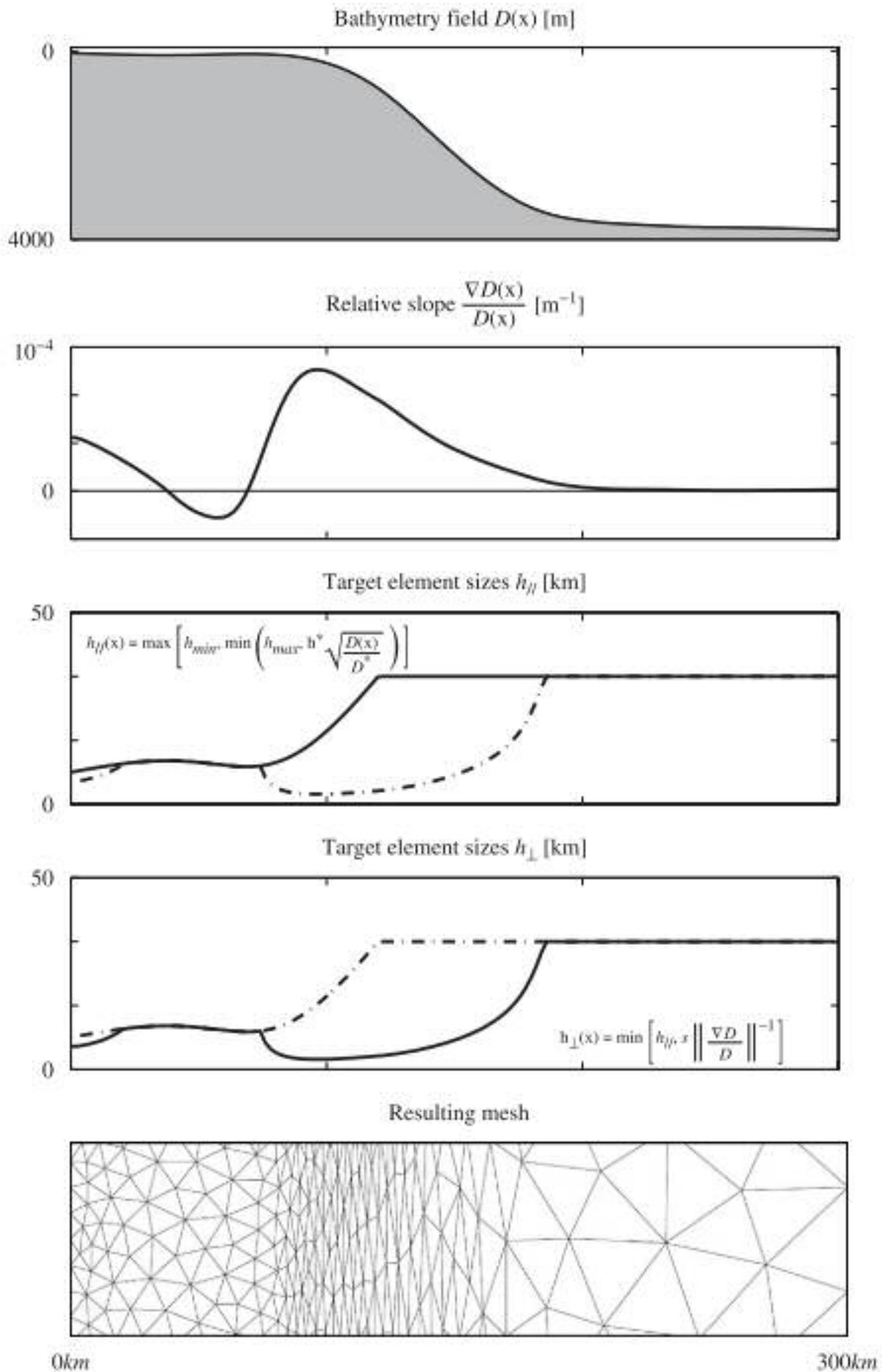


Figure 2.2: Illustration of the anisotropic mesh refinement strategy for an idealised bathymetric profile (Legrand *et al.* 2007).

Lambrechts *et al.* (2008) developed a high resolution, efficient and realistic hydrodynamics model of the whole Great Barrier Reef of complex bathymetry and topography. Authors defined the mesh resolution depending on two a-priori criteria (i.e. to be proportional with the square root of water depth and on the distance to islands and reef), which were blended together for a high resolution in the vicinity of reefs and islands whilst depending only on the bathymetry elsewhere (Legrand *et al.* 2006). The eddies simulated by the two- and the three-dimensional small-scale models were quite similar though the resolution of the former model was coarser.

Greenberg *et al.* (2007) reviewed certain aspects of spatial resolution requirements of oceanic circulation models and the approaches taken in specific applications. Among the resolution issues, the authors addressed the aspect related to the bottom topography at the open ocean, the shelf break and bank sides, and the coast. There were about three quantitative relations (though many qualitative ones) that should influence mesh resolution: i) the Courant number, $C = \frac{u \Delta t}{\Delta x}$, where Δt is the time step, Δx is the grid spacing, u is the acceleration due to gravity, and h is the bathymetric depth (Foreman 1984; Le Provost *et al.* 1995); ii) the topographic length scale, $L = \frac{u^2}{g \Delta z}$ (Loder 1980; Hannah and Wright 1995; Lynch *et al.* 1995); and iii) the localised truncation error estimator (Hagen and Parrish 2004a).

The multi-criteria meshing method (Mazzolari *et al.* 2015) relies on the evidence that modelling the complex multi-scale phenomena need the inclusion and proper reproduction of different factors (i.e. astronomical and meteorological forcing, bathymetry and topography, domain geometry, boundary conditions, significant hydraulic features and computational constraints) that varying over a specific spatial scale. The method associates to each factor considered relevant for the domain discretisation (i.e. resolution criteria) described in terms of a node spacing function (NSF):

$$\Delta x_i = \frac{C_i}{\sqrt{f_i}} \quad \text{Eqn. 2.1}$$

where Δx_i is the node distance requirement for the i -th criterion, and (x, y) the plane coordinates inside the computational domain.

For ocean and coastal shallow water models, Mazzolari et al. (2013) defined a multi-criteria approach to the task of mesh generation. The final NSF to be read in the meshing algorithm through background unstructured mesh was calculated as:

$$\text{Eqn. 2.2}$$

where λ to λ_{max} (i.e. criteria of wavelength-to-grid size ratio, topographic length scale, inverse bathymetry gradient, horizontal length scale and radial function respectively) operate as minimization condition on final target size function, and CFL (i.e. criteria of Courant condition) sets minimum size mesh elements can have. The distribution of element shape quality index, QI , was shown the high number of elements with QI almost attaining 1 that proved the good quality of the mesh.

2.3.2 A-posteriori criteria

A-posteriori mesh sizing criteria (i.e. adaptive remeshing techniques) has been developed as the mesh resolution needed for the result convergence is generally not known a-priori. The a-posteriori remeshing technique is done by optimising an error-based function that may be derived either from the bathymetry/topography field discretisation (Gorman *et al.* 2008) or from the flow solution residual per-element basis (Oden *et al.* 1990; Behrens 1998). The localised truncation error analysis (LTEA) is a recent a-posteriori meshing approach (Hagen *et al.* 2000; Hagen *et al.* 2001; Hagen *et al.* 2002; Hagen and Parrish 2004b; Hagen *et al.* 2006) that estimates error from the discretisation of linearised shallow water equations. The localised truncation error analysis with complex derivatives (LTEA+CD) (Parrish 2007; Parrish and Hagen 2009; Bacopoulos *et al.* 2011) introduces the estimation of spatial variable bottom stresses and Coriolis force in the error expression.

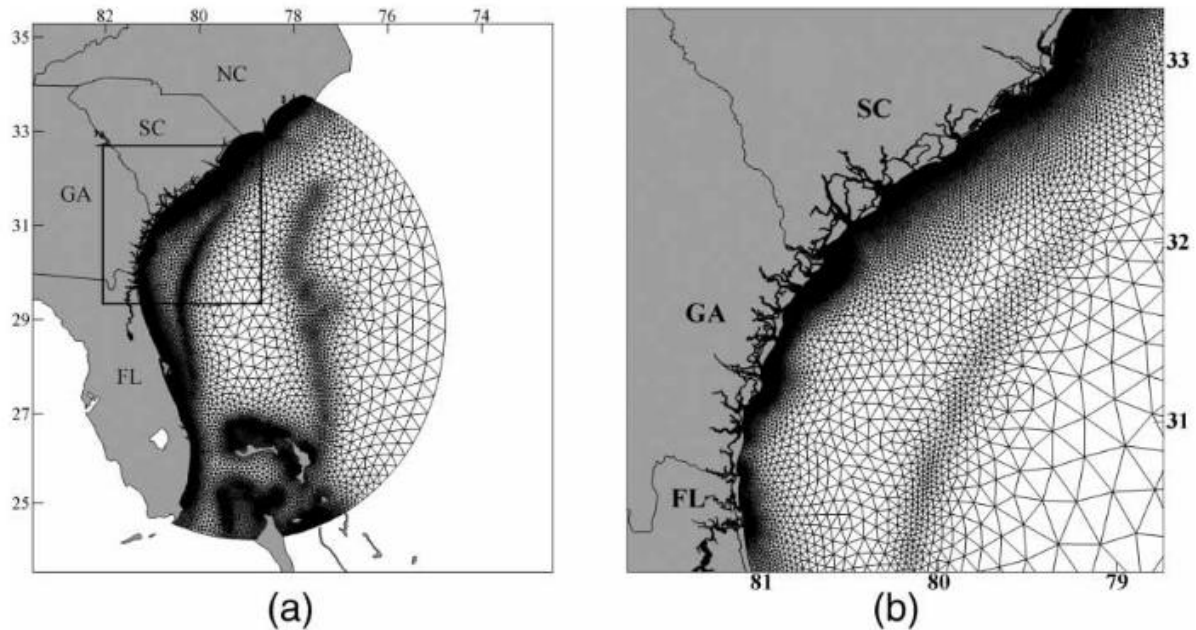


Figure 2.3: (a) Existing mesh of the SAB and (b) inset shows coast details (Bacopoulos *et al.* 2011).

The LTEA+CD is based on the principle of redistributing the nodes of an existing mesh in order to get the localised truncation error as uniform as possible all over the computational domain (Mazzolari *et al.* 2015). The truncation error is obtained as the difference between continuous and discrete forms of the non-conservative shallow water momentum equation (i.e. in its linearised harmonic expression, without the inclusion of advective terms, using complex derivatives, and of the spatially variable bottom stress and the Coriolis force). Modifications to the original algorithm for exploring its behaviour when the re-meshing includes areas not continuously wetted are needed, as the intertidal and supratidal depths are fictitiously decreased in order to assure that all elements remain wet during the simulation. The procedure (i.e. automatized within the mesh generation toolbox of surface-water modelling system) consists of four steps:

1. A simplified linear ADCIRC simulation is run with an existing mesh, by forcing the ocean boundary nodes with the M2 tide amplitudes and phases extracted from the Le Provost tidal database. Nodal factors and equilibrium arguments are set to 0. Minimum water depth is set to 1.25 times the maximum M2 amplitude – for model runs in a wet mode within the estuary.

2. An M2 harmonic analysis of the elevation and velocity output is performed: given the velocity component u and v computed respectively in the x and y direction, the relative and the harmonic velocities are calculated on a per node basis.
3. The localised truncation error is calculated as (Parrish and Hagen 2009):

$$\text{---} \quad \text{Eqn. 2.3}$$

where ω is the frequency of the considered harmonic constituent, Δx , the local element size. The suffix 0 refers to the central node of the valence cell, which is the group of six equilateral triangles superimposed to the mesh and having in common the mesh node "0". σ is the module of the spatially variable bottom stress, calculated on a per node basis, and Ω is the Coriolis term. The superscript "6" refers to the order of complex differentiation. It is possible to set a target σ and to solve for Δx , which becomes the target NSF of the adapted mesh.

4. A target node number for the perspective mesh is set by the user. The NSF values are scaled through an iterative calculation to generate a mesh matching the number of nodes within a given tolerance. A smoothing function is applied to limit the maximum area change transition between adjacent elements. The smoothing is anchored to the minimum value, means that the area bound is set from the smaller to the bigger size.

Bacopoulos et al. (2011) analysed the ratio of scaled results to existing element sizes within the “shallow, shelf, and seaward regions” and along the coastlines between adjacent inlets. Authors derived target element sizes by arranging Equation 2.3 into the form $\Delta x = C \cdot \sigma^{-1/6}$ (i.e. C is an arbitrary scale factor and σ is a deterministic factor), selected a uniform value for C (i.e. to indirectly specify maximum gradient in target element size distribution) and applied Gaussian smoothing to Δx on a domain-wide basis before computing target element sizes (Parrish and Hagen 2007). General resolution patterns along the shelf break and at the edges of Blake’s Plateau and the Bahamas Bank were similar between the existing mesh and target element sizes, while the later was larger the former in open areas (i.e. over the shelf and Blake’s Plateau and in deeper waters) and along coastlines between adjacent inlets.

Mazzolari et al. (2015) assessed the response of a shallow water model when different meshing criteria are applied to the multi-scale ocean-to-basin domain of heavily influenced by wetting and drying hydrodynamics. In the LTEA+CD mesh convergence study, authors iteratively applied the method starting from an initial a-priori mesh of 70 m uniform estuary discretization (i.e. first and second series of the adapted meshes were interpolated to the underlying DEM and from the a-priori initial mesh respectively), with the convergence rate through performance indicators was higher in the reproduction of the free surface water elevation than the currents. Authors also tested a series of the generated mesh according to different meshing criteria, with the indices were not univocally identified an optimal discretisation for the free water surface and currents but was increased the accuracy in reproducing the spatial extension of the wetted area with the LTEA+CD method.

2.3.3 Mesh discretisation at floodplains

Mesh discretisation criteria for intertidal and low-lying areas are more difficult to be expressed analytically due to complex bathymetry and topography and local scale processes. Jones and Richards (1992), Bunya *et al.* (2010) and Westerink *et al.* (2008) recommend including all relevant hydraulic features (i.e. likely to convey/stop inland water propagation) into the discretisation.

2.3.3.1 Significance horizontal length scales

To determine significant horizontal length scales, Bates et al. (2003) conducted a variogram analysis based on the floodplain topography dataset (Marks and Bates 2000). The analysis was indicated that the significant spatial dependence between the topographic point existed below a grid spacing of approximately 10 m.

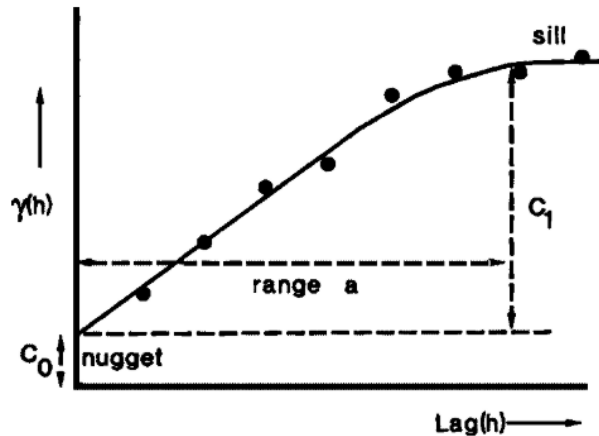


Figure 2.4: A sample model variogram showing range, nugget, sill (Bates *et al.* 2003).

2.3.3.2 Topographically significant points

To determine topographically significant points in the dataset, Bates *et al.* (2003) described methods including the very important point (VIP) method (Chen and Guevara 1987), the hierarchy transform (HT) method (De Floriani *et al.* 1984), and the drop heuristic (DH) method (Lee 1989). The VIP method that was used passed a 3 x 3 window over all grid points and resulted in differences between surfaces of the topographically independent and the topographically optimum which were likely to be hydraulically significant.

In flood inundation models development, Bilskie *et al.* (2015) presented a reproducible and novel semi-automated method for extracting vertical features from the Lidar DEM. To conduct detailed inundation flow simulations for populated areas, Tsubaki and Fujita (2010) developed a comprehensive method using LiDAR data as the source of the land features information. To ensure hydrodynamic blocking features are retained, Hodges (2015) developed new methods for upscaling a digital elevation model (DEM) of topography.

For handling the model stability and system connectivity problems, Li and Hodges (2018) developed practical approaches to correctly model the salinity transport in coastal marsh systems. To enable street-resolving hyper-resolution simulation for a large area, Noh *et al.* (2018) developed a hybrid parallel code for coupled 1D-2D urban flood modelling by combining OpenMP and MPI. In order to model daily flood maps over a 663-ha wetland area, Rapinel *et al.* (2018) combined the high spatial resolution LiDAR data with the high temporal resolution in situ piezometric probe measurements.

2.3.3.2.1 Vertical feature extraction

For detecting raised features (i.e. road beds) to be included in an unstructured mesh, Bilskie et al. (2015) expanded the methods upon the procedures originally described for the Tampa Bay region (Coggin 2008). Boundary lines that are meeting the length, elevation and vertical curvature criteria were extracted for very small area watersheds. The line vertices were distributed to the approximate desired local element size based on the size function of the initial finite element mesh. Distances between separate lines, duplicate lines, small line segment angles, and disconnects between upstream and downstream valley lines were manually assessed prior to the unstructured mesh triangulation. From the aerial imagery comparison, the MSAL model (i.e. contains vertical features along with crest elevation) produced the more accurate simulated inundation extent, followed by the MSAL_noVF_z, and MSAL_noVF model (i.e. contains vertical features barring with crest elevation and nor vertical features neither crest elevation respectively).

For mapping and city modelling purposes, Tsubaki and Fujita, (2010) extracted buildings following three sequential steps: i) the segmentation of domains that belong to the same building, ii) tracing the building boundary shape, and iii) regularization of the boundary (Weng and Quattrochi 2006; Sampath and Shan 2007). By arranging the grid nodes at the edge points, false ground and false building errors (i.e. the categorised area of the correct building raster that compares to the generated grid) were drastically reduced.

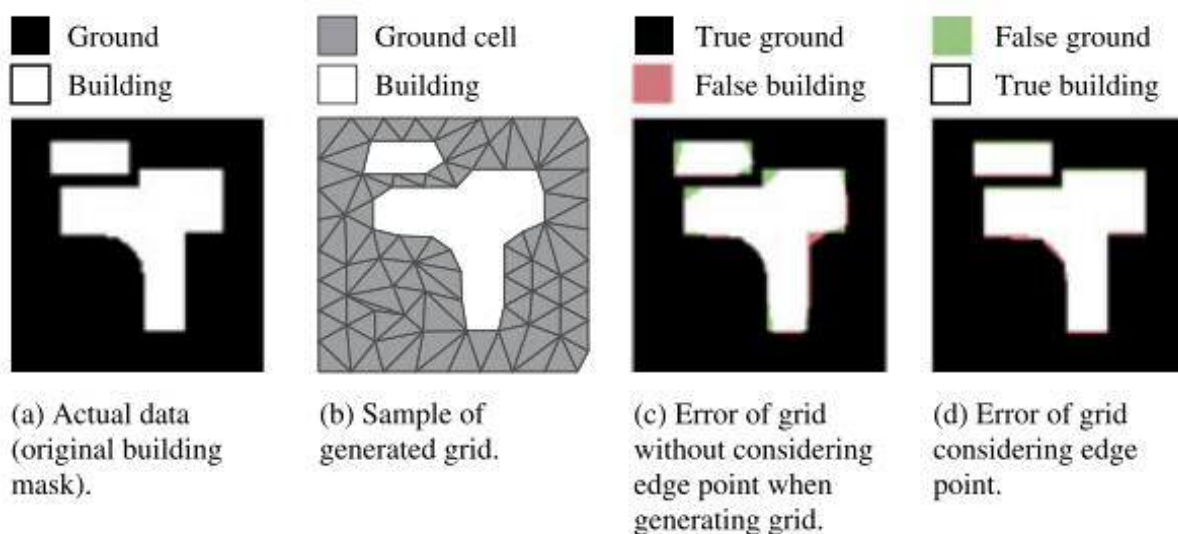


Figure 2.5: Sample of correct building raster, generated grid sample, and error of two different sample grids. (a) Actual data. (b) Sample of generated grid. (c) Error of grid without considering edge point when generating grid. (d) Error of grid considering edge point (Tsubaki and Fujita 2010).

To produce a coarse Cartesian grid at some scale, Hodges (2015) processed the Lidar DEM following the five steps procedure: i) creating a fine-grid background topography, ii) creating a coarse-grid representation of background topography, iii) computing the difference between fine and coarse topography, iv) identifying contiguous objects that occur in the difference set, and v) identifying blocking objects and assigning elevations to grid cell faces. This approach distorted the shape of a blocking feature (i.e. making it rectilinear along grid cell faces) but retained its critical hydrodynamic blocking height characteristics and spatial continuity within the topographic model.

2.3.3.2.2 Channel network extraction

The channel-representation with meshes that simplify the topography is known to affect the routing of flow, caused the displacement of shoreline, the removal of local minima that increased the volume of static water (Caviedes-Voullième *et al.* 2012), and the disappearance of flow variability (Horritt *et al.* 2006). The coarser meshes in the context of groundwater-stream interactions (GSI) modelling (Käser *et al.* 2014), besides is known to delay the arrival time of peak flow due to the increase in channel lengths, also reducing the surface area of exchange between groundwater (GW) and surface water (SW) due to obliterate creeks and low-order streams at the catchment scale.

Following the up-scale approach (Hodges 2015) using a median filter, Li and Hodges (2018) created a coarse-grid raster and a fine-scale of the resolvable background topography representation. Contiguous “positive” and “negative” objects that were not presented in the coarse-grid bathymetry were identified using the difference between the background topography and the fine-resolution topography. Channel grid cells that were identified as the negative objects were resolved at the diagonally connected cells to maintain the connectivity. Results show that different grid resolutions (i.e. 30 m and 15 m) lead to different surface connectivity patterns and neither of these resolutions preserves the 1 x 1 m surface connectivity.

For the mesh generation, Noh et al. (2018) selectively defined variable grid sizing from the non-uniform but structured quadrilateral grid scheme (Liang 2011) as the hyper-resolution grid along or in the vicinity of the road while as the coarser resolution grid for other types of land cover. The analysis was shown that while the terrain that was depicted at the coarse resolution prone to distortion as the width of flow path was smaller than the grid resolution, the hyper-resolution modelling was able to depict the stormwater flow at small scales more realistically.

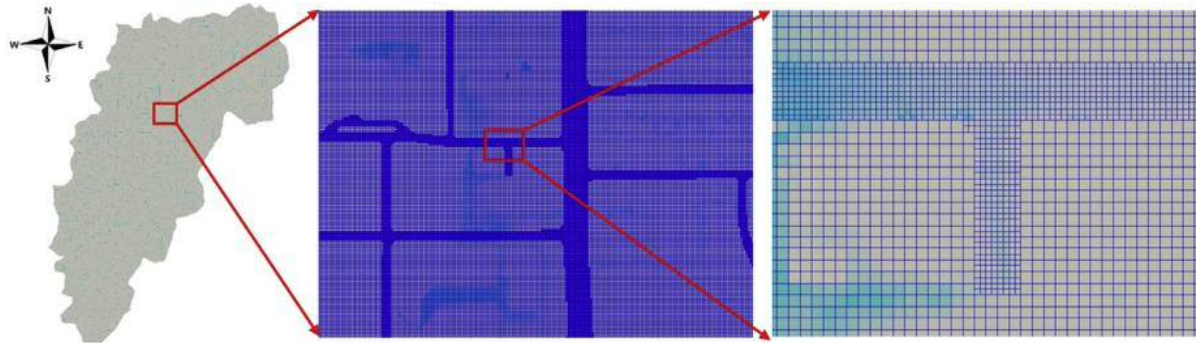


Figure 2.6: An example of variable grid sizing (Noh *et al.* 2018).

To model the flood extent at a daily time step, Rapinel et al. (2018) transformed the LiDAR-based DTM dataset into a binary raster (0 = unflooded; 1 = flooded) according to the measured daily water level by the piezometric probe. Not considering the importance of the hydrological network, vegetation resistance and infiltration in the flow modelling could explain some errors in their simulation

A number of attempts to extract river and channel networks from DEMs and high-resolution lidar data, including flow direction (Jenson and Domingue 1988; Lohani and Mason 2001; Poggio and Soille 2012) and curvature based methods (Liu et al., 2015; Mason et al., 2006).

Jenson and Domingue (1988) developed software that uses neighbourhood techniques as well as iterative spatial techniques. Lohani and Mason (2001) developed a technique for extracting tidal channel networks from Lidar data using a semi-automatic approach. Poggio and Soille (2012) assessed the effects of pit removal methods, data source and flow-routing algorithms on the position of river networks.

Mason et al. (2006) developed a semi-automatic technique to extract tidal channel networks from Lidar data. Liu et al. (2015) proposed an automated method for extracting tidal creeks (AMETC) from Lidar DEMs based on high-level image processing (HLIP) techniques.

For the applications of specific watershed delineation, automatic delineation of sub-watersheds, watershed linkages, drainage networks and overland paths, Jenson and Domingue (1988) produced three data sets of the conditioning phase which were further processed, in the order of i) DEM with depressions filled, ii) data set indicating the flow direction for each cell, and iii) flow accumulation data set. Based on visual comparisons of digitised, manually delineated networks and automatically derived networks on a raster display device, the main channels were described almost identically.

To emulate manual interpretation of tidal channel networks using computer vision techniques, Lohani and Mason (2001) proposed a new approach of sequentially applied image processing for thresholding and joining the channel fragments. The relationship between the drainage density and the watershed area was changed from one part of the network to another, with the values of the scaling exponent of length to the area () were also shown a considerable variation from 0.57 (Rinaldo *et al.* 1999).

To calculate flow direction and flow accumulation, Poggio and Soille (2012) used methods of steepest descent (D8) (O'Callaghan and Mark 1984), multiple flow direction (MFD) (Holmgren 1994) and DInf (Tarboton 1997). The average distance of the extracted river networks calculated from the reference river network using the proposed algorithm by Saito and Toriwaki (1994) was shown that single-flow direction methods provide more accurate positioning in the area of generally well-defined drainage.

Mason et al. (2006) implemented a multi-level knowledge-based approach, whereby low-level algorithms first extract channel fragments based mainly on image properties then a high-level processing stage improves the network using domain knowledge (Wang and Newkirk 1988) of the water flowing downhill under gravity. The technique was superior to standard methods of river network extraction when applied to tidal channels (Bilskie *et al.* 2015).

Liu et al. (2015) extracted tidal creeks from DEMs using a multi-window median neighbourhood analysis (MNA), a multi-scale and multi-directional Gaussian-matched

filtering (GMF) method, and a two-stage adaptive thresholding (TAT) algorithm, with two Lidar DEM datasets of the different spatial resolution were used to test the methods. The visual inspection showed that the AMETC was successfully extracted most of the tidal creeks with the true positive rate (TPR) metric reached 95% – the AMETC was the best among the compared methods of the optimal-elevation threshold method (OCTM), the optimal-curvature threshold method (OCTM), and the D8 method.

2.3.3.3 Features incorporation into mesh discretization

The AFM approach (Hoffmann and Chiang 1993) was applied together with the Laplacian smoothing (Field 1988; Canann *et al.* 1998) for the unstructured grid generation and the overall improvement of the grid quality, respectively (Tsubaki and Fujita 2010).

The strategies in optimising the mesh design for a river network are through minimising the number of nodes while ensuring the process representation and the model convergence (Käser *et al.* 2014). The simplest representation of a channel involves the “V-shape” form of two cross-sectional elements. Defining the size of these elements and ensuring the central segments to match the channel axis are required for the adequate mesh.

For the setting up of a reliable computational domain, three steps for representing the actual topography were proposed (Costabile and Macchione 2015); there are the grid generation process, the grid quality checking and the grid suitability to the topography. With the use of the “unchecked grid” simulation, the result would lead to the underestimation or overestimation of water depths or flooded areas respectively depending on the given conditions.

For the insertion of man-made structures including bridges, buildings and weirs to the computational domain, techniques of the local grid refinement were proposed (Costabile and Macchione 2015). The simulation of varying effects across the section of piers, a detailed computation of backwaters at upstream, and the approximation of high topographic gradients of weirs were allowed with accurate geometric descriptions coupled with the local grid refinement.

2.3.3.4 Sub-grid-scale parameterization

To parameterise the sub-grid-scale algorithm (Bates and Hervouet 1999) for dynamic wetting and drying, Bates et al. (2003) used the leftover data from the mesh generation. A large planar element was replaced with a set of smaller sub-grid planar triangles from a Delaunay triangulation of the sub-grid topographic points. The functions that were calculated for the River Stour Lidar data were discretised in terms of 20 piecewise linear segments representing 5% increments of inundation extent.

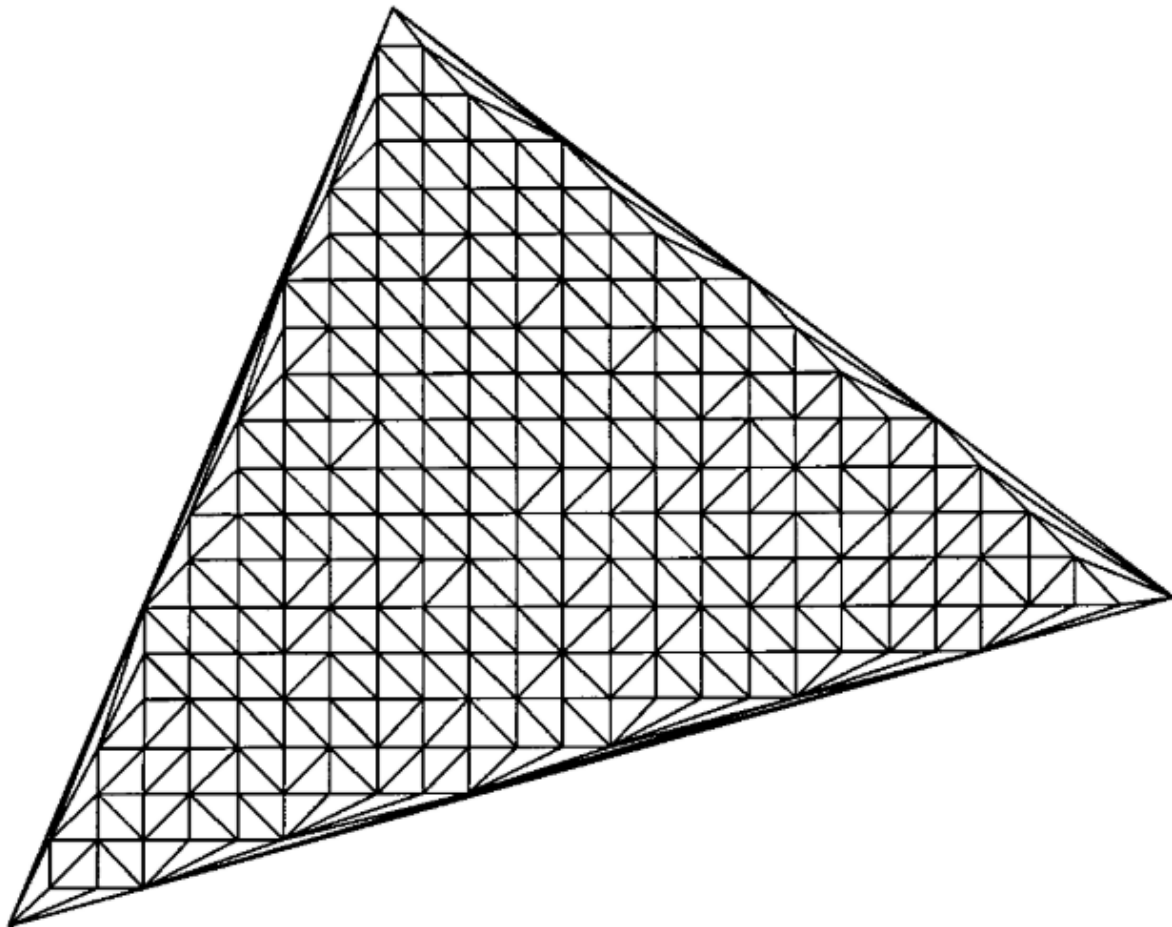


Figure 2.7: An example of a subgrid Delaunay triangulation developed for a single finite element from the mesh. The element contains 219 individual x, y, z -points obtained from laser altimeter survey from which a triangulation consisting of 439 smaller triangles can be calculated (Bates and Hervouet 1999).

To obtain a roughness value for each cell of the domain, Casas et al. (2010) incorporated an explicitly established relation between the depth-averaged velocity from a mixing layer theory (Katul *et al.* 2002) and Manning's n into the 2-D flood model. The Digital Roughness Model

(DRM) along with the local water depth at a given mesh resolution were used to provide a varying spatio-temporal parameterisation of surface friction in the flood model.

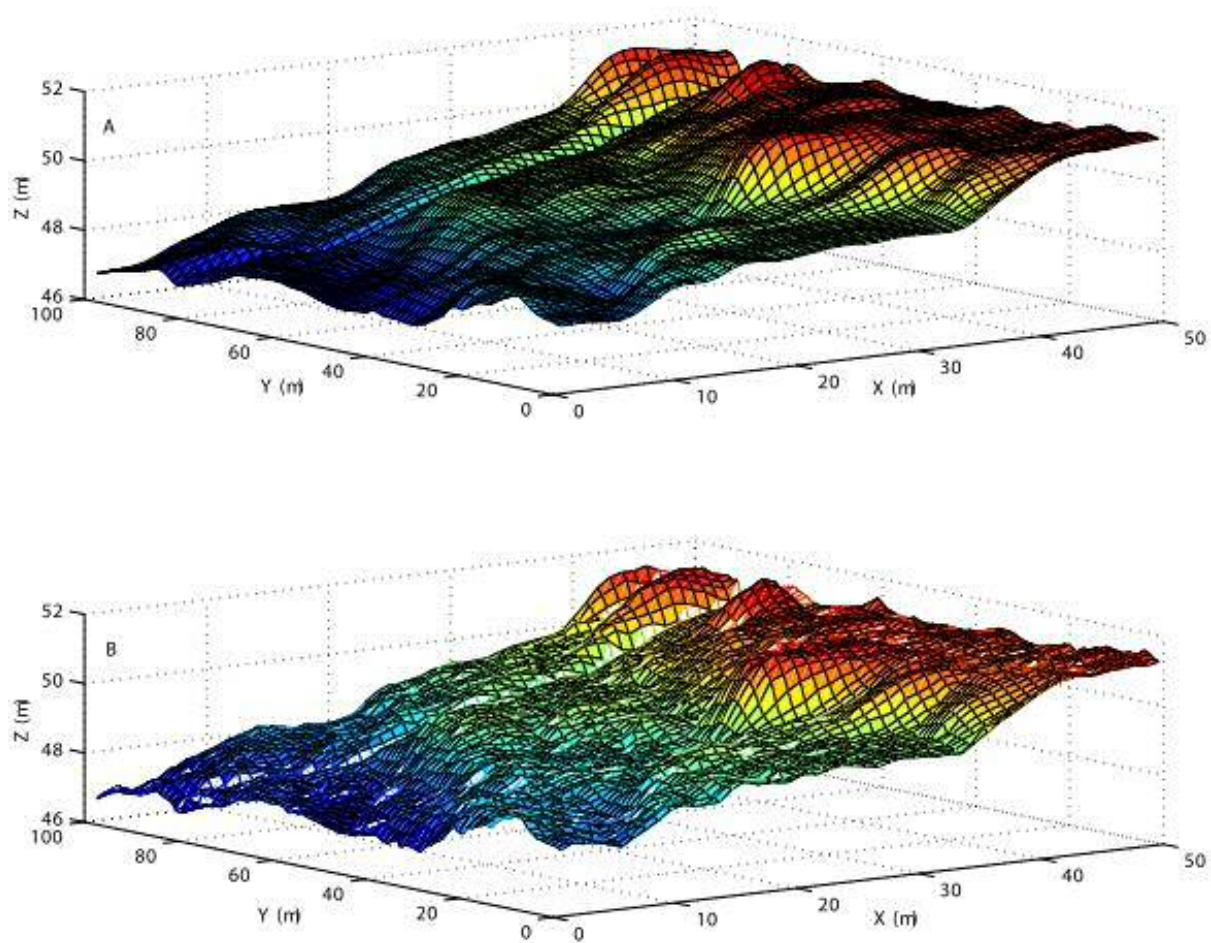


Figure 2.8: Generation of DEMs with additional topographic information. (A) Reference DEM, (DEM^{ref}); (B) DEM with additional topographic content of ± 25 cm ($DEM^{\pm 25cm}$) (Casas *et al.* 2010).

2.4 Overview of floodplain roughness parameterisation

The previous works that concern with evaluating the floodplain roughness that principally causes by the vegetation are outlined by Sellin *et al.* (2003), among them are: i) USDA Soil Conservation Service and related methods, ii) matching photographs, iii) rigid non-submerged vegetation roughness, iv) rigid, non-submerged, incremental vegetation roughness, v) rigid, submerged, incremental vegetation roughness and vi) flexible roughness (non-submerged). Arcement and Schneider (1989) recommended the first two methods to be used for approximating the roughness values before undertaking further analyses.

2.4.1 USDA Soil Conservation Service and related methods

Cowan (1956) developed a procedure for calculating open channel Manning's n values based on the summation of global resistance factors and multiplication with the meandering factor. US Department of Agriculture (1963) Soil Conservation Service adopted the formula and gave a table of appropriate values. Aldridge and Garrett (1973) further modified the formula for use on floodplains, that written as follows:

Eqn. 2.4

where n_0 is the base value of n for the floodplain's natural bare soil surface, C is the correction factor for the effect of the surface irregularities on the floodplain, K is to describe resistance due to the variation in the shape and size of a river channel (i.e. not applicable to the wide floodplain region, hence set to zero), V is the value for obstructions on the floodplain, Ve is the value for vegetation on the floodplain, and S is the correction factor for sinuosity of the floodplain outer boundaries (i.e. equal to 1.0 if flow over the floodplain is assumed to follow straight paths).

Values of n_0 and C are given in tables from Aldridge and Garrett (1973). Values of K for different floodplain types are available: natural channels (French 1985), crops (Ree and Crow 1977), vegetation (Aldridge and Garrett 1973), and heavily vegetated floodplains (Arcement and Schneider 1989).

Using the modified Manning's equation (Petryk and Bosmajian III 1975), Medeiros et al. (2012) determined the bottom friction coefficient with the base Manning's value (n_0) was the summation of contributions from the topsoil (n_{top}), microtopography or surface irregularities (n_{micro}), obstacles in the flood plain (n_{obst}) and low-lying vegetation (n_{veg}). The value for n_0 was calculated based on the in situ soil sample (Limerinos 1970; Marcus *et al.* 1992), with the average estimates of n_{top} , n_{micro} and n_{veg} were obtained from each sites.

Based on land cover information as given in the 2011 National Land Cover Database (NLCD) (Arcement and Schneider 1989; Kalyanapu *et al.* 2010; Homer *et al.* 2012; Medeiros *et al.*

2012; FEMA 2014), Saleh et al. (2017) deterministically estimated the Manning's n using a look-up table which was not treated as a calibration parameter (Schubert *et al.* 2008; Gallegos *et al.* 2009; Schubert and Sanders 2012).

2.4.2 Vegetation drag model

In a tidal marsh, Temmerman et al. (2005) quantified the relative impact of water level fluctuations, micro-topography and vegetation on the spatial flow and sedimentation patterns. In tidal creek-marsh systems, Blanton et al. (2010) showed the sensitivity of numerical simulations of pollutant transport and dispersal to uncertainties in bathymetry and marsh grass density.

For optimal values of the bottom roughness height, z_0 and horizontal eddy viscosity, ν_{xy} , Temmerman et al. (2005) used different combinations and compared the simulated and observed flow velocities time series at the creek system. The three-dimensional plant-flow interaction model was used at the vegetated marsh platform, with the average diameter and numbers of rigid cylindrical plant structures were horizontally defined by assigning vegetation types based on a vegetation map (Koppejan 2000). The flow model calibration resulted in an optimal z_0 value of 0.006 m and ν_{xy} value of 0.0005 m²/s. The flow velocities simulation on the vegetated marsh platform also correspond reasonably well with the field measurements.

To perform the sensitivity of different marsh grass densities to the computed flows and dye tracer concentrations, Blanton et al. (2010) used a frictional drag model specific to marsh grass (Fischer-Antze *et al.* 2001) using a single density value at drying and wetting nodes. The simulated concentration time series of the first tidal cycle severely distorted and reduced far below measured values in subsequent cycles when the model's marsh grass density increased from 0.1 to 3.0 m²/m³. The baseline simulations using low marsh grass density of 0.1 m²/m³ largely compensated the lack of smallest tidal creeks that produced a better agreement between measurement and simulation.

2.4.3 Floodplain roughness parametrisation

Bilskie et al. (2015) presented a reproducible and novel semi-automated method for extracting vertical features (i.e. used in flood inundation models development) from the Lidar DEM.

Authors spatially assigned Manning's n in the floodplain based on the Coastal Change Analysis Program (C-CAP) post-Katrina LULC and other datasets. Bottom friction for continental shelf was based on bottom sediments composition (i.e. 0.022 for sand and 0.012 for mud) (Buczowski *et al.* 2006), was set to 0.025 and 0.012 respectively along the shoreline and depths greater than 200 m (i.e. interpolated to local shelf value at depths less than 5 m) and were assigned to 0.03-0.035 for narrow, shallow, meandering channels (Dietrich *et al.* 2012; Martyr *et al.* 2012).

Schubert *et al.* (2008) approached the problem of flood inundation modelling with an unstructured mesh (i.e. Godunov-based finite volume solver) and examined semi-automated methods of transforming geospatial data to support mesh generation, building representation and resistance parameter estimation. Authors considered the resistance parameter estimation from the combination of landcover classification and feature height data, which was computed for each pixel using a linear scaling model (i.e. depending on user-defined minimum and maximum resistance coefficients for each feature class, and weighting function based on landscape feature height). The observed flood extent to different resistance distributions in both the low-flow and high-flow cases were at least most sensitive at one of four stations.

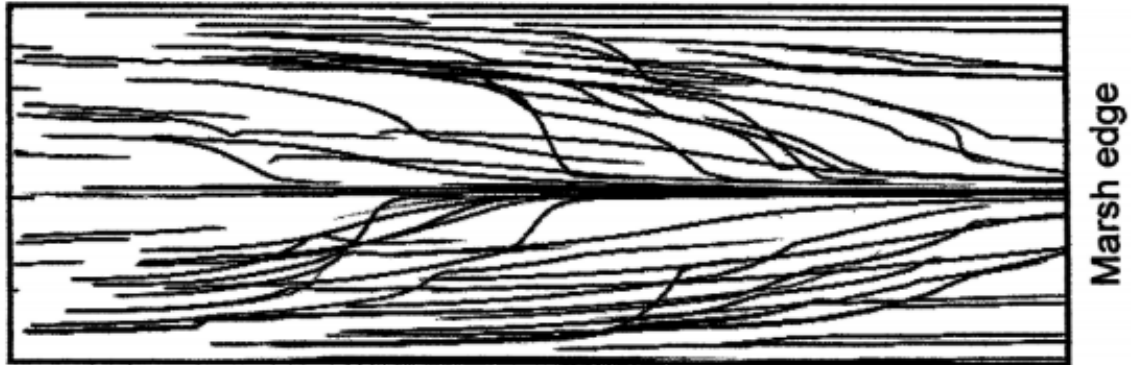
Sullivan *et al.* (2015) characterised the role of small-scale topographic structure on salt marsh circulation and current complexity and the role of this complexity on the cycling and distribution of suspended and dissolved constituents. Authors applied the bottom roughness as calibration variable by adjusting Manning's n values that constrained for the vegetated and unvegetated marsh. The results compared to observations obtained the highest model efficiencies (MEs) by applying Manning's n of 0.017 for the unvegetated marsh and 0.10 for the vegetated marsh, i.e. similar to French (2003).

Azinheira *et al.* (2014) compared the hyporheic solute retention induced by in-stream structures with the surface solute retention on inset floodplains. Authors estimated Manning's roughness coefficient (n) using methods outlined by McCuen (1989) and Arcement and Schneider (1989) for the main channel (i.e. the range of 0.025 to 0.05) and the inset floodplain (i.e. the range of 0.05 to 0.1) respectively, with the values of 0.03 and 0.07 were used. From the sensitivity analysis of varying the n values combination (i.e. base, minimum, maximum), the maximum flow and residence time changes occurred when using the minimum n for channel and the

maximum n for inset floodplain, with no changes in the stored mass on the inset floodplains with varying n .

Lawrence et al. (2004) considered the role of marsh channels in water transfer into and from marsh platforms and addressed two aspects of marsh channel systems arising from the equilibrium model (Allen 2000). Authors used Manning's n of 0.07 for the marsh platform surface with the considered sensitivity analysis up to 0.5 (i.e. very rough boundary), and 0.03 for the marsh channel (i.e. moderately rough bed and banks). The higher roughness values slightly increased and delayed the peak discharge during marsh flooding, while decreased with increasing surface roughness during marsh draining. The principal pathway for the marsh with Manning's n of 0.07 is from marsh edge towards the top, with pathlines majorly left the channel at a significant angle for the very rough marsh.

a)



b)

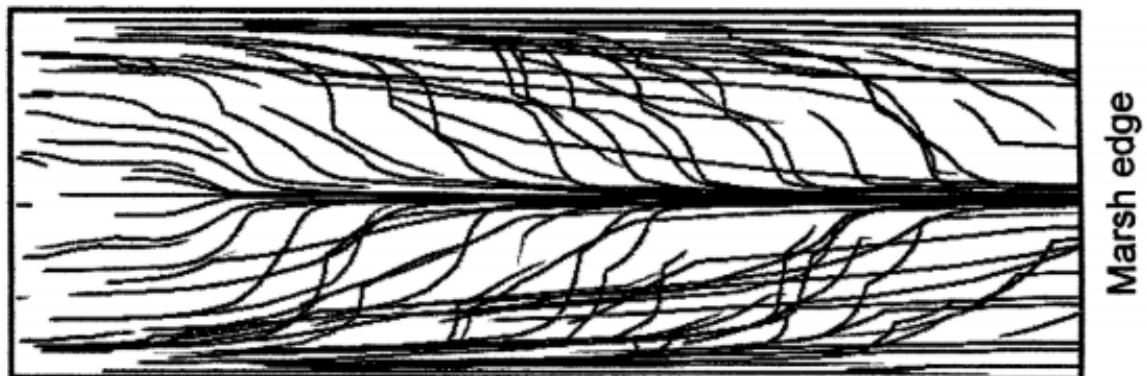


Figure 2.9: Particle tracers for the marsh with channel width of 5 m for (a) moderately rough marsh surface with Manning's $n = 0.07$; and (b) very rough marsh surface with $n = 0.5$ (Lawrence *et al.* 2004).

French (2003) considered the airborne Lidar application with the numerical hydraulic model of morphologically complex estuary in southeast England. Authors specified the bottom friction via Manning coefficients estimated separately for each of four principals 'feature' types: subtidal channel, intertidal channel, tidal flat and saltmarsh, and adjusted the initial Manning values from Arcement and Schneider (1989) as part of the calibration process. The

obtained results with Manning's n of 0.017, 0.022, 0.035 and 0.080 for the respective principal 'feature' types were closed to the initial estimates except for saltmarsh, i.e. was reduced to avoid localised numerical instability of sharp discontinuity between the smooth channel and rough saltmarsh.

2.5 Review on bacteriophage as a microbial tracer

Bacteriophages have been used as microbial tracers in a variety of high dispersion aqueous environments (Wyer *et al.* 2010). In high dilution surface water environments, microbial tracers have been employed successfully, i.e. in rivers (Drury and Wheeler 1982; Rossi *et al.* 1998; Shen *et al.* 2008), lakes (Goldscheider *et al.* 2007), estuaries (Morgan *et al.* 1995) and the marine environment (Pike *et al.* 1969; Drury and Wheeler 1982; Nightingale *et al.* 2000).

Wyer *et al.* (2010) described a study combining microbial tracers, intensive FIO measurement, open channel hydrology and molecular microbial source tracking (MST) to enhance understanding of recreational water quality at Amroth in southwest Wales, UK. Authors introduced microbial tracers to the middle of four stream inputs over a short duration during a rainfall-driven hydrograph event and commenced regular sampling at the near-shore marine waters immediately after the release for the next 44 hours. Results demonstrated the rapid physical linkage between stream inputs 2 and 3 and the bathing water compliance monitoring site under the hydrograph event and tidal state combination. The microbial tracer component of the study further demonstrated the utility of simultaneous multiple tracer releases to understand environmental water movement and connectivity (Goldscheider *et al.* 2007).

Shen *et al.* (2008) evaluated the performance of bacteriophage P22 in a major US river (the Grand River, Michigan) relative to Rhodamine WT (RWT), evaluated the relative importance of different environmental factors that influence the inactivation (loss of virus per unit time) of bacteriophage P22 and examined the behaviour of both tracers as related to catchment-scale properties and processes. RWT and P22 solutions were injected into the river from the Ann Street Bridge and grab samples were collected at four sampling locations. Solute transport in the longitudinal direction was described using the transient storage (TS) formulation (Runkel 1998). The fractional recovery of tracer mass was estimated by integrating the tracer breakthrough data. Due to uncertainty in the initial mass released, the mass estimated at Site 1 was used as the initial mass in the TS modelling for both RWT and P22. Using the inactivation

formulation (i.e. Equation 2.5) that separates contributions between solar radiation and other environmental factors after correctly estimated the dilution effect, the average first-order inactivation rate of P22 in reaches 2 and 3 was found to be 0.27 and 0.57 per day, respectively. Besides inactivation, TS also significantly modifies the distribution of the tracer mass after the initial mixing period (Atkinson and Davis 2000) which relates to land use characteristics and channel complexity (Gooseff *et al.* 2007).

Inactivation formulation:

Eqn. 2.5

where k_{solar} is the rate of inactivation due to solar radiation ($d^{-1} kW^{-1}$), I_{net} is the net shortwave radiation (kW) as a function of time, and k_{other} denotes the loss due to other factors (i.e. temperature, sedimentation, etc).

Charles *et al.* (2009) investigated the potential health hazard from infectious viruses (i.e. coliphages or viruses) that have been detected by polymerase chain reaction (PCR) and their stability in groundwater. Authors set up experiments in microcosms – using raw groundwater (GW) and 1/40 dilution of Ringer’s solution (RS) for the viruses and using GW and synthetic groundwater (SGW) for the phage. A first-order and a biphasic decay model were considered as in Equations 2.6 and 2.7. A log-likelihood method was used to fit the decay models to the data and to compare between both models. The order of virus stability from most to least stable in groundwater, based on first-order inactivation, was: coliphage Φ X174 ($0.5 d^{-1}$) > adenovirus 2 > coliphage PRD1 > poliovirus 3 > coxsackie virus B1 ($0.13 d^{-1}$). The order for PCR results was: norovirus genotype II > adenovirus > norovirus genotype I > enterovirus.

First order decay model:

Eqn. 2.6

where C is the concentration of virus, C_0 is the concentration of virus at time = 0, t is time and k is the decay rate coefficient.

Biphasic decay model:

Eqn. 2.7

where f_1 is the fraction of less stable viruses with a higher decay coefficient k_1 and f_2 is the fraction of more stable viruses with a lower decay rate coefficient k_2 (Cerf 1977; Petterson and Ashbolt 2001).

2.5.1 Environmental stress

Troussellier *et al.* (1998) specified the demographic, physiological and genetic characteristics of populations of enteric bacteria subjected to different stress factors of the marine environment. Authors used strains of *E. coli* and *S. typhimurium* for the experiments. Nutrient deprivation, saline stress and light are three major environmental stresses that were tested. Depending on the type of stress, the culturability and the physiological characteristics of *E. coli* cells were affected to different degrees, i.e. the weakest culturability loss and energy charge decrease by the nutrient deprivation, cell “closure” and a decreased capacity to nutrients transport by hyperosmotic shock and a drastic decrease in culturable cell numbers by light exposure. Information on the pre-adaptation possibilities of enteric bacteria was revealed that their survival in the sea not only dependent on the conditions into which they were released but also the conditions they had previously. In experiments on the role of a general *E. coli* anti-stress response (i.e. *rpoS* gene) (Loewen and Hengge-Aronis 1994) with regards to the culturability, no significant decrease in cfu counts in stationary-phase parental and *rpoS* mutant strains when they were only submitted to nutrient deprivation, yet *rpoS* mutant strains were exhibited a significantly larger decrease than parental strain when were exposed to combined nutrient deprivation, hyperosmotic shock and light exposure.

Martin *et al.* (1998) developed a mathematical model to synthesise conceptual and experimental information on the behaviour of enteric bacteria in seawater. Authors hypothesised that the fate of the cells was dependent on their energetic state and their physiological responses to environmental stresses. In the energetic model, an intracellular compartment, σ which regulates cell behaviour according to three specific thresholds (i.e. σ_{min} , σ_{max} and σ_{crit}) was considered. In the conceptual model of physiological adaptations, exponential

growth phase cells, that responded to different marine environmental stresses were led to three other different cellular states (i.e. , and). Seven functions were used to describe the internal compartment and anti-stress response dynamics – i) uptake of external substrates (), ii) assimilation and growth, iii) maintenance requirements, iv) anti-stress responses, v) loss of culturability, vi) revival of cells and vii) cell lysis. Bacteriological data for calibration and validation steps were obtained from *E. coli* survival experiment in batch microcosms (Troussellier *et al.* 1998). In both the presence and non-presence of osmotic stress in the darkness, the addition of small amounts of assimilable organic matter was led to a decrease of the culturability loss rate. When the light intensity was increased from 10,000 lux to 90,000 lux and without external organic matter, a strong increase of culturability loss rate was observed during the first exposure (i.e. T90 of 9 h and 2.3 h respectively), while the response of was led to the increase in T90 values (i.e. 25 h and 4.8 h respectively) during the following exposure.

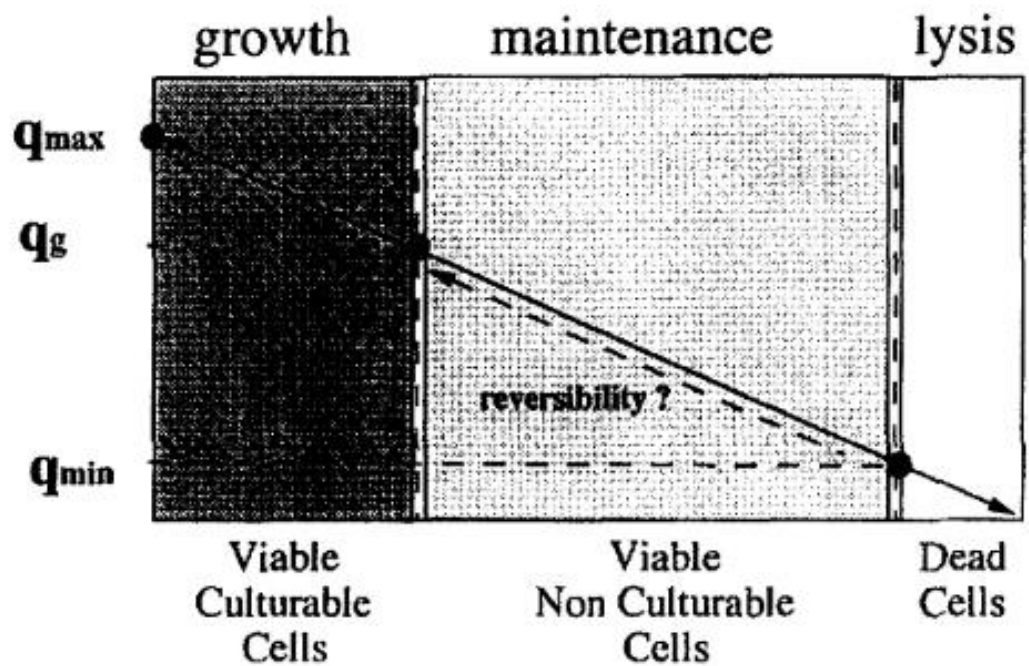
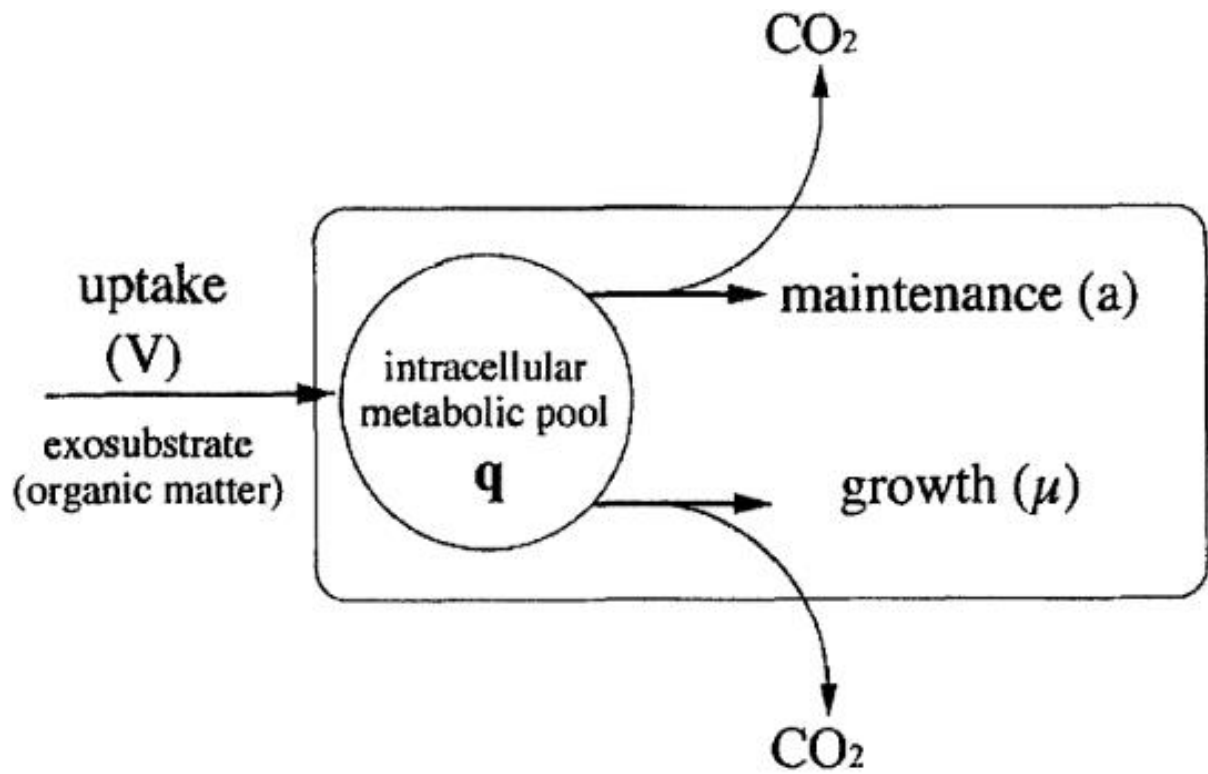


Figure 2.10: Illustration of energy model (Martin *et al.* 1998).

2.5.2 Biphasic decay modelling

Hellweger and Masopust (2008) determined and understood the important fate and transport processes of *E. coli* in Boston's Charles River and the best modelling approaches in the context of managing public health risk. Authors simulated die-off using a biphasic decay model (Geldreich and Kenner 1969; Dutka and Kwan 1980; Thomann and Mueller 1987; Medema *et al.* 1997; Easton *et al.* 2005). The bacterial population was divided into labile (i.e. fast decay) and refractory (i.e. slow decay) fractions, with the die-off was simulated using the first-order decay process, i.e. different rate constants with the calibrated values of 2.5 and 0.25 day⁻¹ for labile and refractory fractions, respectively. The model reproduced the observed spatial and temporal patterns for both surveys, including the long-term trend with higher and lower concentrations respectively during Survey 1 and 2.

2.5.3 GASP mechanism and agent-based modelling

As the growth advantage in stationary phase (GASP) mechanism (Bucci *et al.* 2011) explained the biphasic decay pattern, Bucci *et al.* (2012) further investigated this adaptation mechanism by incorporating it (Figure 2.1) into a surface water model and comparing predictions to laboratory and field data. Authors simulated wild-type (WT) and first-round mutant (M1) of *E. coli* cells that involved five processes: i) death in pure culture (), ii) death due to interaction with the natural biota (), iii) growth () on the natural assimilable organic carbon available to *E. coli* (), iv) endogenous respiration () and v) mutation during division (). Individual cells were simulated as agents of “super-individuals” (Hellweger and Bucci 2009) while the was modelled using the conventional concentration approach. A small amount of biological variability was included to prevent numerical or artificial synchronisation (Hellweger and Bucci 2009) in the model that was applied to laboratory cultures and the Charles River. In a phosphate buffer solution (PBS) and natural river water (NRW), the model was predicted takeover by the mutant after 7 days of aging and 8-9 days of decay respectively. In the Charles River, similar *E. coli* densities were predicted by the rf-PLM and rf-ABM, and the consistent prediction by the m-ABM to the previous models and the data.

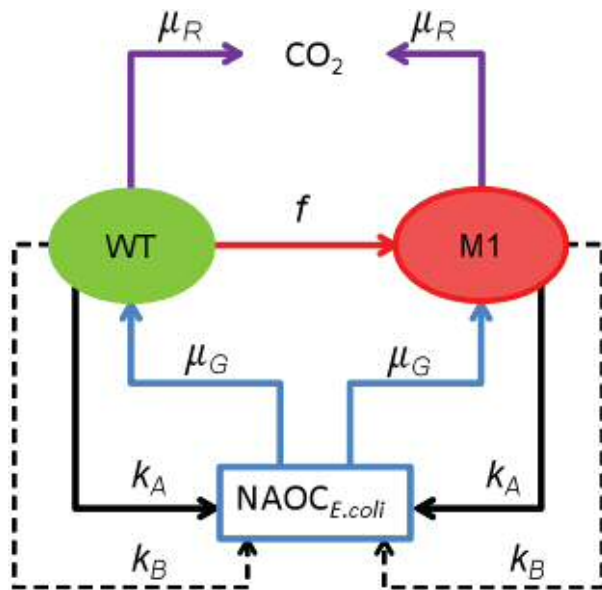


Figure 2.11: Conceptual model of the *E. coli* adaptive mutation using agent-based modelling (Bucci *et al.* 2012).

Brouwer *et al.* (2017) showed that the biexponential model could arise from mechanistic assumptions. Authors considered a family of linear, two-compartmental models that encompasses several possible mechanisms of biphasic decay (Figures 2.2a-d) as in Equations 2.8 and 2.9. The analysis was grounded in three plausible models of pathogen decay, i.e. population heterogeneity, hardening off and viable-but-not-culturable (VBNC). Insights into properties of the model from five theoretical analyses were: the biexponential model described the behaviour of the family of considered mechanisms, the apparent parameters of the biexponential model could be uniquely determined from pathogen concentration data, the general mechanistic model is unidentifiable, identifiable combinations of the model parameters are in the context of the population heterogeneity, hardening-off, and VBNC, and it is impossible to distinguish from the shape of the data alone whether all pathogens or only a culturable fraction were measured. Results through examples demonstrated that data obtained from sampling studies alone could not elucidate the mechanism of decay.

Two-state linear compartmental models:

— Eqn. 2.8

— Eqn. 2.9

where $u(t)$ and $E(t)$ are populations of pathogens in the environment, δ_1 and δ_2 are decay rate coefficients of pathogens, and θ_1 and θ_2 are transition rate coefficients of pathogens, respectively of type 1 (labile) and type 2 (resistant). η is the labile fraction of introduced pathogens, $u(t)$ is the total addition of pathogens into the environment (i.e. shedding), and $E(t)$ is the total pathogen population. The initial conditions are $E_1(t)$ and $E_2(t)$, where $E_1(t)$ is the initial population of pathogens, and $E_2(t)$ is the initial labile fraction of pathogens.

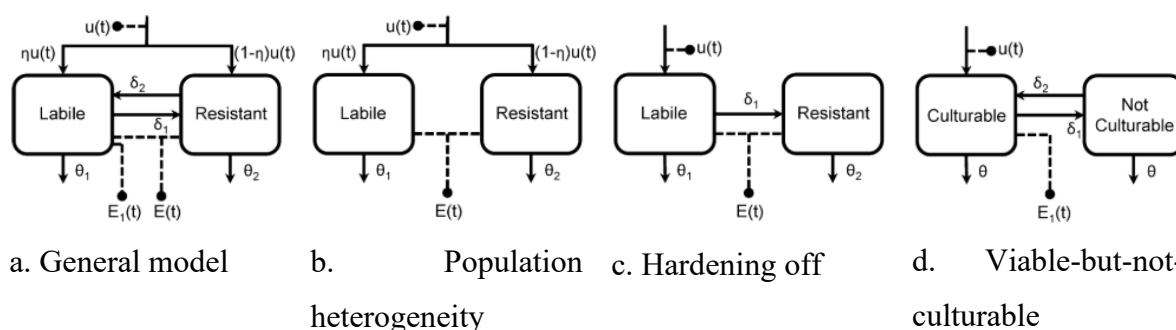


Figure 2.12: General model of biphasic decay and three mechanistic submodels (Brouwer *et al.* 2017). Solid lines are a transfer of pathogens, and the dashed lines indicate the measurement.

2.6 Overview of diffuse source release kinetics

Schernewski *et al.* (2012) presented and applied a three-dimensional model system for the spatial analysis of microbial pollution at the Szczecin Lagoon (southern Baltic) and evaluated its benefit as a water quality management support tool. Authors identified and spatially allocated three major potential sources of *E. coli* bacteria at the surrounding of Ueckermünde beach, i.e. Uecker river, wetlands with cattle, and seabirds with bathing and fisheries. The Lagrangian particle tracking simulations were carried out based on the General Estuarine Transport Model (GETM) steady state flow fields (Burchard and Bolding 2002) for the calculation of *E. coli* concentrations and transport in the lagoon. By assuming a quasi-permanent emission and based on the literature, the waterbody was received daily *E. coli* of $1 \cdot 10^{12}$ for the river, $1 \cdot 10^{12}$ for the wetlands with cattle and $7.5 \cdot 10^{11}$ for seabirds inclusive fisheries and beach visitors. From the model results, *E. coli* accumulations at the nearshore were often observed. Several important emission sources close to the beach (i.e. seagulls or the

river) that ensured a permanent supply of bacteria was among the responsible reasons to these accumulations.

Sanders *et al.* (2005) simulated dry-weather tidal cycling of total coliform (TC), *E. coli* (EC), and enterococci (ENT) concentrations in surface waters of Talbert Marsh, an intertidal wetland in Huntington Beach, California. Authors predicted surface water faecal indicator bacteria (FIB) by solving the transport equations simultaneously with the flow prediction. The FIB loading to surface waters from bird faeces was modelled as non-point source, where the spatially and temporally distributed faeces on the marsh shoals were subjected to sunlight induced die-off during drying (Equations 2.10 and 2.11), and upon flooding by tides, were instantaneously transferred from the marsh banks and into the water columns (Equation 2.12). Model predictions were illustrated an expected response of the TC concentration near the banks and over the shoals of the marsh as the FIB loading by bird faeces was modelled at the interface between wet and dry land.

The build-up and die-off of FIB mass from bird faeces on the marsh shoals were solved using the mass balance equations as follows:

$$\text{—————} \tag{Eqn. 2.10}$$

$$\tag{Eqn. 2.11}$$

where ρ is the surficial FIB density (MPN/m²), L is the FIB loading rate (MPN/ m²/s), A is the exposed intertidal surface area (m²), N is the bird population measured hourly in the marsh, λ is the rate of FIB loading per bird (MPN/bird/s), k is the die-off rate constant (m²/Watts/s) based on Sinton *et al.* (1999) (i.e. identical between on the marsh bank and in the surface water), and I is the solar intensity (Watts/m²) based on data from Grant *et al.* (2001).

The transferred rate of FIB loadings into the water column at sediment/water interfaces was computed using the equation as follows:

$$\tag{Eqn. 2.12}$$

where t_f is the instant time when the land is flooded by the rising tides, and $\delta(t - t_f)$ is the Dirac delta function (s^{-1}).

2.6.1 Parametric release kinetic models

Blaustein, Pachepsky, Shelton, *et al.* (2015) reviewed on microbial release and removal from surface-applied livestock manures and faecal deposits at pastures. Authors described the microbial release process via sort of combination in three stages – i) rain/irrigation water hits and suspends erodible surfaces of animal waste constituents to result sloughing off, ii) water enters animal waste (i.e. internal mixing process) and displaced diluted suspension by portions of leaching water, and iii) pressed out of initial liquid phase from waste matrix then transported organisms from high concentration area to leached domain. The microbial release processes were controlled by combination factors of physical, chemical, and biological, i.e. microbial properties, animal waste source and composition, application method and rate, waste age, vegetation, and precipitation or irrigation. To simulate microbial release from animal manures, three proposed models and their modifications to date were the one-parametric exponential model (Bicknell *et al.* 1996), and the two-parametric Bradford-Schijven (B-S) (Bradford and Schijven 2002) and Vadas-Kleinman-Sharpely (VKS) (Vadas *et al.* 2004) models (see Figure 2.13). Both the two-parametric models have the capacity of simulating faster release at the beginning and slower release at the end as compared to the one-parametric model.

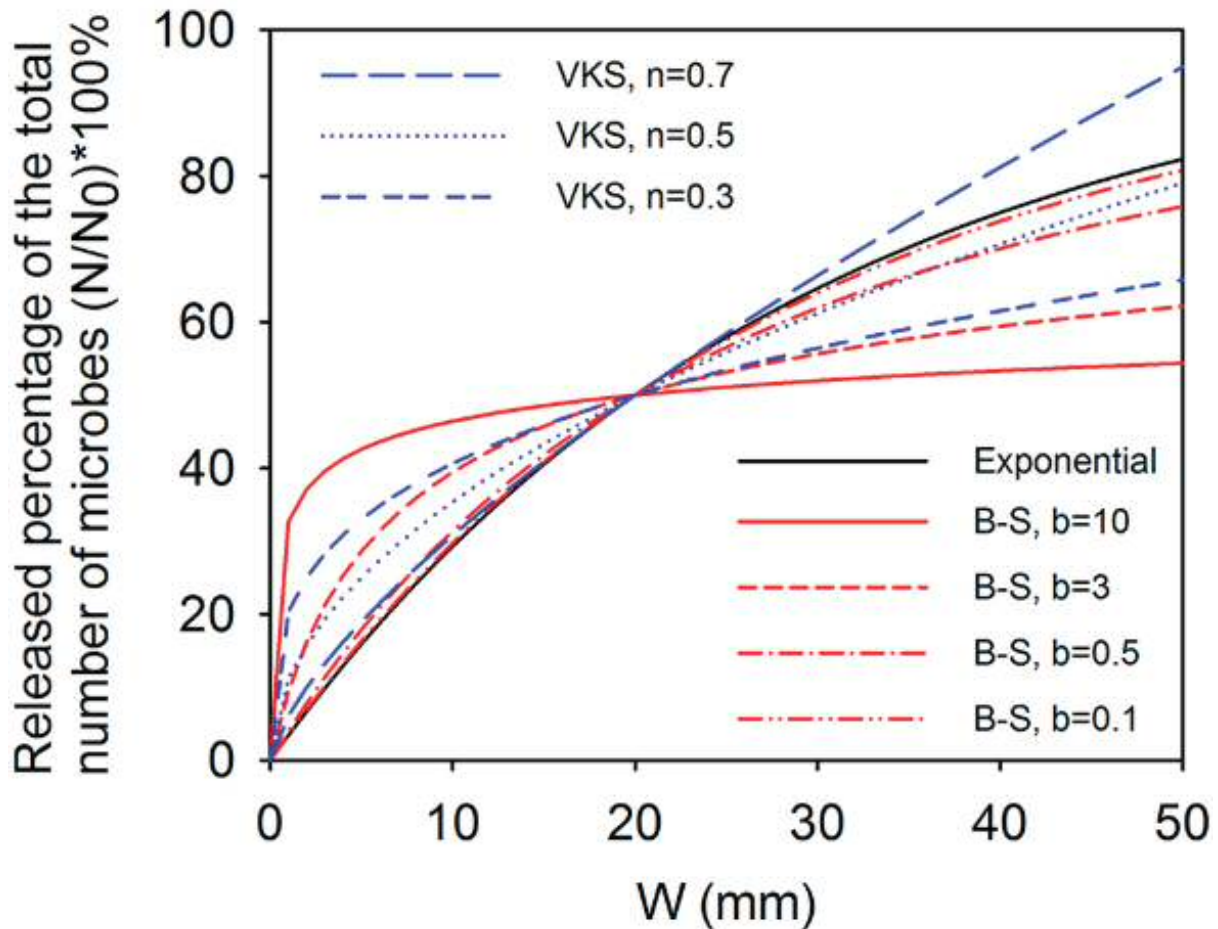


Figure 2.13: Differences in shapes of release curves simulated with three release models: exponential, Bradford-Schijven (B-S), and Vadas-Kleinman-Sharpley (VKS) (Blaustein, Pachepsky, Shelton, *et al.* 2015).

Blaustein, Pachepsky, Hill, *et al.* (2015) evaluated the applicability of known microbial release models to simulate release indicator bacteria from solid cattle manure under the effects of rainfall intensity and slope steepness. Authors modelled the released bacterial group/species and chloride (Cl⁻) as a function of rainfall-depth and a function of time with the one-parametric exponential model (Equation 2.13) and two-parametric Bradford-Schijven model (Equation 2.14). Release model performance was assessed for each model-fit by root-mean-squared-error (RMSE) and Akaike information criterion (AIC) (Burnham and Anderson 2003) values. When evaluated based on the rainfall depth since the initial release, release kinetics were better simulated the bacterial release at different rainfall intensities than on the rainfall time since the initial release (see Figure 2.14). The Bradford-Schijven model was suggested as the preferred model for simulating the bacterial release with consistently lower RMSE and AIC values as compared to the exponential model.

One-parametric exponential model;

— Eqn. 2.13

and two-parametric Bradford-Schijven model:

— Eqn. 2.14

where N is the total number of bacteria or the mass of Cl^- released per unit area of manure application (cfu/m^2 or mg/m^2), N_0 is the initial number of bacteria or mass of Cl^- per unit area of manure application (cfu/m^2 or mg/m^2), R is rainfall depth (mm), and k and n are constants ($1/mm$), α is a dimensionless shape parameter.

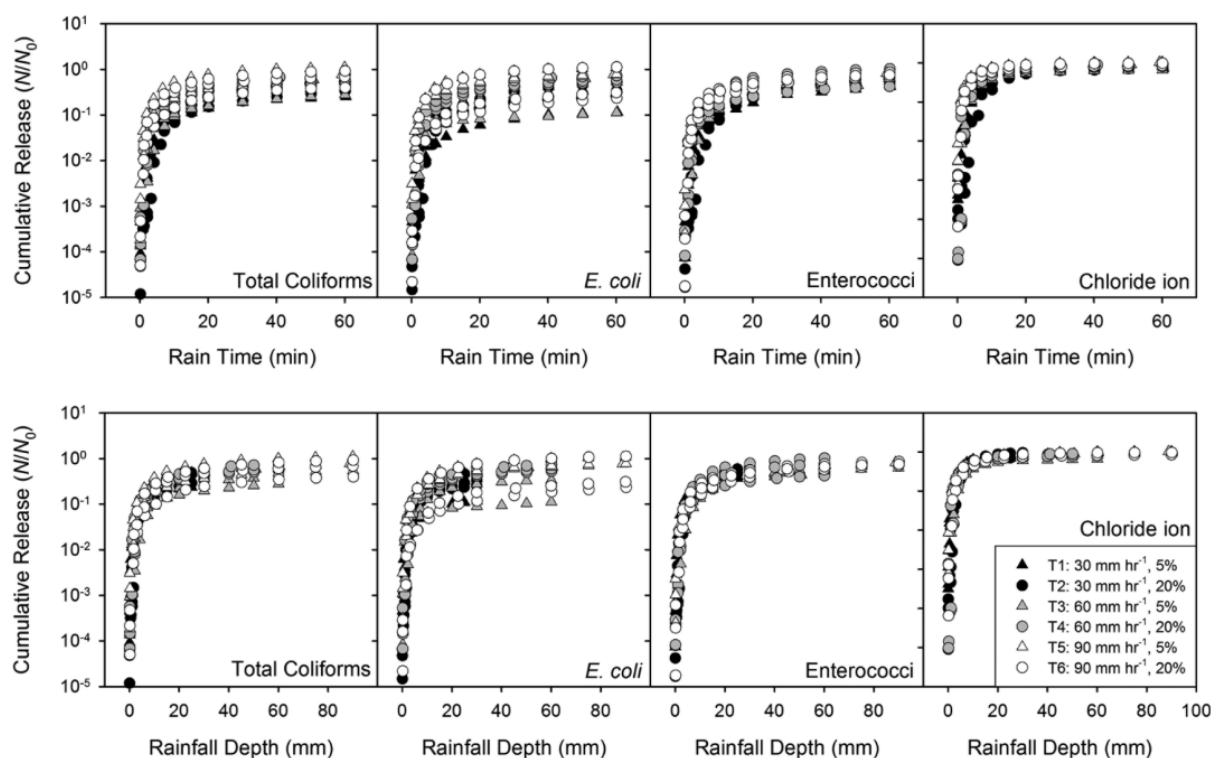


Figure 2.14: Cumulative amounts of bacteria and Cl^- released () as a function of time () since initial release (top row) and rainfall depth since initial release (bottom row) (Blaustein, Pachepsky, Hill, *et al.* 2015).

Guber *et al.* (2006) assessed the applicability of recent models to describe release kinetics of chloride (Cl^-), faecal coliform (FC), organic carbon (OC), and water-soluble phosphorus (P) from the applied bovine manure on slopes with different soil textures and surface covers under simulated rainfall. Authors fitted the one-parametric exponential model and the two-parametric Vadas-Kleinman-Sharpley (VKS) and Bradford-Schijven (BS) models to each of the observed dependence release rates for Cl^- , FC, OC, and P concentrations in the subplot runoff with time. The goodness-of-fit for the model application was assessed by estimating the root mean square error (RMSE). In estimating parameters α and β , variations observed in the two-parametric BS model were less than those for the one-parametric exponential model. Value α was increased linearly from 2.51 to 6.93 h^{-1} with increasing irrigation rate for all plots and all monitored manure constituents (see Figure 2.15). The β variability was higher for bare plots 2 and 4 than for vegetated plots 1 and 3 (i.e. clay loam for odd plots and sandy loam for even plots).

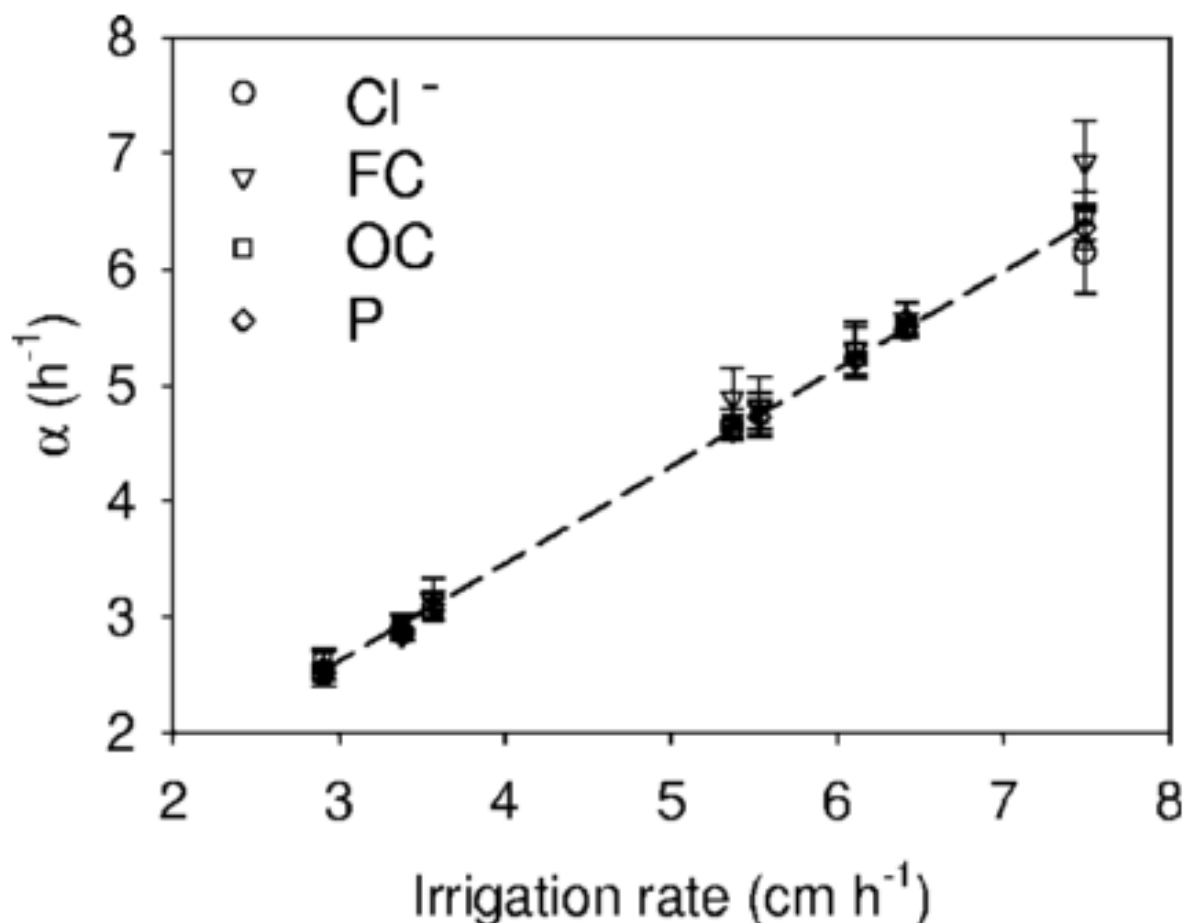


Figure 2.15: Relationship between parameters α in the two-parametric BS model and irrigation rate (Guber *et al.* 2006). A linear regression equation is explaining that relationships were

$\alpha = 0.93 \text{ Irrigation rate} + 0.18$, where α is irrigation rate (cm h^{-1}) similar to Equation 2.17.

Sterk *et al.* (2016) analysed the net effect of climate change on pathogen runoff and human infection risks in the Netherlands. Authors determined pathogen loadings from animals using the method described by Dorner *et al.* (2004). To estimate pathogens removal in manure over time, Equation 2.15 was used to describe processes of die-off as first-order decay reaction and release due to precipitation. The release was modelled using a release function for *Cryptosporidium* and *Giardia* from Dairy Cattle Manure of Bradford and Schijven (2002), as in Equation 2.16. For fitting parameters λ and α , correlation with rainfall intensity by Guber *et al.* (2006) (Equation 2.17) and the range of results from Bradford and Schijven (2002) respectively were used. Pathogen fluxes were added to the WALRUS model (Brauer *et al.* 2014) which was resulted in a number of pathogens entering the quick flow reservoir.

Pathogens removal in manure over time:

$$\frac{dN}{dt} = -\lambda N + \alpha P \quad \text{Eqn. 2.15}$$

where N is a number of pathogens present in manure, t is time, λ (day^{-1}) is the decay rate, and α (day^{-1}) is the release rate coefficient.

A release function from Dairy Cattle Manure of Bradford and Schijven (2002):

$$R = \frac{1}{1 + \exp(-\beta(t - t_0))} \quad \text{Eqn. 2.16}$$

where t (hr) is the time passed since the start of a rainfall event, β (hr^{-1}) and t_0 (-) are fitting parameters.

Correlation for fitting parameter β with rainfall intensity by Guber *et al.* (2006):

$$\beta = 0.0001 I + 0.0001 \quad \text{Eqn. 2.17}$$

where I (mm hr^{-1}) is the rainfall intensity.

2.7 Summary

This chapter reviews the literature on the related topics for providing understanding along with conducting the research. In discretising the unstructured mesh, the sub-grid-scale features should be considered for a realistic but efficient modelling of the flow at the very-shallow hydraulic environment. In term of the numerical representation, obstructions to the flow at floodplains could be parameterised as the bottom roughness besides other strategies based on their suitability. When released in a hostile environment, a specific bacteriophage could response in different ways to the environmental stresses based on their memory of resistance. In modelling the diffuse source, two-parametric release kinetics models that control the initial release rate and determine the shape of release curves should be considered at the wetting and drying boundary.

Chapter 3: Hydrodynamic model development

3.1 Introduction

This chapter was focused on developing and calibrating a hydrodynamic model for the Severn Estuary and Bristol Channel (SEBC) waterbody. Developing a hydrodynamic model for this waterbody was essential to improve the understanding of the processes experienced by the FIOs while being transported in the estuarine environment, from different sources, and on their impacts to water quality at the sites of interest. The open-Source code of the TELEMAC Modelling System was important for the solution of shallow water equations as it comprised a rigorous theoretical framework with flexibility in describing complex geometries (Hervouet 2000) respectively based on the finite element method and the unstructured mesh. The two-dimensional modelling was suitable for simulating the hydrodynamic process in a well-mixed estuary, i.e. the SEBC waterbody (Manning *et al.* 2010; Ahmadian, Falconer, *et al.* 2014) as for optimising the computational cost without sacrificing the result's accuracy.

This chapter was organised as follows: Section 3.2 presented the derivation of Navier-Stokes equations for the solution of the free surface hydrodynamic. Section 3.3 presented the setting up of the two-dimensional modelling domain for the SEBC. Section 3.4 presented the calibration of hydrodynamic processes at several sites within the waterbody. Section 3.5 summarised the chapter.

3.2 Free surface hydrodynamics

The TELEMAC Modelling System was selected over the use of other available models, e.g. EFDC (Hamrick 1992), etc., for modelling the free surface hydrodynamics. TELEMAC with the solution of the finite element method was known as the most robust for the application with the unstructured mesh. The representation of waterbodies with complex shorelines has the advantage over the use of the unstructured mesh as the mesh-nodes can be placed at the finer density to adapt the shoreline changes. The application of regular or curvilinear grid was not satisfying along the complex shoreline as the gap at the grid edges was known to produce erroneous in the result computation. This issue had been overcome with the application of the quadtree mesh (Liang *et al.* 2008; Liang and Borthwick 2009). At floodplains, the unstructured mesh with the finer element resolution can better represent the complex topography with

specific treatments (Chapter 4) as for modelling the wetting and drying process. Besides, the application of the flexible mesh (Symonds *et al.* 2017) opted in Delft3D has an advantage over the abovementioned issues. Derivations for the free surface hydrodynamics in the following sections were based on the framework of the TELEMAC Modelling System.

3.2.1 Definition of domain

The study domain, Ω is referred to Ω_{3D} ; with x , y and z are planes that bounded the volume along the global axes. The domain limits at the bottom and free surface by equations of $z = Z_f(x, y, t)$ and $z = Z_s(x, y, t)$, respectively. The vertical boundary limits laterally the domain for the surface at line Γ . The domain projects on the horizontal plane Ω_{2D} later will become the two-dimensional study domain, denoted as Ω_{2D} .

The domain of calculation then defined as:

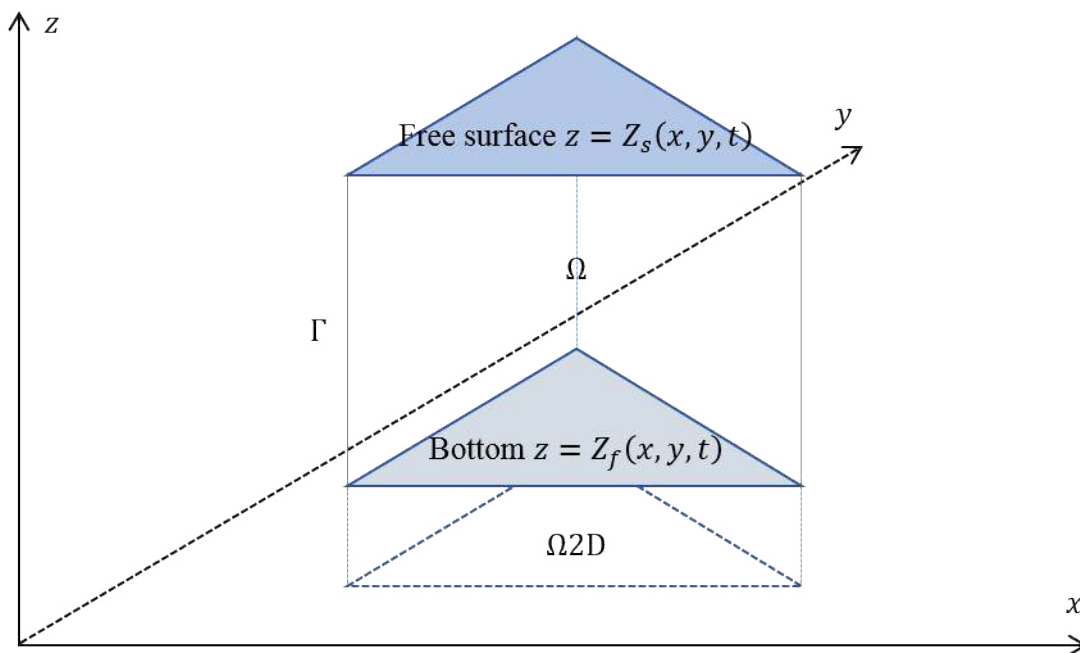


Figure 3.1: Domain of calculation.

The domain of calculation is defined graphically as in Figure 3.1, with the gravitational acceleration directed towards decreasing of z , and the depth of water column is denoted by h . The bottom elevation, z_b is from a provided data of bathymetry or topography, with the depth of water, h is dynamically computed temporally with time, t .

The free surface which varies to the function of x , y and z coordinates, and with time also written as $z = z(x, y, t)$, which further extend to:

$$\text{Eqn. 3.1}$$

The normal vector to the free surface directed towards increasing of z , which external to the water volume is defined as \mathbf{n} , with components as follow:

$$\mathbf{n} = \frac{\nabla z}{|\nabla z|} \quad \text{Eqn. 3.2}$$

and replacing \mathbf{n} to \mathbf{m} for vector normal to the bottom which directed towards decreasing of z , with components as follow:

$$\mathbf{m} = -\frac{\nabla z_b}{|\nabla z_b|} \quad \text{Eqn. 3.3}$$

3.2.2 Free surface Navier–Stokes equations

3.2.2.1 Non-hydrostatic Navier–Stokes equations

The conservation of fluid mass is firstly derived for the study domain, Ω with the density of fluid ρ is expressed as follow:

$$\frac{d}{dt} \int_{\Omega} \rho \, d\Omega + \int_{\partial\Omega} \rho \mathbf{v} \cdot \mathbf{n} \, d\Omega = 0 \quad \text{Eqn. 3.4}$$

The theorem of Leibnitz then breaks down the expression into observed variations within the domain and the flux through the boundary, with \mathbf{v} is the velocity vector with components of (u, v, w) :

— — Eqn. 3.5

The flux through boundary then reduced using the Gauss theorem for a volume integral as

. The local expression by accepting the conservation of mass for any domain,

then presented as follow:

— Eqn. 3.6

The compressible form of mass conservation equation is then simplified by considering the density of fluid as constant:

Eqn. 3.7

From Newton's second law, the dynamic of fluid is written as — when considering the

rigid body. As the fluid is variable in density, the equation is better to write as —

then equivalent to the derivative of momentum contained in the domain, as follow:

— Eqn. 3.8

By using the Leibnitz theorem as in mass, the fluid momentum then breaks down into observed variations within the domain and the flux through the boundary as follow:

— — Eqn. 3.9

The Gauss theorem then reduced the flux of momentum through the boundary for a volume integral, with the external product in order 1 of two tensors, and the tensor operator which is written as .

The force term, \mathbf{F} is the sum of external and contact forces that applied inside and on the surface of the body domain, respectively. The external forces consist of the gravitational acceleration, \mathbf{g} and other forces, \mathbf{f} include the Coriolis effect, etc. The contact forces however applied to the surface element, $d\mathbf{S}$ of the body domain at external normal, \mathbf{n} defined as $d\mathbf{S} = \mathbf{n} dS$, with the stress tensor. The force applied to the body domain, \mathbf{F} then is:

$$\mathbf{F} = \int_V \mathbf{f} dV + \int_S \mathbf{T} \cdot \mathbf{n} dS \quad \text{Eqn. 3.10}$$

By using the Gauss theorem then reduced the contact force at body surface into a volume integral of $\nabla \cdot \mathbf{T}$. The local expression for the momentum of fluid in any domain, then presented as follow:

$$\rho \frac{D\mathbf{u}}{Dt} = \nabla \cdot \mathbf{T} + \rho \mathbf{f} \quad \text{Eqn. 3.11}$$

The compressible form of fluid momentum equation then simplified as non-conservative as in mass conservation equation:

$$\rho \frac{D\mathbf{u}}{Dt} = \nabla \cdot \mathbf{T} + \rho \mathbf{f} \quad \text{Eqn. 3.12}$$

By considering the fluid as Newtonian and incompressible, the stress tensor then can be expressed in the form of below, with p the pressure in pascals, \mathbf{I} the identity tensor, μ the dynamic viscosity, ν the kinematic viscosity, and \mathbf{D} the strain rate tensor:

$$\mathbf{T} = -p\mathbf{I} + \mu \nabla (\nabla \cdot \mathbf{u}) + \mu \nabla^2 \mathbf{u} \quad \text{Eqn. 3.14}$$

$$\mathbf{T} = -p\mathbf{I} + 2\mu \mathbf{D} \quad \text{Eqn. 3.15}$$

As the dynamic viscosity of the fluid is constant in space, the incompressible portion of strain rate tensor \mathbf{D} then is simplified into the form of $\mathbf{D} = \frac{1}{2}(\nabla \mathbf{u} + \nabla \mathbf{u}^T)$.

In using the mass and momentum conservation equations as the form of incompressible, the density variation due to the variable of temperature, and substance of salt or sediment in the water shall consider as sufficiently minor. The established Navier–Stokes equations now can be written in the Cartesian coordinates as:

Conservation of mass:

$$\frac{\partial \rho}{\partial t} + \frac{\partial (\rho u)}{\partial x} + \frac{\partial (\rho v)}{\partial y} + \frac{\partial (\rho w)}{\partial z} = 0 \quad \text{Eqn. 3.16}$$

Conservation of momentum:

$$\rho \left(\frac{du}{dt} + u \frac{\partial u}{\partial x} + v \frac{\partial u}{\partial y} + w \frac{\partial u}{\partial z} \right) = -\frac{\partial p}{\partial x} + \mu \left(\frac{\partial^2 u}{\partial x^2} + \frac{\partial^2 u}{\partial y^2} + \frac{\partial^2 u}{\partial z^2} \right) \quad \text{Eqn. 3.17}$$

$$\rho \left(\frac{dv}{dt} + u \frac{\partial v}{\partial x} + v \frac{\partial v}{\partial y} + w \frac{\partial v}{\partial z} \right) = -\frac{\partial p}{\partial y} + \mu \left(\frac{\partial^2 v}{\partial x^2} + \frac{\partial^2 v}{\partial y^2} + \frac{\partial^2 v}{\partial z^2} \right) \quad \text{Eqn. 3.18}$$

$$\rho \left(\frac{dw}{dt} + u \frac{\partial w}{\partial x} + v \frac{\partial w}{\partial y} + w \frac{\partial w}{\partial z} \right) = -\frac{\partial p}{\partial z} + \mu \left(\frac{\partial^2 w}{\partial x^2} + \frac{\partial^2 w}{\partial y^2} + \frac{\partial^2 w}{\partial z^2} \right) \quad \text{Eqn. 3.19}$$

These forms of equations are now called the non-hydrostatic Navier–Stokes equations as the pressure component yet did not have any hypothesis. The components of u , v , and w in these equations are unknown and need to be solved.

3.2.2.2 Boundary conditions

The domain of study, Ω is now limited for boundaries at the impermeable bottom, the free water surface, the vertical impermeable structures also banks and beaches, and the imaginary boundary for the open sea and river upstream.

From the Lagrangian hypothesis, a particle of water on the free surface is remains attached to the surface as time goes on. Thus Equation 3.1 is valid with its derivative, $\frac{dw}{dt}$ also equal to zero, then written with Euler variables for velocity components of u , v and w that fixed at a point on the water surface as:

$$\text{---} \quad \text{---} \quad \text{---} \quad \text{Eqn. 3.20}$$

then simplified with the free surface normal vector from Equation 3.2 into the form of:

$$\text{---} \quad \text{Eqn. 3.21}$$

The Lagrangian hypothesis also applied to a point at the bottom which written using Euler variables for velocity components at that point, then simplified with the bottom normal vector from Equation 3.3 into the form of:

$$\text{---} \quad \text{---} \quad \text{---} \quad \text{Eqn. 3.22}$$

$$\text{---} \quad \text{Eqn. 3.23}$$

The velocity on a solid boundary wall is a no-slip velocity, but it is quickly become non-zero at just near the wall due to turbulence and a form of the boundary layer. The no-slip boundary conditions usually replaced with the impermeability wall condition and tangential stress due to wall friction, written respectively as:

$$\text{Eqn. 3.24}$$

$$\text{---} \quad \text{Eqn. 3.25}$$

The tangential stress can only be known from the computation of flow, but also will be provided from the turbulence model for certain conditions. The slip condition on the wall then occurs if the tangential stress is neglected.

For the imaginary open boundary, additional information about the pressure, water depth, velocity, discharge, etc. are required, and these will result in difficulties in numerical modelling.

3.2.2.3 Hydrostatic pressure and Boussinesq approximation

The hypothesis of hydrostatic pressure as defined below simplified the vertical velocity, w in the Navier–Stokes equations to form the Saint–Venant equations, with neglecting the diffusion, source and acceleration terms:

$$\rho \frac{dw}{dz} = -\rho g \tag{Eqn. 3.26}$$

When writing the fluid density as $\rho = \rho_0(1 - \beta \Delta T)$, the hypothesis of hydrostatic pressure then further extends to:

$$\rho_0 \frac{dw}{dz} = -\rho_0 g + \rho_0 \beta g \Delta T \tag{Eqn. 3.27}$$

The pressure at a point of elevation z then only depends on the atmospheric pressure acted to the surface of the water and the water column’s weight above it:

$$p = p_{atm} + \rho_0 g (z_0 - z) \tag{Eqn. 3.28}$$

The density difference, $\Delta \rho$ relates to the reference density, ρ_0 is supposedly small and depends on the tracer concentrations that transported in the water mass, which proportionally increase with the concentration difference and express as follow:

$$\Delta \rho = \rho_0 (\beta \Delta T - \alpha \Delta C) \tag{Eqn. 3.29}$$

where the volumetric dilatation coefficients, β can be positive for temperature and negative for salinity and suspended sediment, and α the reference value of tracer C_0 .

The first order pressure gradient term in the momentum equations for both x and y -directions are expressed respectively as follow:

$$\rho_0 \beta g \Delta T \frac{\partial w}{\partial z} \tag{Eqn. 3.30}$$

$$\frac{\partial}{\partial x} \left(\frac{\partial}{\partial x} \right) \frac{\partial}{\partial x} \frac{\partial}{\partial x} \quad \text{Eqn. 3.31}$$

then formed expressions as below based on Equation 3.28:

$$\frac{\partial}{\partial x} \left(\frac{\partial}{\partial x} \right) \frac{\partial}{\partial x} \frac{\partial}{\partial x} \quad \text{Eqn. 3.32}$$

$$\frac{\partial}{\partial x} \left(\frac{\partial}{\partial x} \right) \frac{\partial}{\partial x} \frac{\partial}{\partial x} \quad \text{Eqn. 3.33}$$

The pressure gradients including the effect of atmospheric pressure then deduced into the slope effect of the free surface, $\frac{\partial \eta}{\partial x}$ and two buoyancy source terms; the barotropic and baroclinic, respectively as follows in both x and y -directions:

$$\frac{\partial}{\partial x} \left(\frac{\partial}{\partial x} \right) \frac{\partial}{\partial x} \frac{\partial}{\partial x} \quad \text{Eqn. 3.34}$$

$$\frac{\partial}{\partial x} \left(\frac{\partial}{\partial x} \right) \frac{\partial}{\partial x} \frac{\partial}{\partial x} \quad \text{Eqn. 3.35}$$

The pressure gradient from atmospheric and two buoyancy source terms are then subsequently integrated into the source terms S_x and S_y . The Navier–Stokes equations in the view from the hydrostatic hypothesis and the Boussinesq approximation then are written as follow, with the mass conservation equation remains the same as Equation 3.16:

Momentum conservation equations:

$$\frac{\partial}{\partial x} \left(\frac{\partial}{\partial x} \right) \frac{\partial}{\partial x} \frac{\partial}{\partial x} \quad \text{Eqn. 3.36}$$

$$\frac{\partial}{\partial x} \left(\frac{\partial}{\partial x} \right) \frac{\partial}{\partial x} \frac{\partial}{\partial x} \quad \text{Eqn. 3.37}$$

3.2.2.4 Body forces and source terms

The considering body forces and source terms in the conservation of fluid momentum are the friction at the bottom, the Coriolis and centrifugal forces, the wind force at the surface, the heat exchanges from a waterbody, and the buoyancy terms and atmospheric pressure. Only the bottom friction source term is considered here. By only considering the horizontal component, the bottom shear stress that opposed by the velocity which acts on the bottom of fluid columns is written as follow:

$$\tau_b = -\rho g H \frac{\partial \eta}{\partial x} \quad \text{Eqn. 3.38}$$

The knowledge of flows from hydrodynamic processes is required to understand the stress from the fluid mass at the bottom. The turbulence model is another useful tool to provide modelling of current in the vicinity of the bottom. The shear stress is also written in one dimension with a definition of shear velocity, as follow:

$$\tau_b = \rho u_*^2 \quad \text{Eqn. 3.39}$$

From the dimensional analysis, the shear stress in the vicinity of the bottom is written in the form of below, with C_D the dimensionless friction coefficient, and in the units of $\text{kg} / \text{m} / \text{s}^2$:

$$\tau_b = C_D \rho U^2 \quad \text{Eqn. 3.40}$$

By referring to Equations 3.38 and 3.40, the bottom shear stress with the velocity sufficiently far from the wall can also be written as follow:

$$\tau_b = \rho C_D U^2 \quad \text{Eqn. 3.41}$$

In finite elements, the stress in the form of τ_b will naturally appear as the diffusion term from variational formulations of body forces and source terms.

The stress from shear at the bottom will be either provided from a turbulence model; or from the knowledge of a friction coefficient, and the computed velocity by the hydrodynamic model. When a turbulence model is used with the stress is provided by a formula based on the

roughness expression and flow at, and in the vicinity of bottom respectively, the model often will calculate the shear velocity or the friction coefficient. On the other hand, when estimating the friction coefficient from formulas, the law of bottom shear stress in two dimensions will be used to calculate the flow velocity as a vertical average. Among the formulas for estimating the friction coefficient are as follow:

Chezy formulation with coefficient, C :

$$V = C \sqrt{R S} \quad \text{Eqn. 3.42}$$

Strickler formulation with coefficient, S :

$$V = 48.3 R^{0.475} S^{0.026} \quad \text{Eqn. 3.43}$$

Manning formulation with a coefficient, n (inverse of the Strickler coefficient):

$$V = 48.3 R^{0.475} S^{0.026} \quad \text{Eqn. 3.44}$$

3.2.2.5 Tracer equations

The tracer can be represented either by the temperature of water columns or other physical quantities, i.e. salt, sediment, colouring agent, etc. The classification for the tracer can be as active while interacting with the hydrodynamic flows, otherwise as passive. The water temperature, salinity, and sediment are considered as the active tracers most of the time, with the other water quality constituents served as the passive tracers.

The physical transport of the tracer in a waterbody is depended on the process of advection and diffusion, besides due to the source and sink terms. The tracer transport equation in a conservative form, with S the creation rate by source and/or sink terms, and D the diffusion flux by molecular and/or turbulence is written as follow:

$$\frac{dC}{dt} + V \frac{dC}{dx} = S - D \frac{d^2C}{dx^2} \quad \text{Eqn. 3.45}$$

The diffusion flux which due to the molecular and turbulence process, with the tracer diffusion coefficient is written as follow:

$$\text{Eqn. 3.46}$$

The tracer transport equation in a non-conservative form, which referred to the mass conservation equation, is written in simplified and developed forms as follow:

$$\text{Eqn. 3.47}$$

$$\text{Eqn. 3.48}$$

The no-flux boundary condition is used at the solid boundary, while the flux boundary condition is used at the open boundary, respectively as in Equations 3.49 and 3.50, by representing with the notation \mathbf{n} and \mathbf{m} perpendicularly pointing outwards from the boundaries, which written as follow:

$$\text{Eqn. 3.49}$$

$$\text{Eqn. 3.50}$$

3.3 Model setup

A two-dimensional modelling domain was set up for the computation of the hydrodynamic process at the Severn Estuary and Bristol Channel (SEBC), covering the area of 5,803 km². The modelling domain was extended from the seaward open boundary at the west of the Bristol Channel up to the east of the Severn Estuary until the tidal limit near Gloucester. The seaward open boundary was specified along an imaginary line from Stackpole Head to Hartland Point which the location was away from the study area as for minimising errors originating from the boundary condition. The upstream boundaries of 29 rivers were located based on the information reported by Stapleton *et al.* (2007) as in the Appendix (see Table B.1).

The unstructured mesh was generated for the modelling domain using the freeware mesh generator of Blue Kenue (NRCC), as a single layer bounded by the shoreline that was delineated along channels and estuaries. The generated mesh also included the solid boundary of Caldey Island at the outer Bristol Channel, and Flat Holm and Steep Holm at the Severn Estuary. The triangular elements were generated at a constant size of 1000 m resolution across the modelling domain and were reduced to 100 m resolution near the islands' boundary, producing the total numbers of 14,539 elements and 7,671 nodes. The mesh generation at this stage was the pre-extension to the modelling domain at floodplains of the Loughor Estuary (Chapter 4).

The bathymetry data of the SEBC in the raster format of 100 m resolution was used as the bottom elevation information for the modelling domain. The data was referred vertically at the Ordnance Datum Newlyn (ODN) and was projected horizontally at the Universal Transverse Mercator (UTM) of Zone 30N, identical to the projection of the shoreline and the islands' boundary. The bathymetry data was successfully interpolated to the mesh nodes using the inverse distance interpolation method, results in the deepest elevation of -65 m near the open boundary. The modelling domain with the interpolated bottom elevation that was decreasing towards the east of the estuary is shown in Figure 3.2.

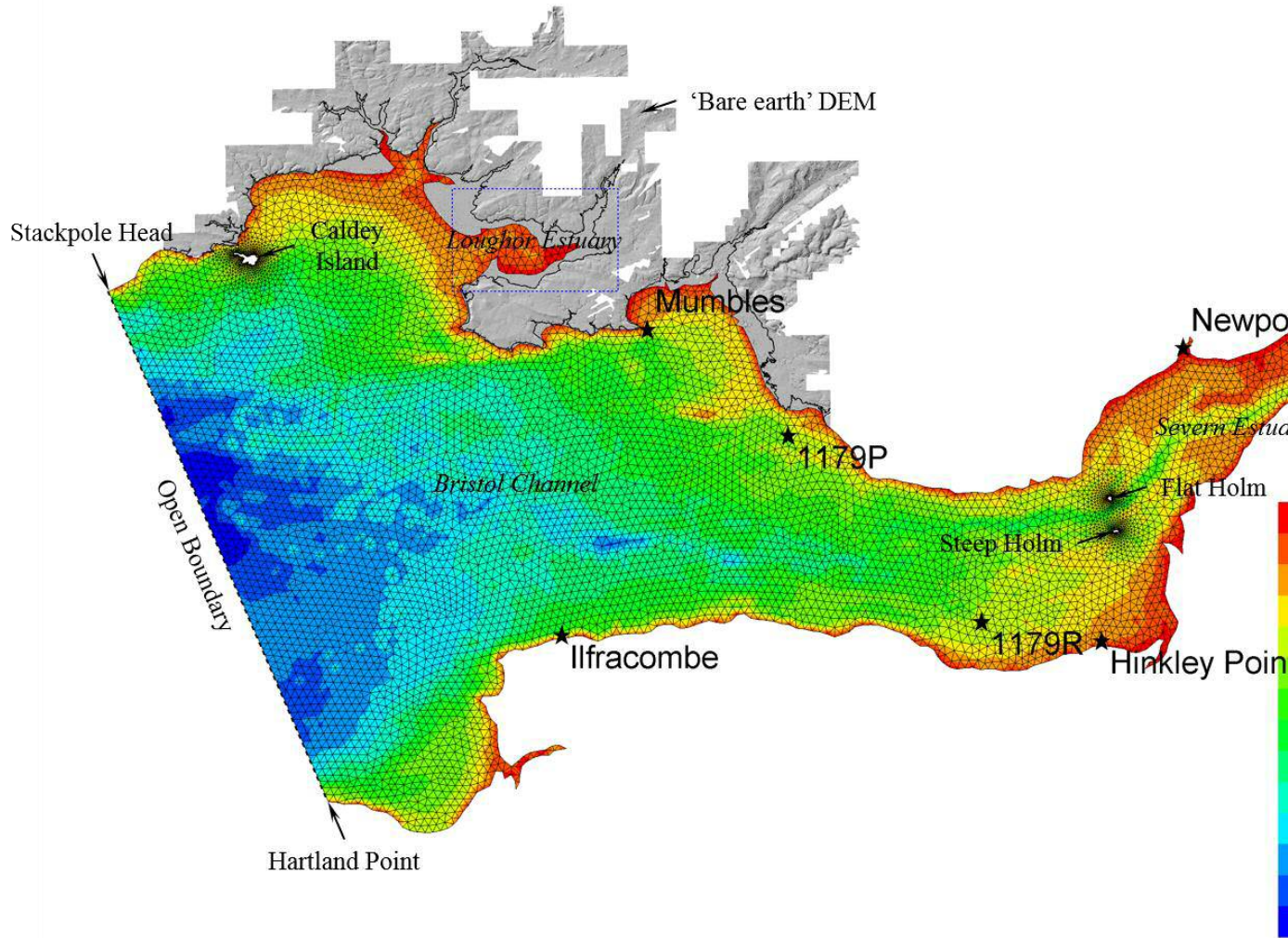


Figure 3.2: Modelling domain of the Severn Estuary and Bristol Channel (SEBC) with the interpolated bathymetry based on Datum Newlyn (ODN), 'bare earth' DEM based on Lidar surveys at South West Wales with the overlaid 10m tidal boundary at seaward and hydrodynamic validation sites.

The 'bare earth' DEM based on Lidar surveys at South West Wales was used for the extension of the modelling domain at floodplains of the Loughor Estuary (see Figure 3.2) and was discussed in the next chapter. The domain extension at the floodplains was directly integrated into the mesh nodes of the SEBC domain. The hydrodynamic computation was iterated seamlessly at the same time step for both waterbodies, treated as a single domain. It means that the hydrodynamic generated within the SEBC was transferred conservatively within the Loughor Estuary. Besides, the TELEMAC Modelling System has a capability of defining the optimum time step for maintaining the computational stability at the finer elements of the floodplains.

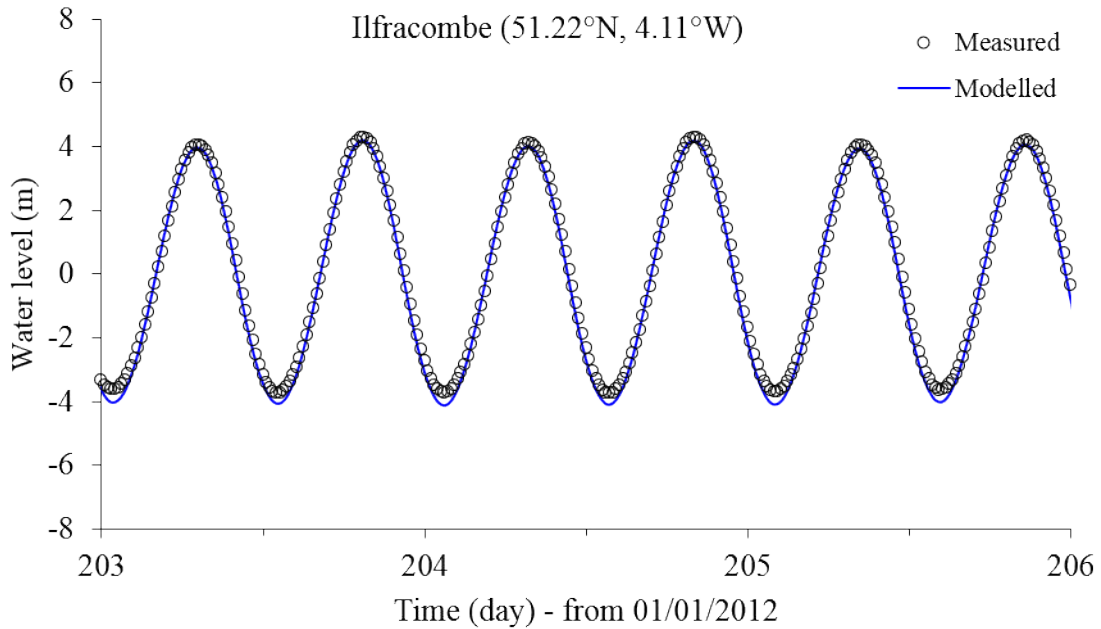
3.4 Hydrodynamic calibration

The modelling domain was specified with the tidal level time series at the seaward open boundary based on the calculation of the Irish Sea regional model (Olbert *et al.*, 2011; Ahmadian *et al.*, 2014), for driving the primary circulation process within the study area. The mean discharges from 29 rivers were included at the upstream boundaries based on the estimated values by Stapleton *et al.* (2007). The measured data of water levels and tidal currents for the hydrodynamic calibration at several locations respectively were based on the tidal gauge database (BODC) and tidal stream table of the Admiralty Chart 1179.

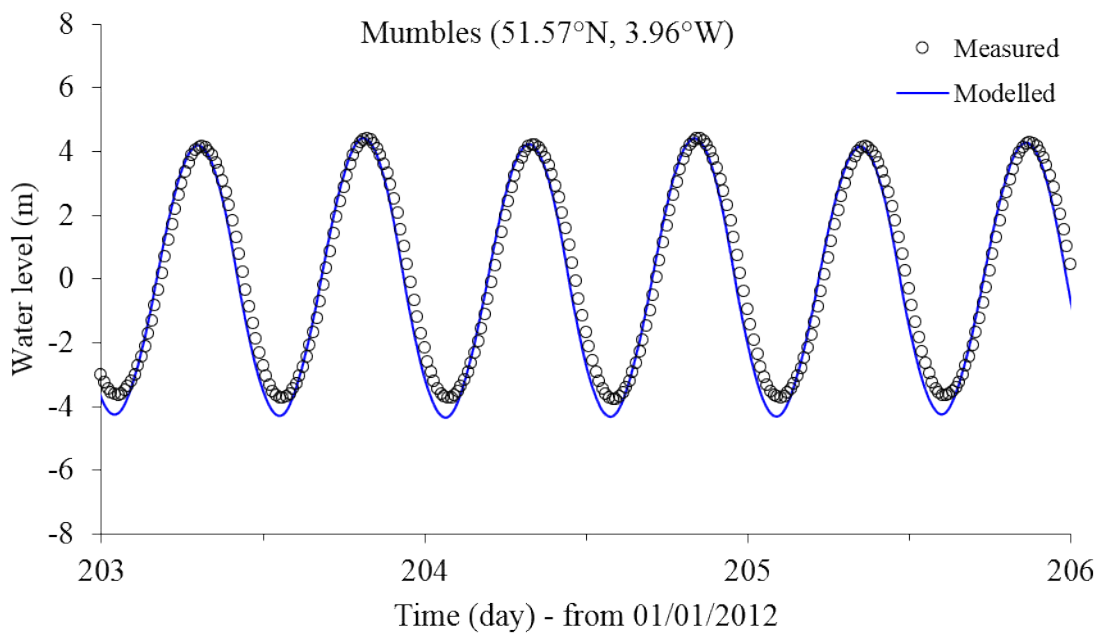
The initial condition for the water level was set at the constant elevation of high water across the modelling domain, referred to the open boundary condition. The current speed was set at null across the modelling domain as the initial condition for the circulation. The salinity and temperature were not modelled in relations of calibrating the primary circulation process. The model was run as a cold start with 20 cycles of a spring tide was forced the circulation process from the seaward open boundary. The model was run at a constant time step of 10 seconds for maintaining the computational stability at minimum grid sizes and accelerated current speeds near the solid boundary.

Hydrodynamic calibrations of the water level and the current circulation within the modelling domain were conducted by adjusting the Manning's value of the bottom roughness parameter. The range of Manning's value at 0.01 to 0.1 (Ji, 2008) was used as the basis for calibrating the hydrodynamic and was assigned at spatially constant across the study area. The modelled water levels, and current speeds and directions were compared to the measured data at Ilfracombe,

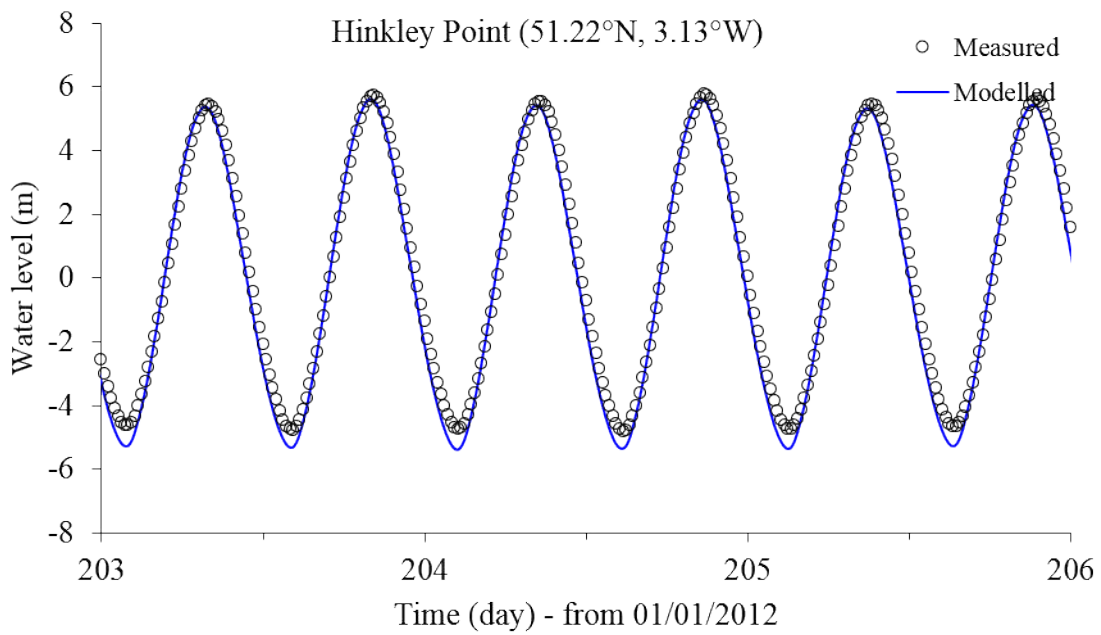
Mumbles, Hinkley Point and Newport, and at sites 1179P and 1179R of the Admiralty Chart respectively. The comparison of the calibrated water levels and current circulations to the measured data at the best-fit Manning's value (i.e. 0.025) are shown in Figures 3.3, 3.4 and 3.5 respectively.



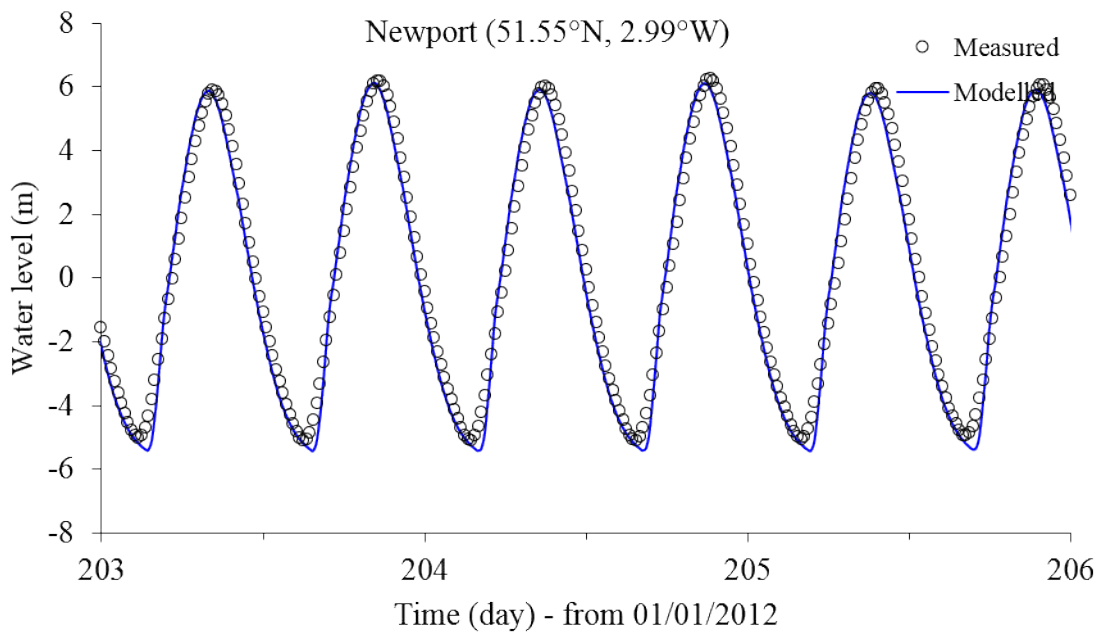
a) Water levels at Ilfracombe.



b) Water levels at Mumbles.

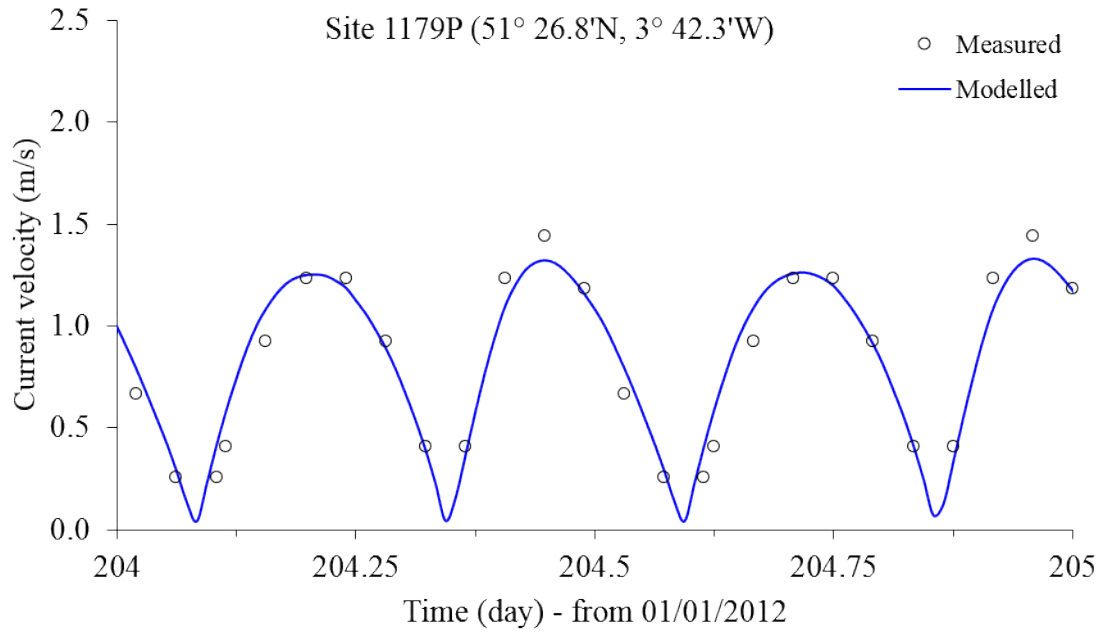


c) Water levels at Hinkley Point.

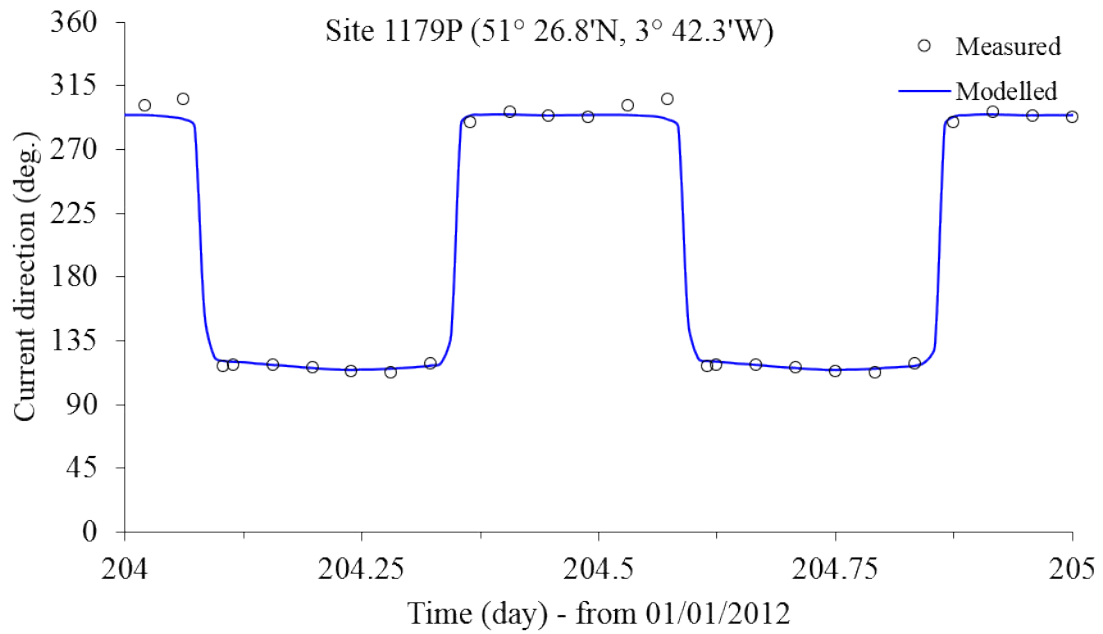


d) Water levels at Newport.

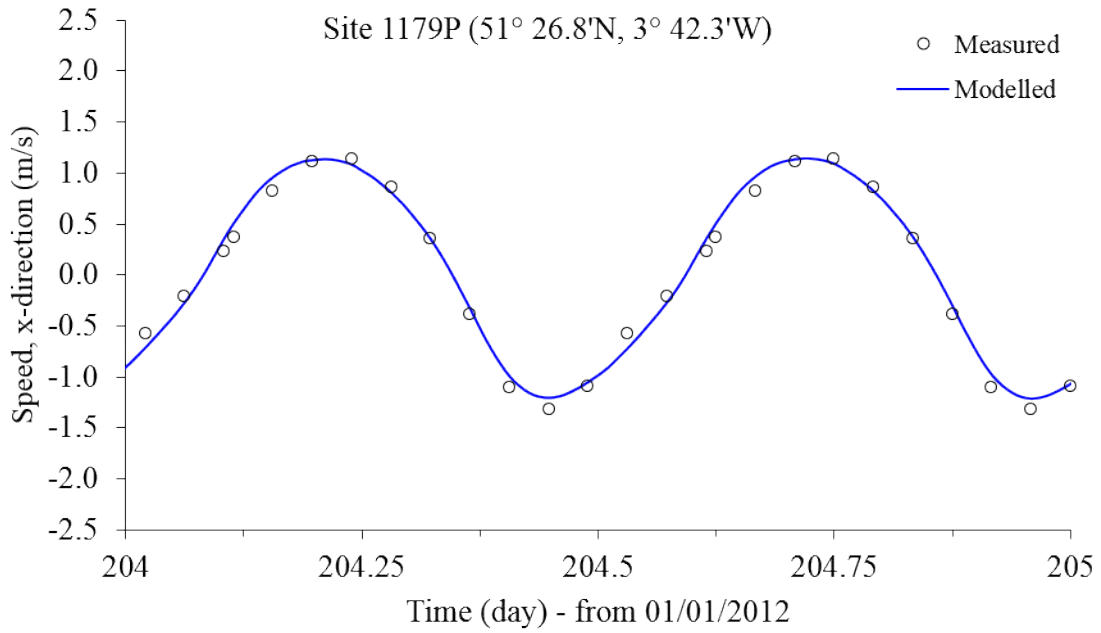
Figure 3.3: Comparisons of calibrated water levels to measured data at Ilfracombe (a), Mumbles (b), Hinkley Point (c) and Newport (d).



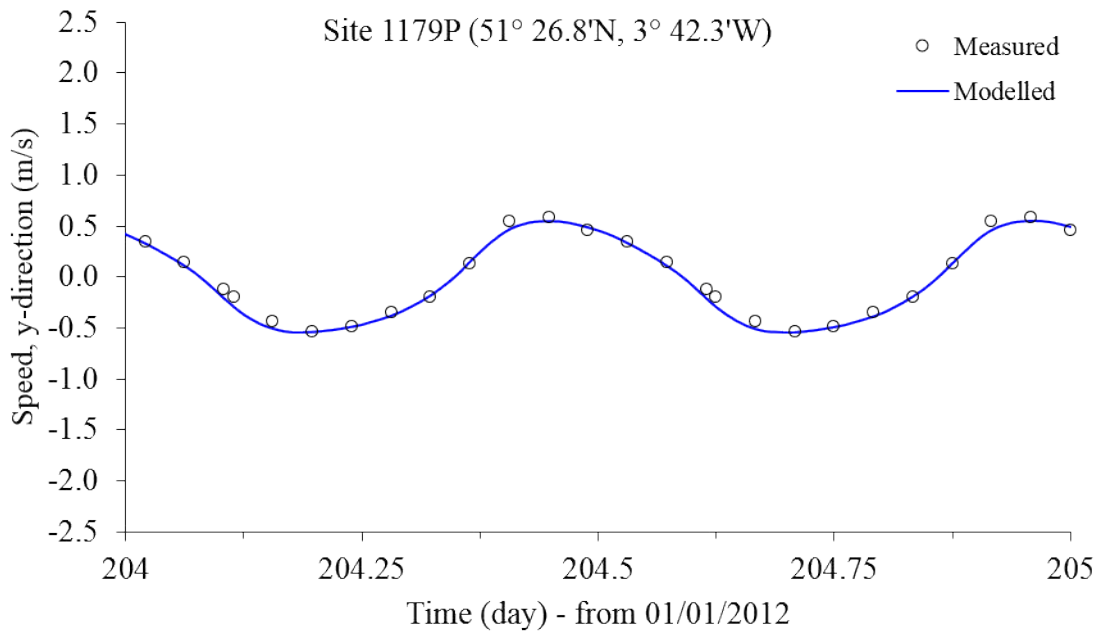
a) Current velocity at site 1179P.



b) Current direction at site 1179P.

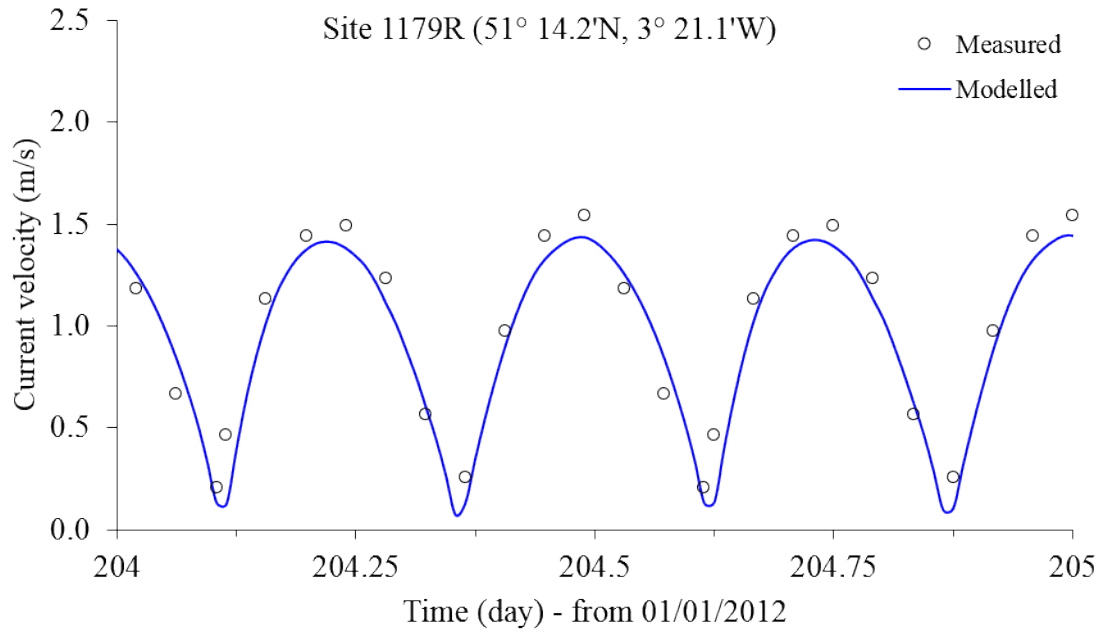


c) Current speed in x-direction at site 1179P.

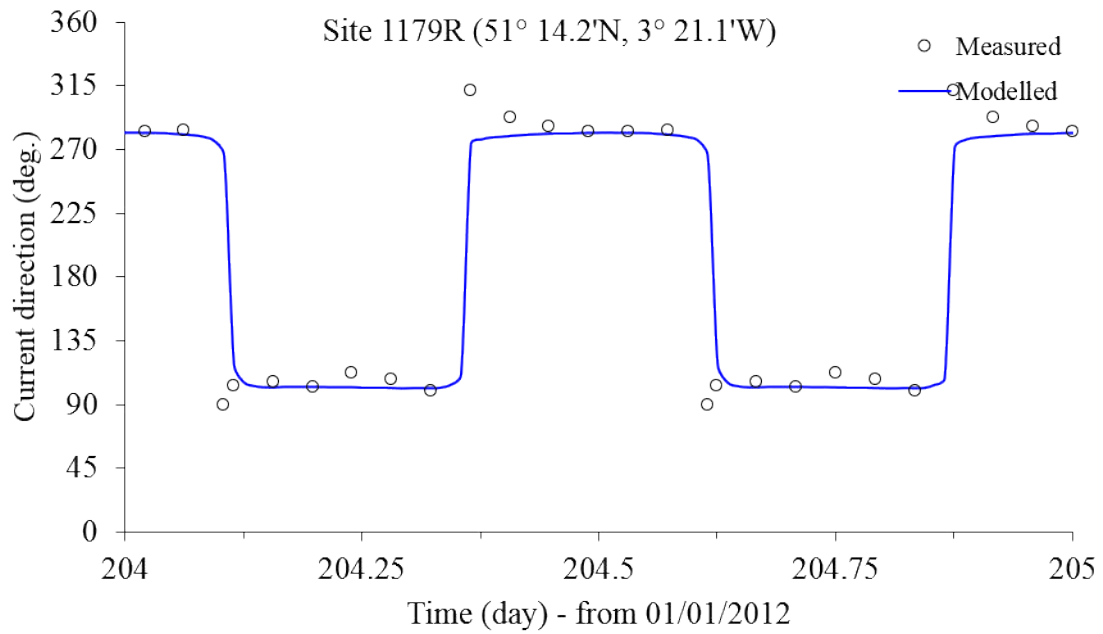


d) Current speed in y-direction at site 1179P.

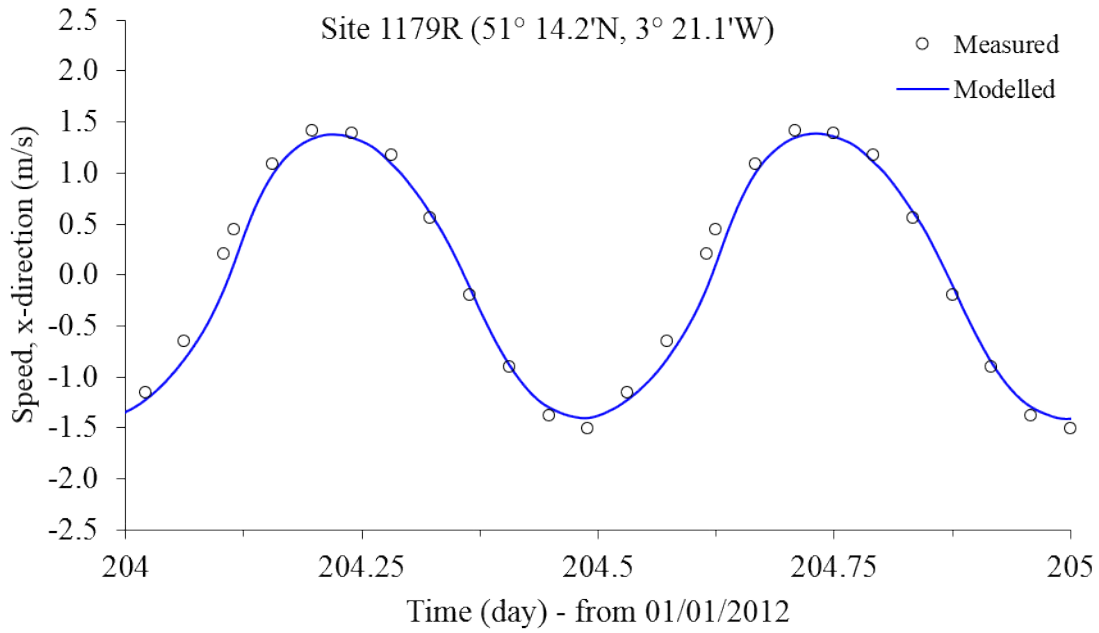
Figure 3.4: Comparisons of the calibrated tidal current for velocity (a), direction (b), and speeds in x- (c) and y-directions (d) to measured data at site 1179P.



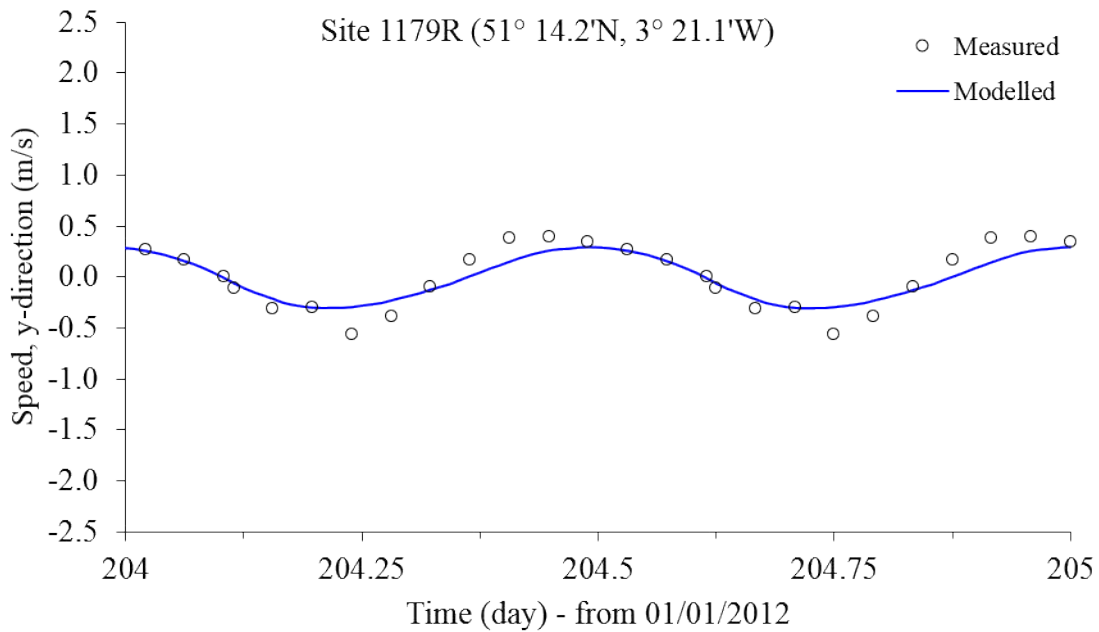
a) Current velocity at site 1179R.



b) Current direction at site 1179R.



c) Current speed in x-direction at site 1179R.

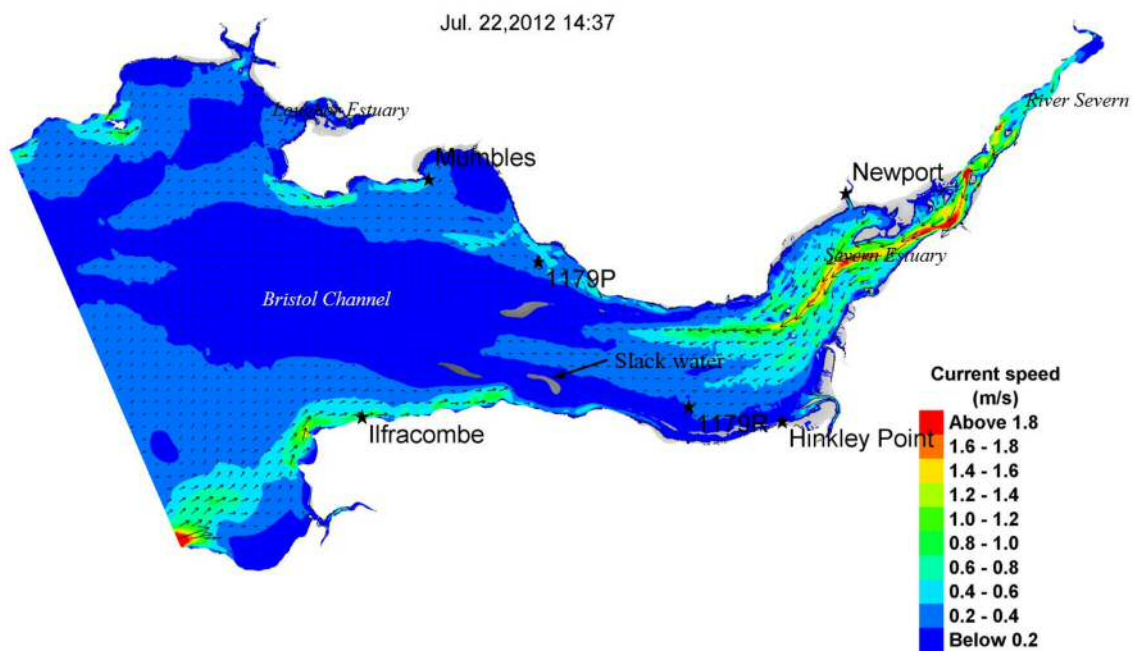


d) Current speed in y-direction at site 1179R.

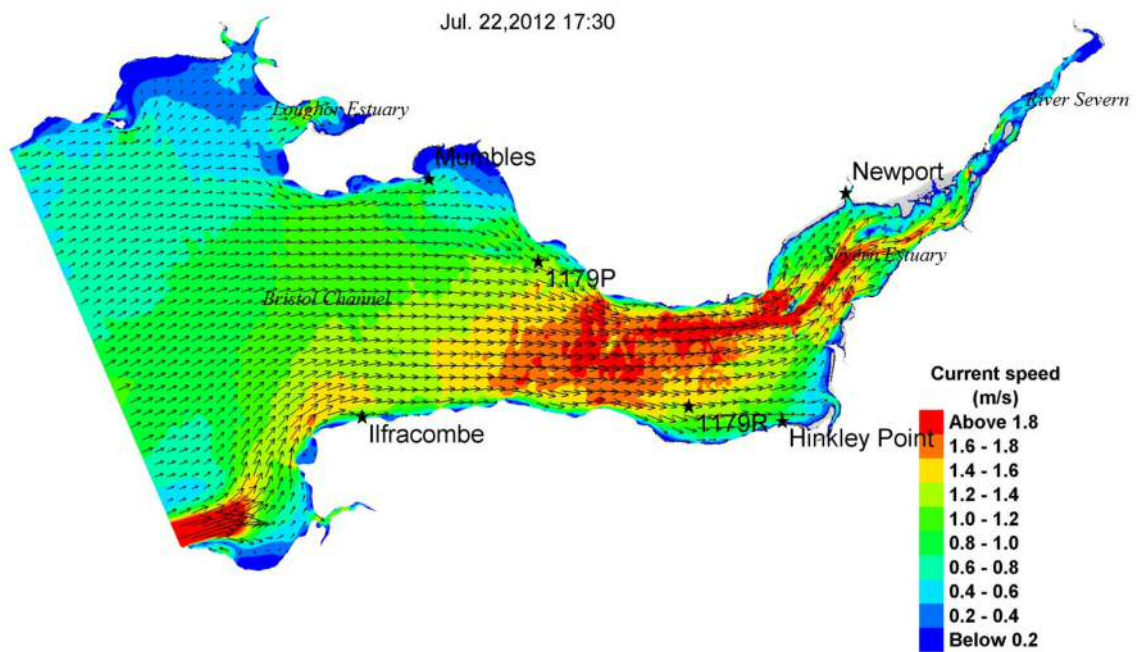
Figure 3.5: Comparisons of the calibrated tidal current for velocity (a), direction (b), and speeds in x- (c) and y-directions (d) to measured data at site 1179R.

General circulation patterns at different phases of a spring tidal cycle in the Severn Estuary and Bristol Channel are shown in Figure 3.6. During low tide, current speed below 0.2 m/s was

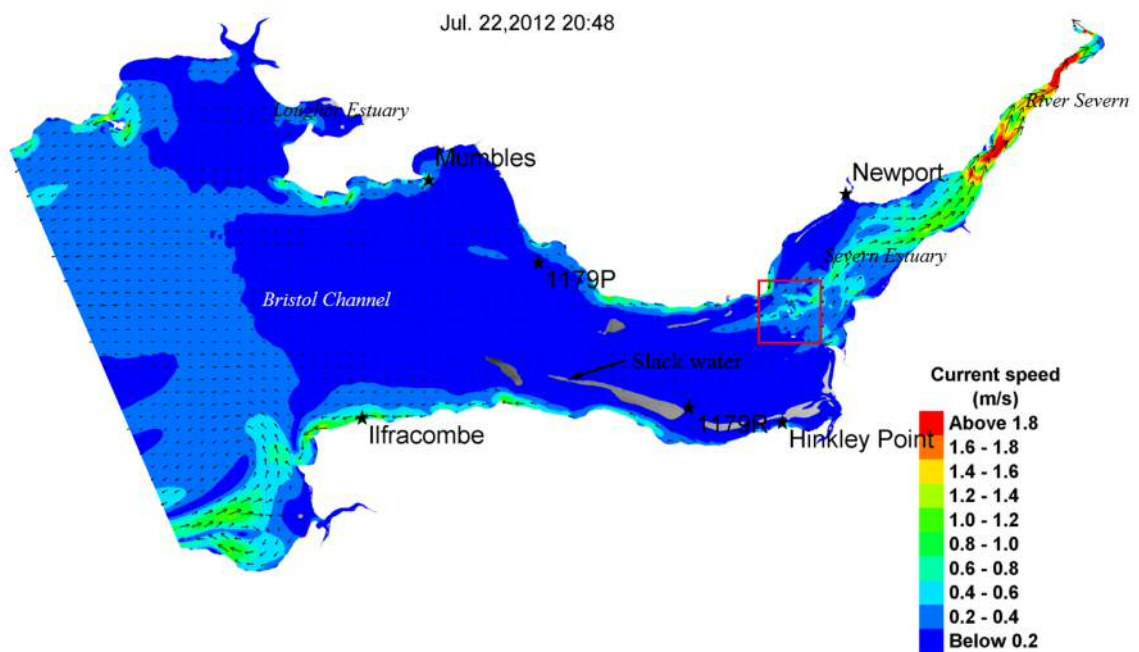
observed at the area of Bristol Channel, with slack waters were spotted around the inner channel. Current speed over 1.6 m/s was still observed along the channel in the Severn Estuary heading downstream. During flood tide, average current speed at 1.0 m/s was observed at the area of Bristol Channel, with speed above 1.8 m/s was observed at the inner channel up to the Severn Estuary. Current acceleration at the south of the open boundary was spotted due to shallow bottom elevation. During high tide, current speed below 0.2 m/s was observed at most of the Bristol Channel, with slack waters were spotted around the inner channel. Increase in speed over 0.6 m/s was spotted along shorelines especially at Ilfracombe besides at River Severn heading upstream. Clear island's wake was also observed at upstream of Flat Holm as shown in Figure 3.6(e). During ebb tide, average current speed at 1.0 m/s was observed at the area of Bristol Channel, with speed above 1.8 was observed at the inner channel up to the Severn Estuary. Current speed below 0.2 m/s was observed around the bays during flood and ebb tides.



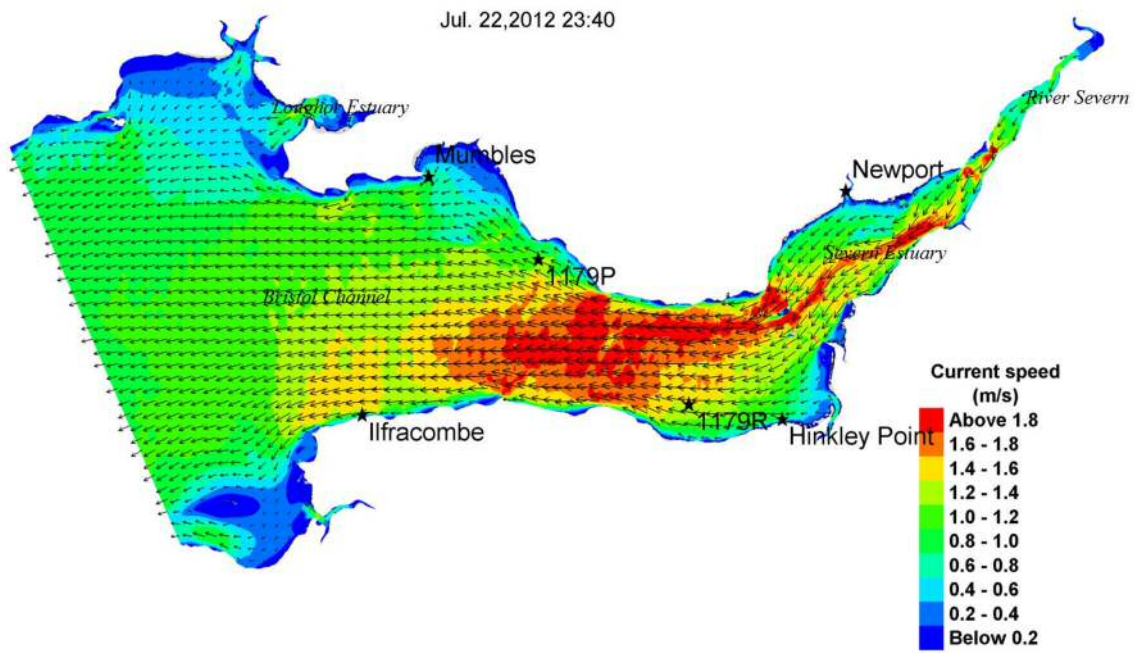
a) Tidal circulation during low tide.



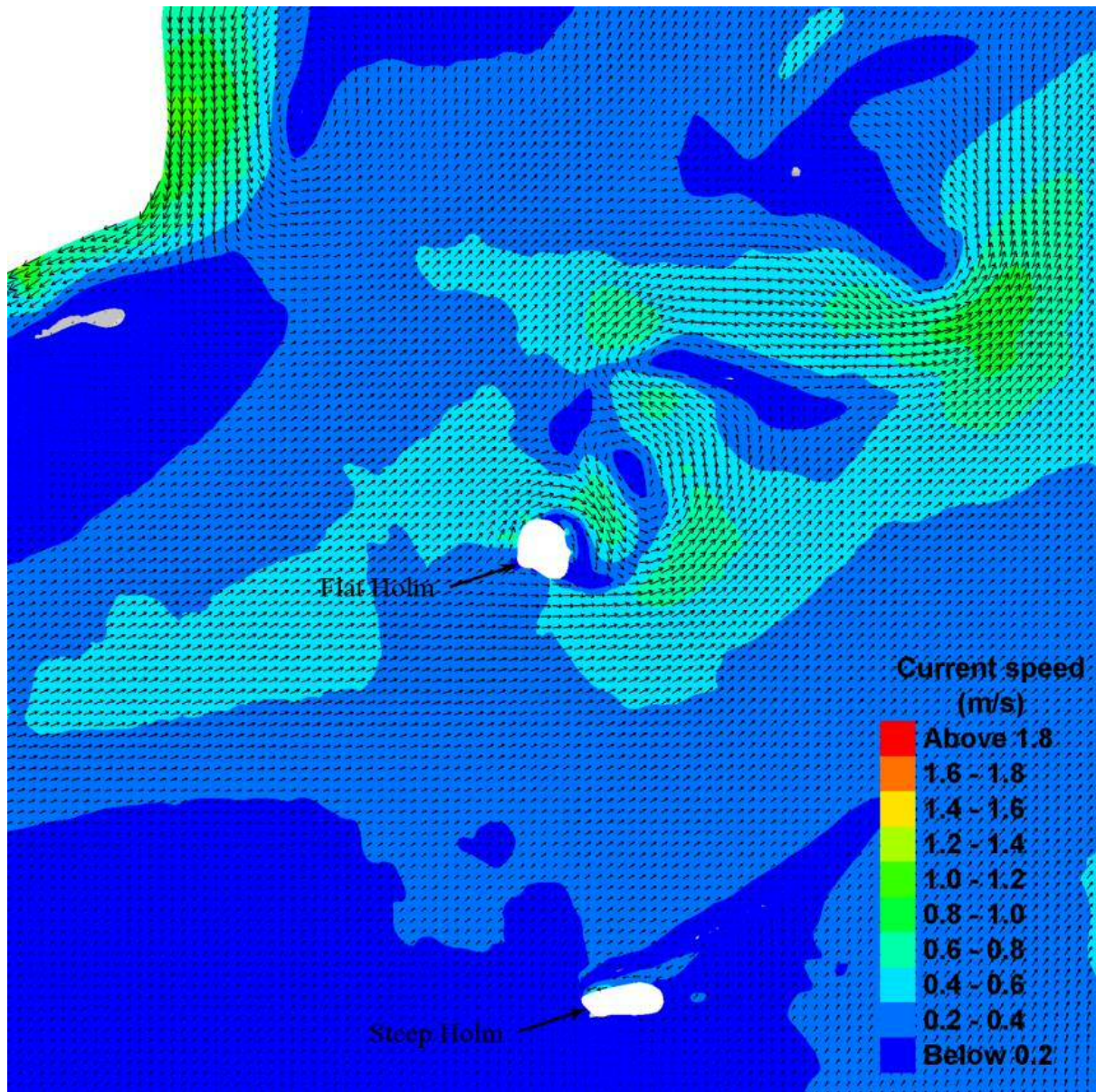
b) Tidal circulation during flood tide.



c) Tidal circulation during high tide. Island's wake formations within the red cell.



d) Tidal circulation during ebb tide.



e) Island's wake formations at upstream of Flat Holm during high tide (see Figure 3.6(c)).

Figure 3.6: General circulation patterns at phases of low tide (a), flood tide (b), high tide (c) and ebb tide (d) during a spring tidal cycle in the Severn Estuary and Bristol Channel. Details of island's wake (e) during high tide.

3.5 Summary

This chapter was focused on developing and calibrating a hydrodynamic model for the SEBC waterbody. Comprising a rigorous theoretical framework with flexibility in describing complex geometries, the TELEMAC Modelling System was employed for the solution of the primary hydrodynamic circulation at the SEBC. Considering the waterbody as a well-mixed estuary, a

two-dimensional modelling domain of the SEBC was discretised based on the unstructured mesh. To establish the primary hydrodynamic circulation, the bathymetric data was priority interpolated to the mesh-nodes which then followed with the specification of tidal and stream forcings at the open boundary. Based on the hydrodynamic calibration at several sites for the water level and the tidal current, the Manning's n of 0.025 was found as an optimum value when compared to the measured data.

Chapter 4: Intertidal floodplains extension

4.1 Introduction

This chapter was focused on extending the modelling domain at intertidal floodplains of the study area, namely the Loughor Estuary. This extension was essential to improve an understanding of the processes experienced by the faecal indicator organisms while being transported in the estuarine environment from different sources, in order to assess their impacts to the water quality at the sites of interest. Extending the modelling domain at intertidal floodplains was crucial for the study area with the large tidal range, i.e. could reach to the maximum of 7.5 m during spring tides near Burry Port (Bakar *et al.* 2017). The high-quality integration between topographic and bathymetric data prior to extending the modelling domain was the key for simulating actual hydrodynamic and transport processes at the floodplains (Eakins and Grothe 2014; Danielson *et al.* 2016). Besides, designing the unstructured mesh at the floodplains was necessary for enhancing the representation of sub-mesh-scale features (Schubert *et al.* 2008) at the same time for optimising the computational cost (Kim *et al.* 2014). Furthermore, the distribution of bottom roughness especially due to vegetations at the modelling floodplains was essential for the correct simulations of circulation and pollutant transport as it is primary in controlling these processes besides the topography (Sullivan *et al.* 2015). The stream discharge as the boundary condition was also essential which acts as the primary transport mechanism that contributes to the flushing ability of an estuary, besides the tide and the density induced circulation (Wang *et al.* 2004).

This chapter was organised as follows: Section 4.2 presented the DEM data processing based on the bare earth as a data source and its issue. This section included methods for the horizontal and vertical datums conversion to common datums, the bare earth separation from artefacts using the land-water boundary mask, the use of a different data source for filling the gap at intertidal areas, and the discussion on results of the integration between topographic and bathymetric data. Section 4.3 presented the intertidal domain extension using an outer boundary above the MHWS. This section included methods for the mesh-nodes placement based on the modelling domain decomposition and mesh resolution functions, the tidal creeks network extraction with vertices redistribution, and the elevation dataset interpolation to the nodes of vertical features and floodplains. Section 4.4 presented the bottom roughness parameterisation at the study domain and included a method for friction sub-domains

characterisation based on principal terrain features. Section 4.5 presented the catchments delineation that contributes stream discharges into the study domain and included a method for the discharge estimation at ungauged stream outlets.

4.2 DEM data processing

4.2.1 Bare earth

The topographic data measured by the Light Detection and Ranging (Lidar) airborne mapping technique, was provided by the Environment Agency and Natural Resources Wales covering the area of South West Wales, i.e. Carmarthen Bay, Loughor Estuary and Swansea Bay. The provided data was in the format of ‘bare earth’ of the digital elevation models (DEMs) of the ASCII raster, and in the tile size of 1 × 1 km² with the resolution of 2 m. The ‘bare earth’ DEMs, which are referred as the DEMs hereafter, was a digital terrain representation on the square grids (Medeiros *et al.* 2011), with any other surface over the earth surface, such as vegetation canopy, man-made structures and water surface, was removed prior to the development of the DEMs (Eakins and Grothe 2014). The provided data was originally referenced to the horizontal and vertical datums of the British National Grid (BNG) and Ordnance Datum Newlyn (ODN), respectively.

Total of 1,666 tiles of 1 × 1 km² raster data, i.e. 945 from SN grid and 721 from SS grid, were mosaicked into 10 × 10 km² raster size using the Data Management Toolbox of ArcGIS, to reduce the number of the tiles into 38 and for simplifying the following data processing steps. The 10 × 10 km² DEMs were represented as Hillshades using the Spatial Analyst Toolbox of ArcGIS as shown in Figure 4.1. The contour line of zero-meter elevation was generated from the DEMs using the Spatial Analyst Toolbox of ArcGIS and was overlaid to the mosaicked data tiles as the delineation of the shoreline.

Figure 4.1 shown that these DEMs were retained the water surface along the nearshore where these airborne bathymetric lidar surveys were unable to measure through surf zones and turbid waters (Eakins and Grothe 2014). The airborne lidar surveys which flew at different tidal levels also known to produce concave and convex spots at the water surface when they were merged at the intertidal zone (Holden 2004), as described in the Appendix (i.e. Figures C.1(a) and

C.1(b)). These spots are shown in Figure 4.2 for the areas of Carmarthen Bay, Loughor Estuary and Swansea Bay. The overlaid contour lines range from -2 m to 2 m on these DEMs emerging the concave and convex spots presentation between the drying intertidal land and the water surface (also known as artefacts, as referred to Eakins and Grothe (2014) and Danielson *et al.* (2016)). These artefacts are critical for the hydro-environmental modelling and particularly for flooding and drying and the water circulation at areas of the land-water interface.

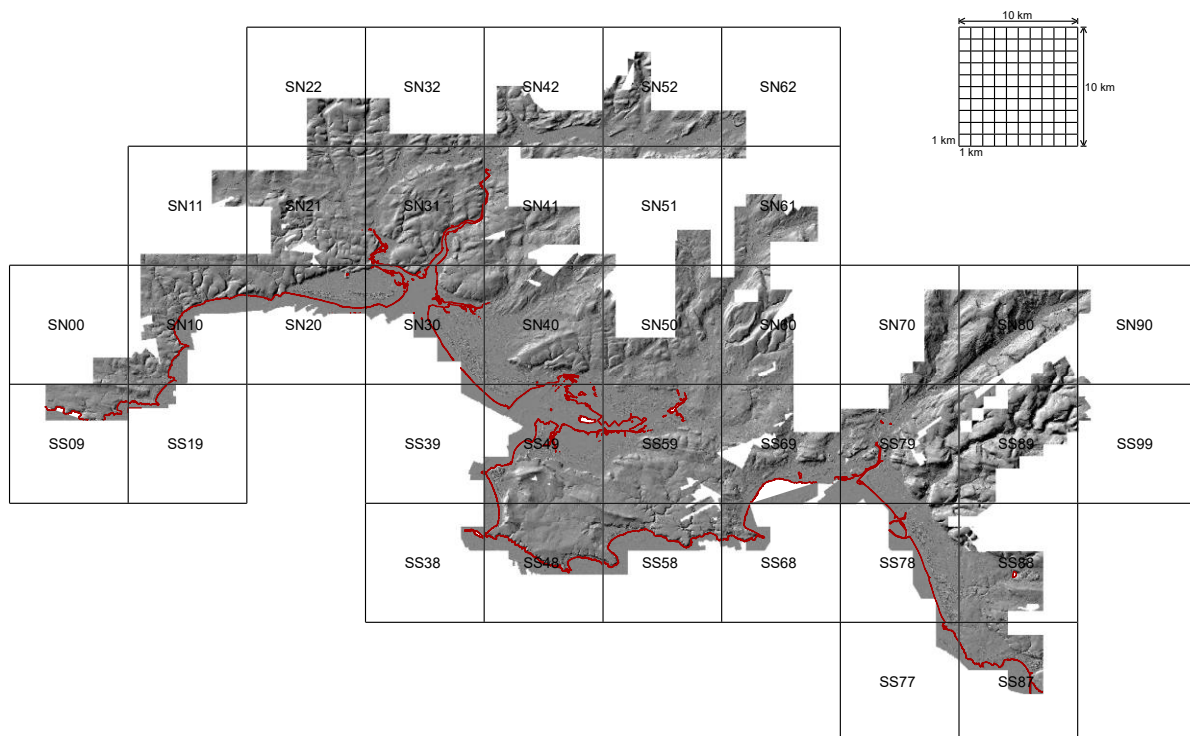
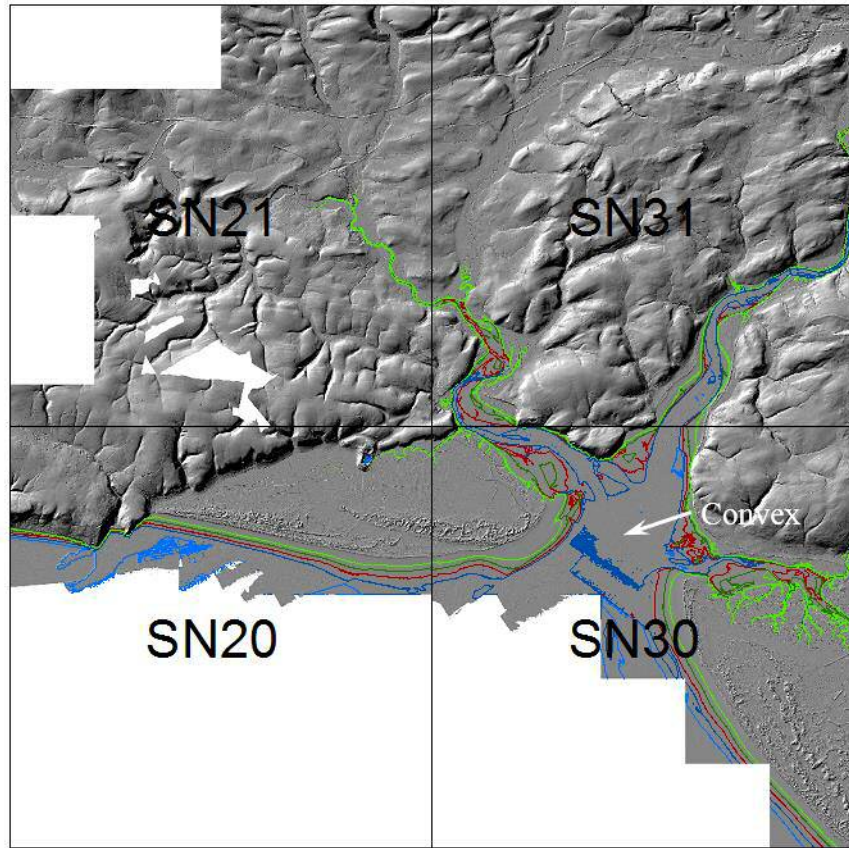
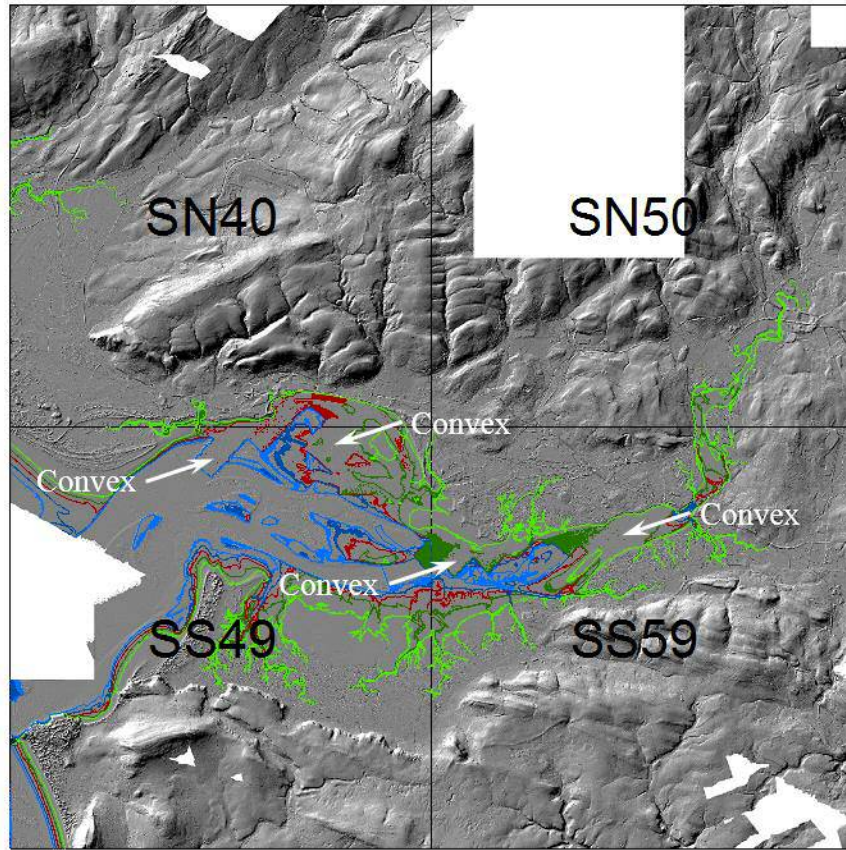


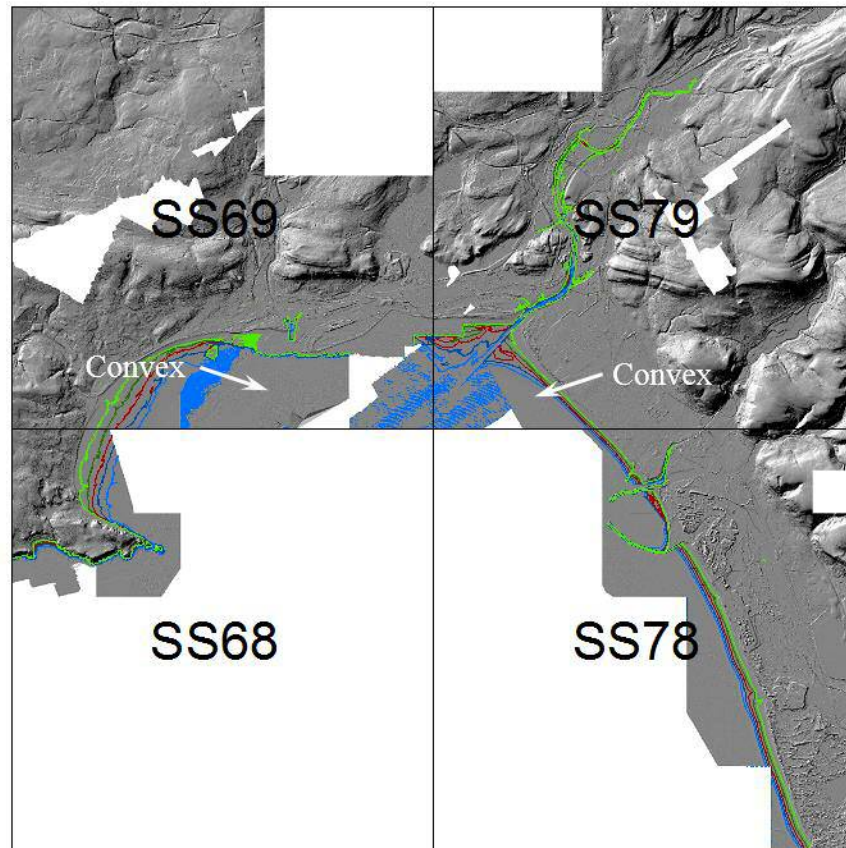
Figure 4.1: Topography of the ‘bare earth’ DEMs for Carmarthen Bay, Loughor Estuary and Swansea Bay, with the overlaid contour line of zero-meter elevation is shown in red. The scale is shown on the top right of the figure.



a) Contour lines at Carmarthen Bay.



b) Contour lines at Loughor Estuary.



c) Contour lines at Swansea Bay.

Figure 4.2: Overlaid contour lines of -2 m (light blue), -1 m (dark blue), 0 m (red), 1 m (dark green) and 2 m (light green) on the DEMs at Carmarthen Bay (a), Loughor Estuary (b) and Swansea Bay (c) that highlighting the convex spots between drying intertidal areas and the water surface.

4.2.2 Horizontal and vertical datums conversion

The common horizontal projection was required, in order to merge between the bathymetric data and the DEMs. The WGS 1984 UTM Zone 30N coordinate system was used as the common horizontal datum similar to the bathymetric data (i.e. as mentioned in Section 3.2.1). The DEMs that originally referenced to the horizontal datum of BNG was projected to the WGS 1984 UTM Zone 30N coordinate system using the Data Management Toolbox of ArcGIS. This process involved the conversion between the geographic (i.e. three-dimensional) and projected (i.e. two-dimensional) coordinate systems and the transformation between the OSGB-36 and WGS-84 geographic systems using the WGS 1984 Petroleum (refer Figure C.2 in the Appendix).

The DEMs and the bathymetric data were both referenced to the vertical datum of ODN. The ODN is the orthometric datum which commonly used for the topographic datasets such as the DEMs data. In this case, the bathymetric data which usually surveyed at the Lowest Astronomical Tide (LAT) of the tidal datum reference, has been converted to the ODN of orthometric datum prior applications (Ahmadian, Olbert, *et al.* 2014).

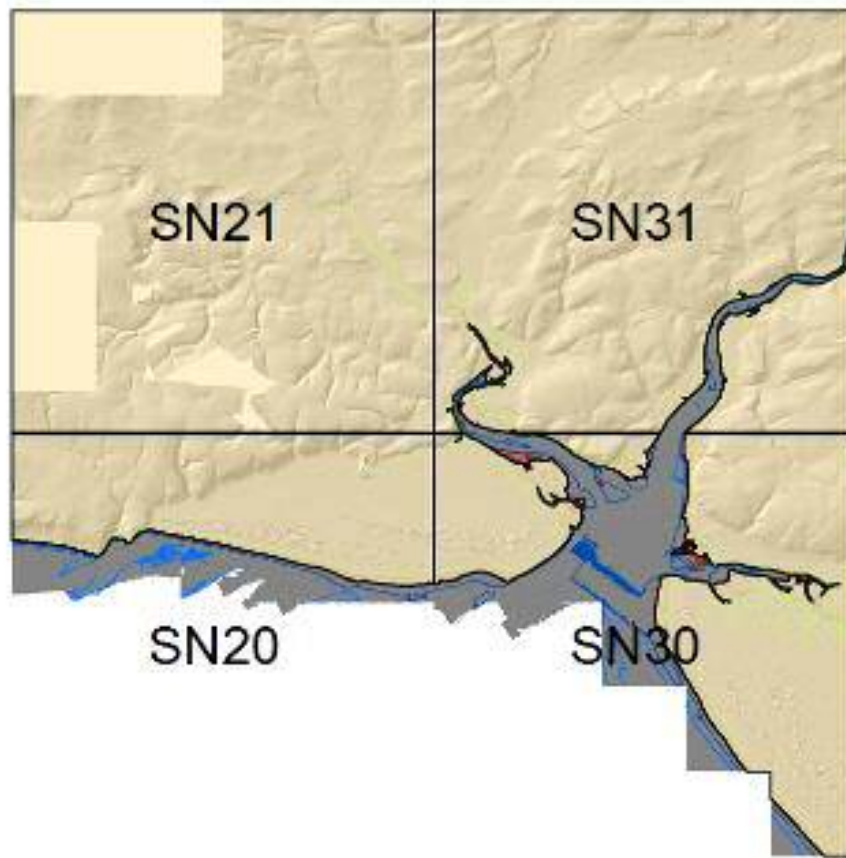
Horizontal datum transformation resulted in the issue known as ‘zero value’ at the edge of data tiles. This issue also terms the ‘data void’. The data void was eliminated from the transformed DEMs, with the resolution was also reduced from 2 m to 8 m for reducing the interpolation cost to the mesh-nodes in the following steps.

4.2.3 Land-water boundary mask

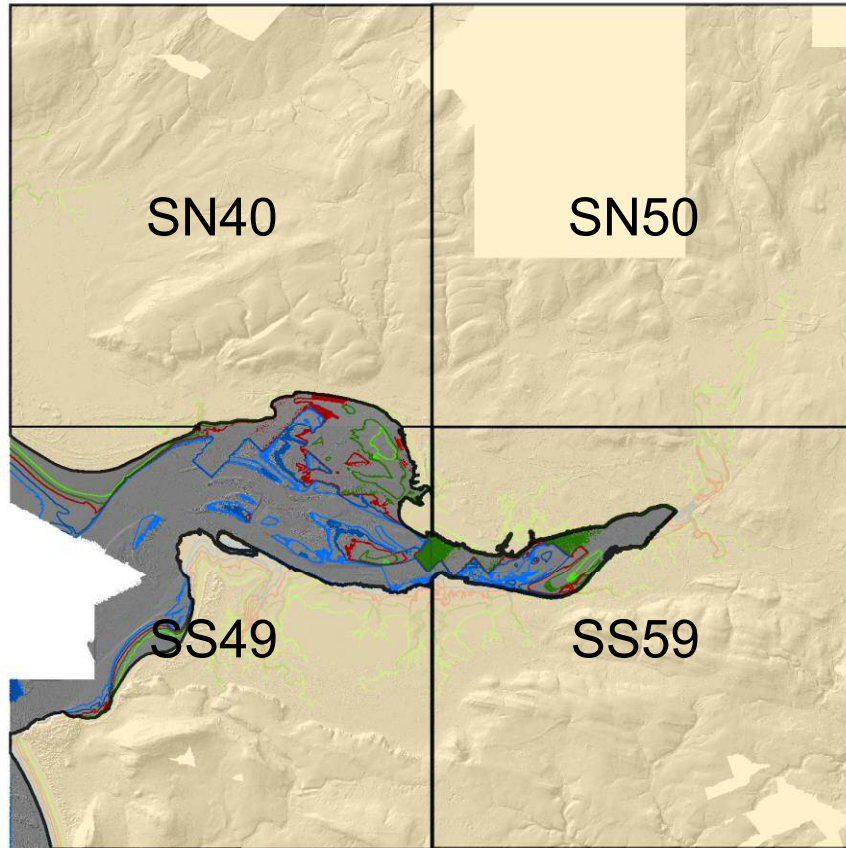
The water surface along nearshores of the DEMs at Carmarthen Bay, Loughor Estuary and Swansea Bay needed to be removed prior to integration with the bathymetric data. Data tiles for the areas of Loughor Estuary (i.e. SN40, SN50, SS49, SS59) and Swansea Bay (i.e. SS68, SS78, SS69, SS79) were examined to delineate the boundary between the land and water, as the drying extension of the intertidal for these areas, due to surveying at different tidal ranges, were uncertain. The overlaid contour lines were evaluated to differentiate between the lines representing the drying areas and the lines which represent the water surface. The priority was given to the lowest contour elevation of drying areas wherever possible, for the maximum extension of intertidal flats. The best contour lines were joined together to form a smooth, continuous-closed boundary that defined the extension of drying intertidal areas, by using AutoCAD (see Table C.1 in the Appendix).

The polygon class of the land-water delineated boundary (i.e. thick-black lines) was used for the conversion of drying areas to the mask raster using the Conversion Toolbox of ArcGIS, as shown in Figures 4.3(b) and 4.3(c) that were overlaid the DEMs and contour lines of Loughor Estuary and Swansea Bay respectively. The generated mask was then used to clip out the water surface along nearshores of the DEMs using the Spatial Analyst Toolbox of ArcGIS, by extracting the elevation cells of DEMs that correspond to the areas defined by the mask raster. The ‘land extracted’ DEMs for the areas of Loughor Estuary and Swansea Bay are shown as

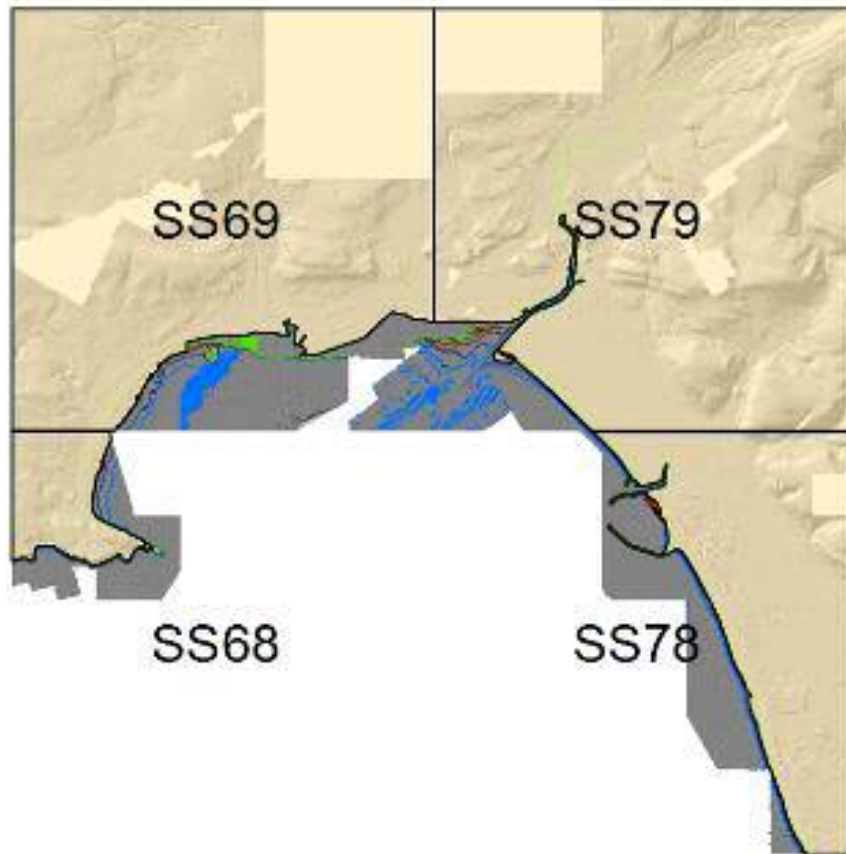
in Figures 4.4(b) and 4.4(c) respectively, which were successfully eliminated the water surface at the maximum of drying intertidal extension.



a) Land-water boundary mask at Carmarthen Bay.

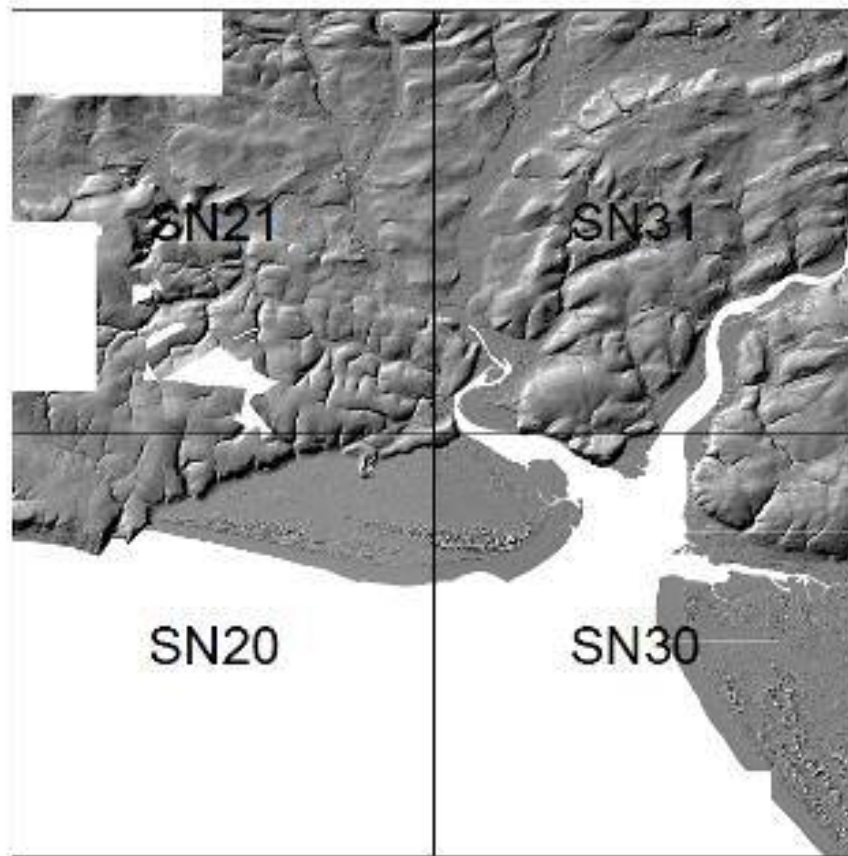


b) Land-water boundary mask at Loughor Estuary.

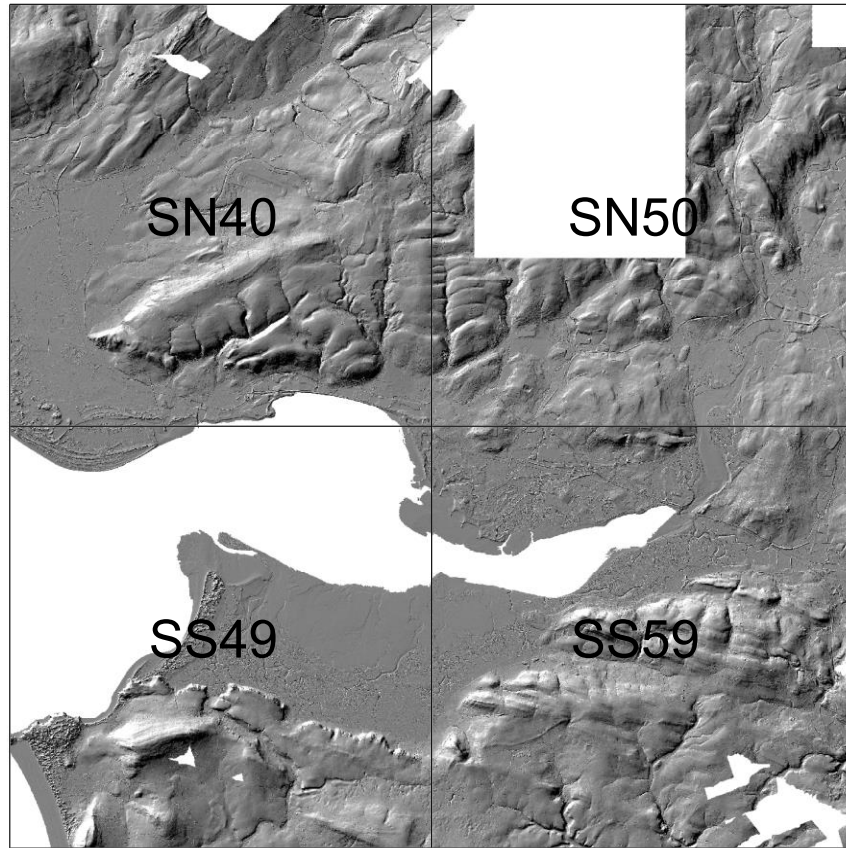


c) Land-water boundary mask at Swansea Bay.

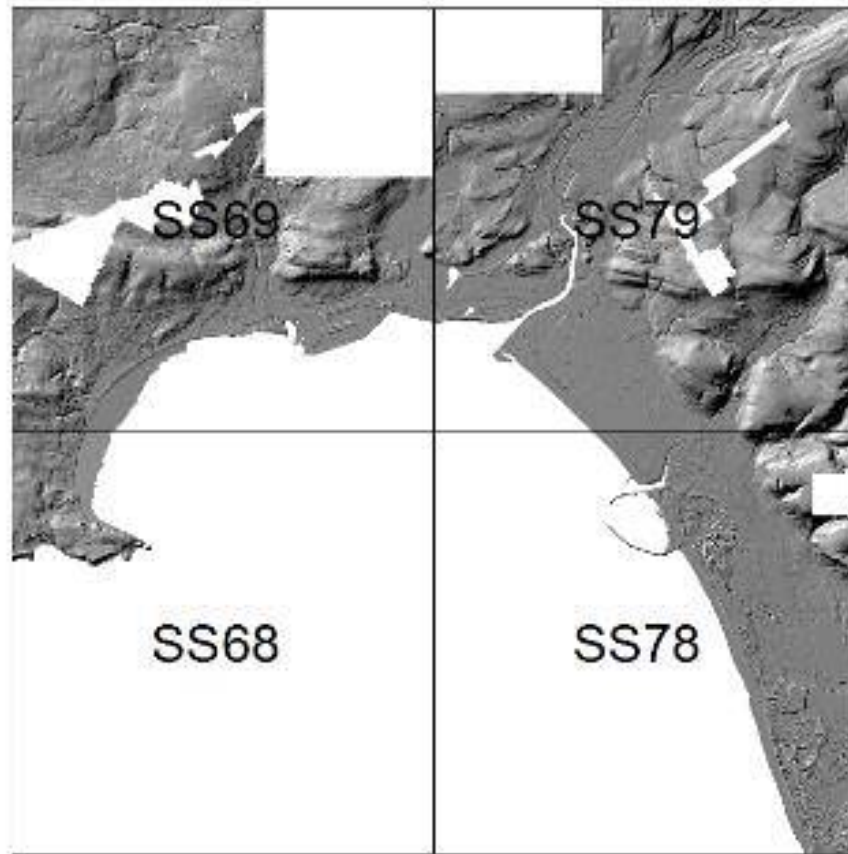
Figure 4.3: Land-water boundary mask overlaid on the DEMs at Carmarthen Bay (a), Loughor Estuary (b) and Swansea Bay (c) with the contour lines as guidance in defining the extension of the intertidal areas.



a) 'Land extracted' DEMs at Carmarthen Bay.



b) 'Land extracted' DEMs at Loughor Estuary.



c) 'Land extracted' DEMs at Swansea Bay.

Figure 4.4: 'Land extracted' DEMs at Carmarthen Bay (a), Loughor Estuary (b) and Swansea Bay (c) with the elimination of water surface at the maximum extension of drying intertidal areas.

The seaward area of the zero-meter contour, which the line was almost identical to the maximum extension of drying intertidal areas, was removed from the DEMs of the Carmarthen Bay area (i.e. SN20, SN30, SN21 and SN31). The polygon class of this closed-boundary feature was converted to the mask raster, in order to extract the elevation cells of DEMs from the defined drying areas, same as the above procedure. The 'land extracted' DEMs for the area of Carmarthen Bay is shown as in Figure 4.4(a), which shows that the water surface below the contour line of zero-meter elevation was successfully removed without retaining the artefacts of surf zones and turbid waters. The 'land extracted' DEMs for the areas of Carmarthen Bay, Loughor Estuary and Swansea Bay were then saved as the ASCII raster before being converted to the pointset data format.

4.2.4 Filling gaps in the intertidal data

The elevation cells beyond the extension of the drying intertidal areas, which had been removed from the DEMs across the Loughor Estuary, had to be replaced with a suitable elevation data prior to integration with the bathymetric data. The term “gap-fill” was used within the context of representing the replacement of this elevation data (Danielson *et al.* 2016). The depth-averaged data from the hydro-environmental model by Liang *et al.* (2013) was used to fill the gaps in the elevation data at these intertidal areas. The depth data of wet cells were extracted from this 50 x 50 m² coarser grid model, with 321 columns and 231 rows, as shown in Figure 4.5. The extracted depth data, however, was not horizontally projected to any coordinate system but was referred vertically to the ODN same as the DEMs.

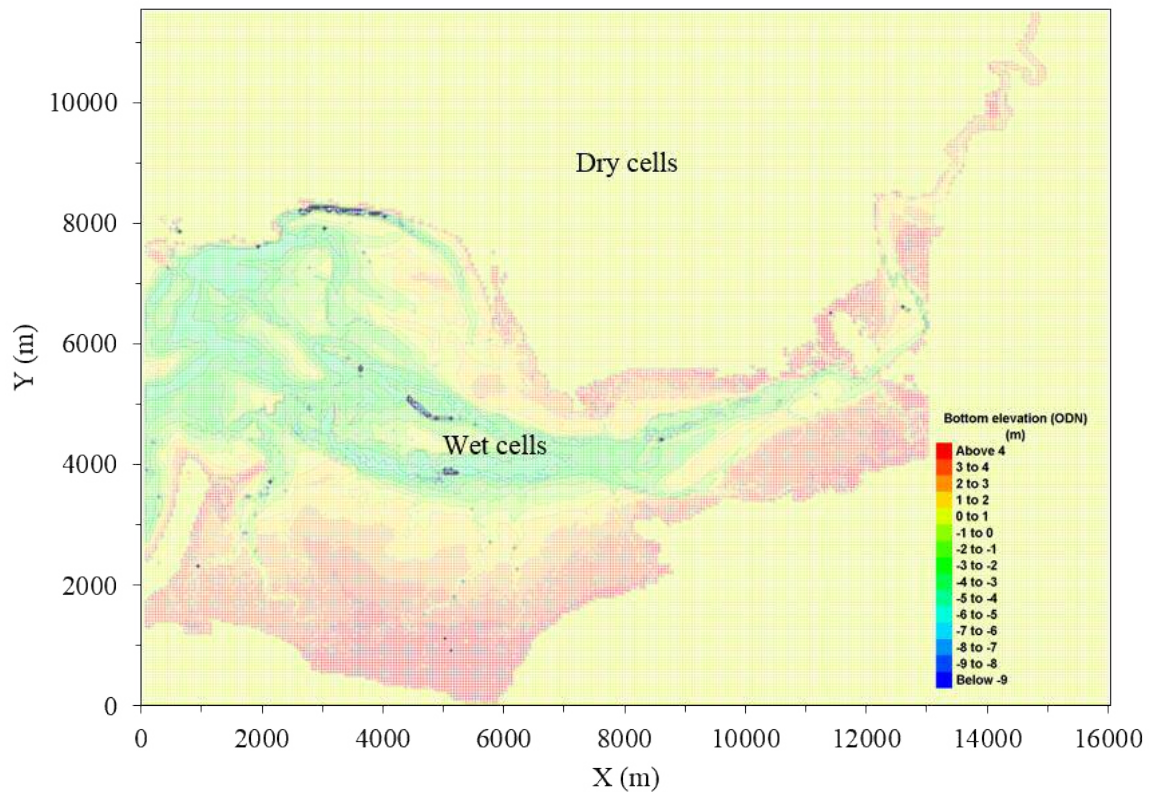


Figure 4.5: The gridded depth-averaged data of the hydro-environmental model by Liang *et al.* (2013). Dry cells are shown in the yellow background (i.e. elevation set to zero) that surrounded by wet cells.

The depth-averaged data from the Liang *et al.* (2013) model which was referred as the bottom elevation hereafter, needed to be projected horizontally to the WGS 1984 UTM Zone 30N

coordinate system, same as the DEMs prior to the integration. The coordinate locations for Loughor Bridge and Burry Port have been marked at both the bottom elevation and the DEMs. The horizontal and vertical distances between Loughor Bridge and Burry Port for both the bottom elevation and the DEMs were determined and found to be identical. The angles at Burry Port from Loughor Bridge were also determined for both datasets, with the angle from the bottom elevation was found to be greater than the angle from the DEMs. The bottom elevation was projected to the horizontal coordinate by translating and rotating this data based at the reference point (i.e. Loughor Bridge), horizontally at 41,310.932 m and vertically at 5,718,619.423 m, and at the angle of 1.17 degree respectively. Readers are referred to the Appendix (i.e. Tables C.2 and C.3) for details of the calculation and the graphical explanation.

The projected bottom elevation with the generated contour lines above zero-meter was overlaid on top of the contours that were generated using the DEMs, as shown in Figure 4.6. The overlaid contour lines were identical at 0, 2 and 4 m elevations and properly merged across the intertidal areas. However, there were discrepancies between the contour lines in regions where the surface slopes were mild such as the North banks near Llanelli and the South of the estuary over the Llanrhidian Marsh. The contours of the DEMs which was the newer data were located several meters seaward compared to the contour lines of the bottom elevation, which indicated the occurrence of the morphological accretion at the banks of the estuary.

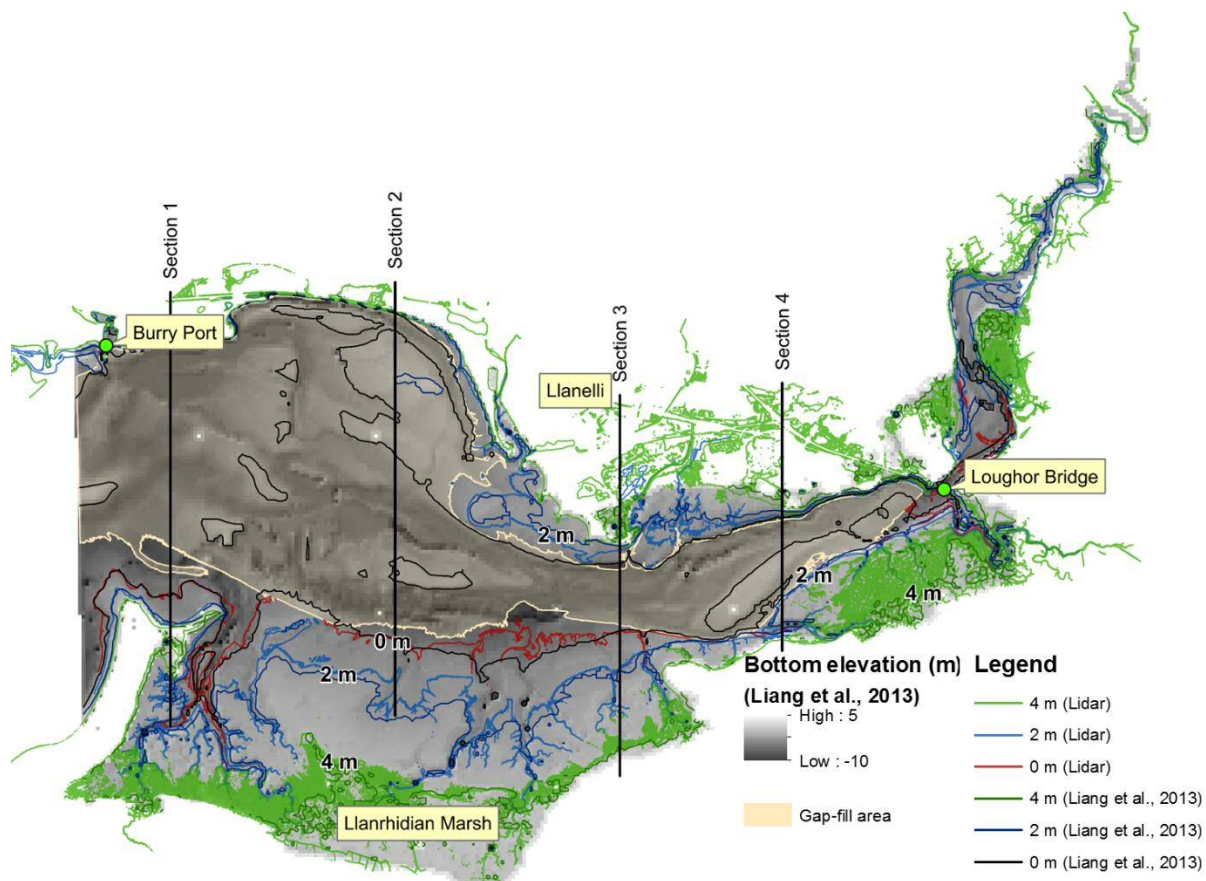
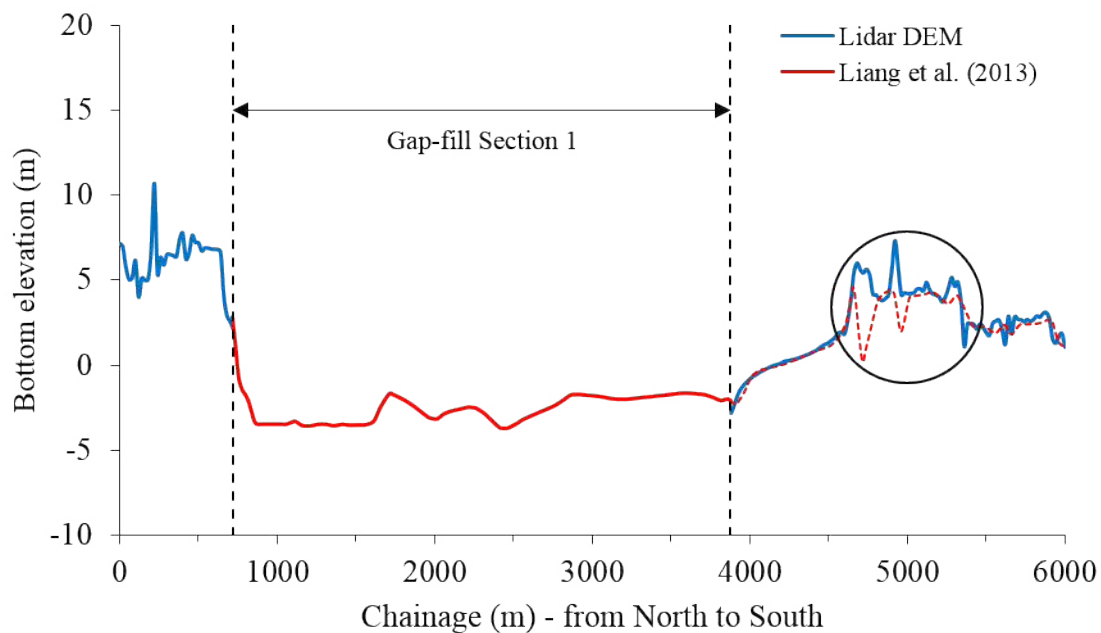


Figure 4.6: The bottom elevation of the Liang *et al.* (2013) model with its contour lines, overlying with contours of the DEMs, a gap-fill polygon at the intertidal area, and the cross-sectional lines.

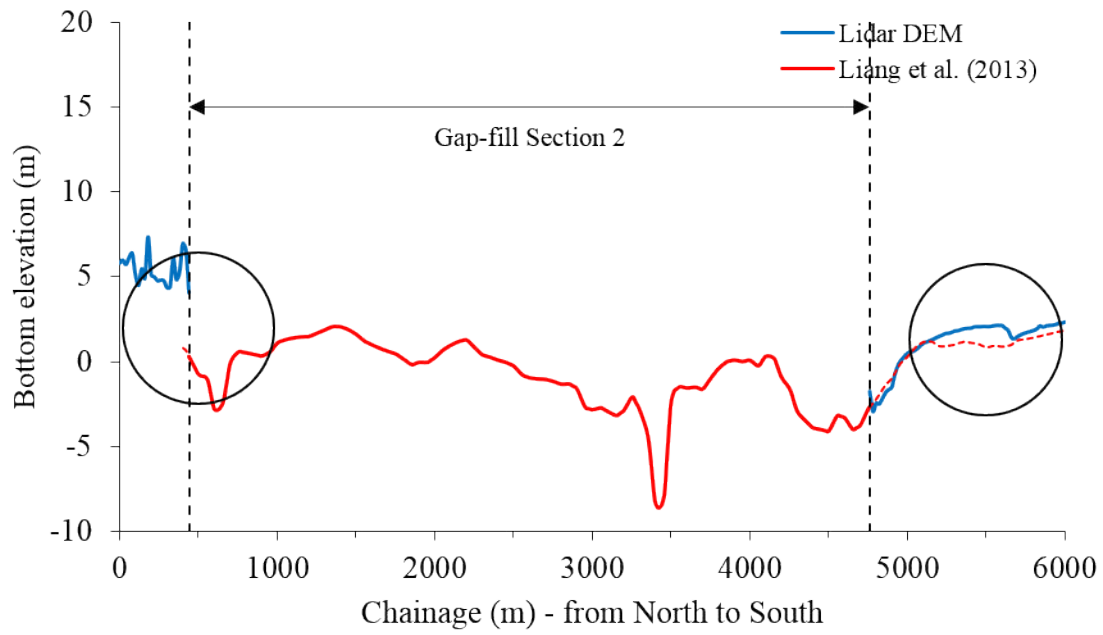
The area where there was a gap across the DEMs of Loughor Estuary is shown in Figure 4.6 as a polygon based on the land-water boundary that was overlaid to the bottom elevation. The polygon mask was covered most of the intertidal area which was below the datum. This gap-fill area extended from Burry Port on the West to the proximity of Loughor Bridge on the East of the estuary. This area was also included two sand banks which were mainly above the datum and located near Llanelli and Llanrhidian Marsh, namely Cefn Padrig Sand and Llanrhidian Sands respectively. The cell's elevations of the defined area were then extracted for the integration between the DEMs at the overland and the bathymetric data at the open water.

In order to investigate the fitting between two datasets, the cross-sections of the bottom elevation profiles comparing the integration between the Liang *et al.* (2013) model and the DEMs were plotted at four different locations along the estuary. Figures 4.7(a) to 4.7(d) show

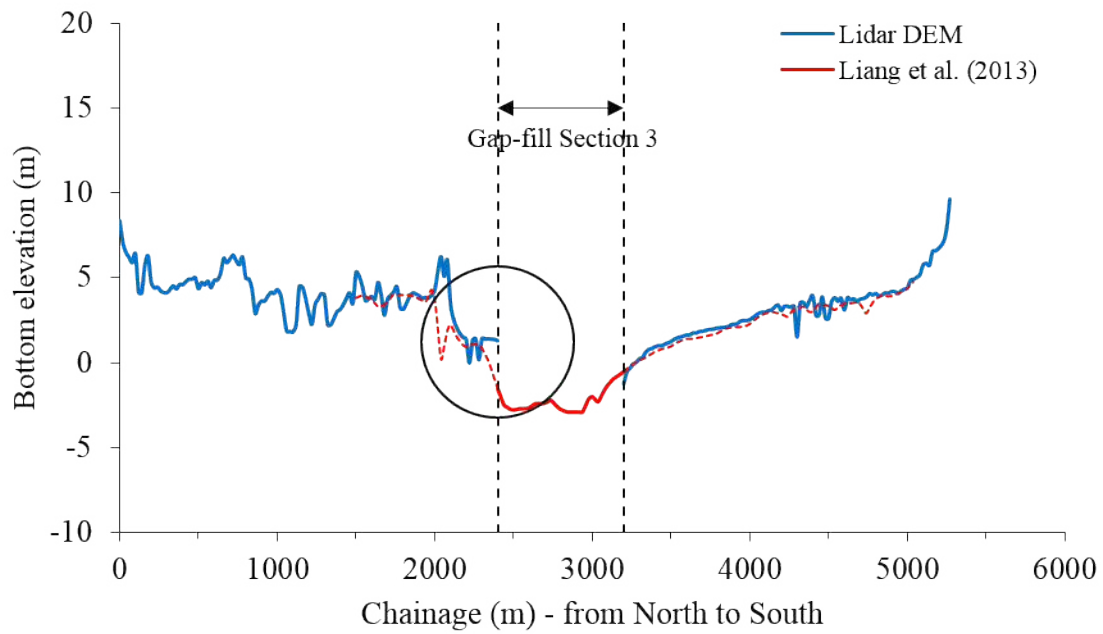
these plots and indicate that the bottom elevation was merged identically with the DEMs at all four sections, as can be seen from the plots of dotted lines beyond the gap-fill sections. However, there was a discrepancy between the bottom elevation and the DEMs at some locations. These included the area between chainage 4,500 to 5,500 at Section 1 and chainage 5,000 to 6,000 at Section 2, the left side of the gap-fill transition at Section 2 and Section 3, and both sides of the gap-fill transition at Section 4. The difference of the elevation between chainage 4,500 to 5,500 at Section 1 could be due to the difference in the data resolution between two datasets. The difference of the elevation between chainage 5,000 to 6,000 at Section 2 could be due to the accretion of sediment that elevated the area in the previous data. For the elevation differences at the near side of the gap-fill transition at Section 2, Section 3 and Section 4, these could be due to the river meandering process that shifted the river position to the South involving the erosion-accretion of sediment.



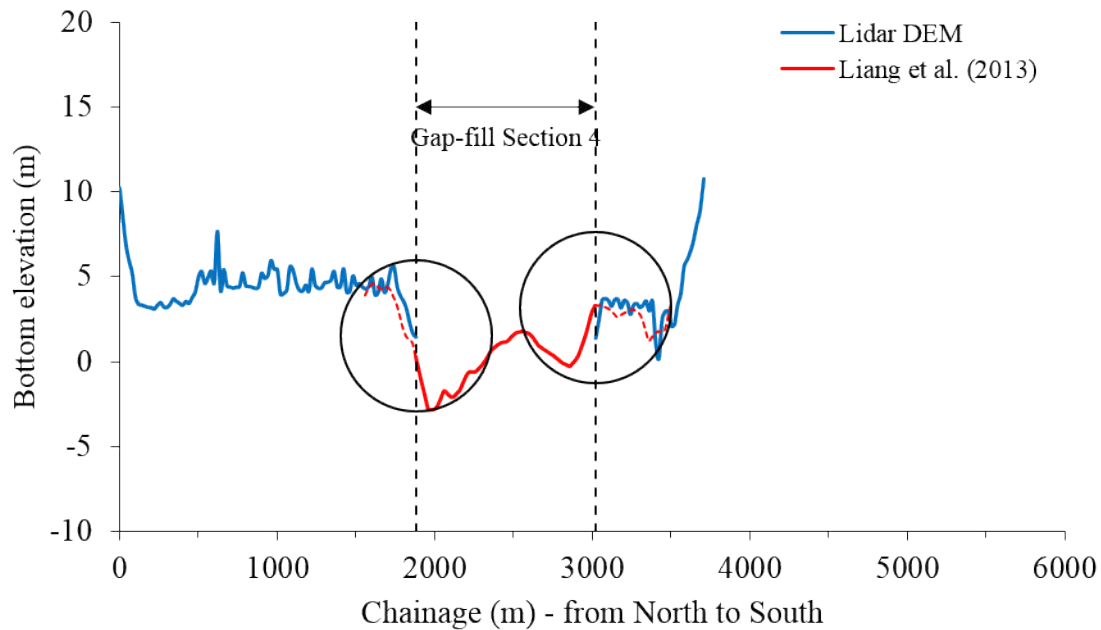
a) Bottom elevation profiles along Section 1.



b) Bottom elevation profiles along Section 2.



c) Bottom elevation profiles along Section 3.



d) Bottom elevation profiles along Section 4.

Figure 4.7: Plots of bottom elevation profiles comparing between datasets of Liang *et al.* (2013) model and the DEMs along Sections 1 (a), 2 (b), 3 (c) and 4 (d), as shown in Figure 4.6.

The difference in the elevation at the chainage far outside the gap-fill transition was less important as the bottom elevation from Liang *et al.* (2013) was superseded with the DEMs. However, the difference in the elevation in the proximity of the gap-fill transition (i.e. at Section 2, 3, and 4) could be erroneous if it was not treated appropriately during the data merging process. To reduce this error while merging the two datasets, the edge of the bottom elevation was extended several meters outwards from the gap-fill area constraint. This extended area was acted as the buffer zone for the overlapping strip and the transition between the edges of two datasets. The width of the buffer zone was dependent on the elevation difference at the edge of the datasets. The maximum extension was 100 m which was applied for a proper data blending at the near side of the gap-fill transition of Section 2, i.e. the elevation difference over 3.7 m.

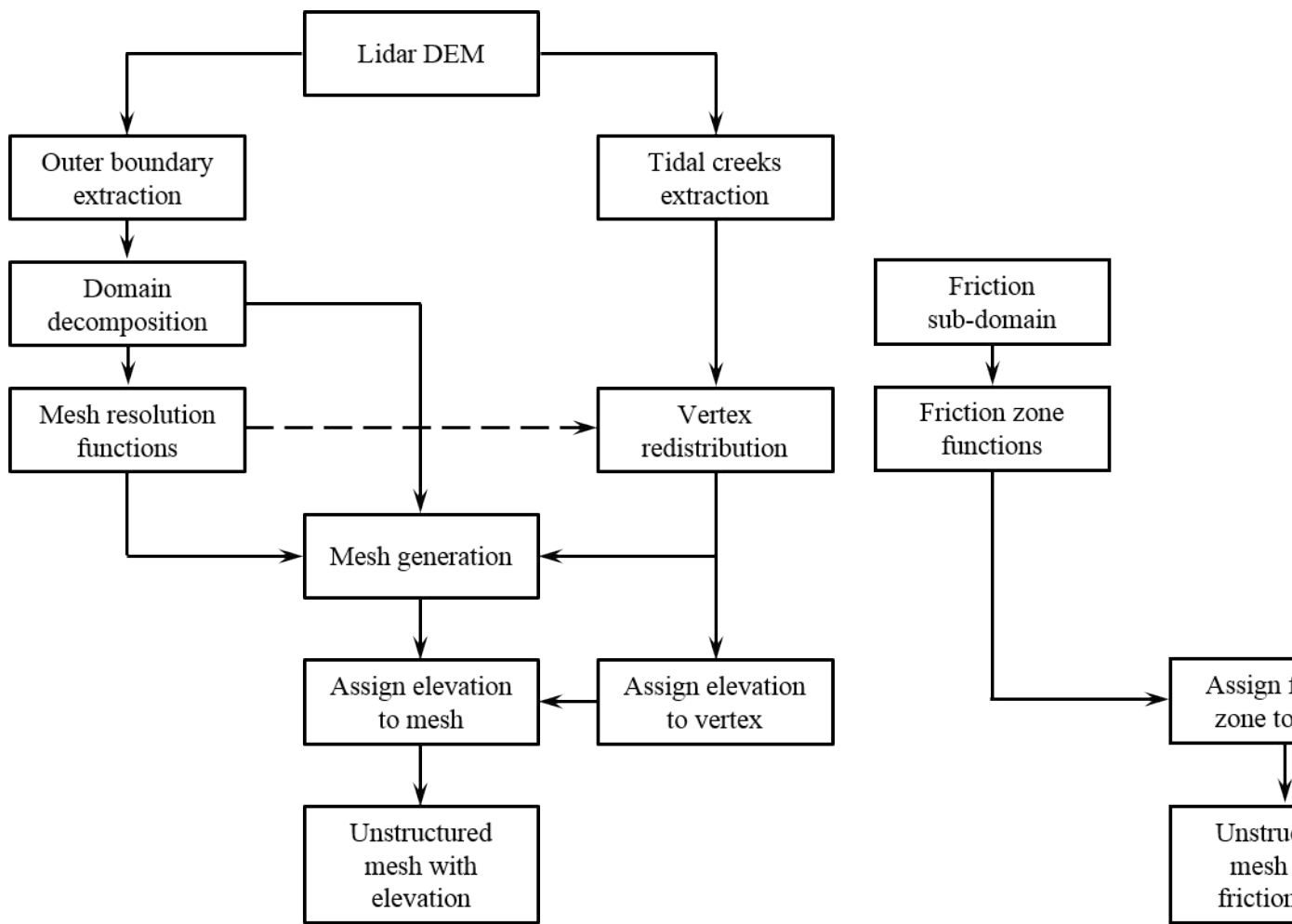
4.3 Intertidal domain extension

The modelling domain at intertidal floodplains required extensions for the improve process of modelling for hydrodynamic and pollutant transport within these areas. The procedure of extending this domain to the intertidal floodplains in Carmarthen Bay, Loughor Estuary and

Swansea Bay is briefly described in the following sub-sections. This procedure was graphically described using the flowchart as can be seen in Figure 4.8(a). The procedure of the refinement of the unstructured mesh and the bottom elevation interpolation was focused on Loughor Estuary.

4.3.1 Outer boundary

The outer boundary for the modelling domain of the South West Wales area was generated at 10 m above the ODN on the topographic DEMs. The boundary of the wetted area was based on the mean high water spring (MHWS) of tidal levels within this area which could reach the maximum level of 4.7 m above ODN near River Neath Entrance at Swansea Bay. At Loughor Estuary and Carmarthen Bay, the MHWS could reach up to 4.14 m and 4.6 m above ODN near Llanelli and Carmarthen, respectively. Furthermore, the tidal propagation during the MHWS in the Loughor Estuary could extend several kilometres up to the tidal limit at Pontarddulais, as can be seen in Figure 4.9. The nearshore circulation besides for capturing the flood inundation during high tides hence can be modelled correctly by extending the outer model boundary above the MHWS.



a) Generation of unstructured mesh, assignment of bottom elevation. b) Assignment of friction zones to

Figure 4.8: The flowchart of procedures for the unstructured mesh generation with the bottom elevation as assignment to the unstructured mesh (b).

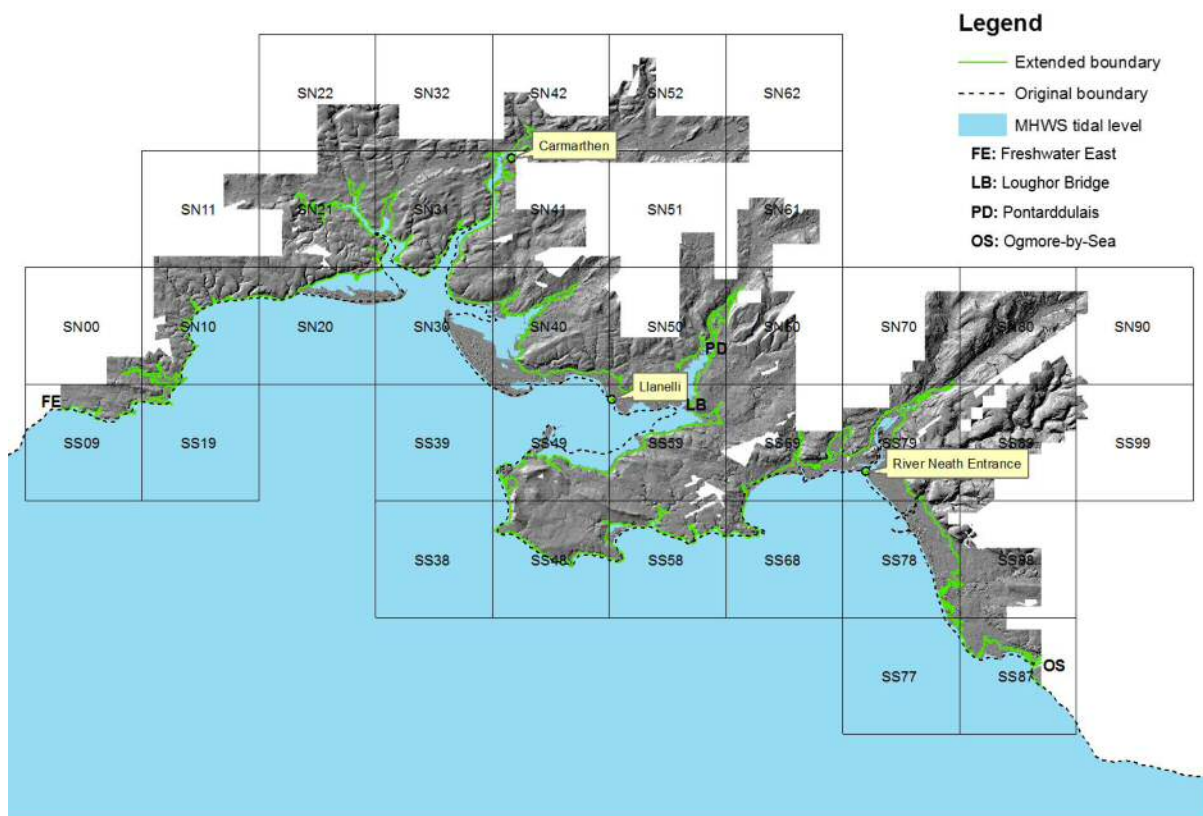


Figure 4.9: The outer boundary extension of the modelling domain with the benchmark of the mean high water spring (MHWS) tidal levels over Carmarthen Bay, Loughor Estuary and Swansea Bay.

4.3.2 Domain decomposition

The domain over Loughor Estuary was categorised into four segments based upon the bottom elevation, as shown in Figure 4.10. The decomposition of domain took place from Outer Bar at the bay and up to the upstream boundary at the tidal limit of River Loughor. This decomposition was conducted to allow the triangulation of the unstructured mesh with different resolutions based on the bottom elevation. Among applications of the domain decomposition was for triangulating the unstructured mesh into several segments before merging them as a single floodplain at the large area, such as the coastal floodplains in Mississippi and Alabama (Bilskie *et al.* 2015).

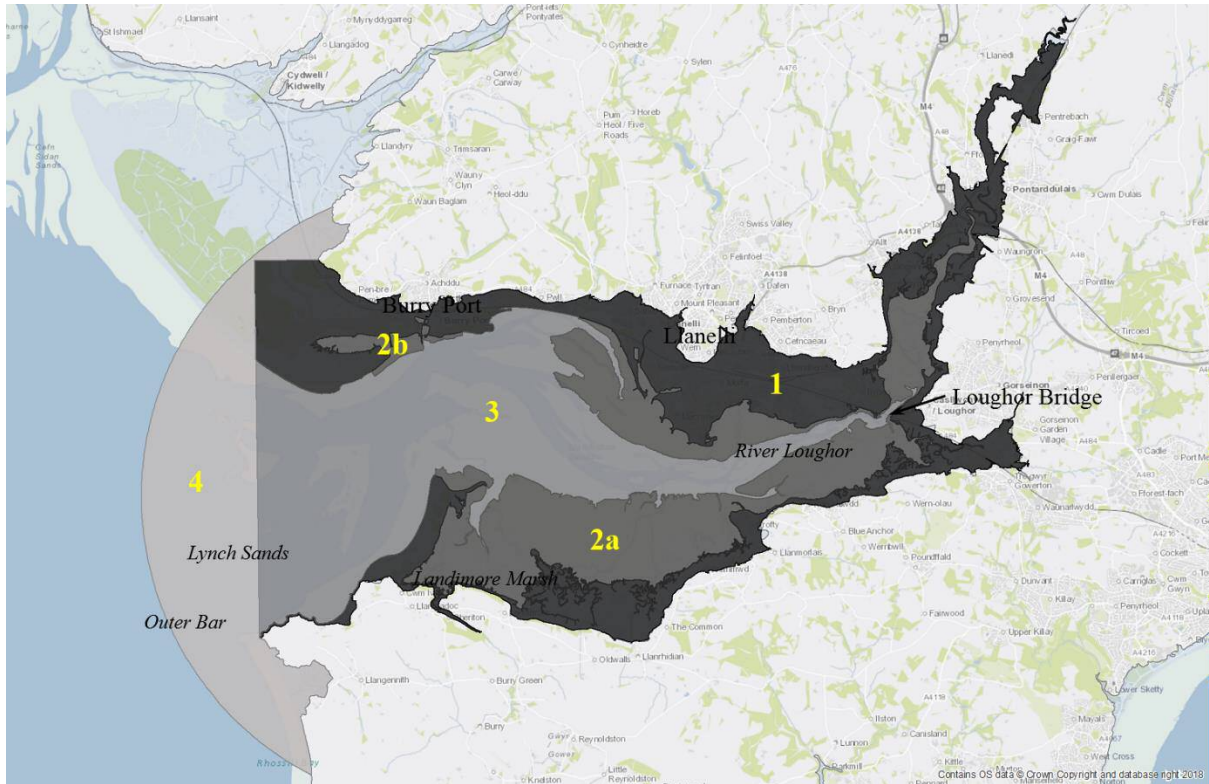


Figure 4.10: The domain decomposition at Loughor Estuary with four segments for the assignment of mesh resolution functions.

The decomposition of the modelling domain was conducted by producing four sets of two-dimensional closed polylines as the outline object, for the mesh triangulation. The closed polyline of CP1 was produced at the bottom elevation between 4 to 10 m, for representing Segment 1 (i.e. including the marshland areas). The closed polylines of CP2a and CP2b were produced at the bottom elevation between 0 to 4 m, for representing Segments 2a and 2b respectively (i.e. including the tidal flat areas). The former polyline covered the area from Llanelli at Northeast to Landimore marshland at Southwest of the estuary. The latter polyline covered the area located near Burry Port at Northwest of the estuary. The closed polyline of CP3 was covered from a downstream section at Lynch Sands and up to near the Loughor Bridge at upstream, represented Segment 3 (i.e. including the intertidal channels). The closed polyline of CP4 was the section between Outer Bar at the bay to Lynch Sands and represented Segment 4 (i.e. including the subtidal channels).

For each segment of the domain decomposition, the unstructured mesh was triangulated based on the defined two-dimensional closed polyline at the constant and minimum resolution. The unstructured meshes for the segments TM1, TM2a and TM2b were triangulated at the constant

resolution of 8 m. For the segments TM3 and TM4, the unstructured meshes were triangulated at the constant resolutions of 20 m and 50 m, respectively. The combined between segments TM1, TM2a and TM2b was also triangulated as the unstructured mesh of TM12a2b, at the constant resolution of 8 m using the two-dimensional closed polyline of CP12a2b as the outline object. These unstructured meshes where the bottom elevation was above 0 m ODN were triangulated with the minimum resolution of 8 m to capture the detail topographic features of the DEMs.

4.3.3 Mesh resolution function

The mesh resolution function, which was used to determine the resolution of the unstructured mesh for each of the decomposition segments, was dependent on the bottom elevation. The assignment of this function was to accommodate the unstructured mesh triangulation with the optimum resolution for a good computational cost (Kim *et al.* 2014), at the same time to enhance the representation of the sub-mesh-scale features from the bare earth topography (Schubert *et al.* 2008). Additional treatments to these vertical features within the unstructured mesh were shown an improvement in the representation of the flood inundation modelling results (Bilskie *et al.* 2015).

Figure 4.11 depicts the resolution functions (i.e. y-axis) that used to assign to the unstructured meshes based on the bottom elevation (i.e. x-axis). The linear function of $y = -2.5x + 30$ was used for the segments TM2a and TM2b which had elevations between 0 to 4 m. The constant mesh resolution was used for three other segments that were located at the elevations between -10 to 0 m and 4 to 10 m. For example, the linear functions of $y = 20$, $y = 30$ and $y = 100$ respectively were used for the segments TM1, TM3 and TM4. The resolution of 1000 m was assigned to the unstructured mesh for the offshore domain (i.e. bottom elevation of less than -10 m) that was beyond the study area.

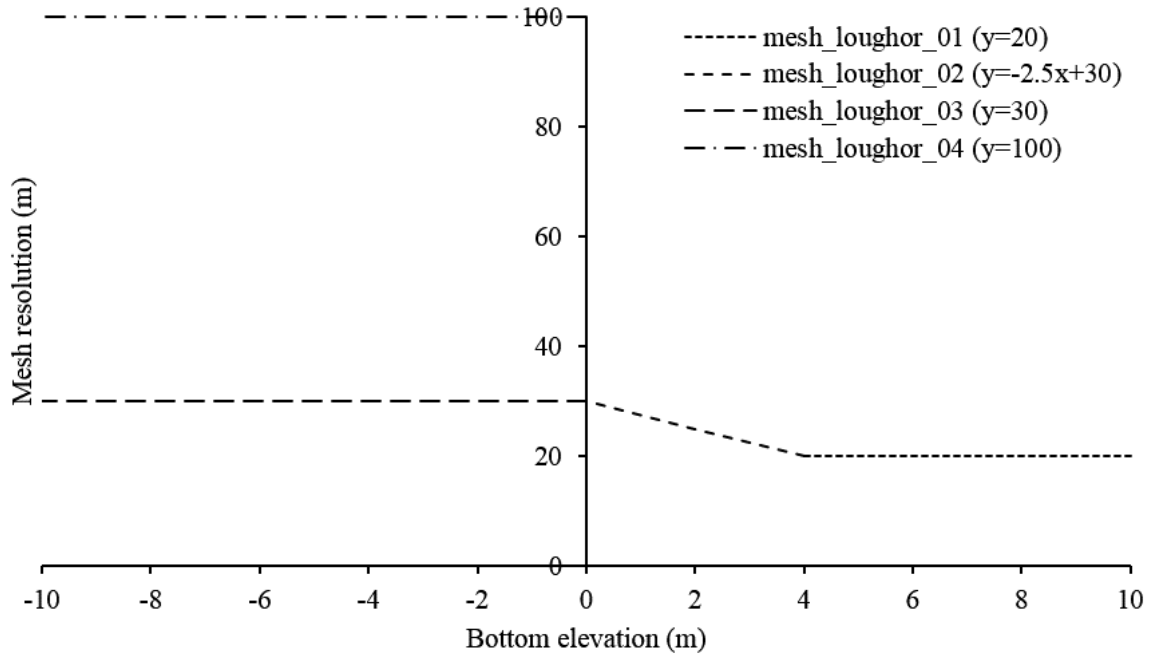


Figure 4.11: Mesh resolution functions (y-axis) for the unstructured mesh triangulation based on the bottom elevation (x-axis).

The decomposition segments with the assigned resolution functions at Loughor Estuary are shown in Figure 4.12. The segments were named after the used functions as TM1-D, TM2a-D, TM2b-D, TM3-D and TM4-D. The resolutions from segments TM1-D, TM2a-D and TM2b-D were saved as the pointset data for the interpolation to the combined segment TM12a2b. This combined segment was named after the interpolated function as TM12a2b-D and was used for the vertex redistribution of the tidal creeks network and for the mesh-nodes placement (i.e. Sections 4.3.4.1 and 4.3.5 respectively).

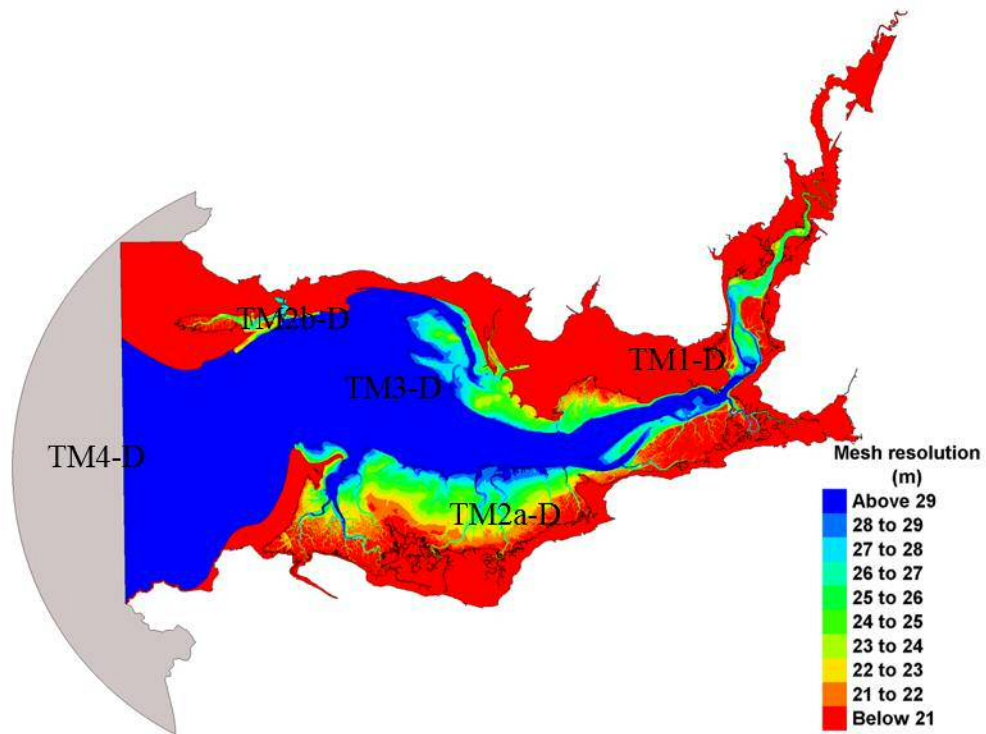


Figure 4.12: The mesh resolution that ranges from 20 m to 100 m at higher and lower bottom elevations respectively, following the order of segments TM1-D, TM2a-D & TM2b-D, TM3-D and TM4-D.

4.3.4 Tidal creeks network extraction

Extracting tidal creeks network was done to improve the modelling of the transport process for the tracers released within the tidal creek-marsh system, i.e. Site 101 – Great Pill and Site 201 – Morlais River (Section 5.2). The transport and dispersal of these tracers that were released directly into the tidal creek-marsh system cannot be modelled accurately without detail information of the creek geometry, surface contours and marsh grass density distribution, as the spatial extent of their initial pollutant will not be large relative to smaller tidal creeks (Blanton *et al.* 2010). By delineating the tidal creeks feature (Mason *et al.* 2006) to be included within the unstructured mesh, the hydraulic conductivity of this conveyance system can be modelled properly as suggested by Westerink *et al.* (2008).

It was assumed that the flow across the ‘bare earth’ surface was always in the steepest downslope direction in order to determine the direction of flow for the tidal creeks network in the DEMs. It was possible to determine the number of cells that flow into a given cell (i.e. flow accumulation) once the direction of flow out of each cell was known. However, there may be

some depressions called sinks that were lower than surrounding cells that will not allow the water to travel out. These sinks were filled with the assumption that it did not occur as the natural feature in the intertidal flat environment (Jenson and Domingue 1988; Tarboton *et al.* 1991; Poggio and Soille 2012). This step was taken to ensure a proper delineation of the tidal creeks network as described in the following paragraphs.

The sink-free of the ‘bare earth’ surface called depression-less DEMs were produced using Hydrology of the Spatial Analyst Toolbox of ArcGIS. The sink raster, which located and identified the depth of these sinks based on the flow direction raster, was firstly created using the Sink tool. An appropriate z-limit value for the sink depths was then determined following these outlines:

- i) the contributing area raster for each sink was created using the Watershed tool (i.e. based on the flow direction raster and pour points feature of the sink raster);
- ii) the minimum elevation raster of each sink in the watershed was created using the Zonal Statistics tool (i.e. based on the contributing area raster and the DEMs with the minimum statistic);
- iii) the maximum elevation raster of each sink along the watershed boundary, after filling, was created using the Zonal Fill tool (i.e. based on the contributing area raster and the DEMs);
- iv) the sink depth raster for each contributing area was created using the Minus tool (i.e. based on the subtraction between values of the maximum elevation raster and the minimum elevation raster).

The depression-less DEMs were finally created by filling all the sinks iteratively based on the DEMs with the z-limit of 3 m using the Fill tool. Figure 4.13 illustrates the profile view of the filled sink at the depth of z-limit.

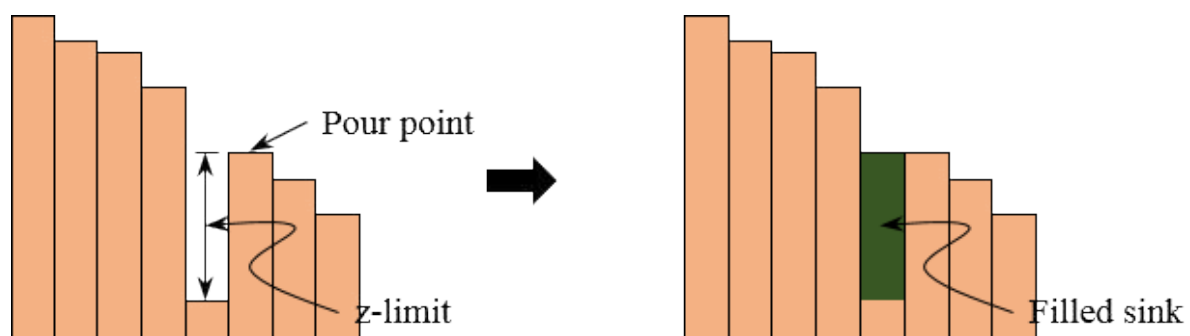


Figure 4.13: The profile view of a sink before and after the iterative filling to the z-limit. The z-limit is the maximum difference specified between the depth of a sink and the pour point for the filling allowance. The pour point is the boundary cell of the lowest elevation within the contributing area of a sink.

The direction of flow was determined based on the depression-less DEMs using the Flow Direction tool, with the surface raster was used as an input in producing the output raster showing the direction of flow out of each cell. Eight-direction (D8) flow model (Jenson and Domingue 1988) was used to determine this flow direction. The D8 flow model considered eight valid output directions related to the eight adjacent cells into which the flow could travel, as shown in Figure 4.14. The direction of flow for each cell was determined by the direction of steepest descent. For example, this was done by allowing a factor of $\sqrt{2}$ for the diagonal neighbours (i.e. the greater distance from the target cell, see Figure 4.14) (Freeman 1991), otherwise 1 for the adjacent neighbours. The neighbourhood was enlarged until the steepest descent was found for the case of the same maximum descent to several cells. Each cell was coded with the value representing the direction of flow when the direction of steepest descent was found. The output raster of the flow direction was named as flowdir_snss.

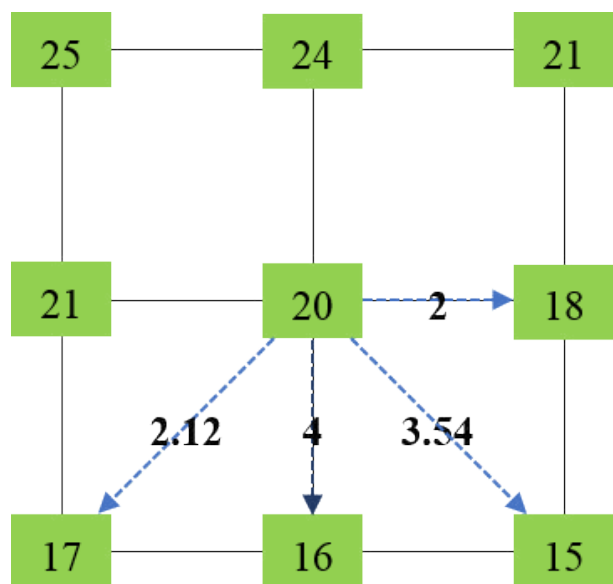


Figure 4.14: The eight valid output directions based on the D8 flow model. The elevation dataset is in green highlight with the descent values in bold. The calculation of the steepest descent allows for the greater distance to diagonal neighbours with a factor of $\sqrt{2}$ (Freeman 1991). The steepest descent is southwards in this example.

The amount of water that flows through a cell that is also known as the flow accumulation was required in defining the tidal creeks network besides the direction of flow from cells. The flow accumulation in its simplest form is the number of upslope cells that flow into each cell, with the location is considered of having a passing stream when enough water flows through each cell (Jenson and Domingue 1988). The Flow Accumulation tool was used to calculate the accumulated flow into each downslope cell using the input weight 1 for each cell. This resulted in the output raster of flow accumulation that was named as flowacc_snss. For defining the stream network aside from tidal creeks, an input weight of a continuous raster that represented the average rainfall during a storm might be used in determining how much rain has fallen within a given watershed.

The tidal creeks network was delineated from the depression-less DEMs using the output from the Flow Accumulation tool. The creeks delineation was conducted by applying a threshold value of 10,000 to the flow accumulation raster using the Con tool. An appropriate threshold value for the stream network delineation could also be determined using an analytical method (Tarboton *et al.* 1991). The raster of the tidal creeks network was created with all cells of more than 10,000 flowing cells into each of them were assigned the value of 1, otherwise, were assigned No Data. This resulted in the linear feature of tidal creeks network and named as con_snss. This linear feature was further analysed using the Stream to Feature tool for creating the accurate feature dataset of stream_con_project.shp. The flowchart of processing the depression-less DEM for extracting tidal creek and river networks is shown in Figure 4.15.

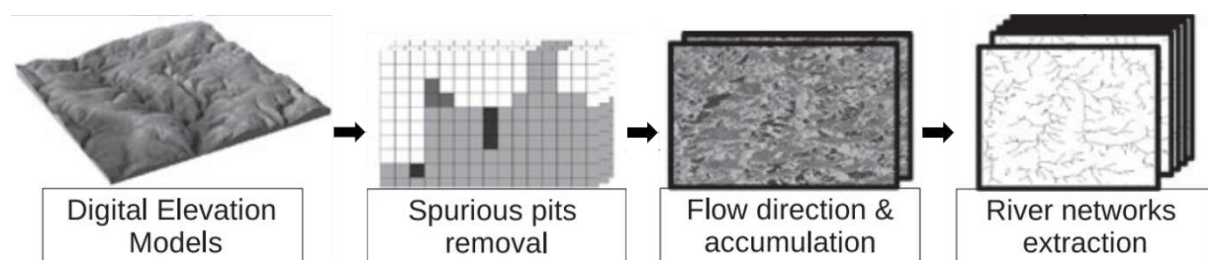


Figure 4.15: Flowchart of processing the depression-less DEM for extracting tidal creek and river networks (Poggio and Soille 2012).

4.3.4.1 Vertex redistribution

As the feature dataset of the tidal creek networks was used for guiding its mesh-nodes placement (Section 4.3.5) at tidal flat and marshland areas, its vertices spacing was important in setting the density of the element edges. The tidal creeks feature of stream_con_project.shp was converted to two-dimensional opened polyline of TCN prior to the application within the Blue Kenue, and its vertices were redistributed to approximate the desired local element size based on the mesh resolution function of TM12a2b-D (see Figure 4.16). The resolution function from this triangular mesh was interpolated to each node of the tidal creeks feature which resulted in a new dataset (i.e. three-dimensional opened polyline) of TCN-D that stored the density information after the coordinates of each node. The final dataset of the tidal creeks feature with the density information that used for guiding this feature's node placement is depicted in Figure 4.17.

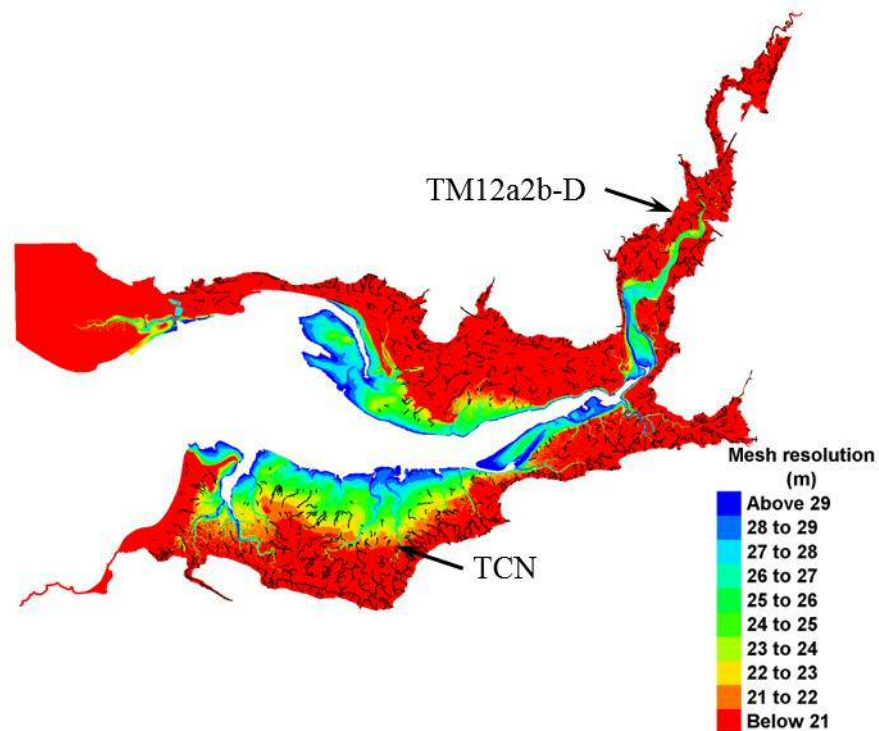


Figure 4.16: The overlaying tidal creeks feature of TCN on the segment with the resolution function of TM12a2b-D.

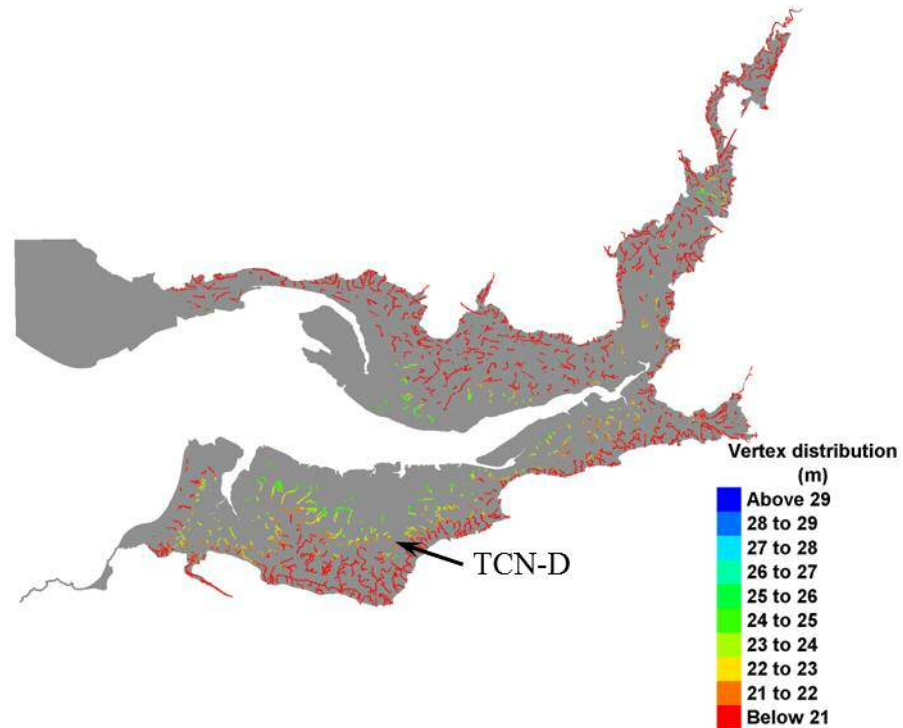


Figure 4.17: Vertex redistribution of the tidal creeks feature based on the mesh resolution function as TCN-D.

4.3.5 Unstructured mesh-nodes placement

The unstructured mesh was refined set over the tidal creeks and floodplains of the Loughor Estuary. The rest of the domain beyond this area was triangulated using the baseline triangulation as discussed in Section 3.2.1. Two major steps of the mesh refinement consisted of the mesh-nodes placement and the elevation dataset interpolation to the nodes, which are described in the following paragraphs.

The T3 Mesh Generator of Blue Kenue was used to generate the two-dimensional unstructured mesh. This mesh generator utilized the dynamic moving front algorithm to place the mesh-nodes and an unconstrained Delaunay Triangulation algorithm to generate the node connectivity (NRCC). The internode spacing of the generated elements was controlled based on the density objects of the three-dimensional opened polyline (i.e. tidal creeks network) and the triangular meshes (i.e. mesh resolution functions). The meshes for the domain decomposition were generated in four stages from upstream to downstream of the study area using the outline objects of closed polylines as the internal boundary. The meshes of the decomposed segments were alternately merged between each stage to form the final

unstructured mesh of a single floodplain. The triangulation stages of the decomposed segments are described in the following paragraphs.

At stage 1, the combined segment between segments TM1, TM2a and TM2b was generated using a closed polyline of CP12a2b as an outline object. A closed polyline of CP1 and triangular meshes of TM2a-D and TM2b-D were used as density objects with a constant edge length of 20 m was defined for the former object, and the opened polyline of TCN-D was used as a soft-line object. The unstructured mesh that was generated from this triangulation and named as segment MNP1 is depicted in Figure 4.18.

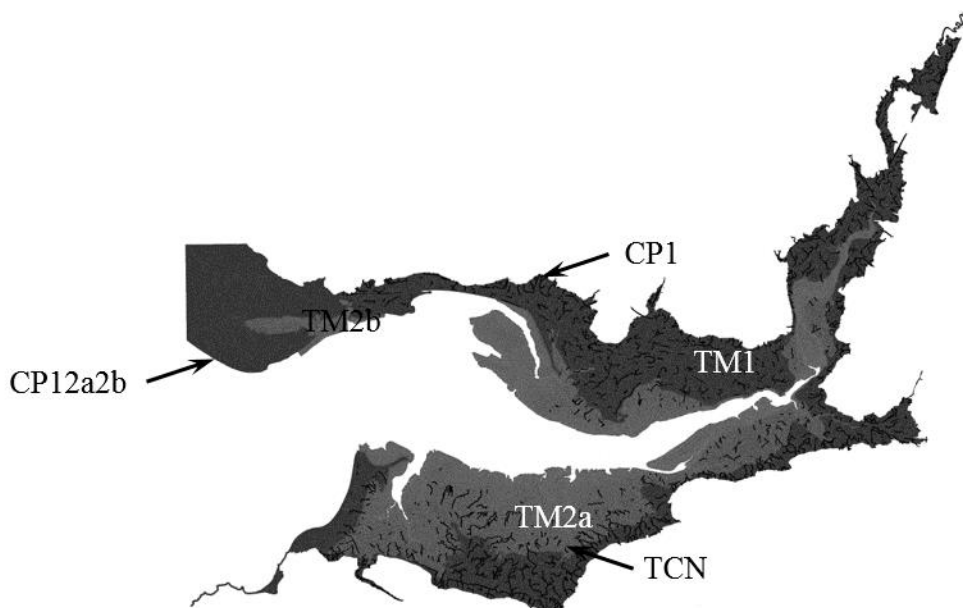


Figure 4.18: Stage 1 of the unstructured mesh triangulation for segment MNP1.

At stage 2, the combined segment between the unstructured mesh of the stage 1 triangulation and the segment of TM3 was generated. The closed polyline of CP3 was used as the outline object and the unstructured mesh of MNP1 as the sub meshes object, with the default edge length of 30 m. The unstructured mesh that was generated from this triangulation and named as segment MNP2 is depicted in Figure 4.19.

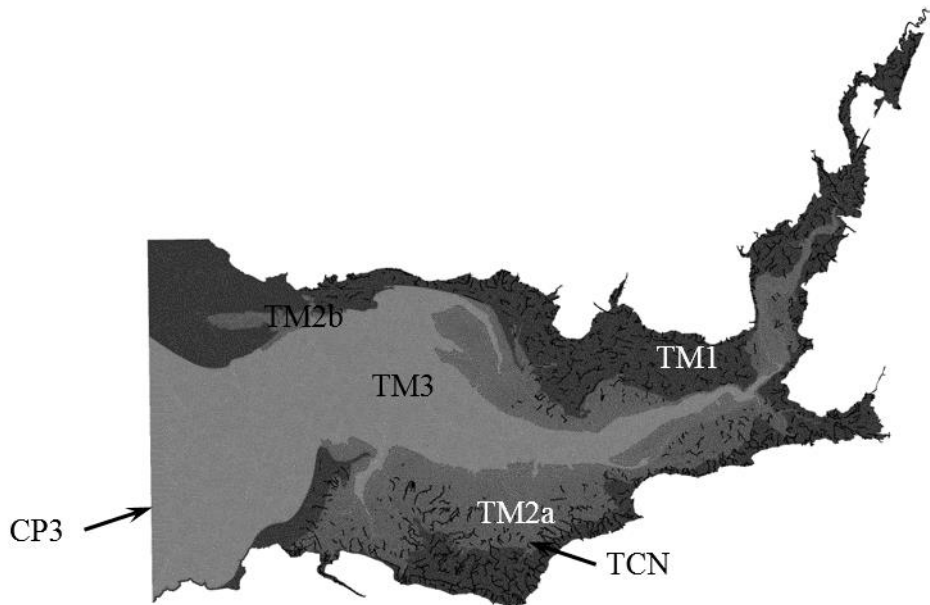


Figure 4.19: Stage 2 of the unstructured mesh triangulation for segment MNP2.

At stage 3, the combined segment between the unstructured mesh of the stage 2 triangulation and the segment of TM4 was generated. The closed polyline of CP4 was used as the outline object and the unstructured mesh of MNP2 as the sub meshes object, with the default edge length of 100 m. The unstructured mesh that was generated from this triangulation and named as segment MNP3 is depicted in Figure 4.20.

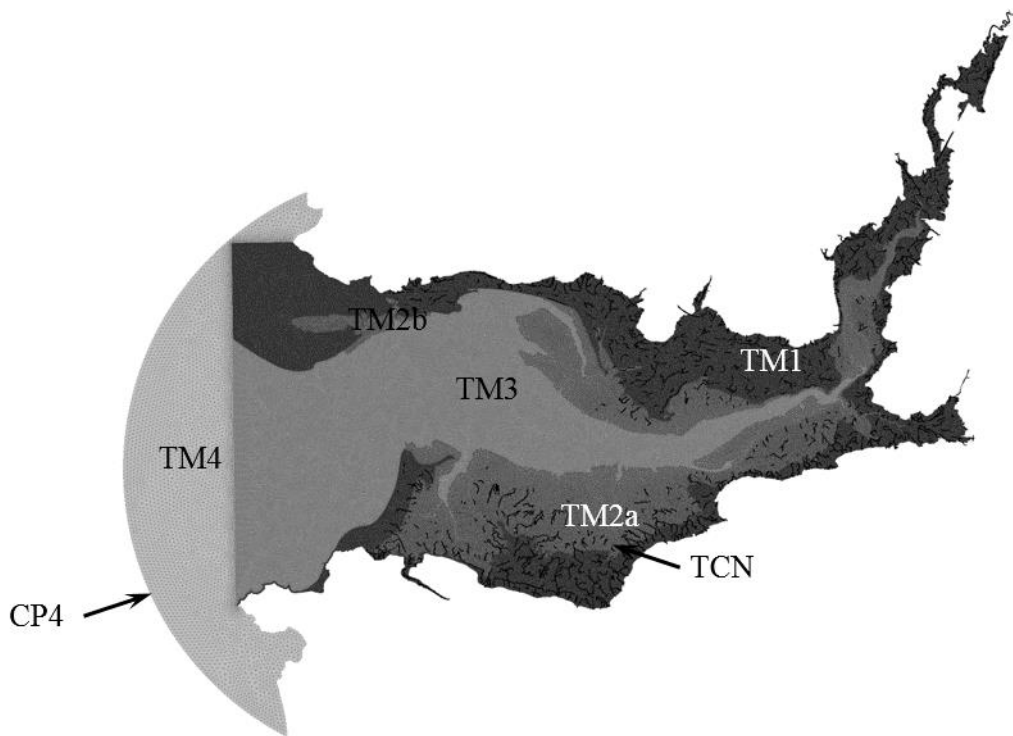


Figure 4.20: Stage 3 of the unstructured mesh triangulation for segment MNP3.

At stage 4, the unstructured mesh for the training walls was generated using two-dimensional closed polylines of wall crowns as the outline objects with the default edge length of 20 m that was named as TMW1. The two-dimensional closed polyline of the 75 m offset from the unstructured mesh of the training walls that was named as CPW2, was used to delete the internal elements of this polyline from the unstructured mesh of the stage 3 triangulation which latter was named as MNP3-R. The edges of the deleted elements were extracted to accurately locate the nodes coordinate and were rebuilt as the two-dimensional closed polyline and named as CPW2-R. The combination of the unstructured mesh of the training walls within the 75 m offset polyline was generated using the closed polyline of CPW2-R as the outline object without resampling and the unstructured mesh of TMW1 as the sub meshes object, with the default edge length of 20 m. This mesh was named as TMW2 and is depicted in Figure 4.21. The unstructured meshes of the training walls (i.e. TMW2) and the deleted elements (i.e. MNP3-R) were merged to form an unstructured mesh that was named as segment MNP4. This segment is depicted in Figure 4.22.

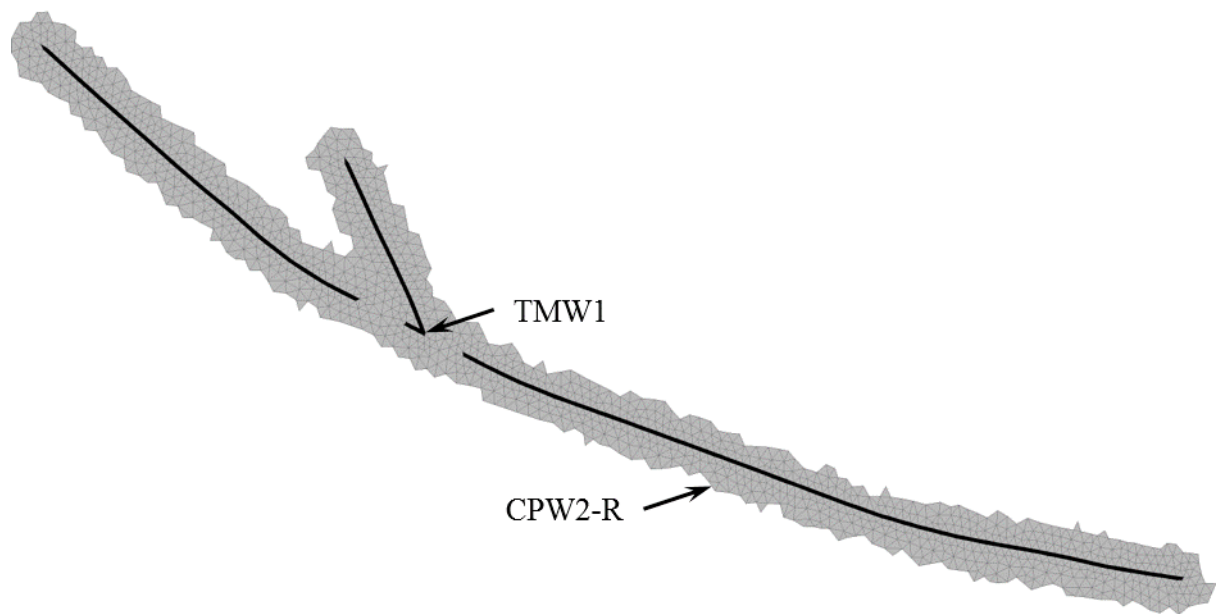


Figure 4.21: The unstructured mesh of TMW2.

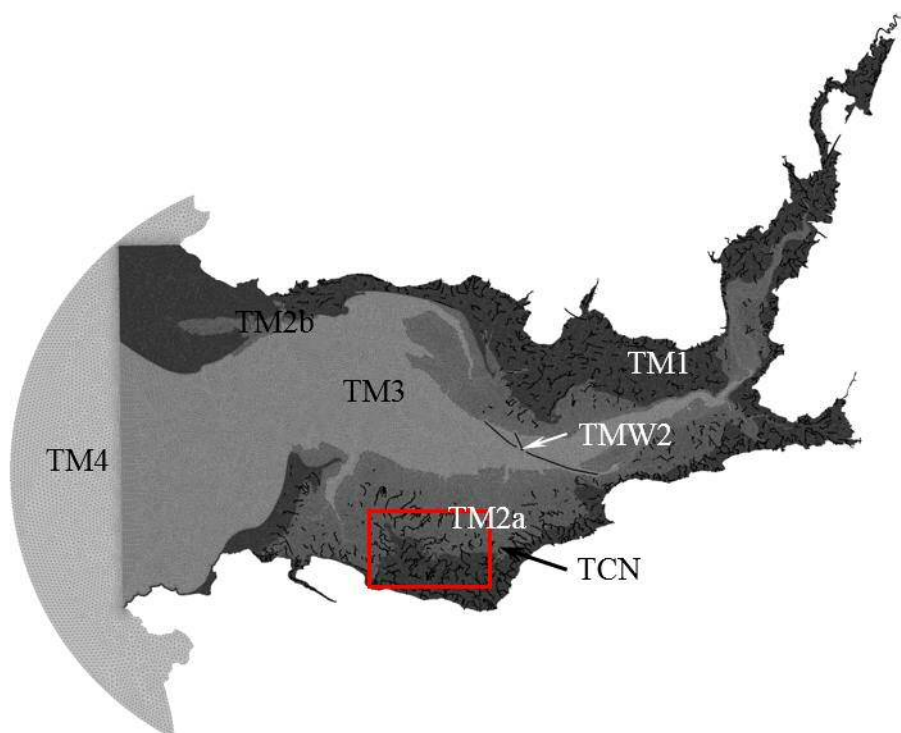


Figure 4.22: Stage 4 of the unstructured mesh triangulation for segment MNP4. The red cell is the area of floodplain under investigation.

Tidal creek networks that were extracted from the depression-less DEM was adequately represented in the unstructured mesh as depicted in Figure 4.23. From the high-resolution image at the floodplain of investigation of the estuary's south (see Figure 4.22), the mesh generator with the guidance of TCN-D was accurately placed the mesh-nodes along with the network of tidal creeks within the meshing structure. The mesh resolution at the edge of TCN and the surrounding floodplain was followed the desired local element size that the density was assigned based on the bottom elevation functions.

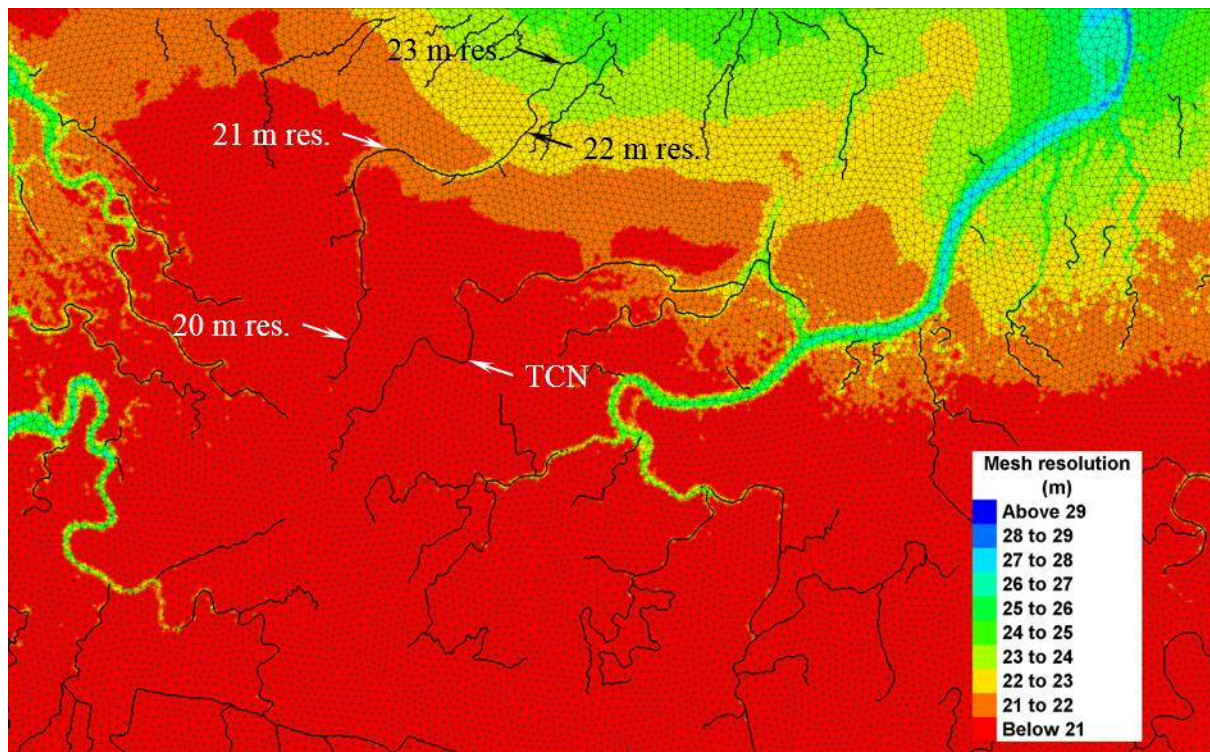


Figure 4.23: High-resolution image of the meshing structure along the TCN at the floodplain of investigation.

4.3.5.1 Elevation dataset interpolation

Two types of criteria were considered in assigning the elevation data to the mesh-nodes as these nodes belong to different categories, such as vertical feature nodes of the tidal creeks and the training walls, and normal floodplain nodes. The mesh-nodes were deemed as nodes of the vertical feature for those laid along with the tidal creeks network and the crowns of training walls. Otherwise, the nodes were attributed to the floodplain. Using the 2D Interpolator of Blue Kenue, the cross-sections for the tidal creeks network were extracted from the DEMs, represented as the three-dimensional opened polyline of TCN-B. The cross-sections for the

crowns of training walls were assigned with the elevation of 1 m and represented as the three-dimensional closed polyline of CPW1-B. The elevation from these cross-sections was then interpolated to the tidal creeks and training wall nodes as the constraint outline using the inverse distance interpolation method, as shown in Figure 4.24. For the other floodplain nodes, the elevation data was interpolated using the same interpolation method. The refined unstructured mesh for the Loughor Estuary contained 243,600 nodes and 480,997 elements, while contained 250,963 nodes and 495,166 elements for the whole modelling domain.

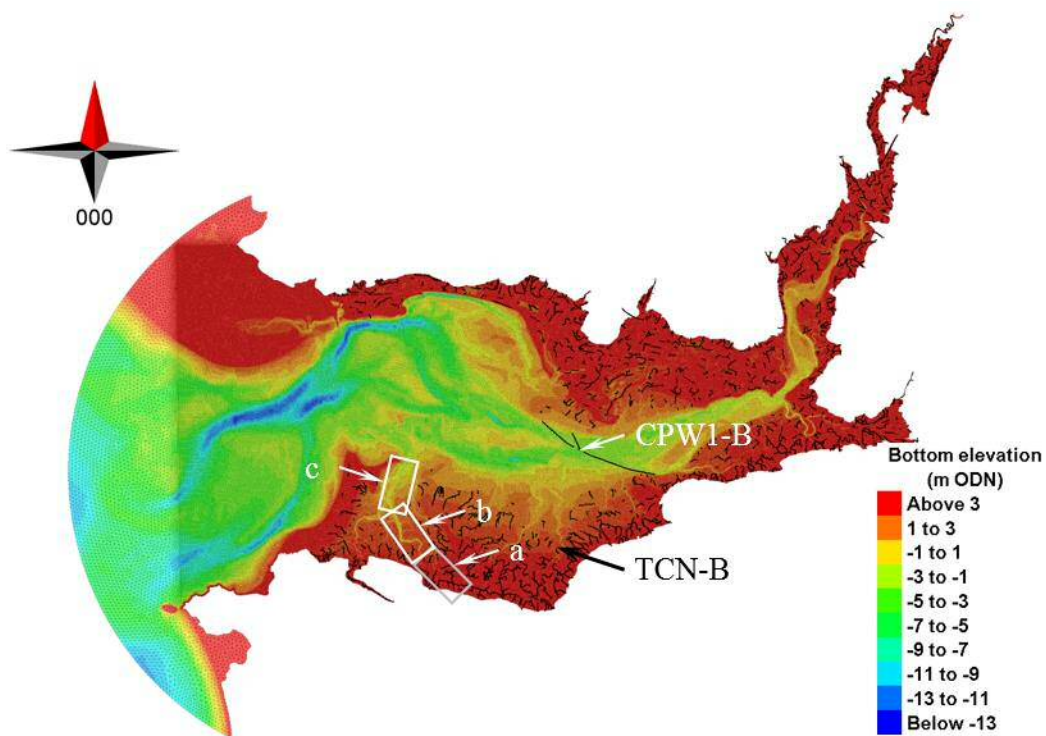
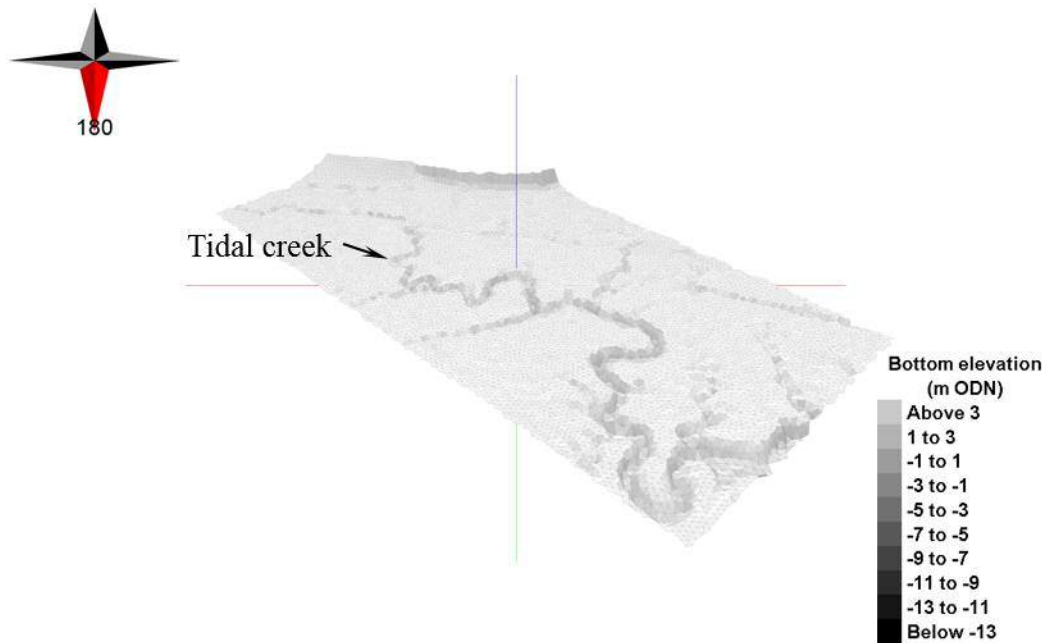


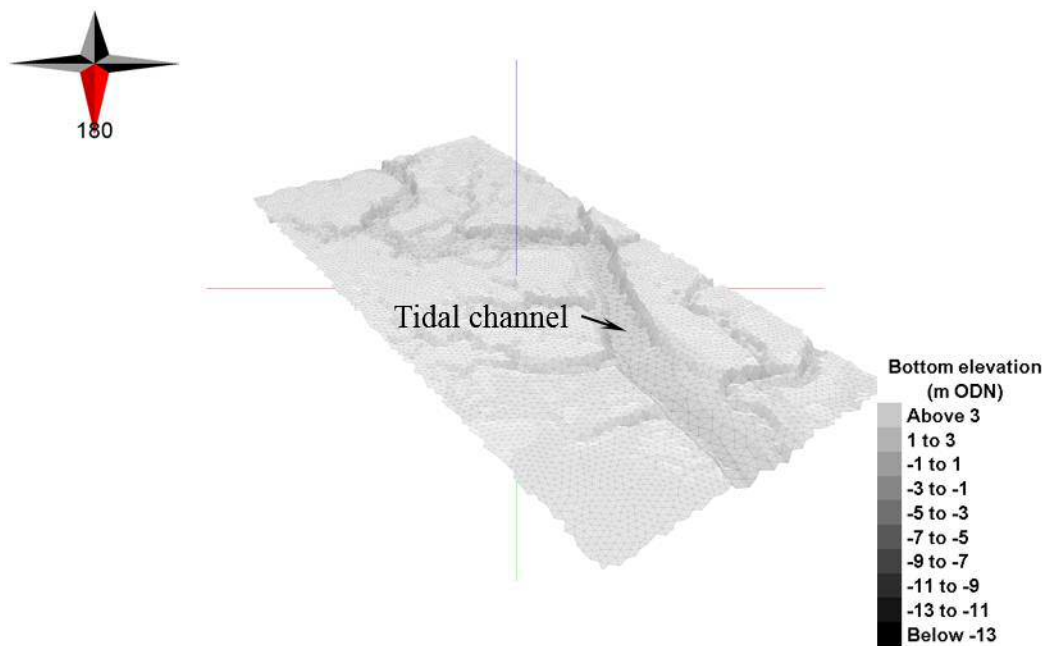
Figure 4.24: Interpolated bottom elevation to the mesh-nodes of vertical features and floodplains. TCN-B and CPW1-B are three-dimensional polylines for tidal creek networks and crowns of training walls respectively. Cells a, b and c represent areas of marshland, tidal flat and intertidal channel.

Based on Figure 4.24, the generated meshes for different regions of the Loughor Estuary are depicted in Figure 4.25. The three-dimensional view of mesh geometry at the marshland was realistically representing the continuous structure of tidal creek networks with the constraint of elevation interpolation at nodes of vertical features. Besides, the views at mesh-nodes of the tidal flat and intertidal channel were realistically representing the continuous geometry of tidal channel along these regions. With the improvement in hydraulic connectivity at the intertidal

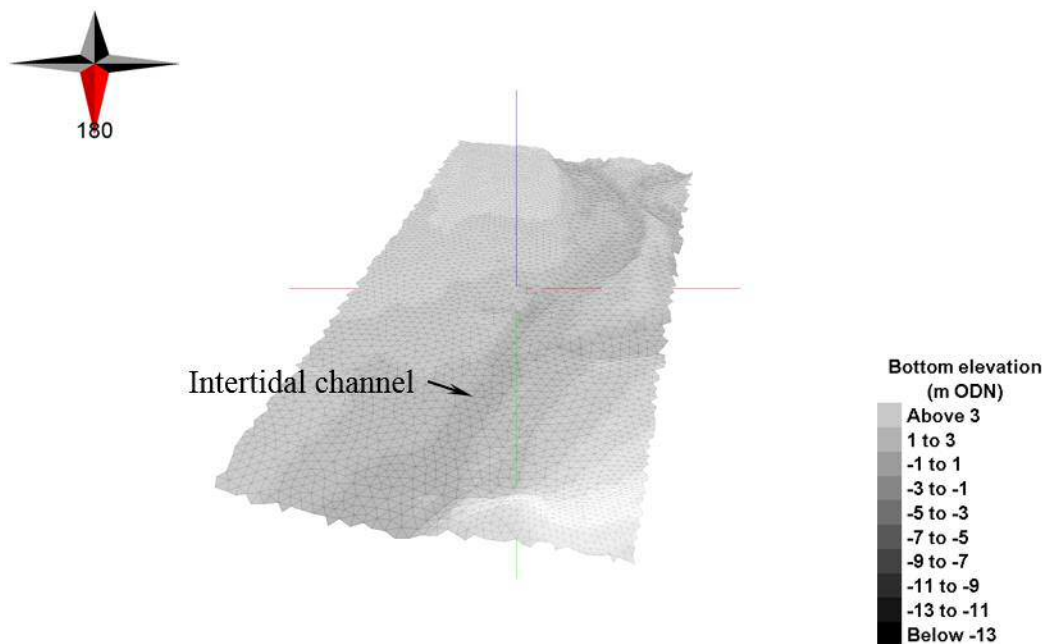
floodplain, the transport process of a pollutant can be modelled properly within this tidal creek-marsh system.



a) Mesh geometry with the elevation at marshland plots within cell a.



b) Mesh geometry with the elevation at tidal flat plots within cell b.



c) Mesh geometry with the elevation at intertidal channel plots within cell c.

Figure 4.25: Three-dimensional views of mesh geometries at the marshland (a), tidal flat (b) and intertidal channel (c) based on Figure 4.22. Views from the North with the horizontal-to-vertical plot at 1:10 scale.

4.4 Bottom roughness parameterization

The modelling domain for the study area of Loughor Estuary was characterised into four friction sub-domains to parametrize the spatially varying bottom roughness based on types of principal terrain features that commonly existed as discussed by French and Clifford (2000), i.e. subtidal channel, intertidal channel, tidal flat and marshland. Subtidal channel friction was used for the offshore domain beyond the Loughor Estuary. The procedure of characterizing these friction sub-domains and parametrizing their bottom roughness is graphically described as in Figure 4.8(b) and through the following paragraphs.

Prior to characterizing the friction sub-domains with different parameters of bottom roughness, two unstructured meshes were generated for representing the study area and the offshore domain and named as TML and TMS respectively. The elevation data were then interpolated

to these unstructured meshes using the inverse distance interpolation method and were saved as the pointset data of PSL-B and PSS-B.

A code number that represented the friction sub-domains was given to each mesh-node. The pointset data of the elevation for the study domain (i.e. PSL-B) were assigned with the number of friction sub-domains that was based on the elevation basis, i.e. Zone 1 represented the elevation between -65 m to -5 m, Zone 2 represented the elevation between -5 m to -1 m, Zone 3 represented the elevation between -1 m to 3 m, and Zone 4 represented the elevation between 3 m to 10 m. The friction sub-domain of Zone 1 was assigned to the offshore domain. The friction sub-domain of Zone 3 was assigned to the tidal creeks network and the crowns of training walls.

Using the 2D Interpolator of Blue Kenue, the friction values of each zone of the study area and offshore domains were interpolated to the mesh-nodes using the inverse distance interpolation method. For the tidal creeks network and the crowns of training walls, the friction zones information from these three-dimensional polylines were interpolated to the respected nodes as the constraint outlines. The inverse distance interpolation method was used with the maximum search distance of 2 m over 20 m (i.e. ratio 1:10). The interpolated values of the friction zones to the mesh-nodes resulted in non-integer values. These values were changed to integer values as follows: Zone 1 for values between 0.0 to 1.0, Zone 2 for values between 1.1 to 2.0, Zone 3 for values between 2.1 to 3.0, and Zone 4 for values between 3.1 to 4.0. The assigned friction zones to the mesh-nodes are depicted in Figure 4.23 which were stored within a formatted data file. This file was read using the `friction_user.f` subroutine.

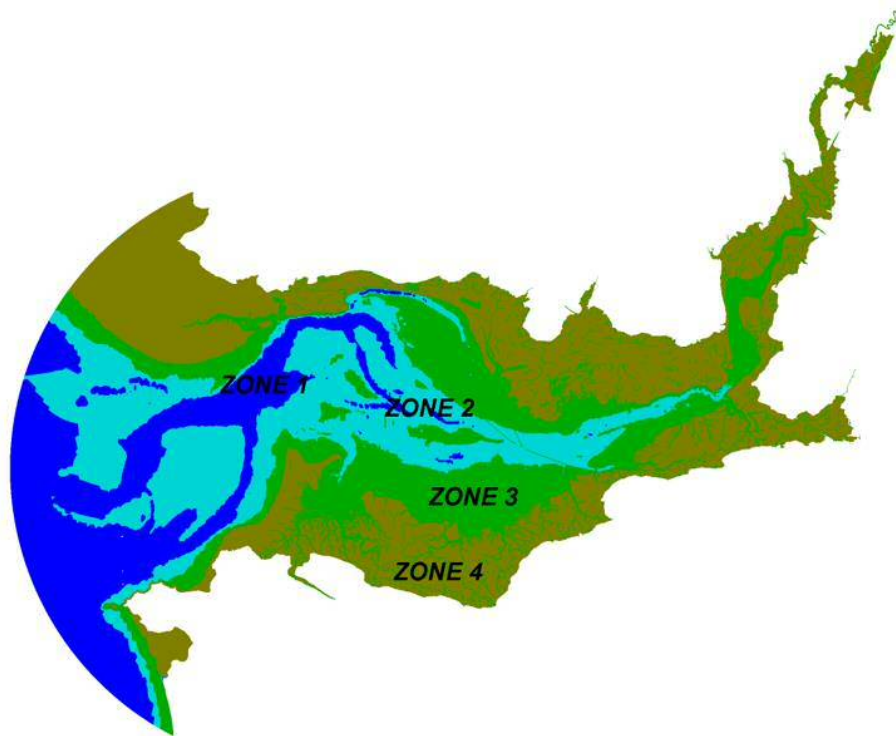


Figure 4.26: The assigned friction of different sub-domains (i.e. Zone 1 for the subtidal channel, Zone 2 for the intertidal channel, Zone 3 for the tidal flat and Zone 4 for the marshland) to the mesh-nodes at the study area of Loughor Estuary.

The mesh-nodes with the same friction sub-domain were assigned to the same bottom roughness parameter in the friction data file. For each friction sub-domain, the bottom condition was defined in the friction data file as the friction formulas and using corresponding roughness values. These friction formulas and roughness parameter values were also used for the boundary condition as a part of the k-epsilon turbulence model with the option of the rough boundary. The Manning's law with the same roughness value was used for both the bottom and boundary conditions with different values assigned to each friction sub-domain. The non-submerged vegetation with diameter and spacing parameters of the roughness element was not implemented in this study.

The Manning's value for each friction sub-domain was estimated based on the calculation of summation of the global resistance factors for floodplains, using the following equation (Arcement and Schneider 1989):

$$\text{Eqn. 4.1}$$

where n_0 is the base value that referred to the natural bare soil surface across floodplains (ranges from 0.025 to 0.032 for firm soil), C_s is the correction factor for the surface irregularities effect across floodplains (ranges from 0.030 to 0.045), and C_v is the vegetation value that accounts the growth density and the average flow depth (ranges from 0.010 to 0.050) (Hall and Freeman 1994).

Due to the unavailability of site-specific data for the bottom roughness at Loughor Estuary, sensitivity analysis on this parameter to the current circulation and pollutant transport processes was carried out within the study domain as described in Section 5.4.1. Four scenarios of the variable bottom roughness were implemented based on the typical range of the global resistance factors, with the uniform, minor, moderate and severe floodplain conditions being considered. These values are summarised in Table 4.1.

Table 4.1: Scenarios of the variable bottom roughness at different friction zones of Loughor Estuary.

Manning's bottom roughness	Uniform	Minor	Moderate	Severe
Zone 1 (subtidal channel)	0.025	0.025	0.025	0.025
Zone 2 (intertidal channel)	0.025	0.025	0.030	0.035
Zone 3 (tidal flat)	0.025	0.030	0.035	0.045
Zone 4 (marshland)*	0.025	0.040	0.060	0.095

* the range for the vegetation resistance factor also based on Hall and Freeman (1994).

Based on the tracer transport calibration in Section 5.4.1, the variable bottom roughness has a clear influence on the retention of FIO at the intertidal floodplain of Loughor Estuary. Further literature searches were informed that floodplains within the study area should be categorised as the moderate roughness condition (see Figure 6.4). This roughness condition was considered for modelling the transport of diffuse FIO source from the marshland and results were discussed in Section 6.3.4.

4.5 Catchments delineation

The stream discharge from the catchments is especially important to understand the flushing process of any pollutant mass that is released at the upstream of the estuary (Wang *et al.* 2004).

The DEMs of the catchments were used for the delineation of the sub-catchment areas that contributed the discharge into the waterbody of Loughor Estuary. The runoff characteristics were derived from the catchments topographical information by using Hydrology of the Spatial Analyst Toolbox of ArcGIS. The sub-catchment areas were delineated by justifying the locations of each stream outlets based on the identified stream network from the depression-less DEMs raster. The same methodology as discussed in Section 4.3.4 was followed here. Figure 4.27 depicts the delineated stream networks and catchment boundaries from 25 sub-catchment areas discharging into the modelling domain of Loughor Estuary. The locations of the stream outlets were connected to the tidal creek networks at upstream of the floodplain areas.

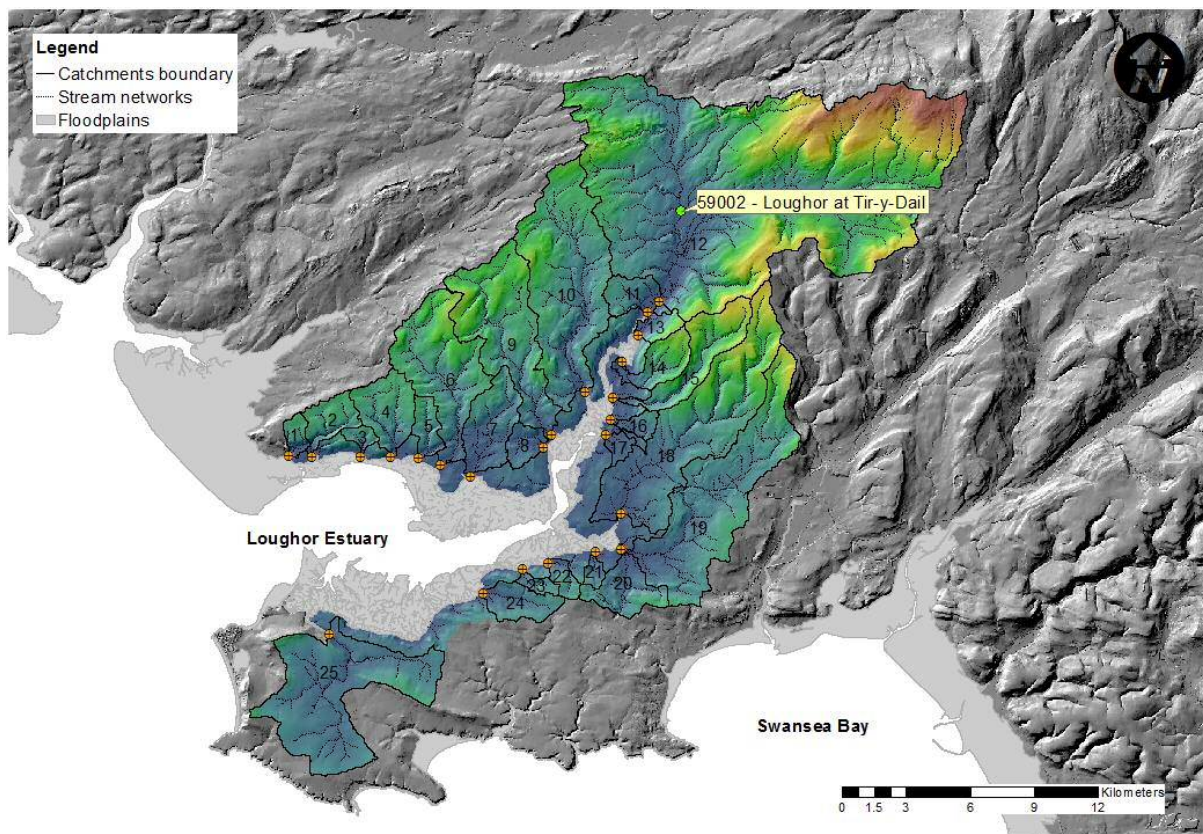


Figure 4.27: The stream networks and catchment boundaries that being delineated to 25 sub-catchments discharging into the Loughor Estuary (● location of gauging station, ⊕ locations of stream outlets).

4.5.1 Streams discharge estimation

For estimating the stream discharge statistics at the 25 ungauged stream outlets, the flow-duration percentiles at 10 percent interval were calculated and used to develop the linear single-regression (LSR) equations. The 10 years mean daily streams discharge measured at 18 gauging stations around the South West Wales, where the Loughor catchment is located, were used to calculate the flow-duration percentiles of the non-exceedance probability for each gauging station by using the following equation (Risley *et al.* 2008):

$$\text{---} \qquad \qquad \qquad \text{Eqn. 4.2}$$

where P is the non-exceedance probability, R is the ranking of modified version from lowest to highest of all daily mean flows for the specified period of record, and N is the total number of daily mean flows. Equation 4.2 was used to find the high and low flows with the high and low percentiles respectively, as summarised in Table C.4 in the Appendix.

The calculated flow-duration percentiles were plotted against the catchment areas of each gauging station as depicted in Figure 4.28. The LSR equations for each flow-duration percentile that were developed based on the areas of gauging catchments are depicted in Table 4.2. These LSR equations are considered valid for estimating the stream discharge statistics at the ungauged streams with the assumption of similar unit area runoffs to areas of the gauged sites as they were strongly correlated for this region. Table C.5 in the Appendix depicts the estimation of the stream discharge statistics based on the LSR equations and the drainage areas of each sub-catchment.

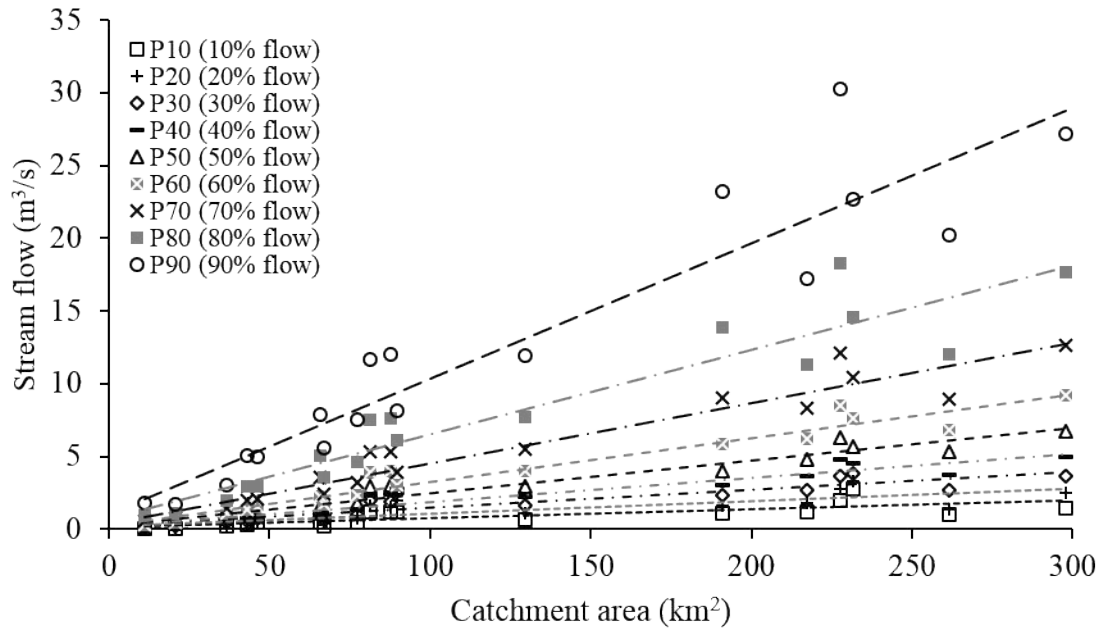


Figure 4.28: The flow-duration percentiles at 10 percent interval that were plotted as the linear single regressions (LSRs) against the catchment areas of 18 gauging station at South West Wales.

Table 4.2: The developed LSR equations for each flow-duration percentile based on the areas of gauging catchments.

Flow-duration percentile	LSR equations	R ²
P10 (10% flow)	$y = 0.0060x + 0.1572$	0.5874
P20 (20% flow)	$y = 0.0086x + 0.2410$	0.6728
P30 (30% flow)	$y = 0.0123x + 0.2569$	0.8174
P40 (40% flow)	$y = 0.0165x + 0.2516$	0.8956
P50 (50% flow)	$y = 0.0223x + 0.2210$	0.9415
P60 (60% flow)	$y = 0.0301x + 0.2541$	0.9468
P70 (70% flow)	$y = 0.0414x + 0.3974$	0.9312
P80 (80% flow)	$y = 0.0582x + 0.7126$	0.8980
P90 (90% flow)	$y = 0.0929x + 1.0714$	0.8859

The appropriate magnitude of river inflows used in the simulation was tested using the transport of salinity in the estuary. The assumption was made that the salinity is a natural conservative tracer that can be used to calibrate the transport process (Gameson 1974). The salinity was used over the microbial tracer as the latter was undergoing decay during the transport (Section 5.4.2).

It was understood that the transport in the estuary requires a correct calibration prior to calibrating the decay process (Chan *et al.* 2015). The sensitivity analysis of salinity to the river inflows is shown in Figure D.1 and Table D.6 in the Appendix. The flow duration percentile of 40% was used based on the measured condition during the microbial tracer release experiment (Section 5.2).

4.6 Summary

This chapter was focused on extending the modelling domain at the intertidal floodplains of the study area. By using the land-water boundary mask, the ‘land extracted’ DEMs for the areas of Carmarthen Bay, Loughor Estuary and Swansea Bay were successfully eliminated the artefacts of surf zones and turbid waters at the maximum extension of drying intertidal areas. By implementing the buffer zone, the elevation differences between two datasets at the proximity of the gap-fill transitions were properly blended in minimizing errors for the integration between the bathymetric and topographic data. With the availability of the topographic DEMs, the outer boundary of the modelling domain was extended above the MHWS at the intertidal floodplains for modelling the correct nearshore circulation besides for capturing the flood inundation during high tides. As the fine-resolution modelling produced better results, the unstructured mesh triangulation together with the elevation dataset interpolation were designed for enhancing the representation of sub-mesh-scale features (i.e. tidal creeks network and training walls) at the same time for optimising the cost. As the vegetation is primary in controlling the circulation and pollutant transport processes, the modelling domain of study was characterised into friction sub-domains based on four principal terrain features which the bottom roughness was parameterized for the sensitivity analysis on these processes. As one of the major transport mechanisms, the stream discharge statistics at the ungauged stream outlets that were estimated based on the developed LSR equations are important as the boundary condition for understanding its contribution to the flushing process of any pollutant mass in the estuary.

Chapter 5: Transport and persistence of microbial tracers

5.1 Introduction

This chapter was focused on modelling the transport and persistence of microbial tracers in the estuarine environment. Modelling these processes with the application of microbial tracers as a surrogate was essential to improve the understanding of the processes experienced by the FIOs while being transported in the estuarine environment, from different sources, and on their impacts to water quality at the sites of interest. Conducting a release experiment of the microbial tracers in the interest waterbody was important in establishing the physical linkage between a series of FIOs sources and water compliance monitoring sites in and around the waterbody (Wyer *et al.* 2010). Validating the hydrodynamic process prior to simulating the transport of FIOs within the waterbody was important to ensure an accurate prediction of the concentration gradient for the later assessment on the impact to human health risks (Huang *et al.* 2015). Understanding the diffusive transport from the modelling perspective was important as the occurrence of this physical process at length scales smaller than the resolvable grid that was represented using eddy viscosity values (Connolly *et al.* 1999) was a scale-dependent (Xu and Chua 2017). As solutes transport was also controlled by transient storage besides dispersion includes due to vegetation (Shen *et al.* 2008), the bottom roughness might have a role to the transport mechanism of the bathymetrically induced dispersion (Ralston and Stacey 2005) at wide intertidal floodplains of an estuary. Conducting a sensitivity analysis on the decay kinetics to the transported microbial tracers was important as these tracers might experience the environmental stress before persisting to the marine environment (Troussellier *et al.* 1998) in the stage of early exposure.

This chapter was organised as follows: Section 5.2 presented a methodology for the microbial tracer release experiment at the Loughor Estuary. Section 5.3 presented the validation to the hydrodynamic processes at several sites within the study area to the measured data. Section 5.4 presented the sensitivity analysis on the decay kinetics besides on the bottom roughness and the diffusive transport of the microbial tracer within the waterbody. Section 5.5 summarised the chapter.

5.2 Microbial tracer release experiment

A microbial tracer release experiment was designed to examine connections between a series of faecal indicator organism (FIO) sources in the Loughor Estuary and points of interest in and around this waterbody. The experiment was conducted by a team from Centre for Research into Environment and Health (CREH) of Aberystwyth University, City and County of Swansea, and Environment Agency Wales as part of the Interreg 4A Smart Coasts and Sustainable Communities Project (Wyer *et al.* 2014).

Four microbiological tracers were introduced simultaneously at each of four release sites on 8th October 2014, one hour after the high tide. The four release sites are at the Great Pill (Site 101), a tidal channel draining through the western part of Llanrhidian Marsh; the Morlais River (Site 201), a tidal channel at the eastern end of the marsh and drains to Salthouse Pill in the estuary; the Loughor Bridge (Site 501), a bridge crossing the Afon Llwycher tidal channel that close to the sewage effluent discharge from Gowerton WwTWs; and the Afon Lliedi (Site 601), a tidal channel draining through Llanelli into the Lliedi/Dafen estuary and then to the Loughor Estuary.

Five sampling sites that were selected in and around the estuary are two designated sampling points (DSPs) at Rhossili (Site 408) and Pembrey (Site 412) that were monitored for bathing water compliance assessment; the Broughton Bay (Site 409), a potential candidate for future designation that was monitored by City and County of Swansea; the Burry Port harbour (Site 411) that relatively close to shellfish beds in the estuary and allows access to the main river channel at all tidal states; and the Loughor Boat club (Site 410), located upstream of all tracer release sites and has been included to observe the tracer back-movement into the estuary during flood tides. Locations of the tracer release and sampling sites are shown in Figure 5.1 (see Tables D.1 and D.2 for the details). The release and sampling sites were selected based on their representation as to the major bacterial inputs and their specific interest as the major receiving waters, respectively. Each of these sites represents different hydrodynamic characteristics that can impact the transport of microbial tracers.

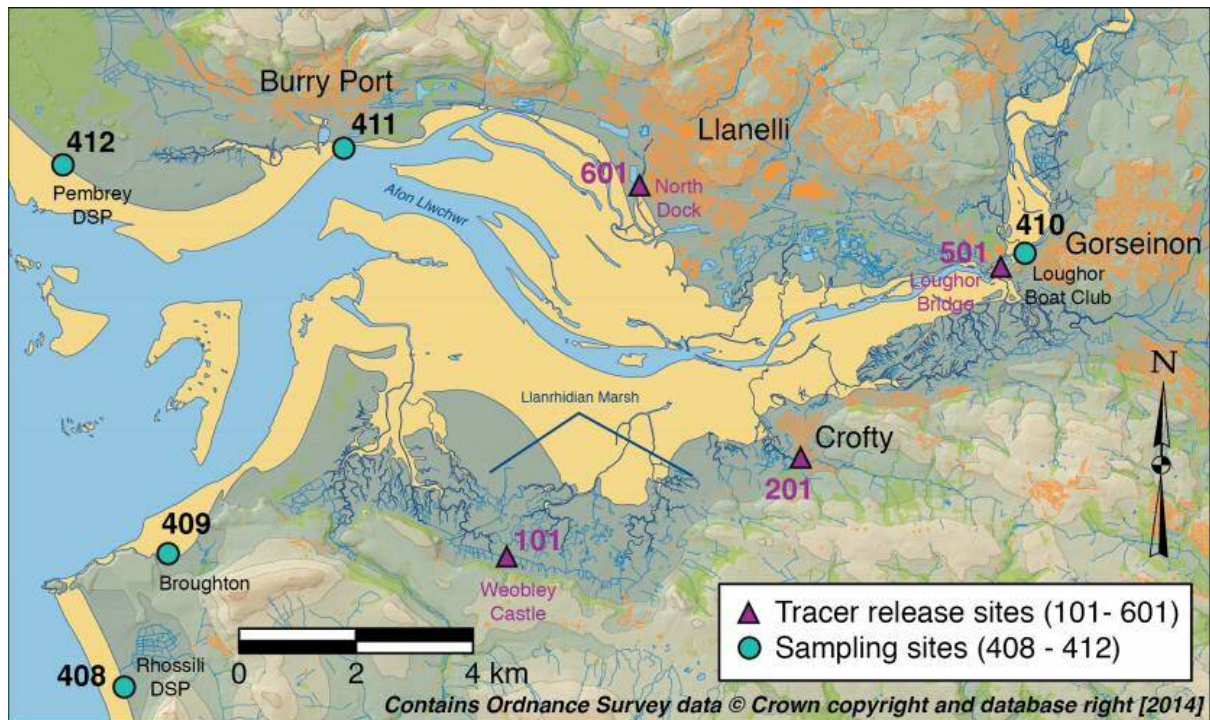


Figure 5.1: Locations of the release and sampling sites for microbial tracers in and around the Loughor Estuary.

Four super-concentrated microbial tracers that were deployed in this study were bacteriophages of *Serratia marcescens* (PJN1 isolated from seawater, host bacterium: *S. marcescens* SM24 (NCIMB 10644)), *Enterobacter cloacae* (phage and host, a wild strain of *Ent. cloacae*, isolated from sewage), MS2 coliphage (NCTC 12847, host bacterium: *E. coli* K12 (NCTC 12846)) and ϕ X174 coliphage (NCIMB 10382, host bacterium: *E. coli* SinsheimerC (NCIMB 12416)) (Wyer *et al.* 2010). These bacteriophages were produced at CREH through the infection of host bacterium during replication and lysis in a batch fermenter, yielded a high titre suspension of phage in plaque forming units (pfu/ml). The MS2 coliphage was usually produced to the highest titre concentration of 1×10^{14} pfu/ml while other phages were produced at the lower titre concentration of 1×10^{13} pfu/ml.

The suitability of specific microbial tracers at four release sites were assessed based on the compromise between their background and titre concentrations. For the background concentrations, samples were collected from each site on occasions in June, July, August, and September 2014. *S. marcescens* and *Ent. cloacae* phages were generally absent from the environmental samples (Tables D.3 and D.4). With the highest titre concentration, the MS2 coliphage was introduced at Site 501 over 11 minutes to produce a total dose of 4.00×10^{17}

pfu. It was expected that this release at the furthest upstream site to increase the ambient concentration above background levels at the sampling sites located downstream. Other microbial tracers were introduced as follows: *S. marcescens* phage was released at Site 101 over 14 minutes with a total dose of 2.75×10^{16} pfu, *Ent. cloacae* phage was released at Site 201 over 7 minutes with a total dose of 4.50×10^{16} pfu, and ϕ X174 coliphage was released at Site 601 over 3 minutes with a total dose of 2.00×10^{15} pfu. Table 5.1 summarises details of the released tracers in the Loughor Estuary. Applications of the bacteriophage as a source tracking tool were conducted elsewhere by Simpson *et al.* (2002) and Shen *et al.* (2008).

Table 5.1: Details of the released microbial tracers at locations along the Loughor Estuary.

Sites	Tracers	Concentration (pfu/ml)	Discharge (m ³ /s)	Release period 8 th October 2014 at BST	Dose (pfu)
Great Pill	<i>S. marcescens</i> phage	5.50×10^{12}	5.95×10^{-6}	07:36 – 07:50 14 minutes	2.75×10^{16}
Morlais River	<i>Ent. cloacae</i> phage	9.00×10^{12}	1.19×10^{-5}	07:00 – 07:07 7 minutes	4.50×10^{16}
Loughor Bridge	MS2 coliphage	8.00×10^{13}	7.58×10^{-6}	07:17 – 07:28 11 minutes	4.00×10^{17}
Afon Lliedi	ϕ X174 coliphage	4.00×10^{11}	2.78×10^{-5}	06:35 – 06:38 3 minutes	2.00×10^{15}

Sampling was commenced during 8th October 2014 at 06:00 BST prior to the first tracer releases in order to establish the background concentration. Regular sampling was continued at hourly intervals for a period of 54 hours after the first releases to observe changes in the concentration. Each sampling position was recorded for the water temperature and other physico-chemical data (e.g. turbidity, conductivity, total dissolved solids and salinity). All samples were collected aseptically into 150 ml pre-sterilised plastic containers and were transported to the laboratory inside lightproof cool boxes.

5.2.1 Microbiological and environmental data analyses

At the laboratory, the microbiological analysis for the phage enumeration was followed the double agar overlay method (Adams 1959; Havelaar and Hogeboom 1984; SCA 2000). Based on Wyer *et al.* (2010), host bacterium broth cultures were grown in a high nutrient medium used for the fermentation, and incubated at 37 °C overnight. 0.1 ml of host bacterium and 1 ml of sample were pipetted into 4 ml of the molten semi-solid overlay (e.g. at 45 °C) and plated onto blood agar base in 90 mm triple-vent Petri dishes. Overlays were allowed to set, and the plates were dried by partly removing the lids and allowing to stand for 15 minutes. The lids were then replaced, the plates inverted and incubated at 37 °C for \pm 3 hours. Plaques were counted following the incubation as areas of lysis that is shown in Figure 5.2. Results from this analysis were used for calibrating the model of microbial tracer transport and decay (Section 5.4).

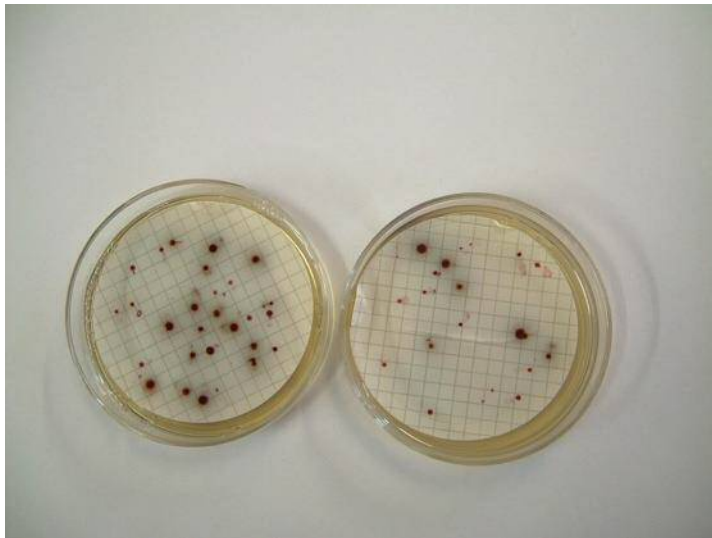


Figure 5.2: Plaques on the agar overlay in Petri dishes.

Besides the microbiological analysis, the collected samples were further analysed for the environmental data (e.g. water temperature, salinity and turbidity) to estimate the decay rate of the microbial tracers in the marine environment. The analysis was included the effect by solar radiations that the data in Figure 5.3 were obtained from the Blackpill meteorological station.

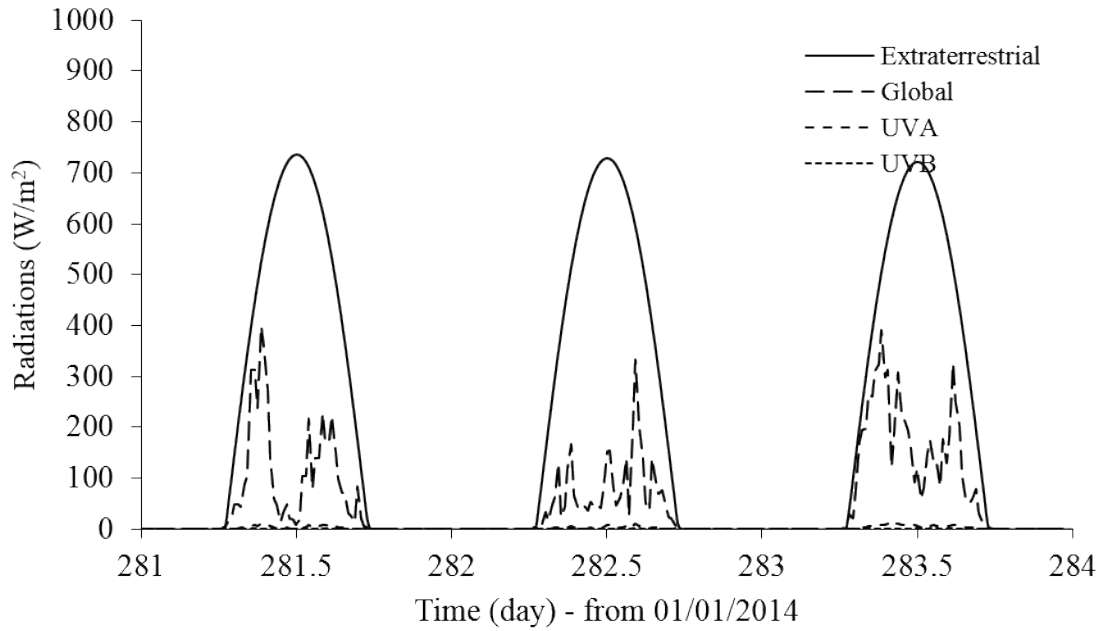


Figure 5.3: The observed solar radiations from the Blackpill meteorological station during the three-days sampling period, consist of extra-terrestrial, global, UVA, and UVB radiations.

The decay rate that was experienced by the microbial tracers in the estuary was estimated for the durations of dark and light periods based on the suggested formulations by Chapra (2008). During the dark period (e.g. from 18:00 to 05:59 BST), the decay rate was estimated due to the natural mortality and osmotic effect respectively by the temperature and salinity (Equation 5.1). While during the light period (e.g. from 06:00 to 17:59 BST), the decay rate was estimated due to the mortality by solar radiations of extra-terrestrial on top of the effect during the dark (Equation 5.2). The radiation mortality was further depending on the light extinction in the water columns that was modelled based on the measured turbidity (Equation 5.3).

Eqn. 5.1

Eqn. 5.2

Eqn. 5.3

where μ_d is the decay rate during the dark (day^{-1}), μ_l is the decay rate during light (day^{-1}), K_d is the light extinction coefficient (m^{-1}), S is salinity (ppt), T is temperature (ppt), I_0 is the light

attenuation coefficient (-), I_0 is solar radiation (W/m^2), z is the modelled water depth (m) and T is turbidity (ntu).

The dark and light decay rates were estimated as the time required for 90% of the total microbial mass to decrease from its initial amount in hours, represented respectively in $T_{90}(\text{dark})$ and $T_{90}(\text{light})$ as follows:

$$\text{Eqn. 5.4}$$

$$\text{Eqn. 5.5}$$

The ranges of the estimated $T_{90}(\text{dark})$ and $T_{90}(\text{light})$ based on the measured data at five sampling sites are depicted in Figure 5.4. $T_{90}(\text{light})$ with the lower values were ranged between the means of 4.54 hours at Burry Port to 8.53 hours at Rhossili DSP. The higher values of $T_{90}(\text{dark})$ were ranged between the means of 49.71 hours at Rhossili DSP to 83.13 hours at Loughor Boat club. The $T_{90}(\text{dark})$ besides its highest mean at Loughor Boat club was also the largest range with the minimum and maximum of 58.64 and 113.02 hours respectively (see Table D.5) due to the large ranges of the environmental parameters.

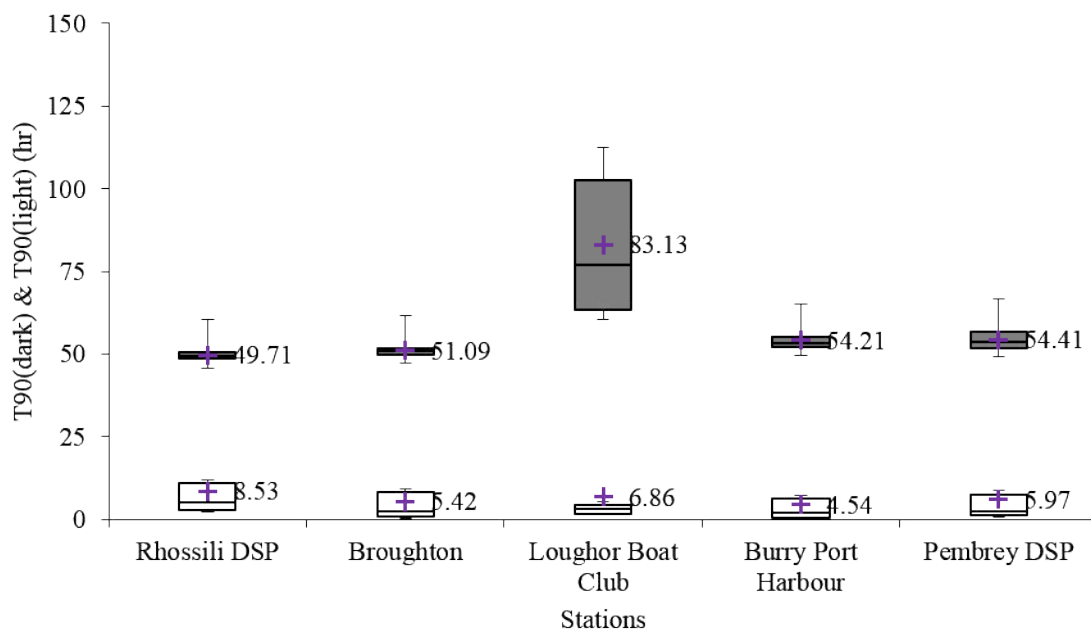


Figure 5.4: Estimated ranges of T90(dark) and T90(light) based on the environmental data measured at five sampling sites.

5.3 Hydrodynamic modelling process

The hydrodynamic model of SEBC with the intertidal floodplain extension at Loughor Estuary was applied for modelling the transport and decay processes of microbial tracers that were released during the field experiment. The hydrodynamic model was firstly tested using the uniform bottom roughness at the floodplains (Section 4.4). Stream discharges from upstream boundaries were approximated at the mean values prior to conducting the sensitivity analysis of tracer transport. The hydrodynamic process was simulated for five days beginning from 7th until 12th October 2014 to include the period of tracer release experiment. The simulation was run at 0.1 second time step with the consideration of computational stability at floodplains with the refined mesh.

5.3.1 Hydrodynamic at intertidal floodplains

The hydrodynamic model at the intertidal floodplains of Loughor Estuary was validated to the measured data. Readers are referred to Figure 5.9 for the locations of validation sites. The simulated results of water level at Burry Port, Llanelli and Lliw were correctly predicted to the measured data as shown in Figures 5.5, 5.6 and 5.7 respectively. These validations were shown similar comparisons to those modelled water level at the SEBC domain (see Figure 3.3). For modelled tidal currents at site 1076H, comparison to the measured data is shown in Figure 5.8. It was observed that the current velocity was significantly improved as compared to the water level at Burry Port between refined and unrefined domains. Thorough mesh refinement though with limited validation data was regarded as majorly improved the hydrodynamic circulation within this region.

Further conducting the sensitivity analysis on scenarios of the variable bottom roughness, significant changes were observed in current velocity at site 1076 (see Figure 5.8). The velocity increment from the uniform to severe roughness was significant especially during ebb tides. It was expected the increase in the roughness at different zones relative to the subtidal channel (Table 4.1) was increased the surface gradient hereinafter the potential energy. Minimum changes were observed in water levels at Burry Port as due to minimum differences in the

roughness at the intertidal channel with different scenarios (see Figure 5.5). For water levels at Llanelli and Lliw, slower tidal propagations were observed for the latter with the increase in roughness towards upstream from uniform to severe scenarios (see Figures 5.6 and 5.7). The increase in bottom roughness especially at the intertidal floodplains will retain higher pollutant mass subsequently lowering the flushing effect of this waterbody.

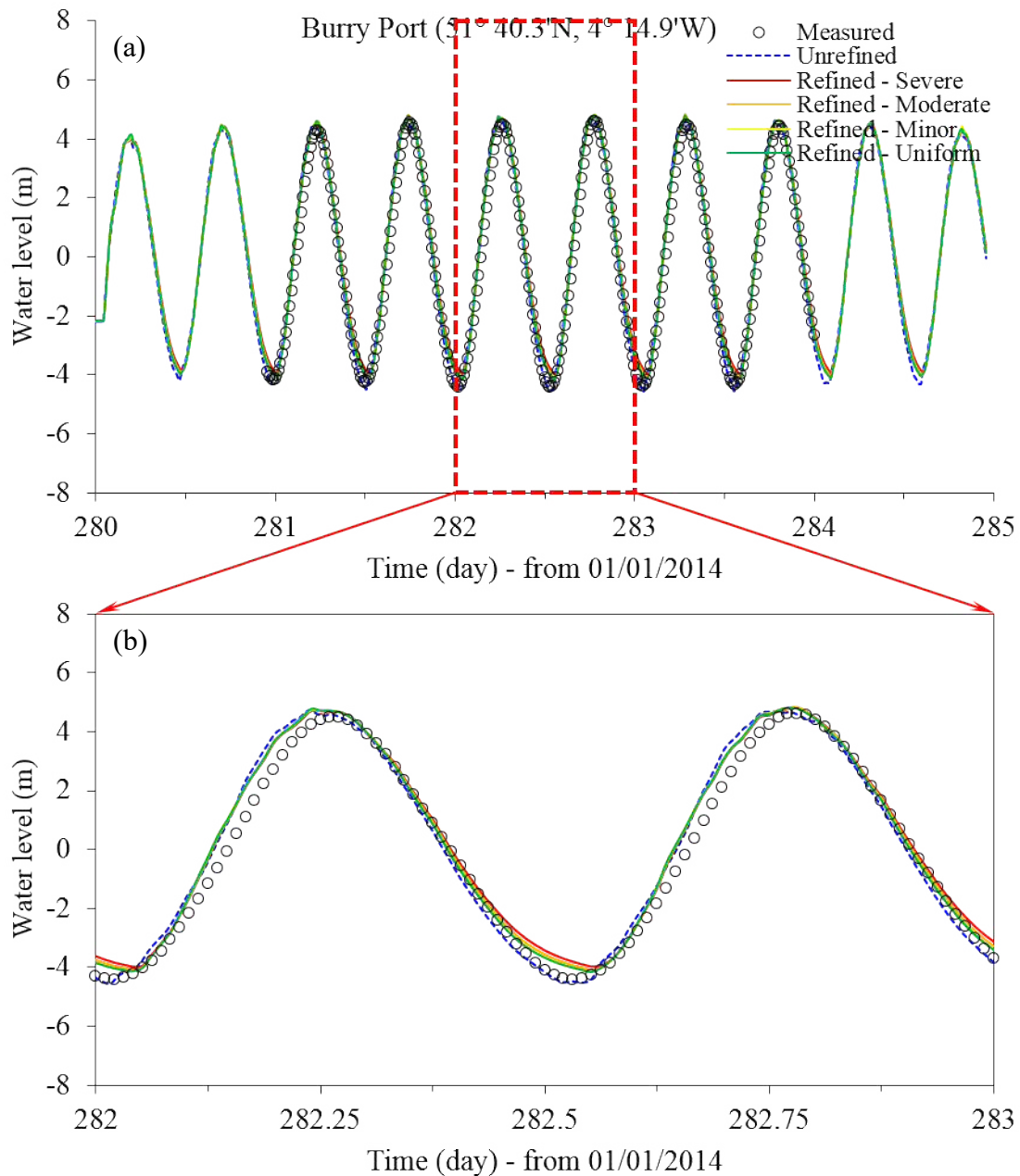


Figure 5.5: Validation of water levels at Burry Port for five days (a) and details of one day (b) between refined and unrefined domains with scenarios of variable bottom roughness.

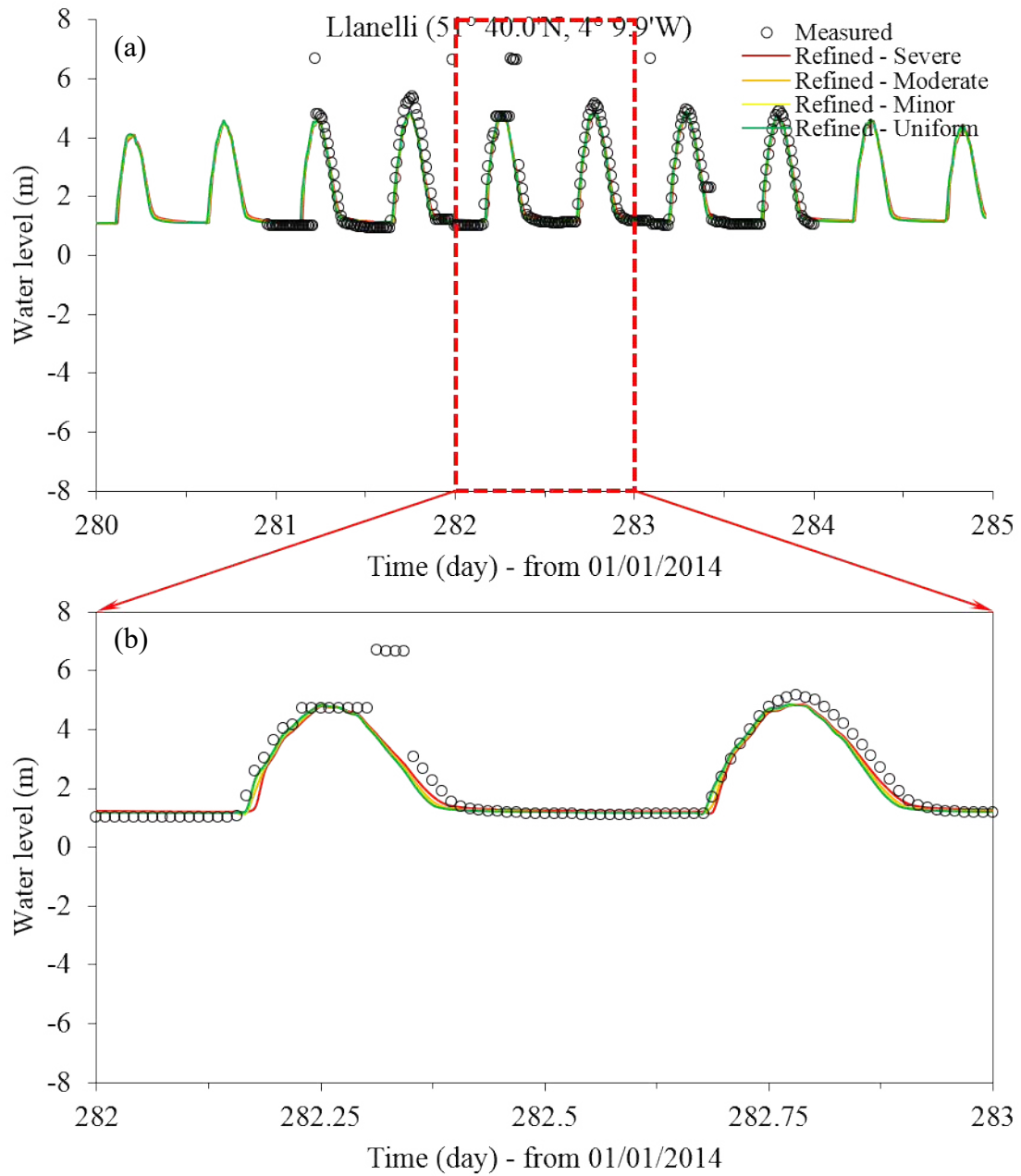


Figure 5.6: Validation of water levels at Llanelli for five days (a) and details of one day (b) with scenarios of variable bottom roughness.

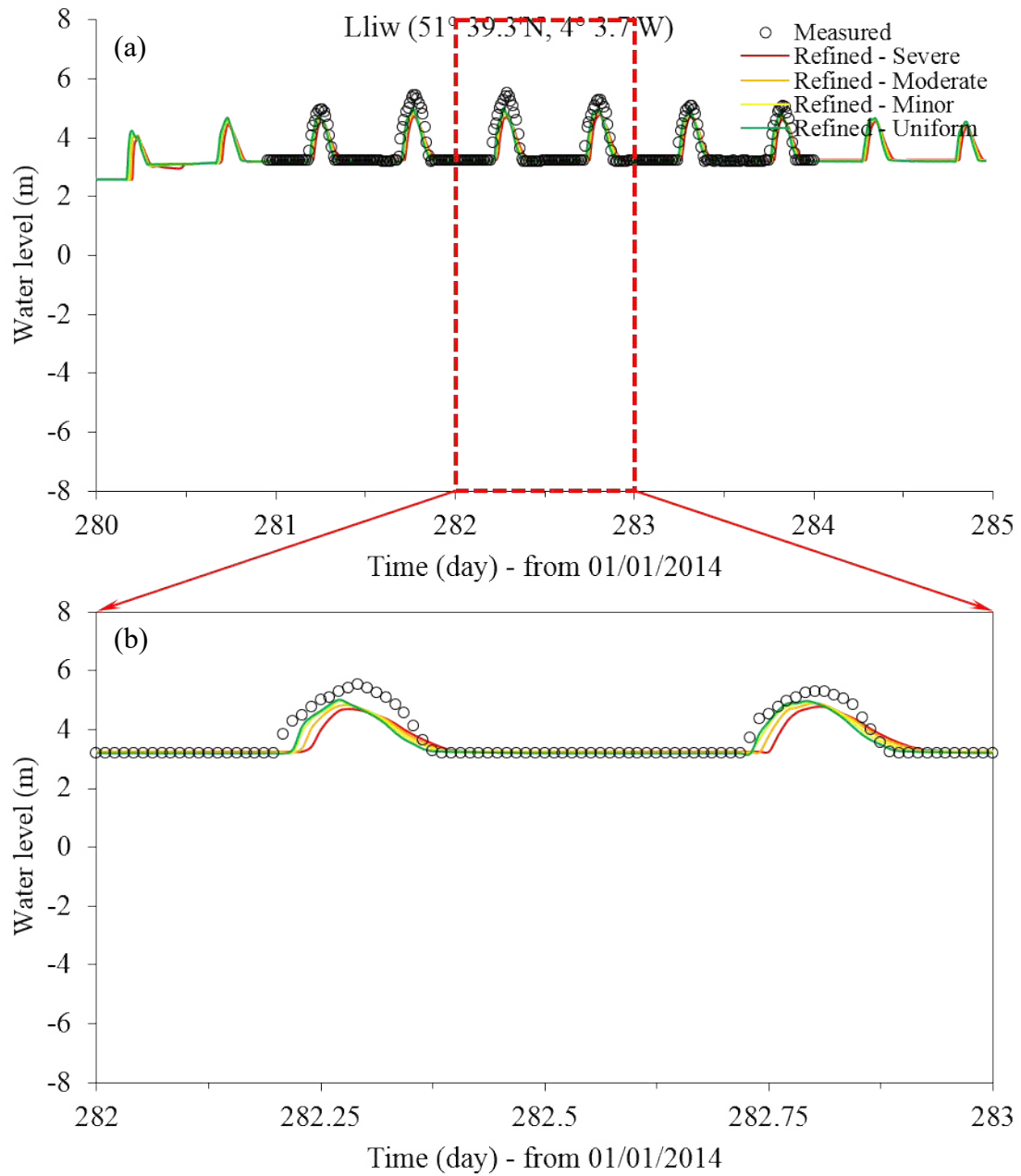


Figure 5.7: Validation of water levels at Lliw for five days (a) and details of one day (b) with scenarios of variable bottom roughness.

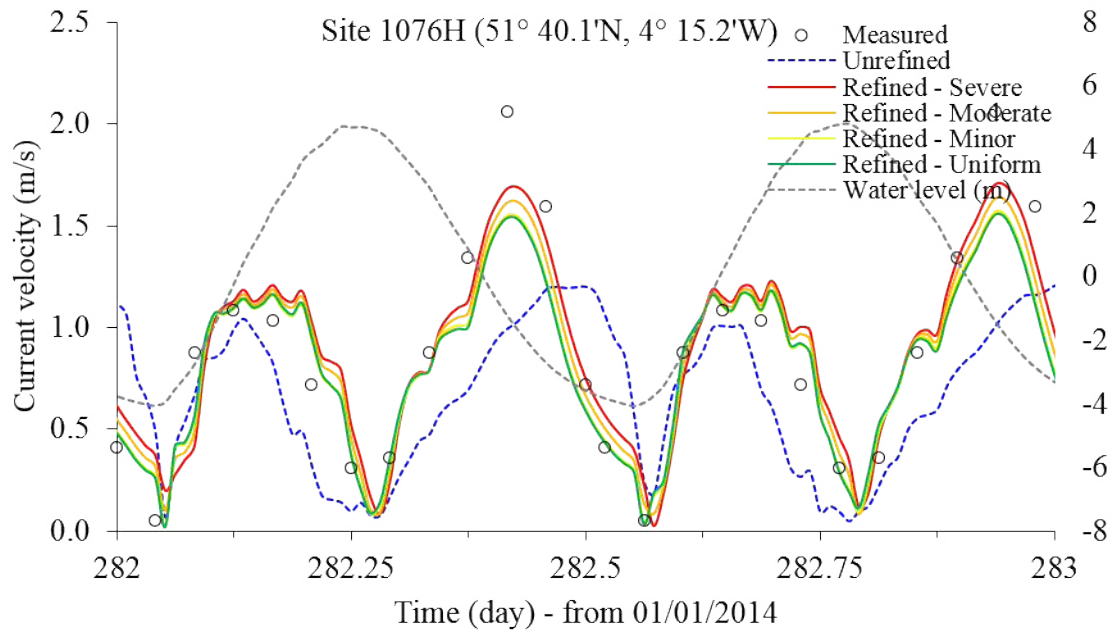
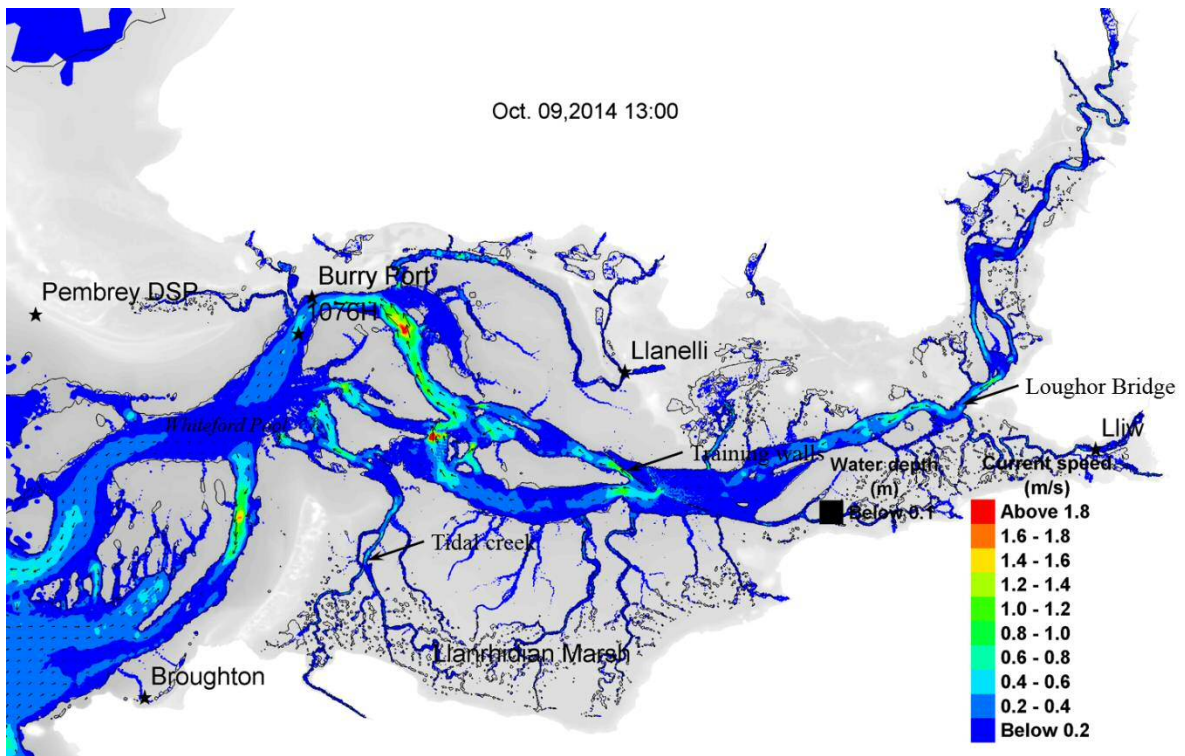
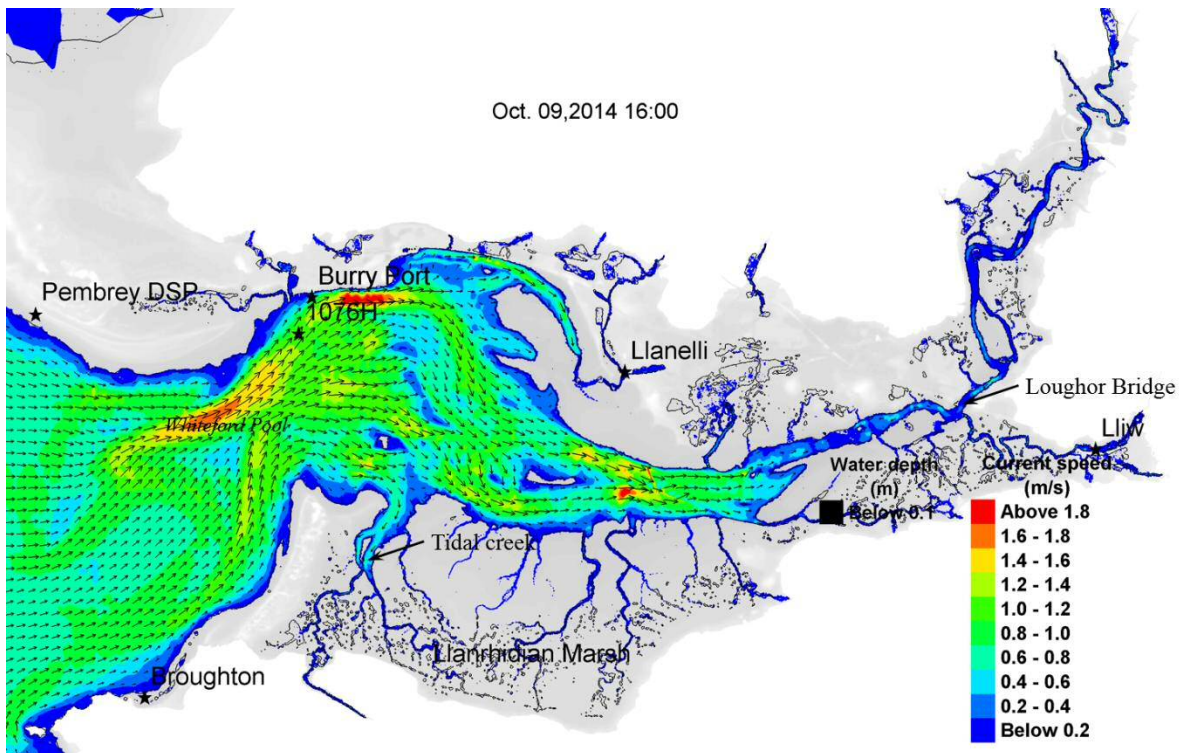


Figure 5.8: Predicted current velocities at site 1076H between refined and unrefined domains with scenarios of variable bottom roughness.

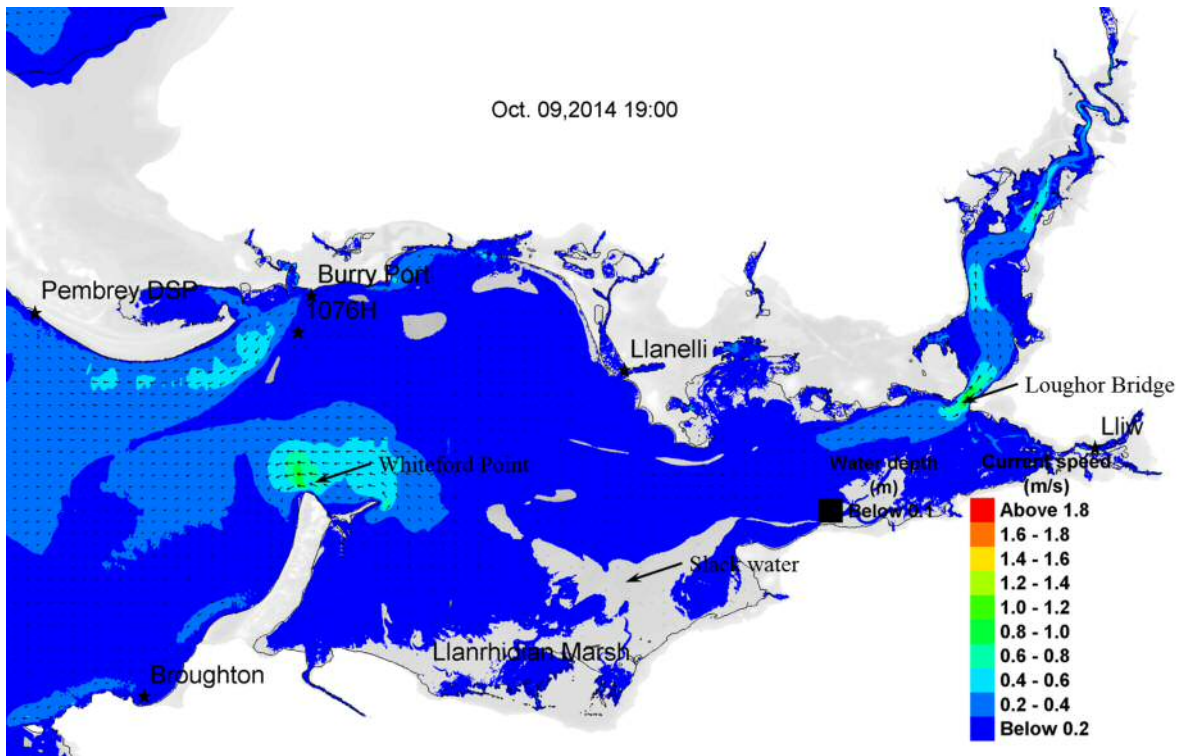
General circulation patterns at different phases of a spring tidal cycle in the Loughor Estuary are shown in Figure 5.9. During low tide, current speed below 0.2 m/s was observed at areas of subtidal and intertidal channels, with speed over 0.6 m/s was spotted along channels at upstream and downstream of Whiteford Pool. Areas of tidal flat and marshland including Llanrhidian Marsh were dried, with features of tidal creek networks and training walls were realistically represented. During flood tide, average current speed at 0.8 m/s was observed at areas of subtidal and intertidal channels, with speed over 1.6 m/s was spotted at Whiteford Pool and near Burry Port. Areas of tidal flat and marshland were still dried, with the propagation of flood currents through tidal creeks was observed. During high tide, current speed below 0.2 m/s was observed at most of the flooding areas, with slack waters were observed around Llanrhidian Marsh and elsewhere. Increase in speed over 0.6 m/s was spotted at Whiteford Point besides at Loughor Bridge heading upstream. During ebb tide, average current speed at 0.6 m/s was observed at areas of subtidal and intertidal channels, with speed above 1.8 m/s was spotted along channels at upstream and downstream of Whiteford Pool. Areas of tidal flat and marshland began to dry and exposing the tidal creek networks. Placing the mesh-nodes and interpolating its bottom elevation based on the vertices were emphasised as important in designing the unstructured mesh. The circulation patterns were generated at the scenario of moderate bottom roughness.



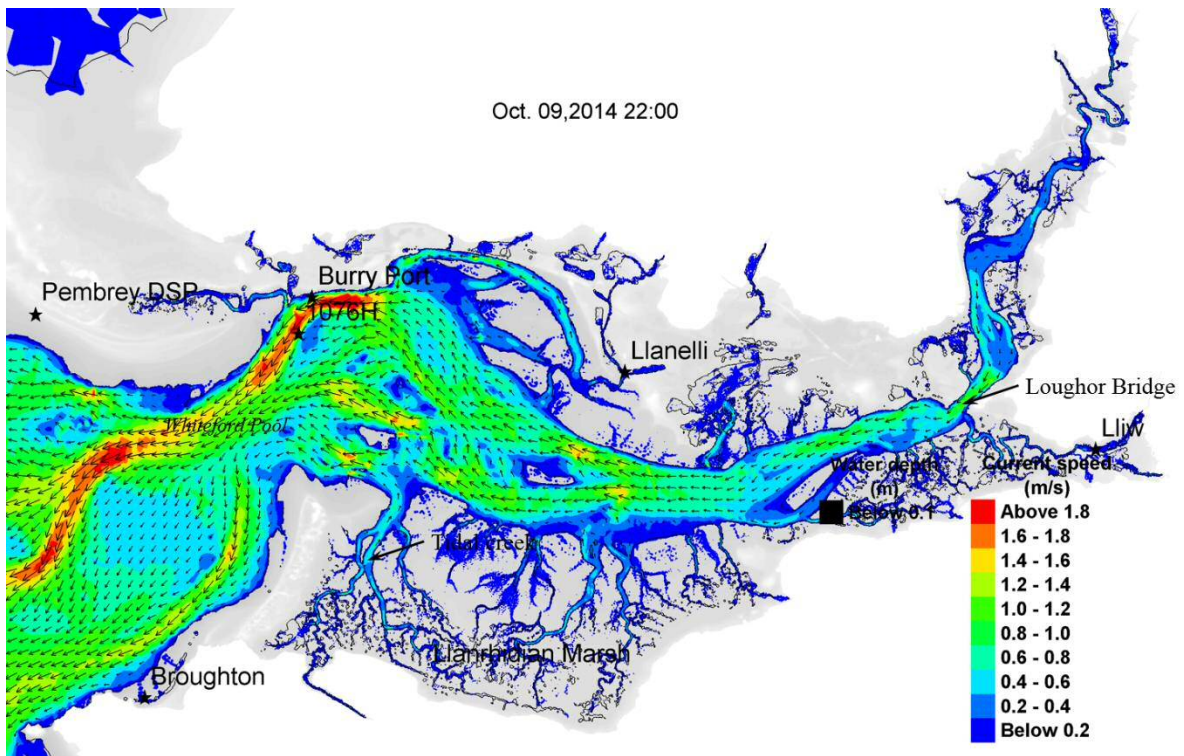
a) Tidal circulation during low tide.



b) Tidal circulation during flood tide.



c) Tidal circulation during high tide.



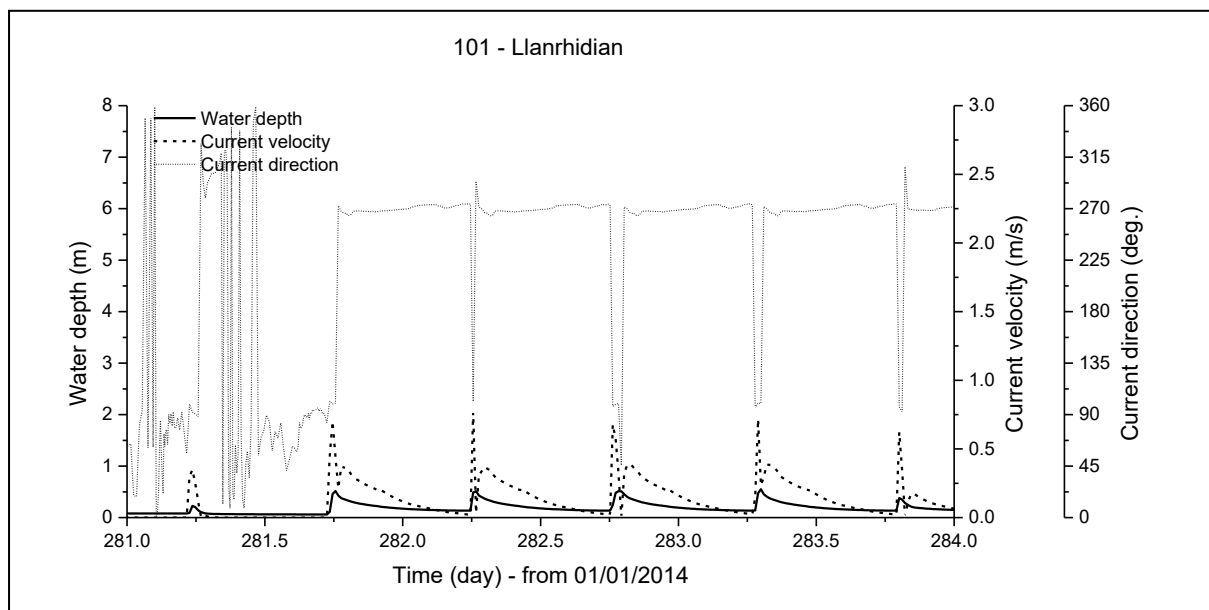
d) Tidal circulation during ebb tide.

Figure 5.9: General circulation patterns at phases of low tide (a), flood tide (b), high tide (c) and ebb tide (d) during a spring tidal cycle in Loughor Estuary.

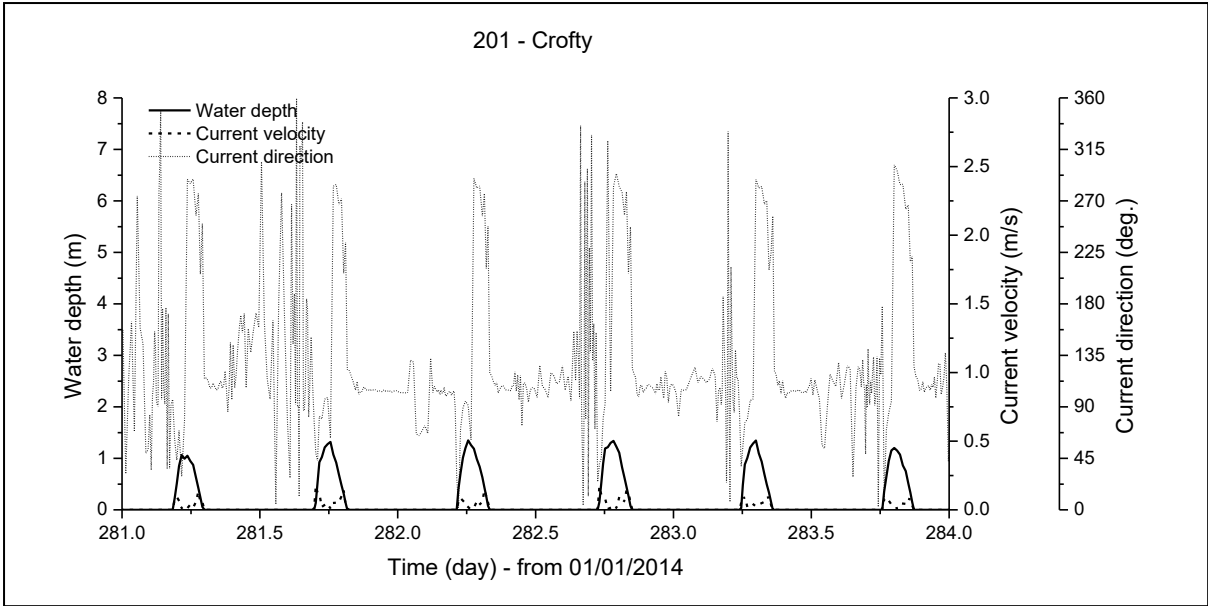
The model was simulated during a period of spring tidal cycles concurrence with the available data for the hydrodynamic validation of prior to modelling the transport and decay of tracers. It was advised that slower tidal currents during neap tides could lead to the less flushing effect subsequently would cause the worst-case condition in term of the pollutant transport. This case scenario should be considered further with comprehensive data monitoring campaigns.

5.3.2 Hydrodynamic at release and sampling sites

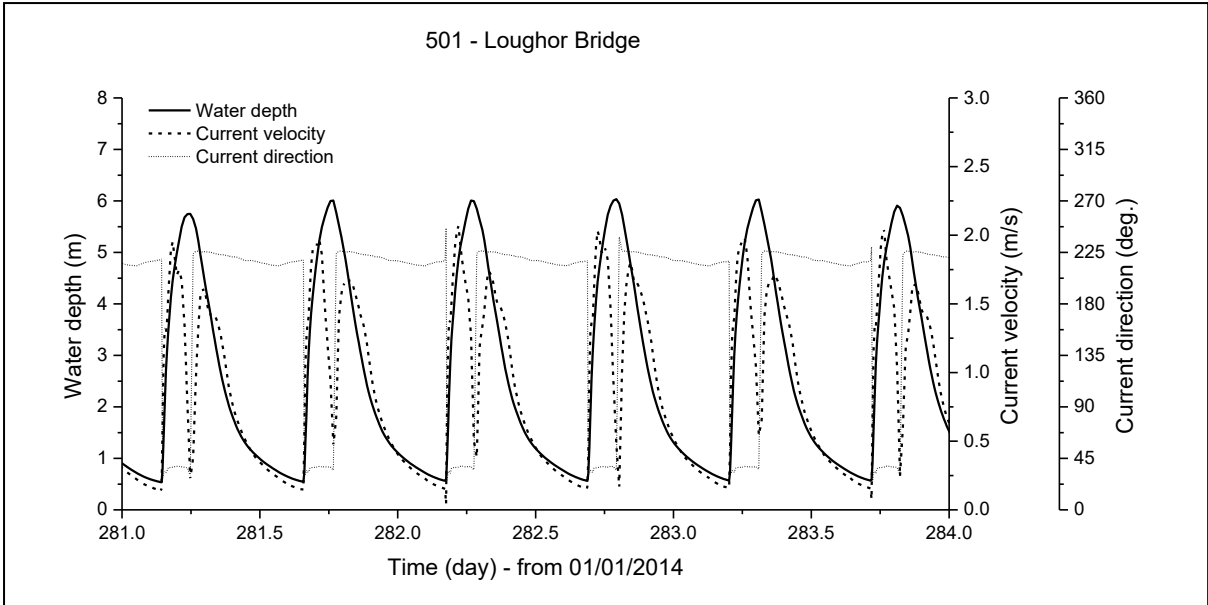
Figures 5.10 and 5.11 illustrate time series of the modelled water depth, water level and tidal current at the release and sampling sites, respectively. It is worth noting that the hydrodynamic processes at the release sites are dependent on the tidal process, together with the river discharges from upstream of the Loughor catchment.



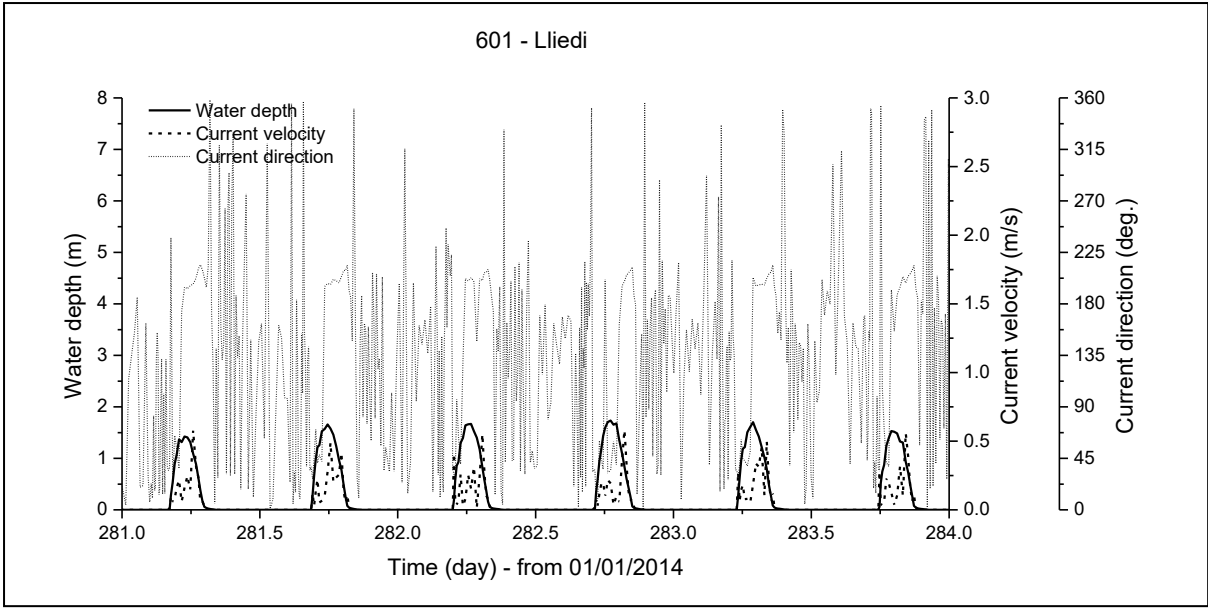
a) Water level, current velocity and direction at Great Pill.



b) Water level, current velocity and direction at Morlais River.

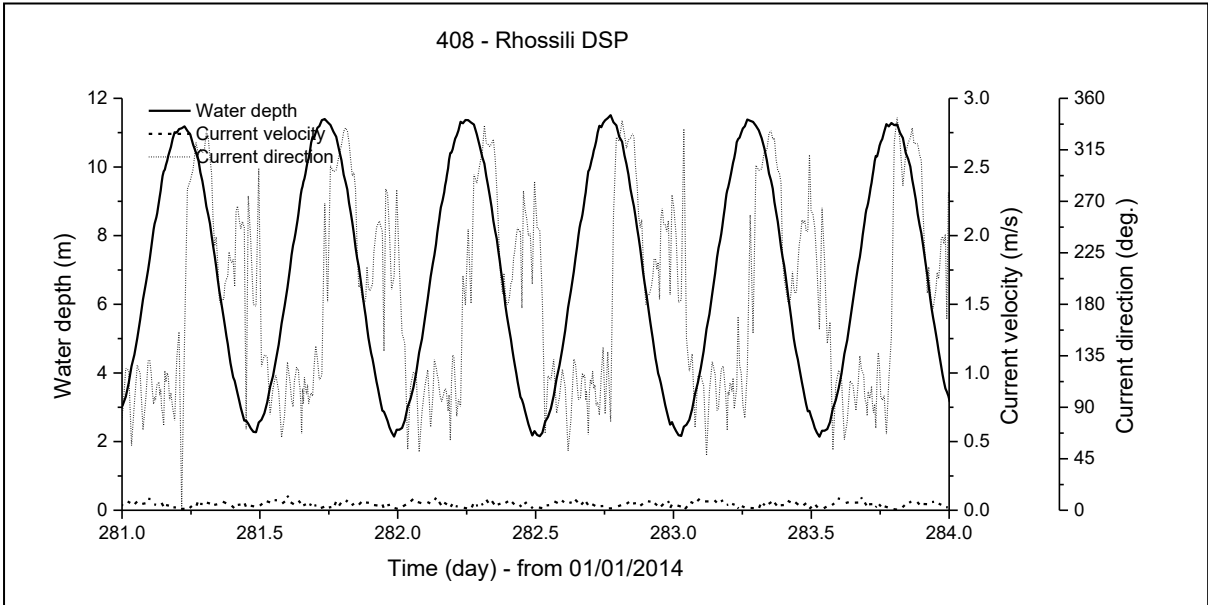


c) Water level, current velocity and direction at Loughor Bridge.

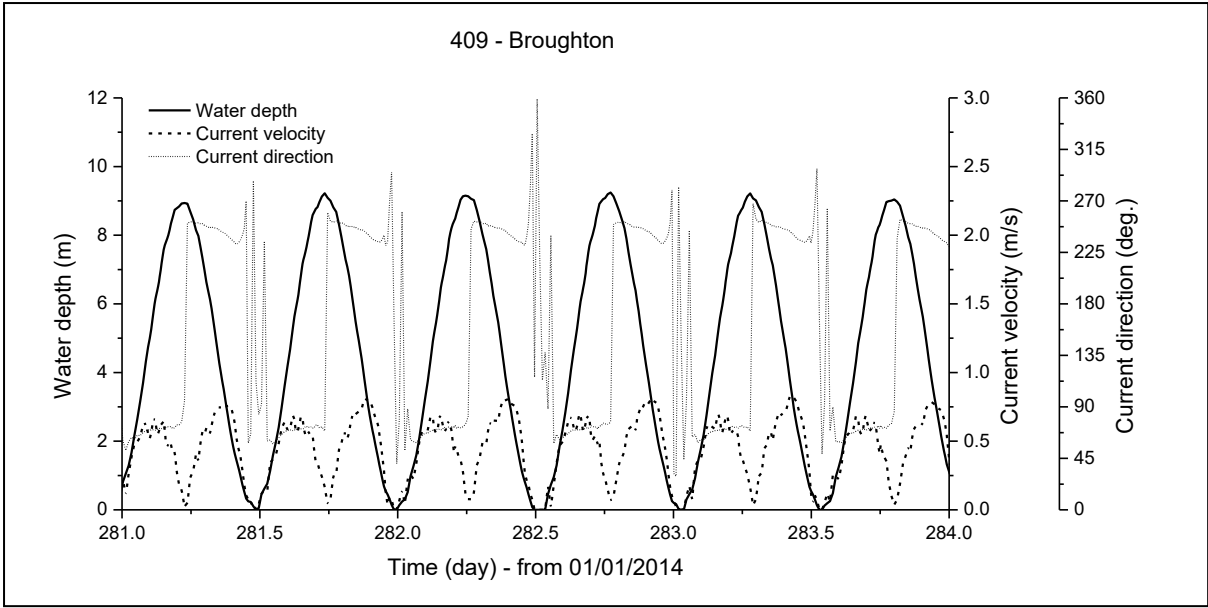


d) Water level, current velocity and direction at Afon Lliedi.

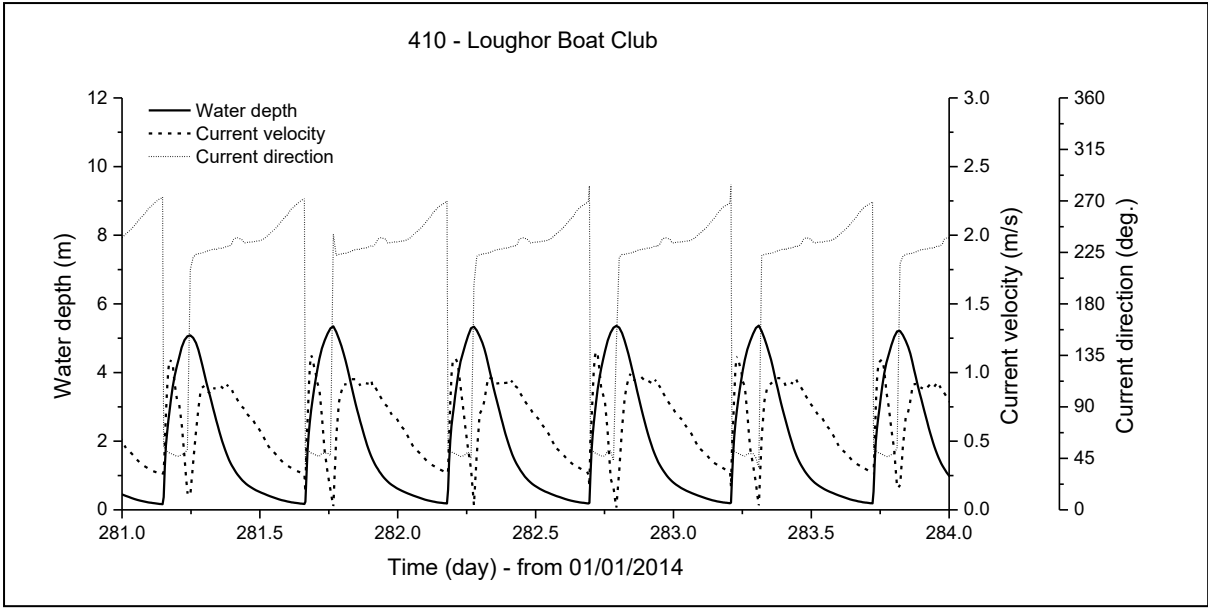
Figure 5.10: Modelled water level, current velocity and direction at the tracer release site of a) Great Pill, b) Morlais River, c) Loughor Bridge and d) Afon Lliedi.



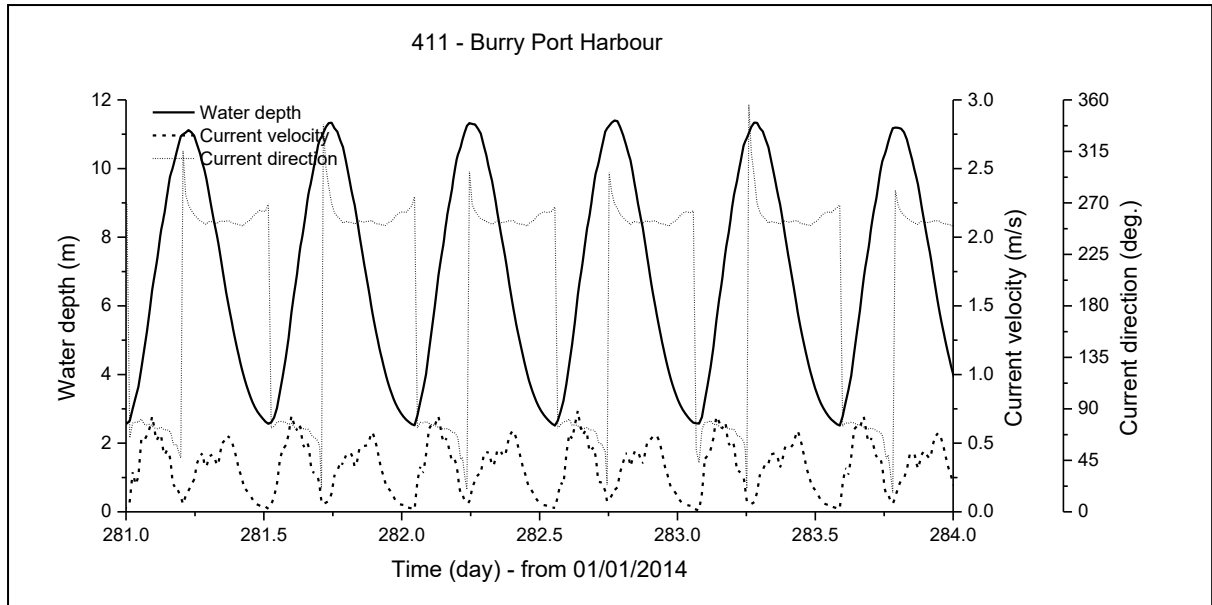
a) Water level, current velocity and direction at Rhossili DSP.



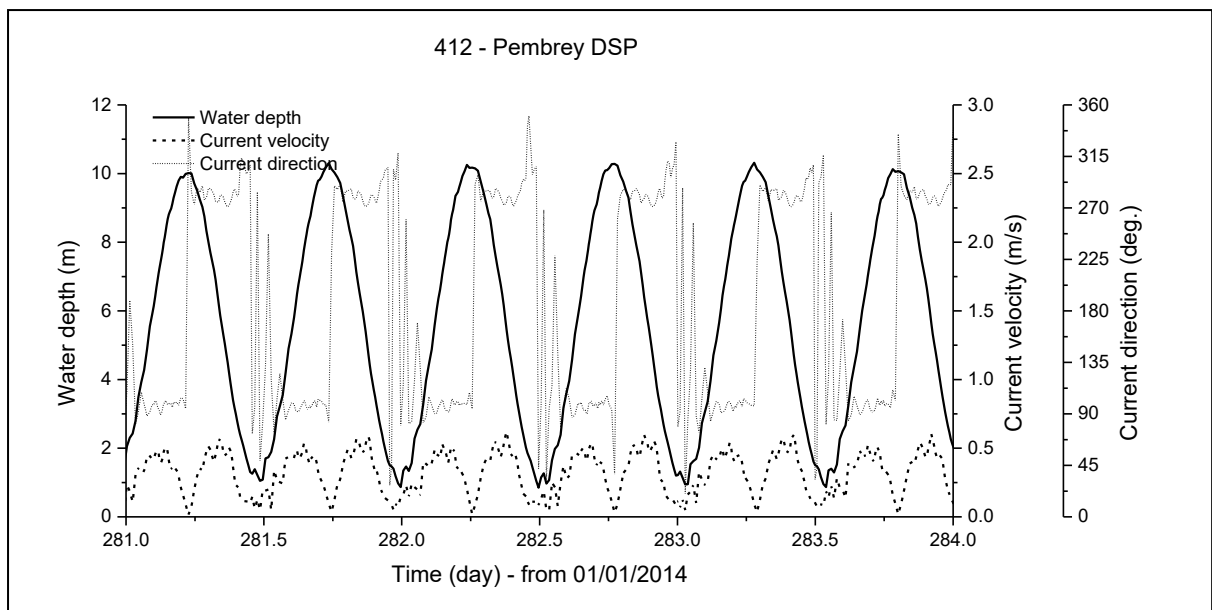
b) Water level, current velocity and direction at Broughton.



c) Water level, current velocity and direction at Loughor Boat Club.



d) Water level, current velocity and direction at Burry Port.



e) Water level, current velocity and direction at Pembrey DSP.

Figure 5.11: Modelled water level, current velocity and direction at the tracer sampling site of a) Rhossili DSP, b) Broughton, c) Loughor Boat Club, d) Burry Port and e) Pembrey DSP.

5.4 Tracer transport and decay modelling processes

The microbial tracers that were released into the Loughor Estuary were simulated within the model domain as an input source at a specific temporal and spatial scales. The release condition of a specific tracer at the temporal scale was based on the information of concentration,

discharge and release period (see Table 5.1). At the spatial scale, the release condition was based on the information of horizontal coordinates at a specific site (see Table D.1). For example, the MS2 coliphage with the concentration of 8.00×10^{13} pfu/ml and the discharge of 7.58×10^{-6} m³/s was introduced on 8th October 2014 at 7:17 a.m. over the period of 11 minutes at Loughor Bridge with the coordinates of 51.66° N, 4.08° W to produce a total dose of 4.00×10^{17} pfu.

In this study, only the MS2 coliphage was considered for modelling the transport process of microbial tracers in the Loughor Estuary. This tracer was used for calibrating the transport model as it's released at the furthest upstream site with the highest titre concentration was regarded as the best to increase the ambient concentration above background levels at the sampling sites. Other microbial tracers that released elsewhere especially at site 101 – Great Pill and site 201 – Morlais River were not considered in this modelling study as the transport process within the tidal creek-marsh system requires further improvement. Besides, different bacteriophages that were informed to behave in different ways within the same environment require further understanding, i.e. through in vivo, in vitro and in silico studies.

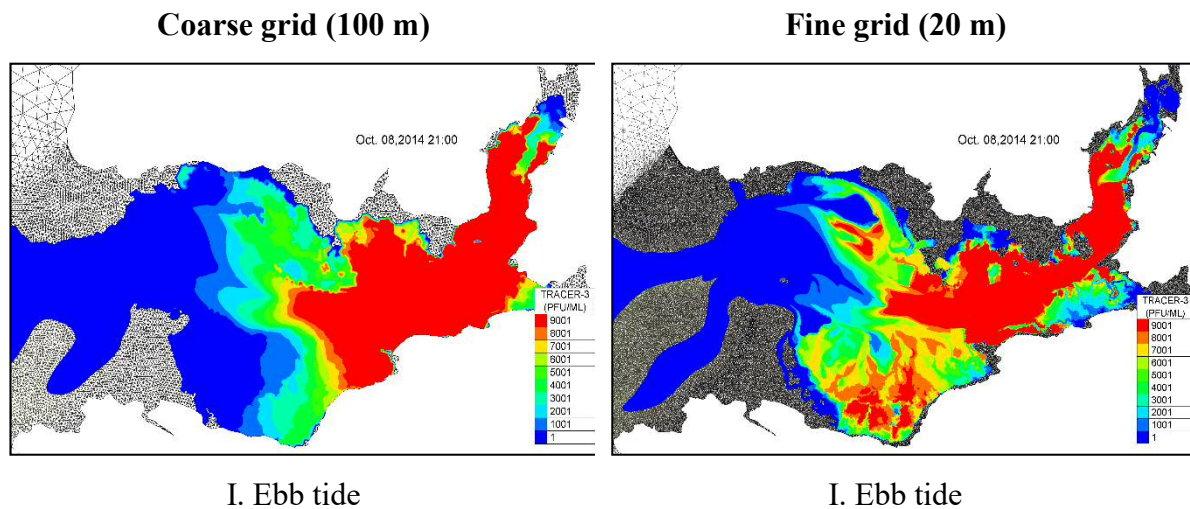
5.4.1 Transport calibration

The tracer of MS2 coliphage was firstly considered as a conservative mass and the model was simulated for the transport processes of advection and dispersion. The evaluation on grid sizes has been conducted for the sensitivity of dispersion transport at two identical meshes of 100 m and 20 m resolutions. The evaluation was initially conducted at the molecular diffusivity of 1×10^{-10} m²/s (Chapra 2008). The transport sensitivity was further evaluated for the longitudinal dispersion between 1×10^1 m²/s to 1×10^3 m²/s based on the eddy diffusivity (Chapra 2008). The simulation was generated at the scenario of uniform bottom roughness for generalising the roughness effect to the dispersion transport in this estuary.

Results for the simulation of transport sensitivity based on the molecular diffusivity are shown in Figure 5.12. The simulation depicts the difference in the transfer and retention of MS2 coliphage to the intertidal floodplains between two different grid sizes at different tidal phases. During ebb tide, the tracer mass was transported downstream along the highly advective intertidal channel. The tracer mass was then concentrated along this channel at a similar extent

for both grids during low tide. More tracer mass was observed retained at the southern marshland for the finer grid as compared to the coarser grid. This was due to the difference in transport patterns at floodplains between two grids during the previous flooding. The finer grid with a better representation of the complex topography was expected in resulting the higher roughness effect as compared to the coarser grid.

During flood tide, the tracer mass was transported back to the upstream along the highly advective intertidal channel. The retained mass at the southern marshland was in the same condition as the previous tidal phases. Most of the tracer mass was then concentrated upstream for the coarser grid during high tide. The retained mass at the southern marshland was observed as less dispersed for the finer grid. These results have explained the less sensitivity of the dispersion process at the highly advective areas with the different grid sizes, but the process was prominent at the intertidal floodplains with the slower current. The decrease in grid sizes has varied significantly the dispersion transport of pollutant, thereby highlighting the importance of representing the accurate bed features at the floodplains.



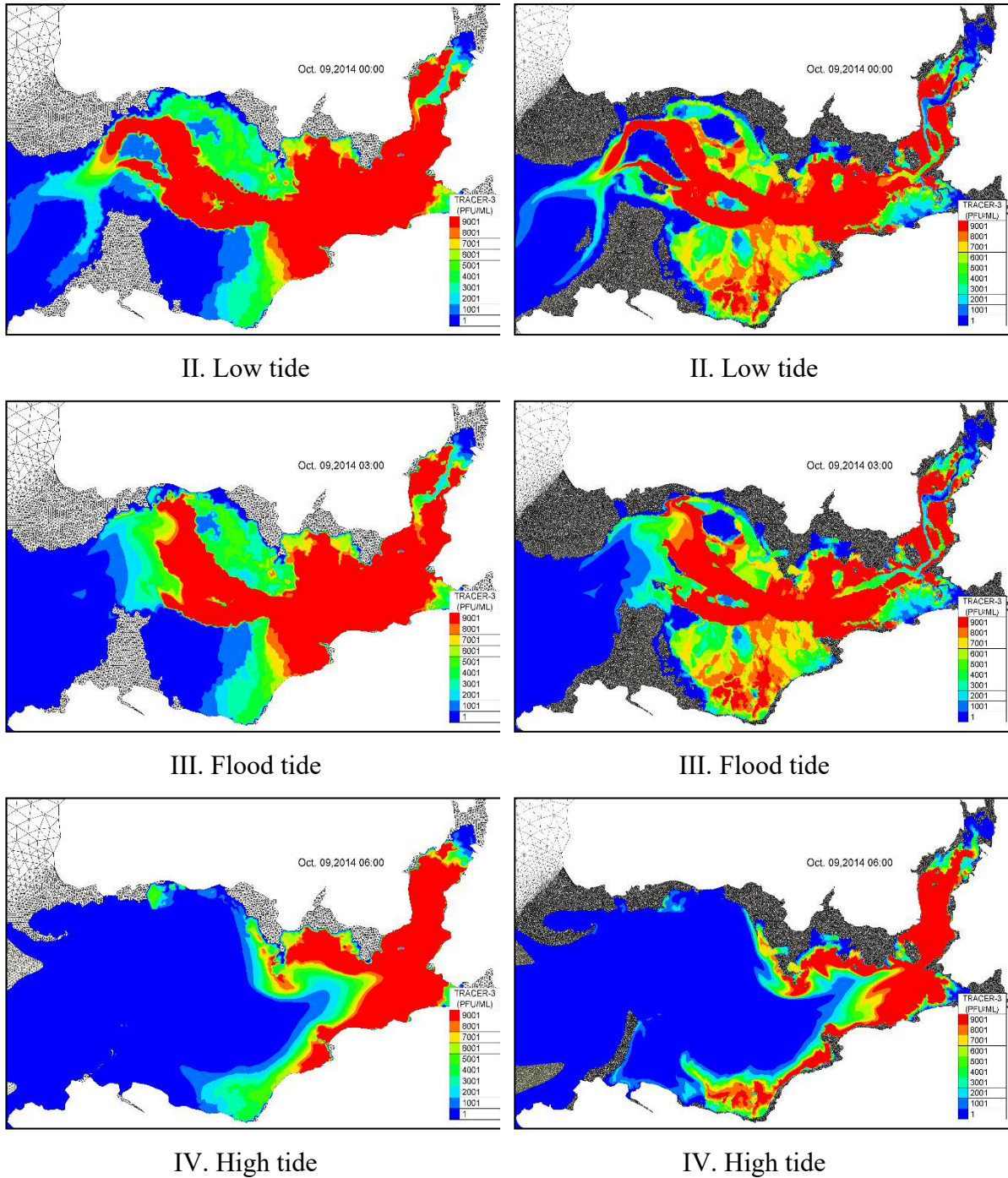
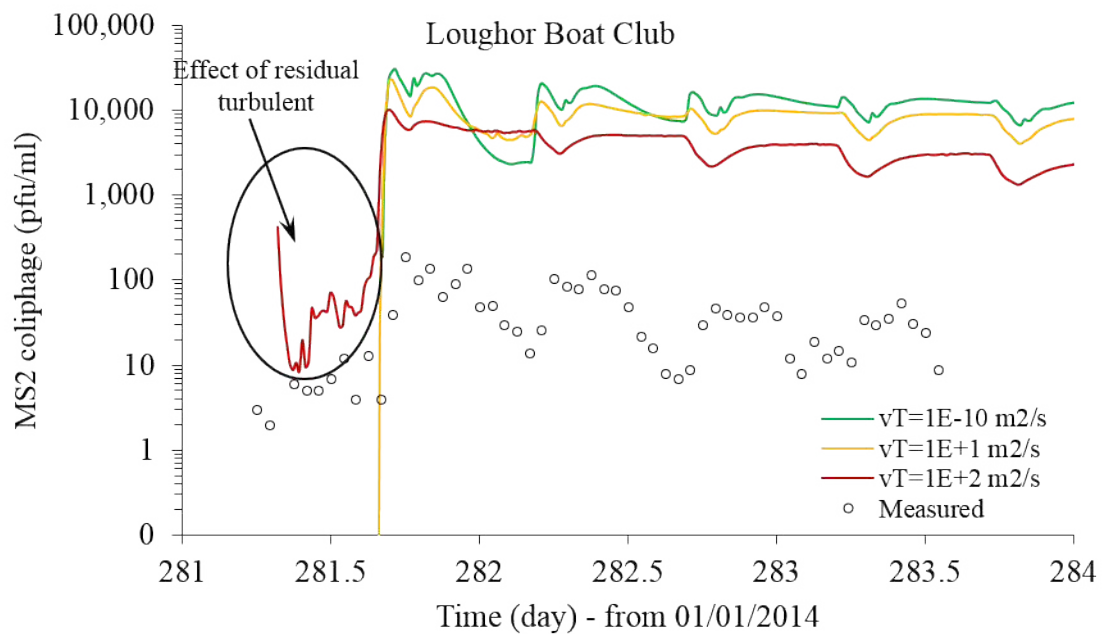


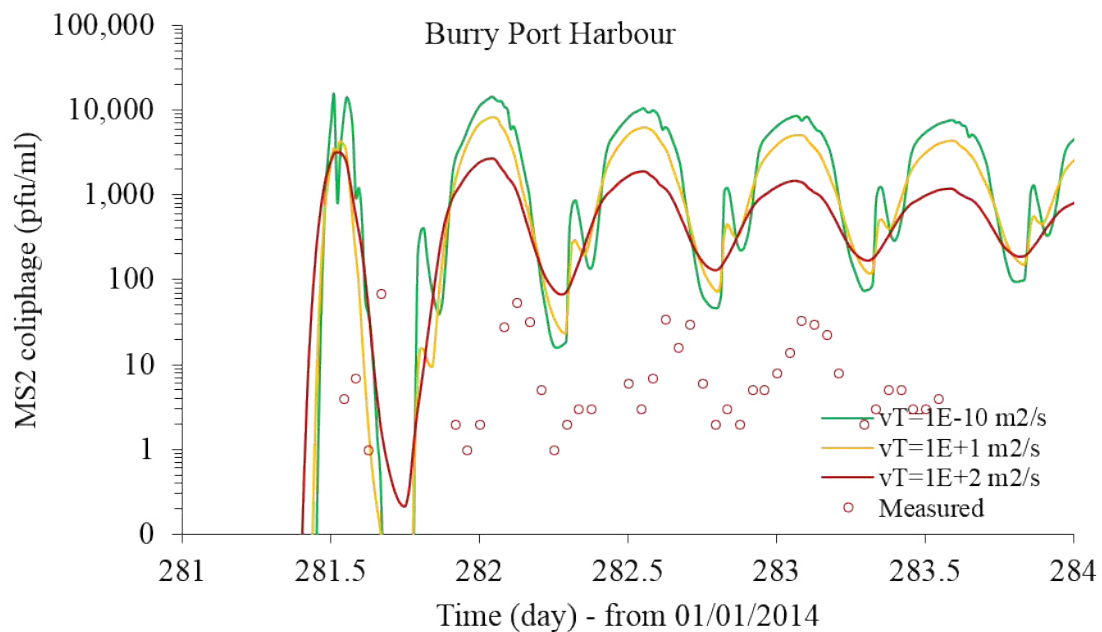
Figure 5.12: Effects of different grid resolutions on the dispersion transport of MS2 coliphage at the molecular diffusivity of $1 \times 10^{-10} \text{ m}^2/\text{s}$.

Further evaluating the transport sensitivity for the longitudinal dispersion based on the eddy diffusivity at an identical grid size, results in Figure 5.13 have shown that the process was more sensitive even at the highly advective areas. The increase in the eddy diffusivity has decreased the concentration gradients of MS2 coliphage at Loughor Boat Club and Burry Port Harbour. The effect of residual turbulent dispersion was spotted at Loughor Boat Club for the modelled

dispersion with the diffusivity of $1 \times 10^2 \text{ m}^2/\text{s}$. Similar dispersion patterns were observed for the modelled concentrations at both sites. The modelled results however were overpredicted the measured data by 100-fold.



a) Longitudinal dispersion at Loughor Boat Club.



b) Longitudinal dispersion at Burry Port Harbour.

Figure 5.13: Calibration results of the estuarine longitudinal dispersion as compared to the measured data at Loughor Boat Club (a) and Burry Port Harbour (b).

The transport sensitivity of MS2 coliphage mass by the advection process has been evaluated by assigning multi friction sub-domains over the floodplains, particularly where the natural features vary significantly. The inter-tidal areas have been divided into four friction sub-domains with different natural bed features, and the estimation on Manning's n values across the floodplains have been calculated using the Equation 4.1 (Arcement and Schneider 1989) as described in Chapter 4. The Manning's n values for each friction sub-domain is estimated based on the summation of global resistance factors for floodplains, which are the base value that referred to the natural bare soil surface across floodplains, the correction factor for the surface irregularities effect across floodplains, and the vegetation value that accounts the growth density and the average flow depth (Hall and Freeman 1994). The friction sub-domains have been characterised as the subtidal channel, intertidal channel, tidal flat and marshland areas (French and Clifford 2000), and are illustrated in Figure 4.26 of Chapter 4.

The zones with higher bottom roughness locally decreased the advective transport of the tracer mass when compared to the base value. However, limited currents data in the main channels and the marshlands were available to validate the roughness values for the various zones accurately. It is due to the tidal range and limitations of the main channel and the nature of the marshlands. Since there only one source of tracer existed in the estuary (Wyer *et al.* 2014), microbial tracer could be used to validate the model hydrodynamics and the roughness values used for the various zones. It was based on the view that accurate tracer predictions required accurate hydrodynamic model predictions. The tracer concentration results at the estuarine transport scale using different roughness scenarios are illustrated in Figure 5.14. This Figure shows a significant reduction in the lateral transport rates with increased bottom roughness values from the middle of estuarine channels to the marshlands but slightly increased transport rates longitudinally, with decreased bottom roughness values from the upstream channel to the estuarine downstream region. The reduction in the tracer concentration at Loughor Boat Club was deemed to be more significant, in comparison with the concentration at Burry Port Harbour with the increased bottom roughness values, as illustrated in Figure 5.15. However, these changes in the roughness reduced the tracer concentration at significant amounts for the zones of dunes and marshlands at the Southern region of the estuary. Calibration of the hydrodynamics based on tracer transport required tracer monitoring at various points in each zone. Due to the lack of this type of tracer concentration observations, tracer concentrations could not be used in selecting an accurate value for each roughness zone in this study.

Therefore, variable bed roughness values could not accurately be justified and subsequently were not utilised in this study.

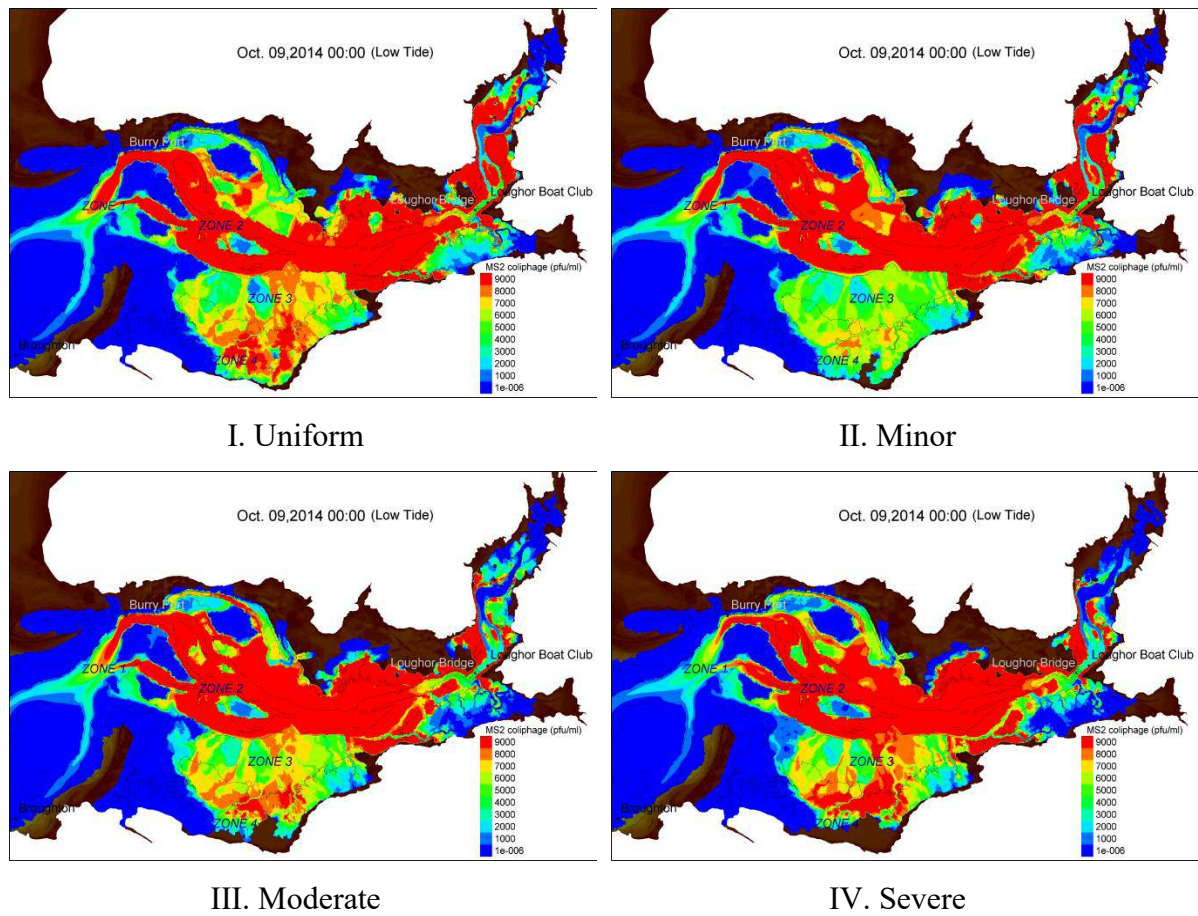
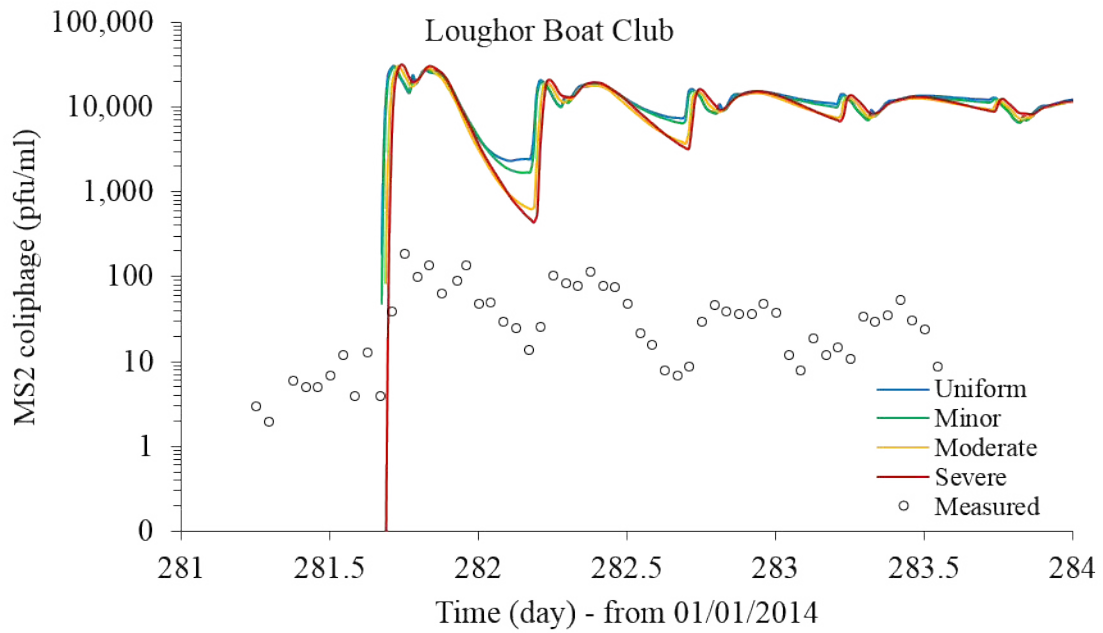
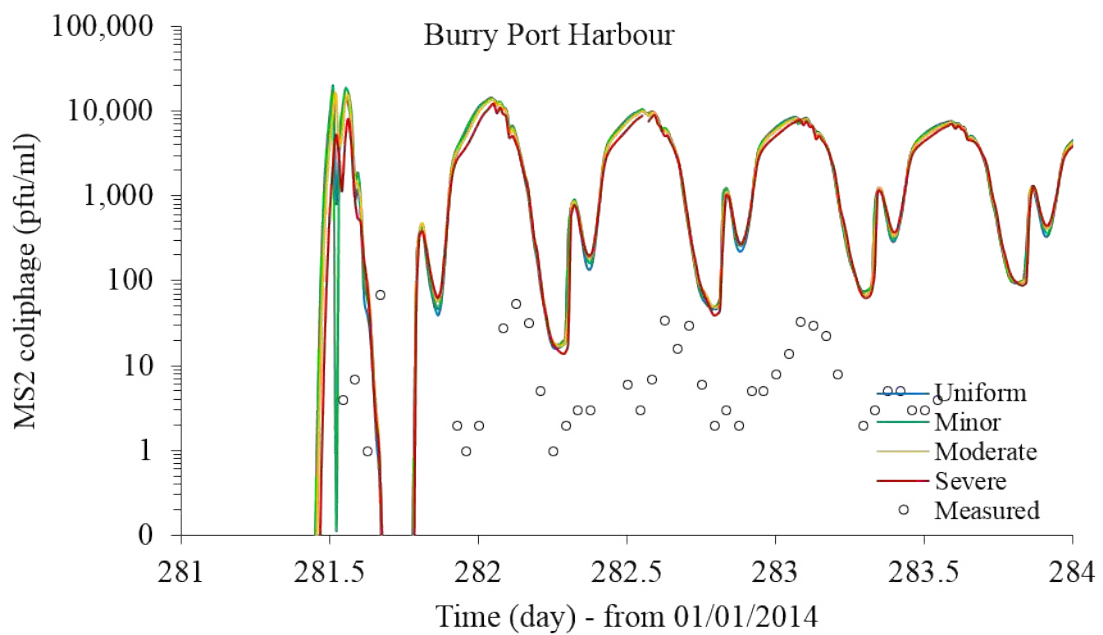


Figure 5.14: Transport fields of microbial tracers after 18 hours of release for a range of multi-zones for bottom friction.



a) Advection transport at Loughor Boat Club.



b) Advection transport at Burry Port Harbour.

Figure 5.15: Calibration results of the advection transport with varied bottom roughness at multi-zones as compared to the measured data at Loughor Boat Club (a) and Burry Port Harbour (b).

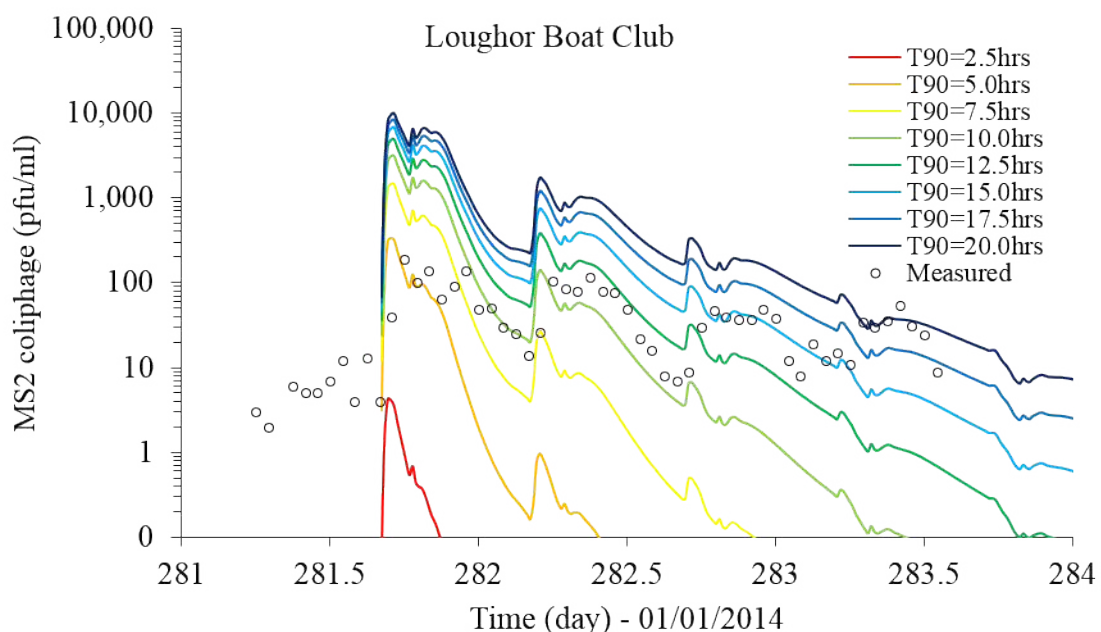
5.4.2 Decay calibration

Although the released microbial tracers were isolated from the seawater and sewage, the literature suggested that they were undergoing decay processes in space and time due to the dynamic estuarine environment (Kay *et al.* 2005). In this modelling work, the decay process of the tracers is presented as a simple first order degradation, with the decay rate being represented by T_{90} values (Schnauder *et al.* 2007) as in the following equation:

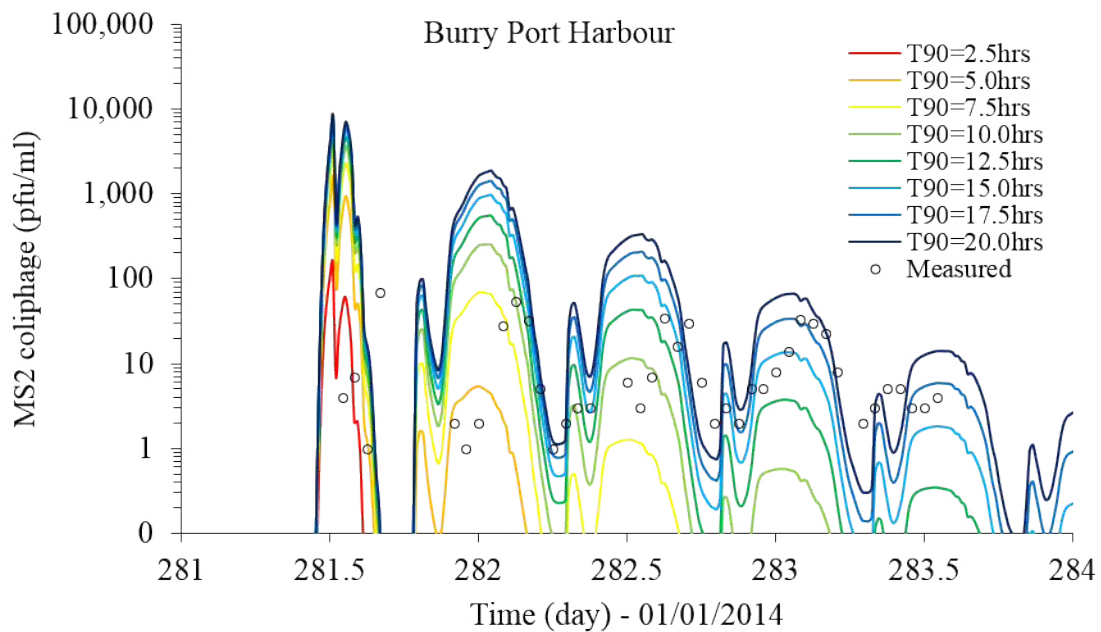
Eqn. 5.6

Initially, the decay process of the microbial tracers was modelled at the constant rates of spatial and temporal resolution, with the T_{90} values tested in the range of 2.5 – 20 hours. The constant decay rate reduced the total mass of the released microbial tracers exponentially with time, with the effects of the estuarine environmental dynamics being excluded to gain an understanding of the impact of the decay process.

By modelling the microbial tracer decay with constant rates in space and time, this basic decay process is incapable of simulating any interactions between the tracer decay and the dynamic estuarine environment. The T_{90} values tested were from 2.5 to 20 hours, as illustrated in Figure 5.16, however reducing the magnitude of the predicted tracer concentrations to the level of measured data, suggested the correct range of microbial decay rates for the estuarine environment.



a) Simple first order decay at Loughor Boat Club.



b) Simple first order decay at Burry Port Harbour.

Figure 5.16: Results of simple first order decay calibration for a range of constant T_{90} values compared to measured data at Loughor Boat Club (a) and Burry Port Harbour (b).

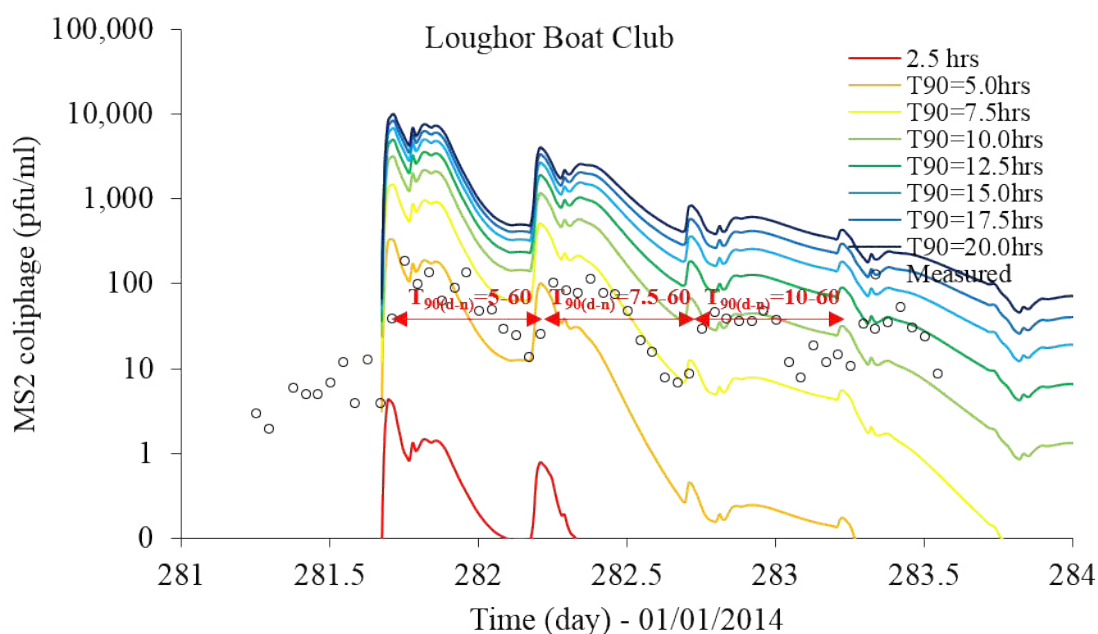
The exponential mass reduction of the microbial tracer for constant rates continuously decreased the tracer concentration at the sampling locations, but these values were not suitable in comparison with the measured data for longer periods. The results also suggested that the decay rate of the microbial tracer was higher during the early release and reduced gradually with time as the mass was transported, in an analogous manner to the environmental shock process.

5.3.2.1 Day-night decay

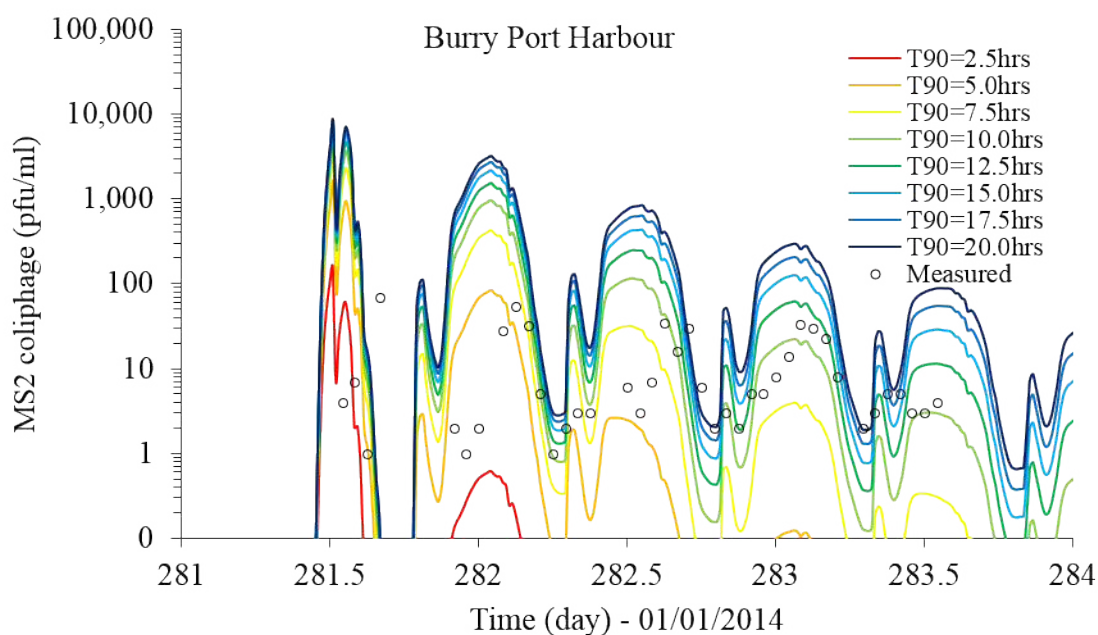
In considering the effects of the estuarine environmental dynamics, especially the inactivation of microbial tracers with sunlight, the decay process was modelled using different rates during day and night times. The T_{90} value was set as a spatial constant in the range of 2.5 – 20 hours during the daytime and increasing in the range of 30 – 60 hours during night time. The process was modelled from 6 am to 6 pm using the daytime decay, then followed by the nighttime decay for the next 12 hours etc.

The microbial tracer inactivation by sunlight is dynamic in time and space, which depends on the intensity of radiation due to both atmospheric conditions and light penetration through the water column. However, simplification of this process is required to gain an understanding of the decay sensitivity due to the effect of sunlight.

Following the decay modelling of the microbial tracer using different decay rates for day and night times, the approach showed an improvement to the modelled results, for the alternate lower and higher ranges of the T_{90} values during the day and night times respectively. The improvement in the modelled results, however, only occurred for a duration period of less than 12 hours.



a) Day-night time decay at Loughor Boat Club.



b) Day-night time decay at Burry Port Harbour.

Figure 5.17: Results of day-night time decay calibration for a constant night T_{90} of 60 hours and a range of day T_{90} values of 2.5 – 20 hours compared to measured data at Loughor Boat Club (a) and Burry Port Harbour (b).

As illustrated in Figure 5.17, at Loughor Boat Club, the modelled concentration converged to the measured data for 12 hours, beginning at 281 JD (Julian date) at 6 pm with day-night values of 5-60 hours, followed for the next 12-hour duration with day-night values of 7.5-60 hours, and continuously in the same pattern. The predicted concentrations at Burry Port Harbour also improved in comparison with measured values when different day and night time decay rates were used.

5.3.2.2 Two-stage decay

A simple first-order degradation is an approach used to represent the survival of the microbial tracers in natural waterbodies, but in reality, the process is non-linear as microbial inactivation interacts with the dynamic environment. Several studies of the bacterial survival in a natural waterbody have suggested that bacteria undergo a two-stage degradation as they are exposed (Bowie *et al.* 1985; Crane and Moore 1986). The model equation used for this modelling work can be written as:

where C_t is the bacteria concentration at time t , C_0 and C_0' are the initial microbial concentrations for two hypothetical stages, and k and k' are the constant decay rates for two hypothetical microbial stages. The decay rates can also be represented by the T_{90} values, as given in Equation 5.7. Figure 5.18 illustrates the total mass balance for the typical bacteria after undergoing the two-stage decay process.

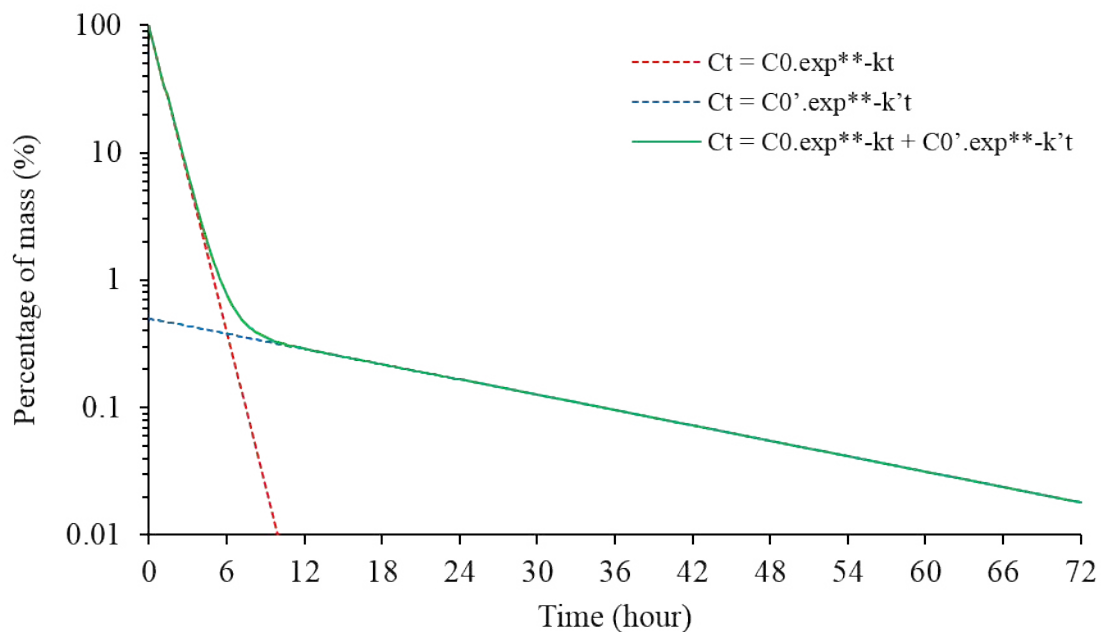


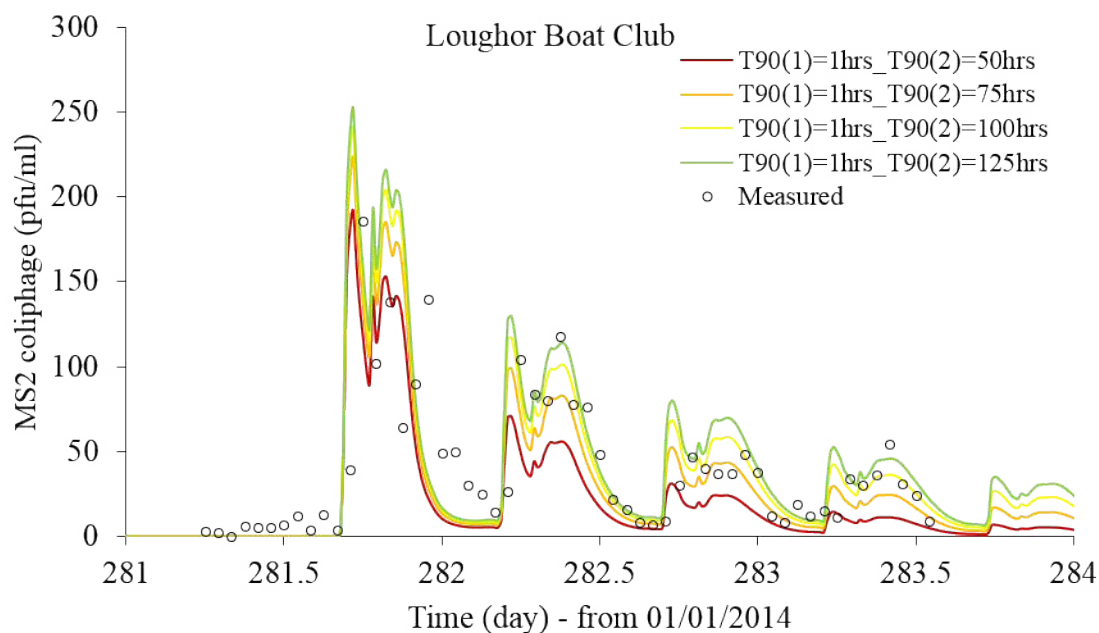
Figure 5.18: Typical two-stage bacterial decay mass balance.

The two-stage microbial decay is a process of combining the two first-order kinetic decay processes that occur simultaneously, with the two hypothetical microbial groups that decay at different rates. The first stage decay process takes place with the microbial group with higher initial counts and with a higher decay rate. This decay process, which occurs over a short period, also considers the environmental shock effect to the bacteria as they are introduced to the natural waterbody for the first time. The second stage decay results in the remaining bacteria being of a lower initial count, with the lower rate. The rates for both the first and second stage decay rates are functions of salinity, temperature, and solar radiation and turbidity. Table 5.2 illustrates the specific values of parameters used for the two-stage microbial decay model of this work.

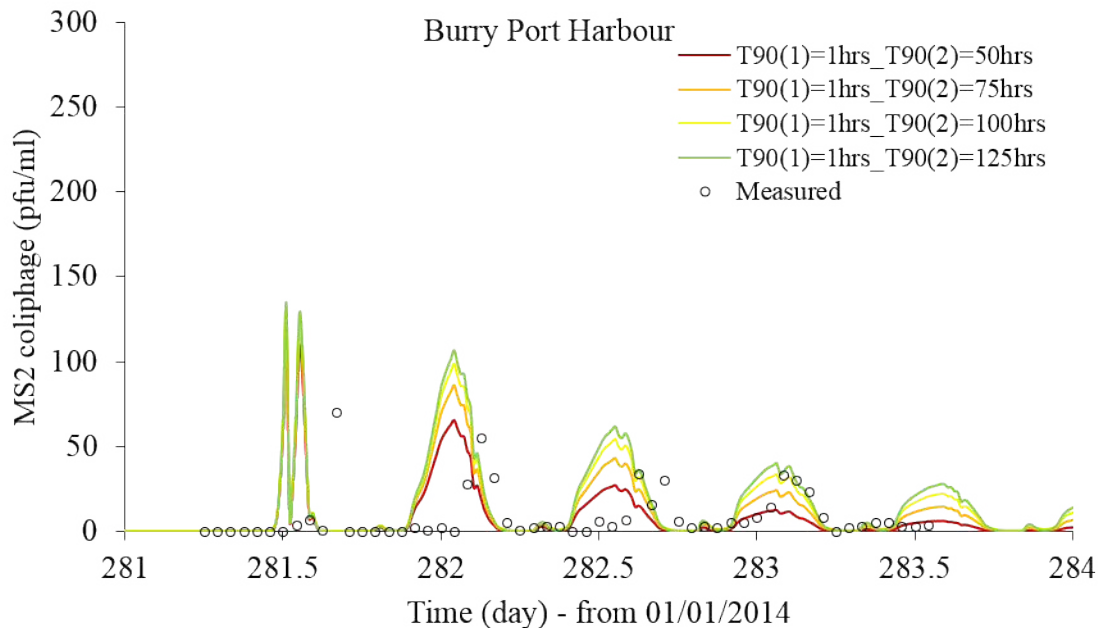
Table 5.2: The parameter values for the two-stage bacterial decay model.

Parameter	Bacterial concentration and decay rates	Mass percentage and T90 values
(pfu/ml)	3.96E+17	99 %
(pfu/ml)	4.00E+15	1 %
(1/hour)	2.3026	T90 = 1 hours
(1/hour)	0.0184 – 0.0461	T90' = 50 – 125 hours

Figure 5.19 illustrates the transport results of the modelled microbial tracer after considering the two-stage decay processes at Loughor Boat Club and Burry Port Harbour. From the results of the two-stage decay, the first peak of concentration of the tracer at Burry Port Harbour was overestimated when compared with the measured data, but the subsequent peaks in concentration closely matched the measured data. It is because the first peak results from the first stage mass of the 3 hours T₉₀ value. The T₉₀ value of less than 3 hours for the first stage decay could be used for modelling the process correctly at Burry Port Harbour.



a) Two-stage decay at Loughor Boat Club.



b) Two-stage decay at Burry Port Harbour.

Figure 5.19: Results of the transported microbial tracer after considering the two-stage decay processes with a $T_{90}(1)$ value of 1 hour and $T_{90}(2)$ values ranging from 50 to 125 hours at Loughor Boat Club (a) and Burry Port Harbour (b).

The modelled microbial tracer concentrations at Loughor Boat Club were estimated closely and within the range of measured data for all the concentration peaks, which represented the correct initial tracer mass of 99% for the second stage decay within the T_{90} value range of 50 to 125 hours. The significant decrease from the second to the third peak concentration at Loughor Boat Club is thought due to the effect of solar radiation and the dispersion process.

The results of the modelled microbial tracer during slack and low tides at Loughor Boat Club are estimated correctly compared to the measured data, which also represents a proper flushing effect from the upstream discharge of the river catchments. Elliot *et al.* (2012) have estimated the average river discharges to be approximately $5 \text{ m}^3/\text{s}$ from the upstream catchments.

The transport and decay of FIOs have a direct influence on the bacterial concentration in the estuary that was informed of the water quality status of the waterbody. The releasing of microbial tracers in Loughor Estuary was idealising scenarios of releasing the sewage effluent from WwTWs within this waterbody. The release of FIOs at a different time between spring and neap tidal cycles will have different short-term impacts on water quality in the estuary.

Higher tidal ranges within the highly dispersive environment during spring tides will flush out the FIOs mass and reduce its concentration faster respectively due to high dilution effect and strong tidal current, as compared to neap tides. Besides, the release of FIOs at a different time along the season also would have different impacts on water quality. Stronger solar irradiance during summer will reduce the FIOs concentration faster due to the higher decay rate, as compared during winter. During high rainfall events however, high discharge rate from the upstream will flush the estuary faster, yet more bacterial loading from the catchment will enter the waterbody through CSOs and bypassing the WwTWs. For the long-term water quality impact, the highly persistence FIOs (e.g. antibiotic resistance viruses) will be transported farther from sources and will remain longer in the waterbody as compared to the labile ones. Modelling the accurate processes of FIOs transport and decay over the spring-neap tidal and seasonal conditions besides considering the case of long-term impacts are the engineering significance that helps the WwTW managers in practising at the best management level.

5.5 Summary

This chapter was focused on modelling the transport and persistence of microbial tracers in the estuarine environment. From the assessment on the tracer suitability at release sites, the MS2 coliphage due to its highest titre concentration was assigned at the furthest upstream site of Loughor Bridge. As results of extending the modelling domain at the intertidal floodplains, the modelled tidal current at Site B besides the water level at Burry Port, Llanelli and Lliw were significantly improved. As results of the nodes placement and the elevation interpolation based on the designed vertices, the inundation extends and the sub-mesh-scale features representation at floodplains were realistically simulated. From the modelled results at tracers' release sites, the hydrodynamic simulations at sites along the creek networks were depending on the stream discharges during drying, otherwise were depending on the tidal propagation. From the sensitivity analysis on the diffusive transport, the diffusivity of the tracer was decreased with the increase in the mesh resolution and the tracer's concentration gradient was increased with the decrease of the former parameter. From the sensitivity analysis on the bottom roughness, the retention of the microbial tracer at floodplains was increased with the increase in the roughness during low tides while the tracer concentration in subtidal channels was less sensitive to the roughness changes during high tides. Based on the two consecutive analyses, the microbial tracer transport that was modelled as a conservative mass was over predicted the measured concentration over hundred-folds at upstream and downstream of the estuary. From

the decay calibration, the modelled of tracer concentrations from the constant decay and the day-night decay simulations were agreed to the observed data at different decay rates within the period of 12 hours or less and at the different time. Results from the decay calibration were further shown that MS2 coliphage was experiencing the biphasic decay with the T_{90s} were ranged at 1 hour and from 50 to 125 hours for the first and second components decay respectively.

Chapter 6: Transport and decay of FIOs from a diffuse source

6.1 Introduction

This chapter was focused on modelling the transport and decay of faecal indicator organisms (FIOs) from intertidal marshlands as the diffuse source. Modelling these organisms from the diffuse source was essential to improve the understanding of their impacts to water quality at the sites of interest, after being transported in the estuarine environment. Quantifying the environmental loading of these organisms was the first step towards predicting the exposure risk of faecal contamination from the source of livestock origin (Dorner *et al.* 2004). The release of these organisms from an agricultural setting was simulated using a release-kinetic model, as the process was known to be controlled by the combination of physical, chemical and biological factors (Blaustein, Pachepsky, Shelton, *et al.* 2015). The process of decay experienced by these organisms while being transported in the estuary was modelled based on the range of the site-specific conditions (Bakar *et al.* 2017). The contamination of shellfish to these organisms was estimated based on a shellfish-to-water concentration ratio (Riou *et al.* 2007) – their accumulation dynamics were depending upon the species physiology and environmental interactions (Campos *et al.* 2013).

This chapter was organised as follows: Section 6.2 presented the materials and methods for modelling the transport and decay of FIOs from intertidal marshlands as the diffuse source. This section included descriptions for the study area about a grazing marshland and shellfish harvesting waters and statistical analyses for the interpretation of results. This section also described methods for modelling the bacteria deposition at the grazing marshland, their release into water columns, the transport and decay in the estuarine water and the exposure risk to the shellfish flesh. Section 6.3 presented the results and discussion on findings based on the modelling works. This section included the validation on hydrodynamic results at the study area, results on the bacteria deposition, their release modelling based on two cases, the transport and decay and the exposure risk to the shellfish, both were based on two scenarios.

6.2 Materials and methods

6.2.1 Study area

The diffuse source of FIOs from a large area of historically grazed salt marshes, namely the Llanrhidian Marsh on the North Gower coast, was inferred as one of the probable sources that contributed to the reason for failure (RFF) at the designated shellfish waters of Burry Inlet (BI) North and BI South (Section 1.3, Table A.1 and A.2). The shellfish hygiene surveys were carried out within this area during March and October 2012 by the Environment Agency Wales (EAW) alongside the stock assessment surveys. 60 stations were selected for the flesh sampling based on a standard grid survey for the cockle stock. These stations included 50 cockle beds (i.e. 34 on BI South, 16 on BI North) and ten mussel beds (i.e. six on Whiteford Scar, four on other established beds) as can be seen in Figure 6.1.

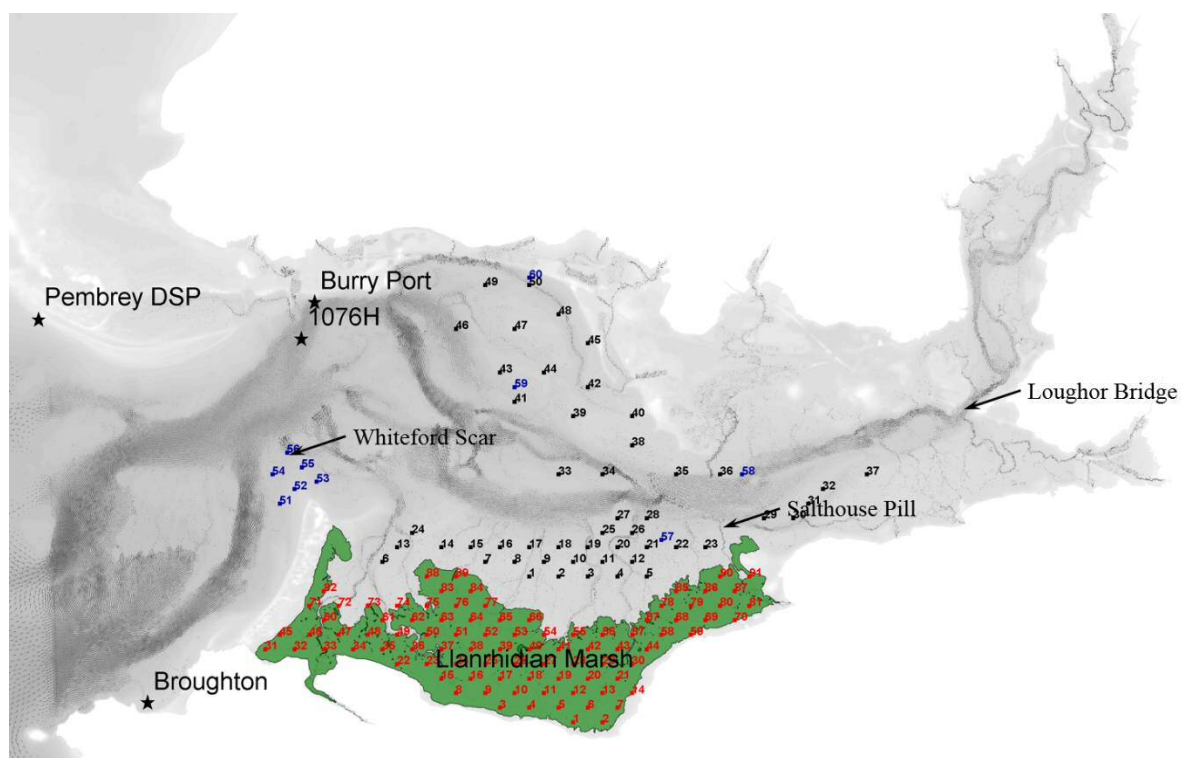
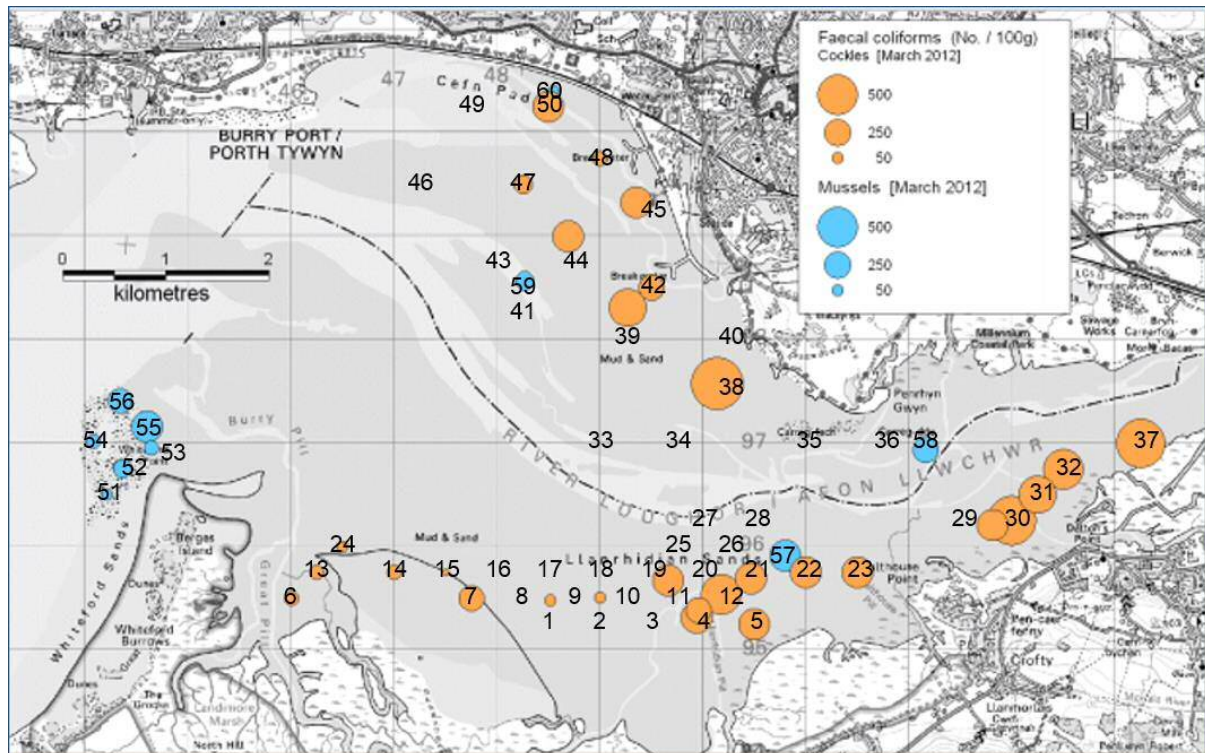


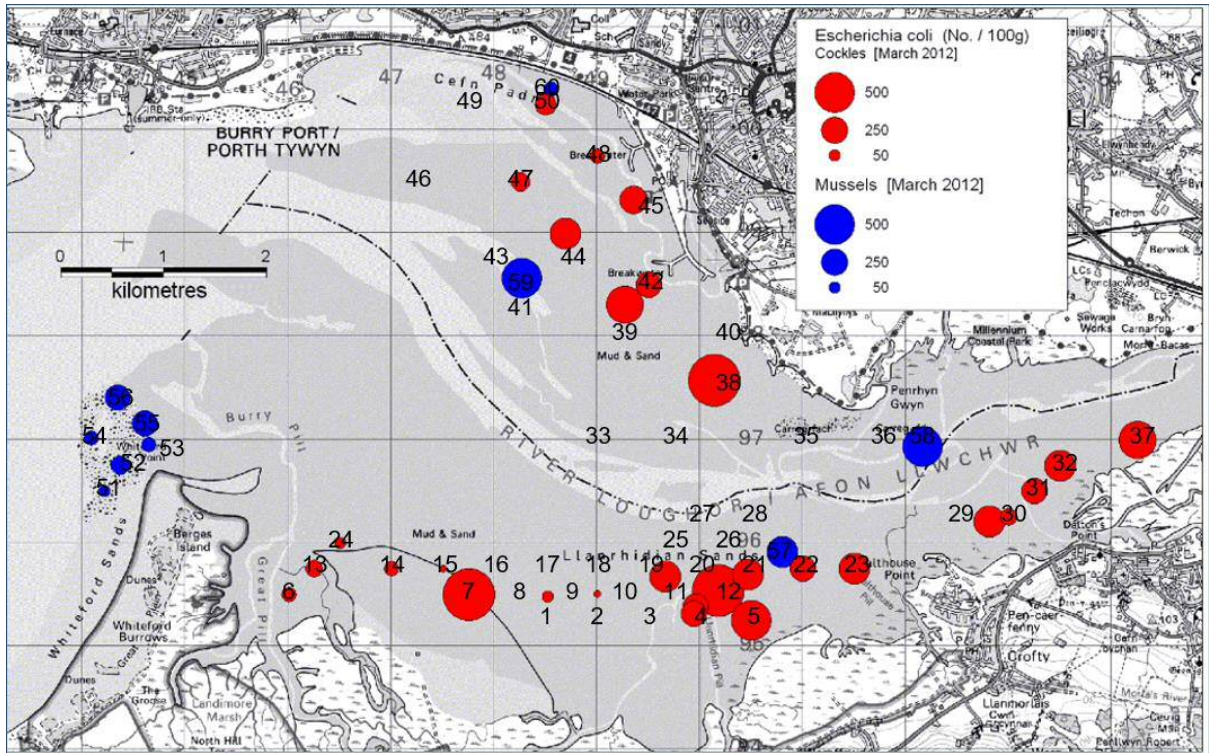
Figure 6.1: Locations of shellfish beds for cockle (i.e. site 1-50, ■) and mussel (i.e. site 51-60, ■), grazing area of the Llanrhidian Marsh (i.e. green area) and modelling observation points (i.e. site 1-91, ■) within the area of Loughor Estuary. Hydrodynamic observations at Burry Port and site 1076H, and water quality monitoring at Pembrey DSP and Broughton.

Results of the hygiene survey during March and October 2012 are shown in Figure 6.2 and 6.3 respectively, as the concentration distributions of faecal coliform (FC) and *E. coli* at the shellfish beds. The range of FC and *E. coli* concentrations during the October's sampling (i.e. FC: 50 – 18,000 cfu/100 ml) was relatively broad and more typical to the result obtained during routine monitoring programmes, as compared to the March's sampling (i.e. FC: 20 – 790

cfu/100 ml). This variability was due to lower bacterial contamination levels during the earlier sampling in March 2012 as compared to October 2012 (Youell *et al.* 2013a; Youell *et al.* 2013b). At BI South, the distribution concentrations of FC and *E. coli* during both sampling periods were at the tendency of increasing localised hot spots in the adjacent of Llanrhidian Marsh and Salthouse Pill. The combination of bacteriological inputs from trade discharges and historical land grazing activities were suggested as impacting this region.

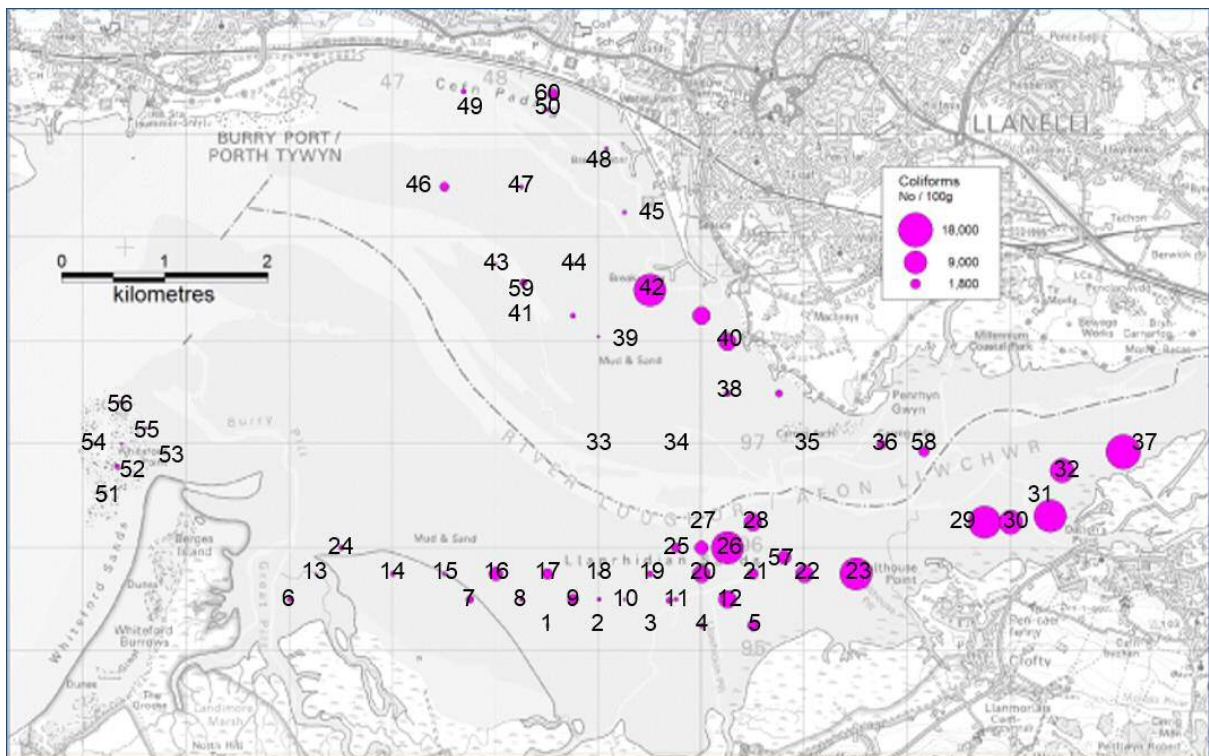


a) Faecal coliform (FC) concentrations at shellfish beds.

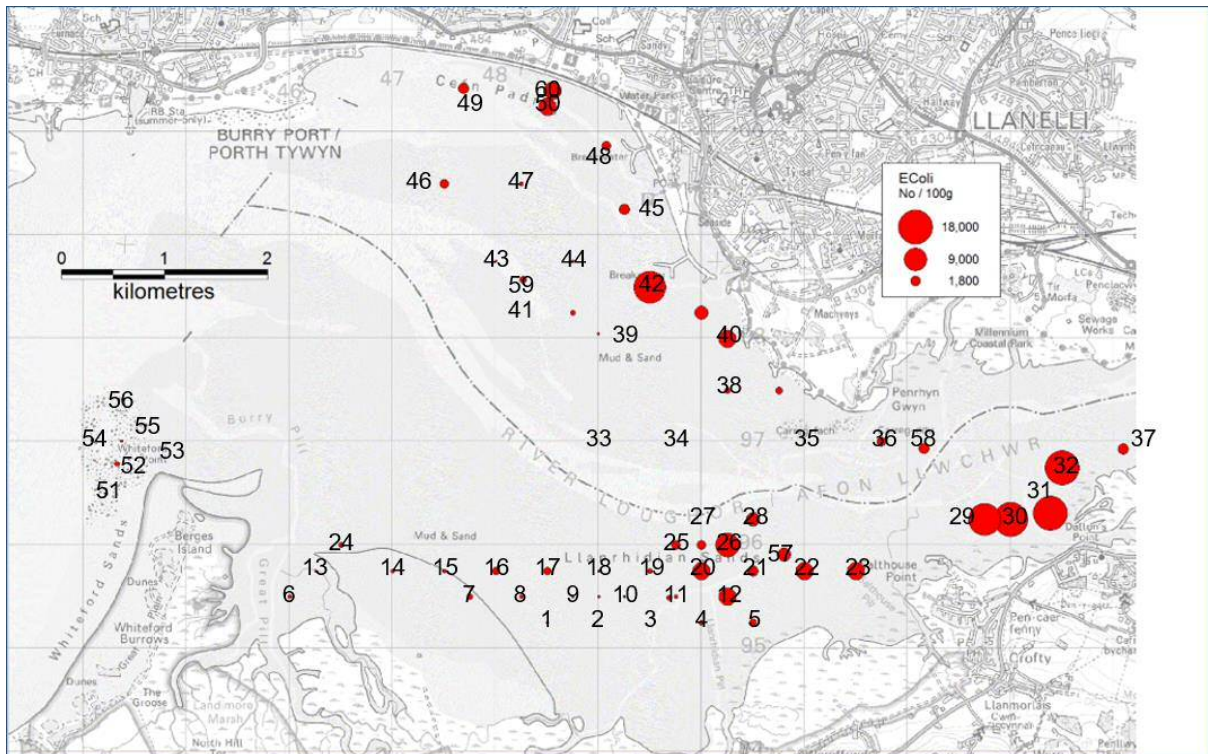


b) *E. coli* concentrations at shellfish beds.

Figure 6.2: Hygiene survey results of faecal coliform (FC) and *E. coli* for March 2012 that represented from 60 sampling stations, including 50 cockle beds and ten mussel beds (Youell *et al.* 2013a; Youell *et al.* 2013b).



a) Faecal coliform (FC) concentrations at shellfish beds.



b) E. coli concentrations at shellfish beds.

Figure 6.3: Hygiene survey results of faecal coliform (FC) and E. coli for October 2012 that represented from 60 sampling stations, including 50 cockle beds and ten mussel beds (Youell *et al.* 2013a; Youell *et al.* 2013b).

The historically grazing area of the Llanrhidian Marsh was an area of 12.05 km² that was flooded during high tides. The vegetation cover of numerous species within this marshland was shorter than other areas due to a heavily grazing activity by sheep and horses (Malki 2009). 91 observation sites were selected uniformly over the whole grazing area (see Figure 6.1) to assess the transport and decay behaviours of FIOs from the diffuse source and onto the shellfish beds, besides on the marshland retention capacity. This assessment was made reasonably correct provided that the hydrodynamic process at this very-shallow intertidal environment was accurately modelled based on the previous works (Chapters 4 and 5).

6.2.2 Loading deposition of FIOs

The FIOs loading from the domestic animal at the grazing marshland was calculated as a product between the population density, volume of manure and pathogen prevalence. Sheep were considered as the main domestic animal that grazed at the marshland during low tides,

while other animals including horses and wildlife were also inhabited this area. The population density of the sheep grazing at the marshland was assumed to be at the constant of 500 animal/km² based on the value reviewed by Ferguson *et al.* (2008). The manure production rate from this grazing animal was assumed to be at a constant of 1 kg/animal/day, also based on the value of literature. The *E. coli* was chosen to be modelled at the prevalence of 1.6×10^7 cfu/g based on the literature value for the UK. The *E. coli* loading from the grazing sheep at the marshland was modelled at the deposition rate of 3.33×10^5 cfu/m²/h.

The deposition of FIOs was modelled as the diffuse source that spatially and temporally distributed through the grazing area during drying periods. The grazing area was the exposed intertidal marshland between the water line of low tides and up to approximately 5 m elevation above the ODN. This exposed area was temporally evolved during tidal cycles as a result of modelling the wetting and drying process, with the maximum extension being approximately equal to 12.05×10^6 m² during low spring tides. The modelled of FIOs deposition at the exposed intertidal marshland during grazing periods was written using the equation as follows:

Eqn. 6.1

where (cfu/s) is the deposition rate of FIOs, (animal/km²) is the population density of grazing sheep, (kg/animal/day) is the manure production rate from this animal, (cfu/g) is the prevalence of *E. coli* in the manure, and (m²) is the exposed area of the grazing marshland.

The loading of FIOs at the exposed intertidal marshland during grazing periods was modelled as the build-up of a conservative mass without considering any losses and will be released into the water columns upon flooding by tides. It was based on the assumption that FIOs deposition was large enough relative to the losses by decay during drying periods (Schernewski *et al.* 2012). The balance of the build-up loading at the grazing marshland with the subsequent releasing was modelled using the differential equation that was written as follows:

— Eqn. 6.2

where λ (cfu/s) is the build-up loading of FIOs, and α (-) is the FIOs release coefficient from manures. The FIOs deposition was stopped upon flooding as the grazing animal escaped from the area at 10 cm water depth, with the event reoccur for the next tidal cycles at the same conditions. The FIOs loading was released at different rates depending on the application of release models.

6.2.3 Release-kinetic of FIO

The release of FIOs loading from the deposited manure upon flooding by tides was modelled in two releasing modes, which were as the instantaneous flushing (IF) (i.e. wash-off model by Sanders *et al.* (2005)), and with the consideration of two-parametric Bradford-Schijven (B-S) release-kinetic model (Bradford and Schijven 2002). The instantaneous flushing of FIOs was modelled as the surficial loading exchanges from the intertidal marshland and into the water columns by the moment of the grazing area being flooded. The FIOs build-up was released in total during a single computation time step when the irrigation depth of a computation node equal to h_{th} of 10 cm, with the release coefficient was idealised as functions that were written as follows:

Eqn. 6.3

where $\delta(t)$ is the Dirac delta function of time t and irrigation depth h , t_{th} (s) is the threshold of releasing time, and h_{th} (m) is the threshold of releasing depth, where α was also the function of irrigation depth.

The release of FIOs using the Bradford-Schijven (B-S) release-kinetic model was considered as the surficial loading exchanges from the intertidal marshland and into the water columns that was known to experience several processes controlled by the combination of physical, chemical and biological factors (Blaustein, Pachepsky, Shelton, *et al.* 2015). The exchange of surficial loading was modelled as the proportion between the temporal release and the total FIOs build-up from the flooded area, with the release coefficient was written as the function of the irrigation depth and fitting parameters as follows:

-

Eqn. 6.4

where d (m) is the irrigation depth, and k_1 (h^{-1}) and k_2 (-) are the fitting parameters that control the initial release rate and determines the shape of the release curve respectively.

The FIOs release was modelled with three threshold depths, i.e. of 1×10^{-3} , 1×10^{-2} and 1×10^{-1} m, and with the k_1 value of 0.1 was used for the vegetated and sandy loam surface (Guber *et al.* 2006). The fitting parameter k_2 was modelled as a linear relationship to the irrigation rate that was written as follows:

$$\text{---} \tag{Eqn. 6.5}$$

where I (m/s) is the irrigation rate for every computation time step, and 3.6×10^5 is the conversion factor from units of m/s to cm/h .

For modelling the release of FIOs from the deposited manure, the discharge rate of flooding at the grazing area was calculated as the input source for the release models of IF and B-S release-kinetic. The discharge rate was calculated as the product between the area of grazing that being flooded and the changes in irrigation rates during computation time steps that were written as follows:

$$\text{---} \tag{Eqn. 6.6}$$

where Q is the discharge rate (m^3/s), and A (m^2) is the flooding area of the grazing marshland.

The discharge rate calculated for the release models was applied in different ways depending on the conditions of releasing. For the B-S release-kinetic model, the discharge rate was applied as the continuous series of computation with the minimum value of irrigation depth being set at 1×10^{-6} m. For the release model of IF, the discharge rate was only applied during a single computation time step when the irrigation depth of a computation node equal to of 10 cm, with the irrigation rate was idealised as functions that were written as follows:

$$\text{---} \tag{Eqn. 6.7}$$

where $\delta(t)$ is the Dirac delta function of time t and irrigation depth d , and t (s) and d (m) are the same parameters used in Equation 6.3.

Besides the discharge rate of flooding at the grazing area, the concentration of FIOs was also calculated as the input source for modelling its releases from the deposited manure, using both the IF and B-S release-kinetic models. The FIOs concentration was calculated as the division between its release rate and the discharge rate of flooding during computation time steps that were written as follows:

$$\text{-----} \quad \text{Eqn. 6.8}$$

where C (cfu/ml) is the concentration of FIOs, and R (cfu/s) is the FIOs release rate. Depending on the conditions of release models, the concentration of FIOs was calculated differently between the models of IF and B-S release-kinetic. The releasing rate of FIOs loading from the grazing marshland upon flooding then was modelled based on the calculation of its concentration and the discharge rate of flooding.

6.2.4 Transport and decay of FIO

The shallow water equations have been solved for the surface elevation and current flow patterns using the finite element method. The continuity and momentum conservation equations were solved respectively as written in the following form:

$$\text{---} \quad \text{Eqn. 6.9}$$

$$\text{---} \quad \text{---} \quad \text{---} \quad \text{---} \quad \text{and} \quad \text{Eqn. 6.10}$$

where h (m) is the water depth, and u, v (m/s), $i = 1, 2$ are the two components of the horizontal velocity, g (m/s^2) is the gravitational acceleration, z (m) is the surface elevation, Q (m^3/s) is the source/sink of water inputs, u, v (m/s^2), $i = 1, 2$ are the two components of

source/sink of horizontal momentum including the bottom friction parameter, and ν (m²/s) is the eddy with molecular viscosities of water that calculated from the turbulence closure model.

From the calibration of the transport model in Section 5.4.1, the microbial tracer was used to validate the model hydrodynamics and roughness values at floodplains. Four scenarios of variable bottom roughness at floodplains resulted in a significant reduction in the tracer concentration at tidal flats and marshlands with the changes of roughness from uniform to severe. This microbial tracer, however, was inadequate in justifying specific roughness values for each friction zones due to the lack of observations of their concentrations at floodplains.

For the purpose of studying the transport of FIOs from the intertidal marshland as a diffuse source, the scenario of moderate bottom roughness at floodplains was further considered at the study area of Loughor Estuary. The Manning's values used at the friction sub-domains with the moderate scenario were 0.025 for the subtidal channel, 0.030 for the intertidal channel, 0.035 for the tidal flat and 0.060 for the marshland (Table 4.1). This scenario was considered the most appropriate condition for the floodplains of the study area as compared to the bottom roughness values used in the literature (see Figure 6.4). The used values were at the maximum difference of -33.33% from the value used by French (2003) for the marshland, and at the minimum difference of +14.29% from the values used by Lawrence *et al.* (2004), Cea and French (2012) and Azinheira *et al.* (2014) for the tidal flat. Besides, the used values for the subtidal channel, the intertidal channel and the tidal flat were identical with the values used by Bilskie *et al.* (2015).

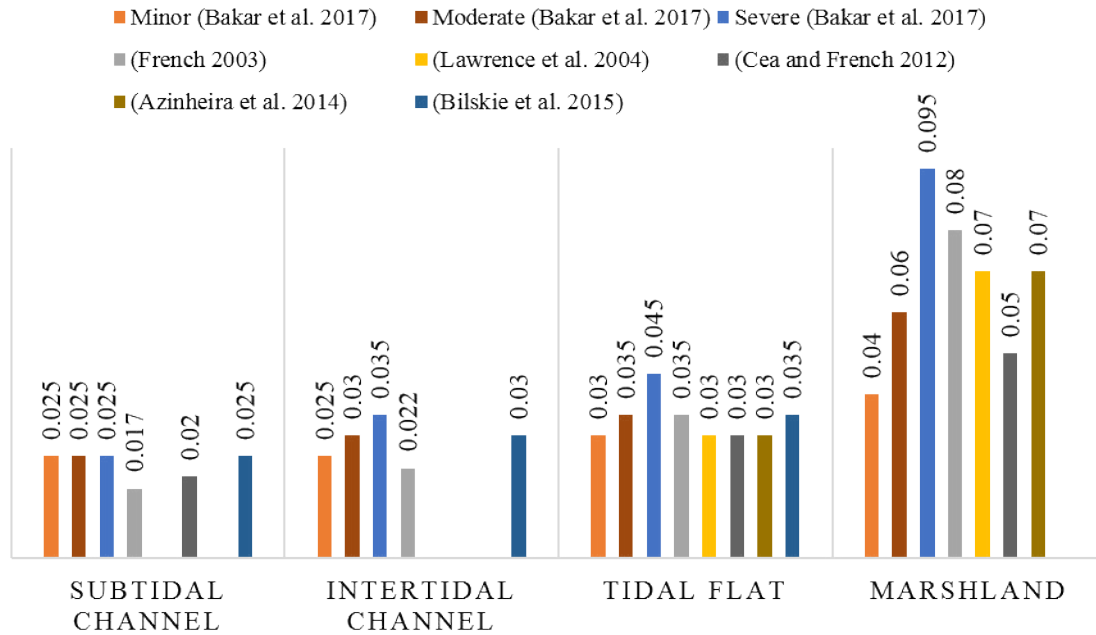


Figure 6.4: The Manning's values used at the friction sub-domains of Loughor Estuary based on Bakar *et al.* (2017) as compared to the values from the literature.

The catchment inflow of 40% was used as the source of water volume to the continuity equation (Equation 6.9). This percentage was based on the sensitivity analysis conducted on the transport of salinity (Figures D.1(a-d) and Table D.6), that was based on the measured conditions during the microbial tracer release experiment from 8th until 10th October 2014 (Section 5.2).

The depth-averaged mass transport equation has been solved to model the FIOs transport using the finite volume method, in order to ensure the conservation of mass. The FIOs transport equation was solved for with the inclusion of a first-order kinetic decay rate and was written as follows:

$$\frac{\partial C}{\partial t} + \frac{\partial}{\partial x} (u C) - \frac{\partial}{\partial x} (E \frac{\partial C}{\partial x}) - K C = 0 \tag{Eqn. 6.11}$$

where C (cfu/ml) is the FIOs concentration, E (m^2/s) is the FIOs dispersion coefficient, u (m/s) is the FIOs decay rate, which is also expressed as the T_{90} value (Equation 5.6), giving the equivalent time required for the inactivation of 90% from the total FIOs count.

Based on the calibration of the transport model (Section 5.4.1), the value of E was used at the constant of $1 \times 10^{-10} m^2/s$ (Chapra 2008) with the application of the k-epsilon turbulence

closure model. This value at the molecular diffusivity level was used with regard to the role of the turbulence closure model that was for modelling the longitudinal dispersion of estuarine eddy diffusivity.

The transport of FIOs was modelled in two scenarios, either as the conservative or nonconservative mass. The conservative mass scenario was considered to benchmarking the FIOs transport process solely without considering the decay effect. In the natural estuarine environment, the FIOs, however, was experienced the decay process as they were transported within the waterbody. For modelling this process, a constant decay rate of T_{90} at 14.9 hours was considered. This value was based on the findings from the field experiment by Kay *et al.* (2005) and the modelling work by Bermúdez *et al.* (2014). Although the findings also suggested the day-night decay rates of T_{90} -day at 7.7 hours and T_{90} -night at 25 hours, these values were not further tested. This decision was made based on the assumption that the idealised *E. coli* loading of 3.33×10^5 cfu/m²/h (Section 6.2.2) was at the minimum level to produce an identical difference between the two cases (i.e. constant and day-night decays) while they were transported.

6.2.5 Shellfish exposure to FIOs

The transported FIOs in the water columns that exposed to the shellfish flesh at their beds north of the grazing marshland was modelled as the exposure time and exposure severity with the consideration of dynamic accumulation and depuration processes by this filter-feeder. The filter-feeder was considered to expose with the FIOs at the threshold concentration, C_{300} of 300 cfu/100 ml following the guideline standard of Shellfish Waters Directive (2006/113/EC) (Kay *et al.* 2008). The exposure time of filter-feeders to the FIOs was modelled as the increment and decrement in the computation time step respectively when the ambient FIOs concentration was exceeded and lowered than the C_{300} threshold. The increment in the time step being modelled as for idealising the FIOs accumulation process in the shellfish flesh when the ambient FIOs concentration was exceeded the C_{300} threshold, and vice versa for idealising the FIOs depuration process from the shellfish flesh. The piecewise function of the FIOs exposure time to the shellfish flesh was written as follows:

Eqn. 6.12

where t_n (s) and t_{n-1} (s) are the exposure time at current and previous computation time steps respectively, Δt (s) is the computation time step, C_a (cfu/ml) is the ambient FIOs concentration, and C_{th} (cfu/ml) is the threshold concentration of FIOs exposure.

The exposure severity of filter-feeders to the FIOs was modelled along with modelling the exposure time for this species that considered the accumulation and depuration processes. The exposure severity idealising the FIOs accumulation in the shellfish flesh was modelled as the increment in the exposure time with the magnitude of ambient FIOs concentration as this concentration value exceeding the C_{th} threshold. Conversely, the exposure severity idealising the FIOs depuration from the shellfish flesh was modelled as the decrement in the exposure time with the magnitude of the concentration gradient between the ambient FIOs and the C_{th} threshold, as this concentration value lowered than the C_{th} threshold. The assumption was made that the shellfish will equalise the FIOs in the flesh to the ambient concentration during depuration. The piecewise function of FIOs exposure severity to the shellfish flesh was written as follows:

Eqn. 6.13

where S_n (cfu/ml*s) and S_{n-1} (cfu/ml*s) are the exposure severity at current and previous computation time steps respectively.

6.2.6 Statistical analyses

Four statistical variables were used as the standard set of measures in this modelling work for evaluating performances of the developed model. The mean error (ME) was the mean difference between observed and predicted values, where the zero value indicated the ideal model, while the nonzero value indicated the bias model towards overprediction (i.e. negative ME) or underprediction (i.e. positive ME). The ME was calculated as follows:

—

Eqn. 6.14

where n is the number of observation-prediction pairs, y_i is the value of i -th observed data, and \hat{y}_i is the value of i -th predicted data.

The mean absolute error (MAE) was the mean absolute value of the differences between observed and predicted values, where the magnitude indicated the average deviation between both values and eliminated the cancelling effects of positive or negative errors. The MAE was calculated as follows:

$$\text{MAE} = \frac{1}{n} \sum_{i=1}^n |y_i - \hat{y}_i| \quad \text{Eqn. 6.15}$$

The root-mean-square error (RMSE) (i.e. standard deviation) was the average of the squared differences between observed and predicted values, and a weighted equivalent to MAE (i.e. larger weightings from larger observation-prediction differences), with the zero value, indicated the ideal model. The RMSE was calculated as follows:

$$\text{RMSE} = \sqrt{\frac{1}{n} \sum_{i=1}^n (y_i - \hat{y}_i)^2} \quad \text{Eqn. 6.16}$$

The relative error (RE) was the ratio of the MAE to the observed mean, provided the sense of how well the prediction compared to the observed mean, with the observation-prediction discrepancy was expressed as the percentage. The RE was calculated as follows:

$$\text{RE} = \frac{\text{MAE}}{\bar{y}} \quad \text{Eqn. 6.17}$$

where \bar{y} is the observed mean.

The relative RMS error (RRE) was the ratio of RMS error to the observed change, that overcomes the false prediction accuracy as the very large mean values of some state variables may lead to unacceptable prediction errors. The RRE was calculated as follows:

$$\text{RRE} = \frac{\text{RMSE}}{\Delta y} \quad \text{Eqn. 6.18}$$

where \bar{O}_{max} and \bar{O}_{min} respectively are the maximum and minimum values of observations.

The statistical analyses for the FIOs mass balance were conducted, with respective variables from the B-S release-kinetic model of different \bar{O} as the predicted parameter and were compared to respective variables from the IF release model of $\bar{O} \geq 10^{-1}$ m as the observed parameter.

6.3 Results and discussion

6.3.1 Hydrodynamic validation

The developed hydro-environmental model has been calibrated for the hydrodynamic process over the SEBC (Section 3.4), with the predicted surface elevation and tidal current using the refined domain were validated at Burry Port and site 1076H respectively (Section 5.3.1). The validated surface elevation during the spring tidal condition was compared well with the measured data (see Figures 5.4 and 5.5). The validated tidal current although in a good correlation with the measured data, was underpredicted the maximum value by 0.5 m/s during ebb tides (see Figure 5.4). Considering this issue, the flow model could reduce the transport rate of FIOs during the flushing process. The measured current for site 1076H, however, was obtained from the Admiralty Chart 1167 that were surveyed during the year 1977, which might not represent the real condition during the validation period. The estuary was also experienced the active bed morphological changes, with the sediment accretion has narrowed the BI mouth between years 1876 and 2000 (Elliott, Burdon, Callaway, Franco, Hutchinson, Longshaw, Malham, Mazik, Otto, Palmer, Firmin, *et al.* 2012). Hence the underprediction of the maximum current during ebb tides near the validation site should be expected. The validated tidal current has also characterised this estuary with a standing wave and its lower subtidal channel with the ebb current dominant.

6.3.2 FIOs loading deposition

Figure 6.5 depicts the modelled time series of the FIOs loading deposition () in relation to the irrigation depth () at a test node during the first tidal cycle. The loading deposition was calculated at 1.62×10^7 cfu/dt for every time step during the period of 1.49 hours from the

beginning of the simulation. The loading deposition then was stopped at 280.0619 JD after the irrigation depth at the test node was exceeded the value of 10 cm. The loading deposition for the from equal or greater than 1×10^{-3} m to 1×10^{-1} m based on the B-S release-kinetic model, and equal or greater than 1×10^{-1} m based on the IF model were stopped at the same time as the irrigation depth from both models were produced an identical result.

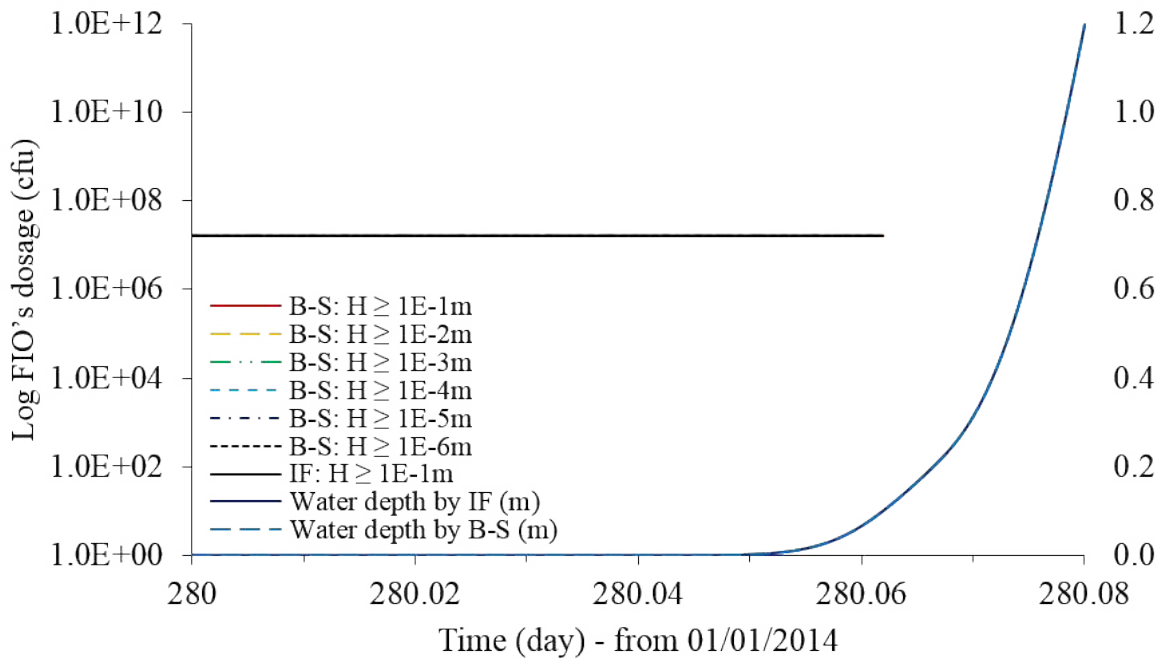


Figure 6.5: Time series of the FIOs loading deposition () at different releasing depths based on the B-S and IF release models.

6.3.3 FIOs release modelling

6.3.3.1 Case 1: Release modelling at a node scale

The result of the fitting parameter () in relation to the irrigation rate () is depicted in Figure 6.6 as the modelled time series at the test node during the first tidal cycle. From the B-S release-kinetic model, the parameter for the equal or greater than 1×10^{-3} m was begun the earliest at 280.0488 JD with the lowest value of 1.94 h^{-1} . The parameter for the equal or greater than 1×10^{-2} m was followed at 280.0539 JD with the increasing values of $1.37 \times 10^1 \text{ h}^{-1}$. The parameter for the equal or greater than 1×10^{-1} m was the highest with the value of $6.95 \times 10^1 \text{ h}^{-1}$ that began the latest at 280.0619 JD. The time series

of the parameter α for different H based on the B-S release-kinetic model were increased in a similar profile as the irrigation rate was gradually increased during the flooding period. The values of the fitting parameter α at different H with different releasing times are shown as in Table 6.1.

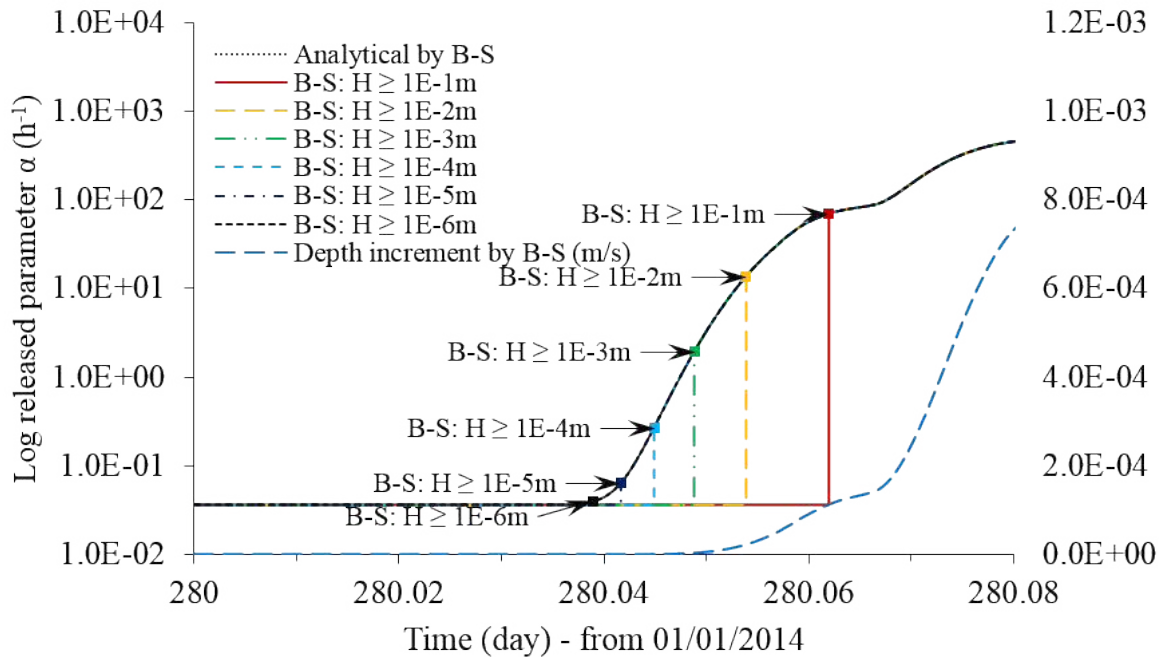


Figure 6.6: The time series of the fitting parameter (α) at different releasing depths based on the B-S release-kinetic model.

Table 6.1: The values of the fitting parameter (α) at different releasing depths with different releasing times.

Threshold depth, H (m)	Release time (JD)	Fitting parameter, α (h^{-1})
B-S: $H \geq 1 \times 10^{-1}$	280.0619	6.95×10^1
B-S: $H \geq 1 \times 10^{-2}$	280.0539	1.37×10^1
B-S: $H \geq 1 \times 10^{-3}$	280.0488	1.94

The result of the FIOs release coefficient (α) in relation to the irrigation depth (H) is depicted in Figure 6.7 as the modelled time series at the test node during the first tidal cycle. From the B-S release-kinetic model, the release coefficient for the H equal or greater than 1×10^{-3} m was begun the earliest at 280.0488 JD with the lowest value of 8.31×10^{-1} . The release coefficient for the H equal or greater than 1×10^{-2} m and 1×10^{-1} m respectively were

the highest with the value of 1.00 that began at 280.0539 JD and 280.0619 JD. The time series of the release coefficient for different based on the B-S release-kinetic model were increased in a similar profile as the irrigation depth was gradually increased during the flooding period. The values of the FIOs release coefficient at different with different releasing times are shown as in Table 6.2.

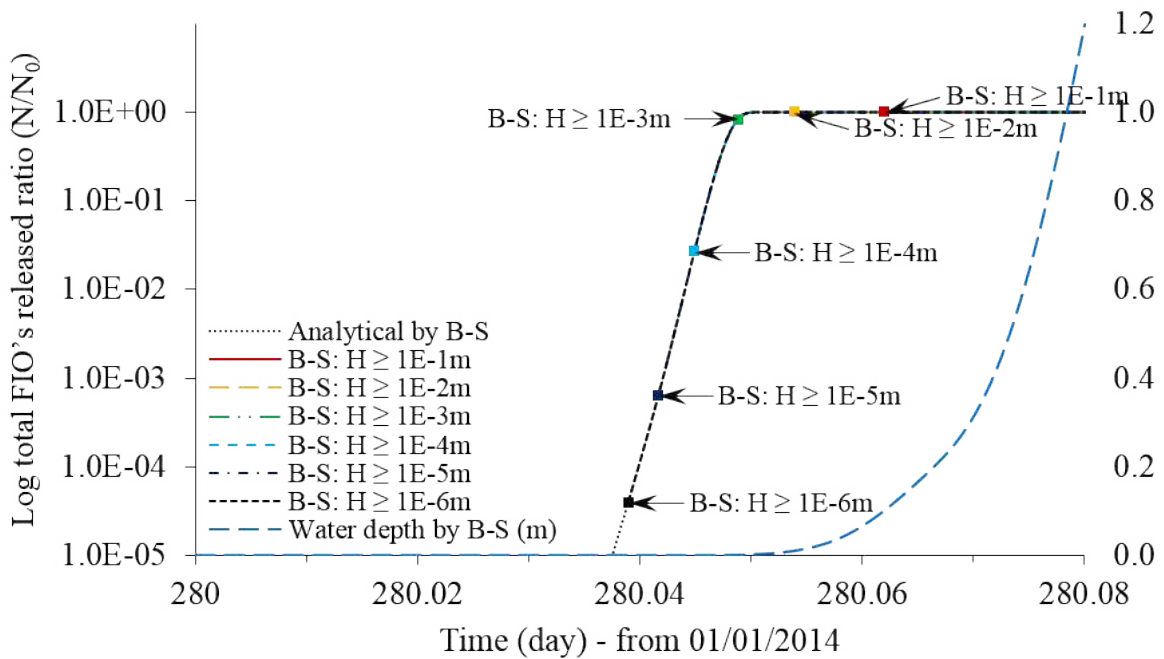


Figure 6.7: The time series of the FIOs release coefficient () at different releasing depths based on the B-S release-kinetic model.

Table 6.2: The values of the FIOs release coefficient () at different releasing depths with different releasing times.

Threshold depth, H (m)	Release time (JD)	Release coefficient,
B-S: $H \geq 1 \times 10^{-1}$	280.0619	1.00
B-S: $H \geq 1 \times 10^{-2}$	280.0539	1.00
B-S: $H \geq 1 \times 10^{-3}$	280.0488	8.31×10^{-1}

The result of the flooding discharge rate () in relation to the irrigation rate () is depicted in Figure 6.8 as the modelled time series at the test node during the first tidal cycle. From the B-S release-kinetic model, the discharge rate for the from equal or greater than 1×10^{-3} m to 1×10^{-1} m were begun the same at 280.0380 JD with the value of $3.0 \times 10^{-3} \text{ m}^3/\text{dt}$, as

the minimum value of irrigation depth was set at 1×10^{-6} m. For the IF release model, the discharge rate with the of 10 cm was occurred at 280.0619 JD with the value of $7.0 \times 10^1 \text{ m}^3/\text{dt}$. The time series of the discharge rate for different based on the B-S release-kinetic model were increased in a similar profile as the irrigation rate was gradually increased during the flooding period.

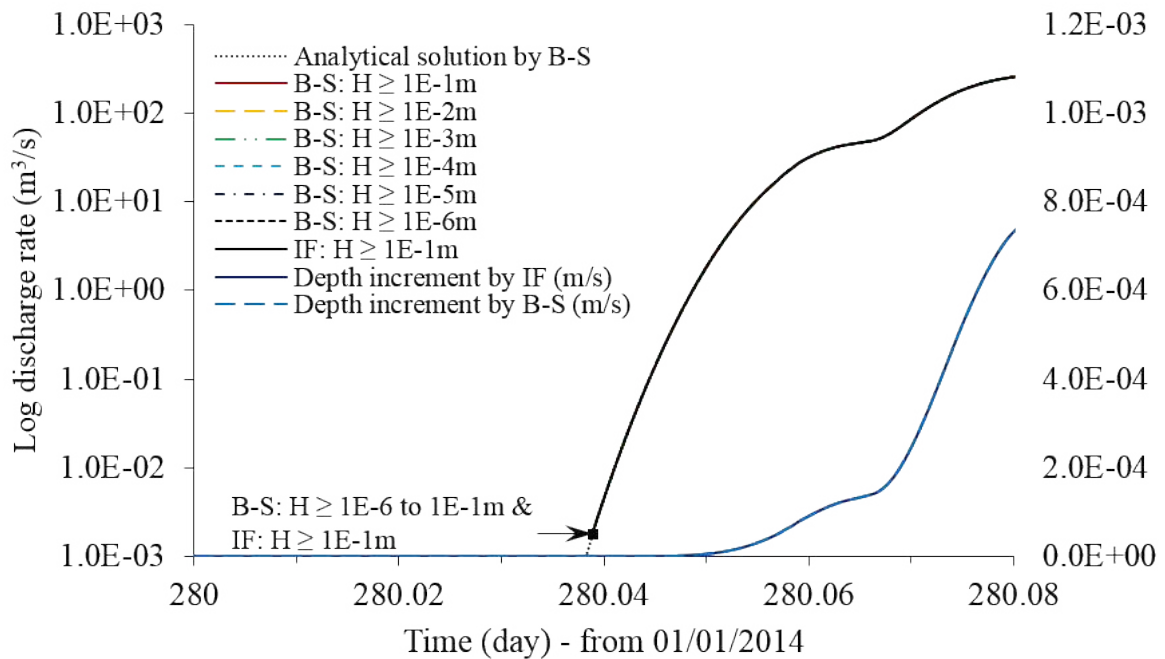


Figure 6.8: The time series of the flooding discharge rate () at different releasing depths based on the B-S and IF release models.

The result of the FIOs release concentration () in relation to the irrigation rate () is depicted in Figure 6.9 as the modelled time series at the test node during the first tidal cycle. From the B-S release-kinetic model, the release concentration for the equal or greater than 1×10^{-3} m was the highest with the value of 1.06×10^5 cfu/ml that began at 280.0488 JD before merged to the analytical solution at 280.0489 JD with the value of 1.45×10^1 cfu/ml. The release concentration for the equal or greater than 1×10^{-2} m was begun at 280.0539 JD with the lower value of 1.95×10^4 cfu/ml before merged to the analytical solution at 280.0539 JD with the value of 2.09 cfu/ml. For the release concentration with the equal or greater than 1×10^{-1} m, both from the B-S and IF release models have occurred the same at 280.0619 JD with the value of 4.42×10^3 cfu/ml. The time series of the release concentration based on the B-S release-kinetic model that began earlier were also stopped at

280.0619 JD with the value of 4.13×10^{-1} cfu/ml. The values of the FIOs release concentration at different releasing times are shown as in Table 6.3.

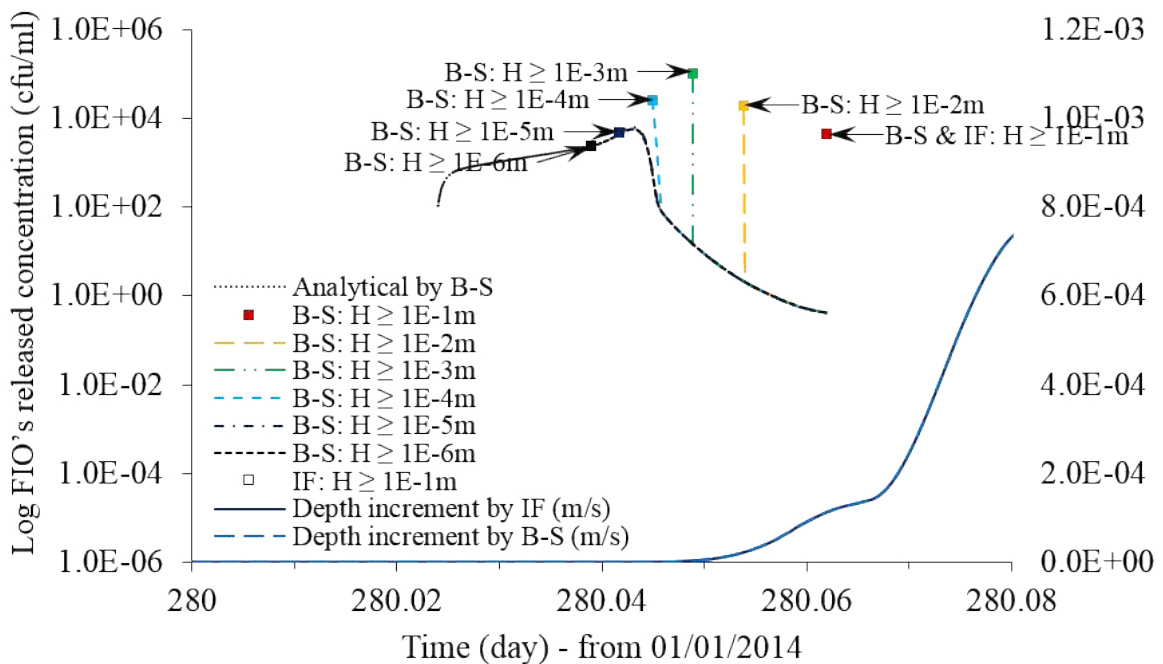


Figure 6.9: The time series of the FIOs release concentration () at different releasing depths based on the B-S and IF release models.

Table 6.3: The values of the FIOs release concentration () at different releasing depths with different releasing times.

Threshold depth, H (m)	Release time (JD)	Release concentration, (cfu/ml)
B-S: $H \geq 1 \times 10^{-1}$	280.0619	4.42×10^3
B-S: $H \geq 1 \times 10^{-2}$	280.0539	1.95×10^4
B-S: $H \geq 1 \times 10^{-3}$	280.0488	1.06×10^5

The released percentage of total FIO at different releasing depths based on the B-S and IF release models were plotted against the water depth in Figure 6.10. As the B-S release model was applied at between 1×10^{-3} m and 1×10^{-1} m, the plot was extended to of 1×10^{-6} m in order to understand the release impact based on this condition. The designed release was included based on Equation 6.4 for observing the model limitation. The released of FIO at of 1×10^{-1} m was at 100% in a single time step. The released of FIO at

of 1×10^{-2} m was begun at 87.16%, at 12.84% lower than the designed release. The released of FIO at 1×10^{-3} m was begun at 65.81%, at 25.06% higher than the designed release. The FIO was constantly released at 0.01% following the initial release at the rate of FIO deposition. The released of FIO at lower than 1×10^{-3} m was overloading the mass into the waterbody as compared to the designed release.

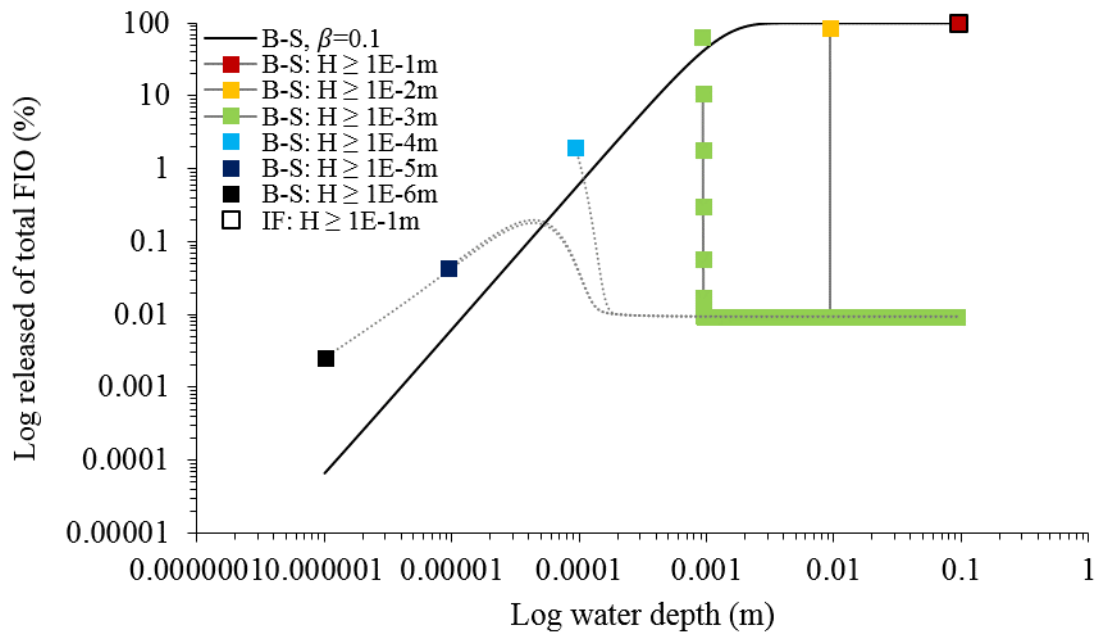


Figure 6.10: Percentage of total FIO released at different releasing depths based on the B-S and IF release models. The black-solid line indicates the designed release at the node with $\beta = 0.1$.

The lost percentage of FIO mass at different releasing depths based on the B-S and IF release models were plotted against the water depth in Figure 6.11. The plots were extended to 1×10^{-6} m in order to understand the released impact based on this condition. Two groups of mass loss were observed from the plots, with the lost through releasing was many times higher than the lost through transport. The lost through releasing was copying trends of the released mass as in Figure 6.8. Overall, the mass loss was observed below 1% of the released mass, with the lost at 1×10^{-1} m was at an average of $1 \times 10^{-14}\%$.

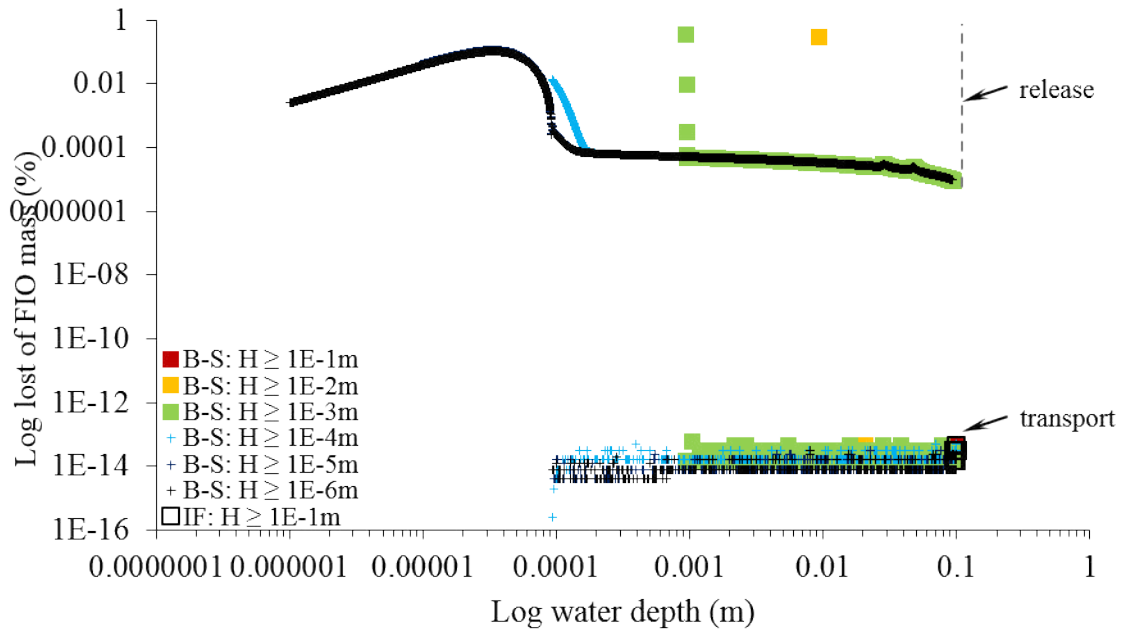


Figure 6.11: Percentage of FIO mass lost at different releasing depths based on the B-S and IF release models.

The result of the FIOs mass balance based on the numerical computation is depicted in Figure 6.12 as the modelled time series at the test node during the first-four tidal cycles. From the IF release model and during the first tidal cycle, the mass balance for the equal or greater than 1×10^{-1} m was levelled at 280.0616 JD with the value of 9.07×10^{10} cfu. With the average mass increment of 2.58×10^{11} cfu for every tidal cycle, the mass balance during the fourth tidal cycle was levelled at 281.5880 JD with the value of 8.64×10^{11} cfu. The highest mass increment was between the third and the fourth tidal cycles with the value of 2.64×10^{11} cfu, and the lowest was between the first and the second tidal cycles with the value of 2.50×10^{11} cfu. The values of the FIOs mass balance that levelled at different tidal cycles with different mass increments are shown as in Table 6.4.

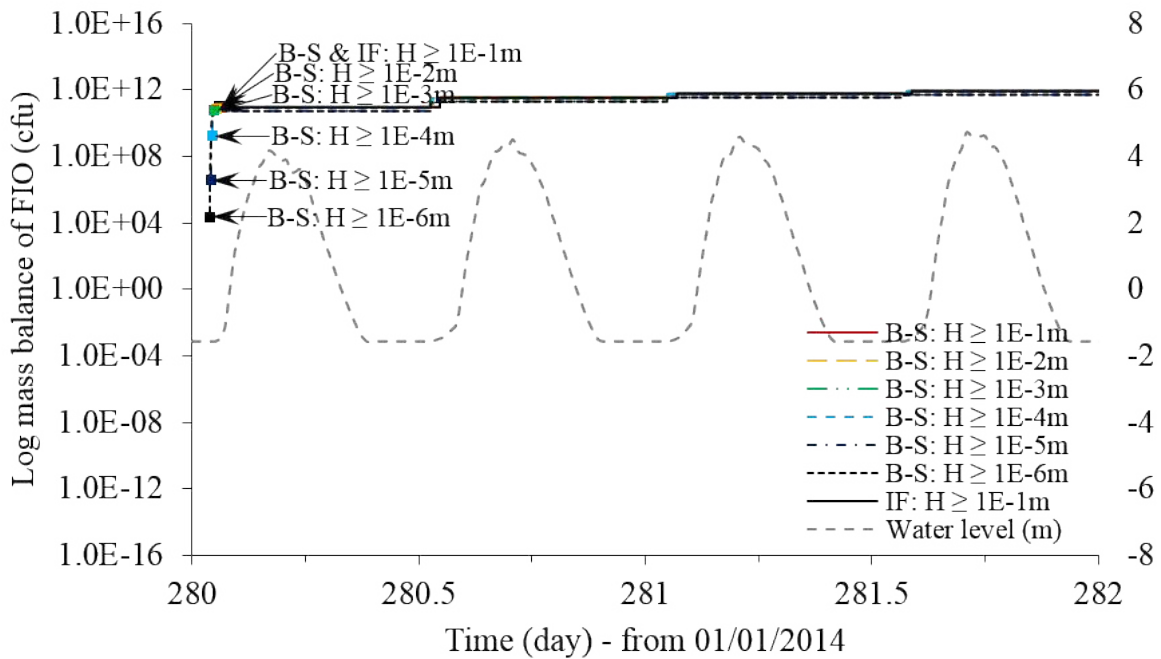


Figure 6.12: The time series of the FIOs mass balance at different releasing depths based on the B-S and IF release models.

Table 6.4: The values of the FIOs mass balance from the IF release model with the releasing depth equal or greater than 1×10^{-1} m that levelled at different tidal cycles with different mass increments.

	Mass balance (initial)		
	Time (JD)	Level (cfu)	Difference (cfu)
Cycle no. 1	280.0616	9.07×10^{10}	2.50×10^{11} 2.59×10^{11} 2.64×10^{11}
Cycle no. 2	281.5468	3.40×10^{11}	
Cycle no. 3	281.0697	6.00×10^{11}	
Cycle no. 4	282.5880	8.64×10^{11}	

Table 6.5 shows the result of the statistical analyses for the FIOs mass balance at the test node. No differences were observed in the mass balance between the B-S and IF release models for the equal or greater than 1×10^{-1} m. From the B-S release-kinetic model, the mass balance for the equal or greater than 1×10^{-2} m and 1×10^{-3} m were overpredicted, with the highest overprediction was from the equal or greater than 1×10^{-3} m with the ME of -5.97×10^9 cfu. The errors between the observed and predicted mass balance were increased from the equal or greater than 1×10^{-2} m to the equal or greater

than 1×10^{-3} m, with the highest error was from the equal or greater than 1×10^{-3} m with the MAE of 8.59×10^9 cfu (RE=1.87%) and the RMSE of 4.20×10^{10} cfu (RRE=5.43%).

Table 6.5: The result of the statistical analyses for the FIOs mass balance at the test node.

H (m)	$\geq 1 \times 10^{-1}$	$\geq 1 \times 10^{-2}$	$\geq 1 \times 10^{-3}$
ME (cfu)	0.00	-5.25×10^9	-5.97×10^9
MAE (cfu)	0.00	6.44×10^9	8.59×10^9
RE (%)	0.00	1.41	1.87
RMSE (cfu)	0.00	3.79×10^{10}	4.20×10^{10}
RRE (%)	0.00	4.91	5.43

6.3.3.2 Case 2: Release modelling at the marshland scale

The result of the FIOs release rate, i.e. the product between its release concentration () and the flooding discharge rate (), is depicted in Figure 6.13 as the modelled time series at the grazing marshland during the first-four tidal cycles. From the B-S release-kinetic model and during the first tidal cycle, the release rate for the from equal or greater than 1×10^{-3} m to 1×10^{-1} m was at the average of 1.08×10^8 cfu/dt, with the release rate for the equal or greater than 1×10^{-1} m was lower at the average of 6.79×10^7 cfu/dt. During the second-to-fourth tidal cycles, the release rate for the from equal or greater than 1×10^{-3} m to 1×10^{-1} m was at the average of 2.72×10^8 cfu/dt, with the release rate for the equal or greater than 1×10^{-1} m was higher at the average of 2.75×10^8 cfu/dt.

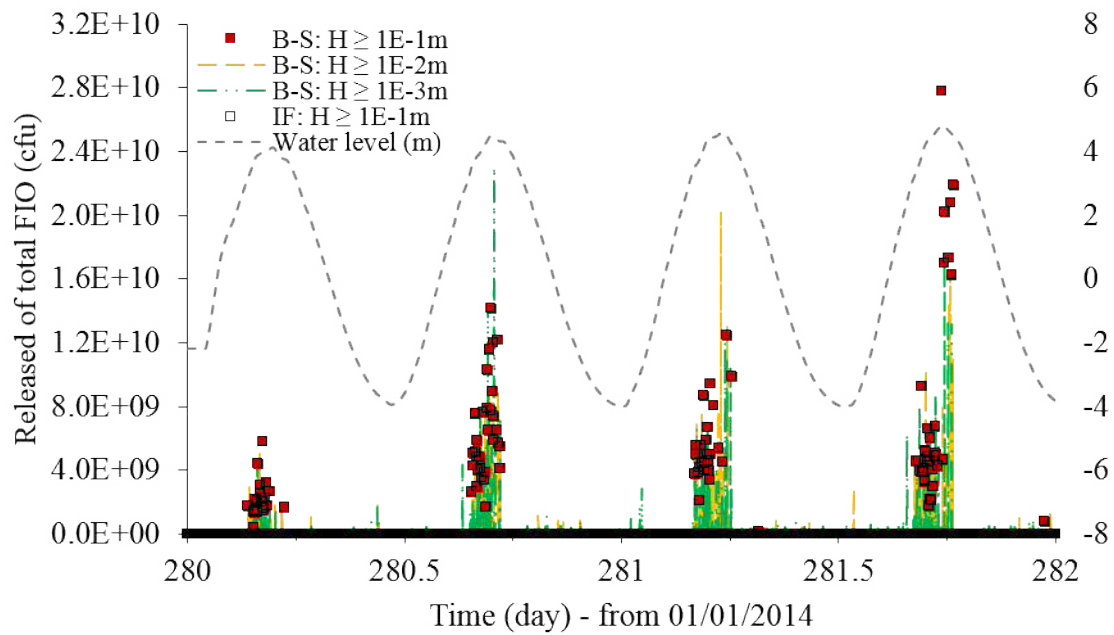


Figure 6.13: The time series of the FIOs release mass at different releasing depths based on the B-S and IF release models.

Table 6.6 shows the result of the statistical analyses for the FIOs release rate at the grazing marshland during the first tidal cycle. No differences were observed in the release rate between the B-S and IF release models for the equal or greater than 1×10^{-1} m. This was due to the release at this water depth was occurred at the same time step. From the B-S release-kinetic model, the release rate for the equal or greater than 1×10^{-2} m and 1×10^{-3} m were underpredicted, with the highest underprediction was from the equal or greater than 1×10^{-2} m with the ME of 3.97×10^7 cfu/dt. The underprediction at of 1×10^{-2} m was expected due to the lower FIO released as compared to the designed (see Figure 6.10). However, the underprediction at of 1×10^{-3} m was expected due to the higher FIO lost as compared to the lost at of 1×10^{-1} m (see Figure 6.11). The errors between the observed and predicted release rate were decreased from the equal or greater than 1×10^{-2} m to the equal or greater than 1×10^{-3} m, with the lowest error was from the equal or greater than 1×10^{-3} m with the MAE of 1.43×10^8 cfu/dt (RE=211%) and the RMSE of 5.20×10^8 cfu (RRE=8.96%). This statement agrees with the abovementioned reasons.

Table 6.6: The result of the statistical analyses for the FIOs release rate at the grazing marshland during the first tidal cycle.

H (m)	$\geq 1 \times 10^{-1}$	$\geq 1 \times 10^{-2}$	$\geq 1 \times 10^{-3}$
ME (cfu)	0.00	3.97×10^7	3.59×10^7
MAE (cfu)	0.00	1.45×10^8	1.43×10^8
RE (%)	0.00	2.13×10^2	2.11×10^2
RMSE (cfu)	0.00	5.80×10^8	5.20×10^8
RRE (%)	0.00	10.0	8.96

Table 6.7 shows the result of the statistical analyses for the FIOs release rate at the grazing marshland during the second-to-fourth tidal cycles. No differences were observed in the release rate between the B-S and IF release models for the equal or greater than 1×10^{-1} m as it occurred at the same time step. From the B-S release-kinetic model, the release rate for the equal or greater than 1×10^{-2} m and 1×10^{-3} m were overpredicted, with the highest overprediction was from the equal or greater than 1×10^{-2} m with the ME of -3.04×10^7 cfu/dt. This condition should be further investigated as the representation of results was in the opposite way as compared to the FIO release during the first tidal cycle (see Table 6.6). The MAE and RMSE between the observed and predicted release rate were decreased from the equal or greater than 1×10^{-2} m to the equal or greater than 1×10^{-3} m, respectively with the lowest error was from the equal or greater than 1×10^{-3} m with the MAE of 4.29×10^8 cfu/dt (RE=156%) and with the RMSE of 1.80×10^9 cfu (RRE=6.47%). This statement agrees with the above.

Table 6.7: The result of the statistical analyses for the FIOs release rate at the grazing marshland during the second-to-fourth tidal cycles.

H (m)	$\geq 1 \times 10^{-1}$	$\geq 1 \times 10^{-2}$	$\geq 1 \times 10^{-3}$
ME (cfu)	0.00	-3.04×10^7	-1.33×10^7
MAE (cfu)	0.00	4.35×10^8	4.29×10^8
RE (%)	0.00	1.58×10^2	1.56×10^2
RMSE (cfu)	0.00	1.94×10^9	1.80×10^9
RRE (%)	0.00	6.98	6.47

The result of the FIOs mass lost based on the numerical computation is depicted in Figure 6.14 as the modelled time series at the grazing marshland with the conservative mass during the first-four tidal cycles. From the B-S release-kinetic model and during the first tidal cycle, the

mass loss for the from equal or greater than 1×10^{-3} m to 1×10^{-1} m was at the average of 4.35×10^4 cfu/dt, with the mass loss for the equal or greater than 1×10^{-1} m was lower at the average of 5.86×10^2 cfu/dt. During the second-to-forth tidal cycles, the mass loss for the from equal or greater than 1×10^{-3} m to 1×10^{-1} m was at the average of 1.03×10^5 cfu/dt, with the mass loss for the equal or greater than 1×10^{-1} m was lower at the average of -2.45×10^3 cfu/dt (i.e. gaining mass).

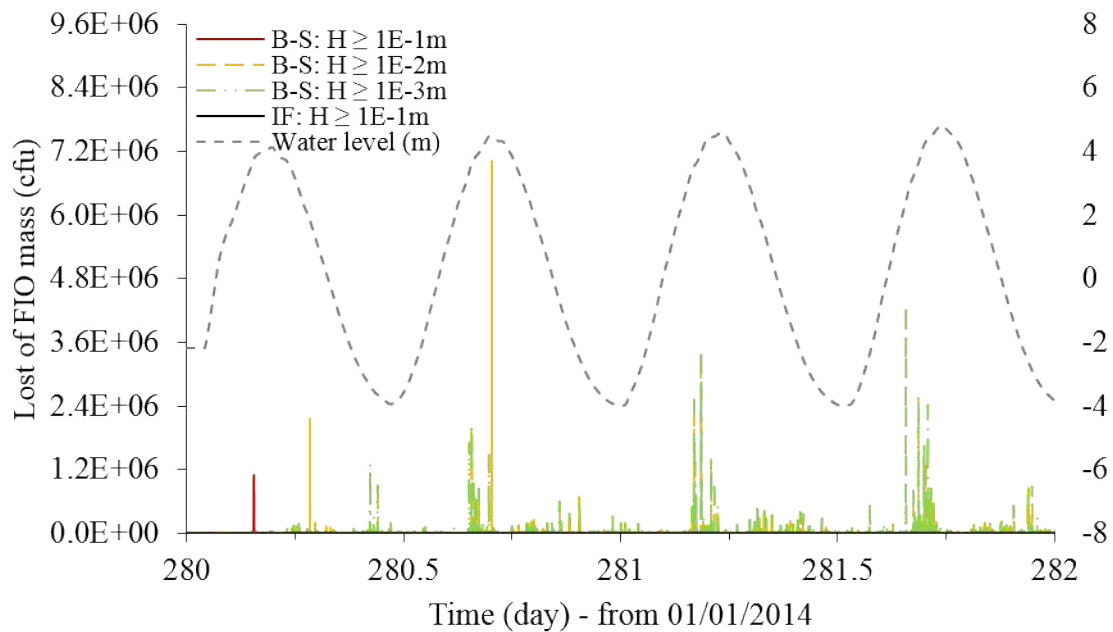


Figure 6.14: The time series of the FIOs mass lost with the conservative mass at different releasing depths based on the B-S and IF release models.

Table 6.8 shows the result of the statistical analyses for the FIOs mass loss at the grazing marshland with the conservative mass during the second-to-fourth tidal cycles. The difference was observed in the mass lost between the B-S and IF release models for the equal or greater than 1×10^{-1} m with the ME of -2.08×10^{-3} cfu/dt. From the B-S release-kinetic model, the mass loss for the equal to or greater than 1×10^{-2} m and 1×10^{-3} m were underpredicted, with the highest underprediction was from the equal or greater than 1×10^{-3} m with the ME of 4.44×10^4 cfu/dt. The MAE and RMSE between the observed and predicted mass loss were increased from the equal or greater than 1×10^{-2} m to the equal or greater than 1×10^{-3} m, respectively with the lowest error was from the equal or greater than 1×10^{-2} m with the MAE of 2.97×10^4 cfu/dt (RE=-1210%) and with the RMSE of 2.24×10^5 cfu/dt (RRE=6.06%).

Table 6.8: The result of the statistical analysis for the FIOs mass lost with the conservative mass at the grazing marshland during the second-to-fourth tidal cycles.

H (m)	$\geq 1 \times 10^{-1}$	$\geq 1 \times 10^{-2}$	$\geq 1 \times 10^{-3}$
ME (cfu)	-2.08×10^{-3}	2.91×10^4	3.77×10^4
MAE (cfu)	2.08×10^{-3}	2.97×10^4	4.44×10^4
RE (%)	-8.49×10^{-5}	-1.21×10^3	-1.81×10^3
RMSE (cfu)	2.85×10^{-3}	2.24×10^5	2.36×10^5
RRE (%)	7.71×10^{-8}	6.06	6.40

The mass loss from the model was defined as the decreased in the FIO mass as compared to the initial loading that entered the waterbody. This non-conservative condition would result in the transport model to become the unbalance in mass. The conservation of mass was very important in modelling the pollutant transport process as the accurate pollutant mass will determine the accurate concentration of a pollutant in the waterbody, provided the hydrodynamic was correct. The mass lost within this scope of study was arose mainly due to the improper and/or unrefined treatment in modelling at the wetting and drying boundary. This judgement was supported based on results in Figure 6.11, as the FIO lost during the release was many times higher than the lost during the transport. The mass loss was increased significantly as for the lower values due to the non-conservative condition at the partially wet-dry elements without special treatment.

The result of the FIOs mass balance based on the numerical computation is depicted in Figure 6.15 as the modelled time series at the grazing marshland with the conservative mass during nine tidal cycles. From the IF release model and during the first tidal cycle, the mass balance for the equal or greater than 1×10^{-1} m was levelled at 280.6326 JD with the value of 4.35×10^{10} cfu. With the average mass increment of 1.67×10^{11} cfu for every tidal cycle, the mass balance during the ninth tidal cycle was levelled at 284.7667 JD with the value of 1.38×10^{12} cfu. The highest mass increment was between the third and the fourth tidal cycles with the value of 2.18×10^{11} cfu, and the lowest was between the eighth and the ninth tidal cycles with the value of 1.38×10^{11} cfu.

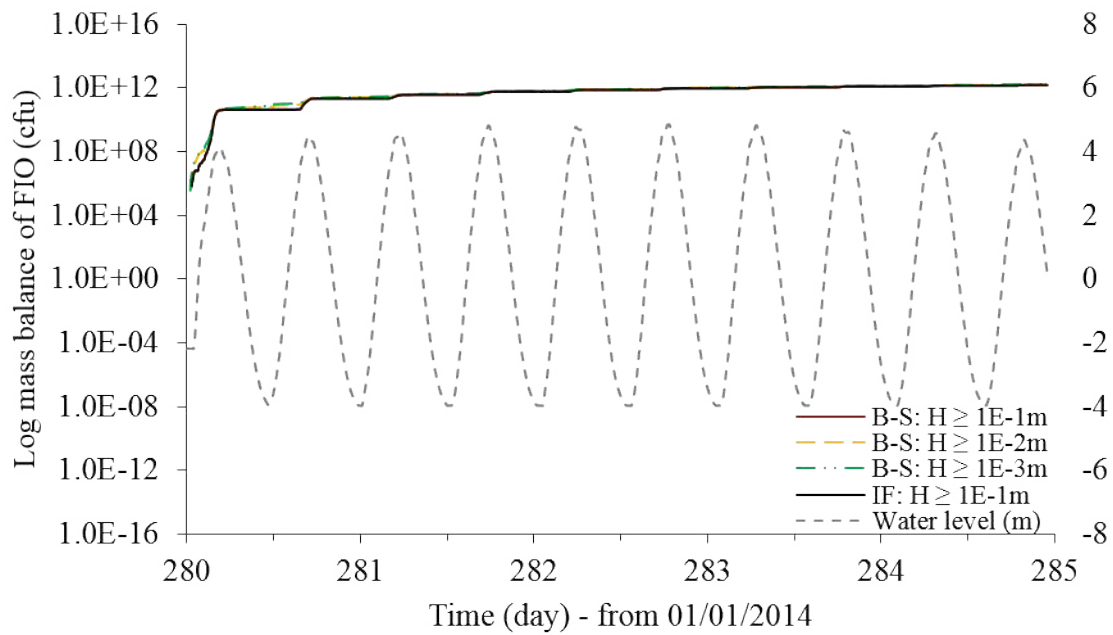


Figure 6.15: The time series of the FIOs mass balance with the conservative mass at different releasing depths based on the B-S and IF release models.

Table 6.9 shows the result of the statistical analyses for the FIOs mass balance at the grazing marshland with the conservative mass. The difference was observed in the mass balance between the B-S and IF release models for the equal or greater than 1×10^{-1} m with the ME of 8.33×10^7 cfu. From the B-S release-kinetic model, the mass balance for the equal to or greater than 1×10^{-2} m and 1×10^{-3} m were underpredicted, with the highest underprediction was from the equal or greater than 1×10^{-3} m with the ME of 8.30×10^{10} cfu. The errors between the observed and predicted mass balance were increased from the equal or greater than 1×10^{-1} m to the equal or greater than 1×10^{-3} m, with the highest error was from the equal or greater than 1×10^{-3} m with the MAE of 8.30×10^{10} cfu (RE=11.3%) and the RMSE of 9.77×10^{10} cfu (RRE=6.5%).

Table 6.9: The result of the statistical analyses for the FIOs mass balance with the conservative mass at the grazing marshland.

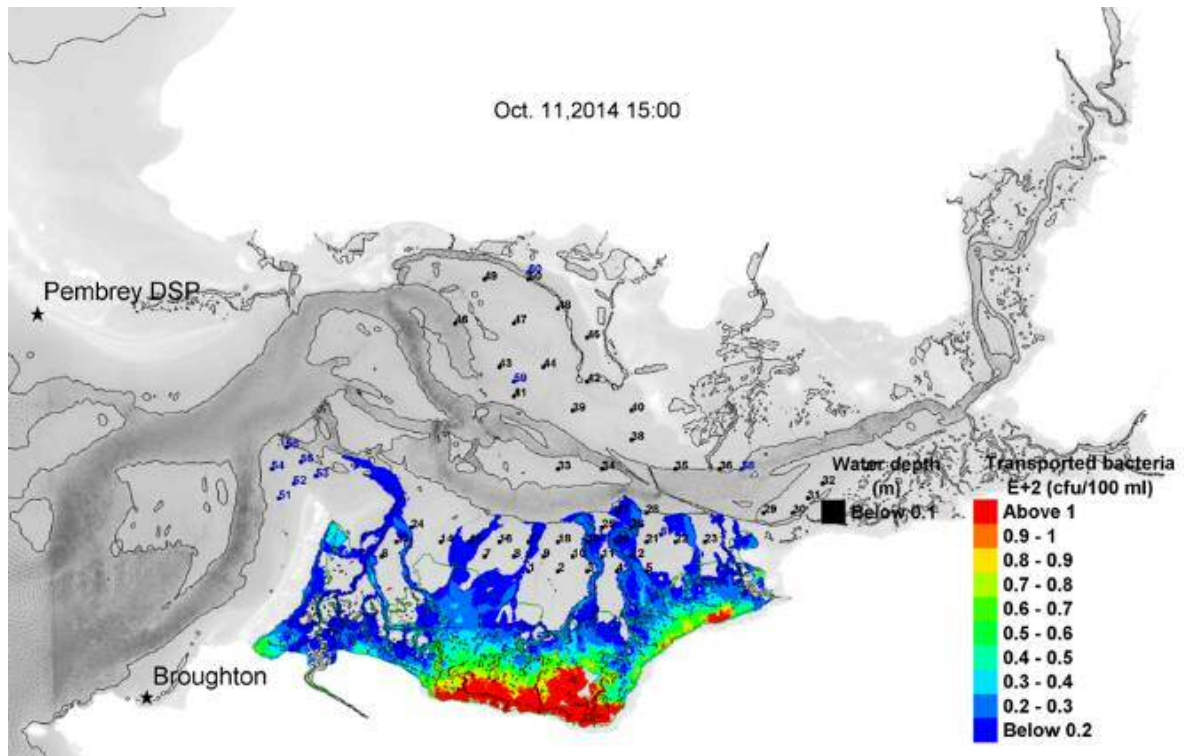
H (m)	$\geq 1 \times 10^{-1}$	$\geq 1 \times 10^{-2}$	$\geq 1 \times 10^{-3}$
ME (cfu)	8.33×10^7	6.18×10^{10}	8.30×10^{10}
MAE (cfu)	8.33×10^7	6.18×10^{10}	8.30×10^{10}
RE (%)	1.13×10^{-2}	8.42	1.13×10^1

RMSE (cfu)	1.06×10^8	6.92×10^{10}	9.77×10^{10}
RRE (%)	7.02×10^{-3}	4.60	6.50

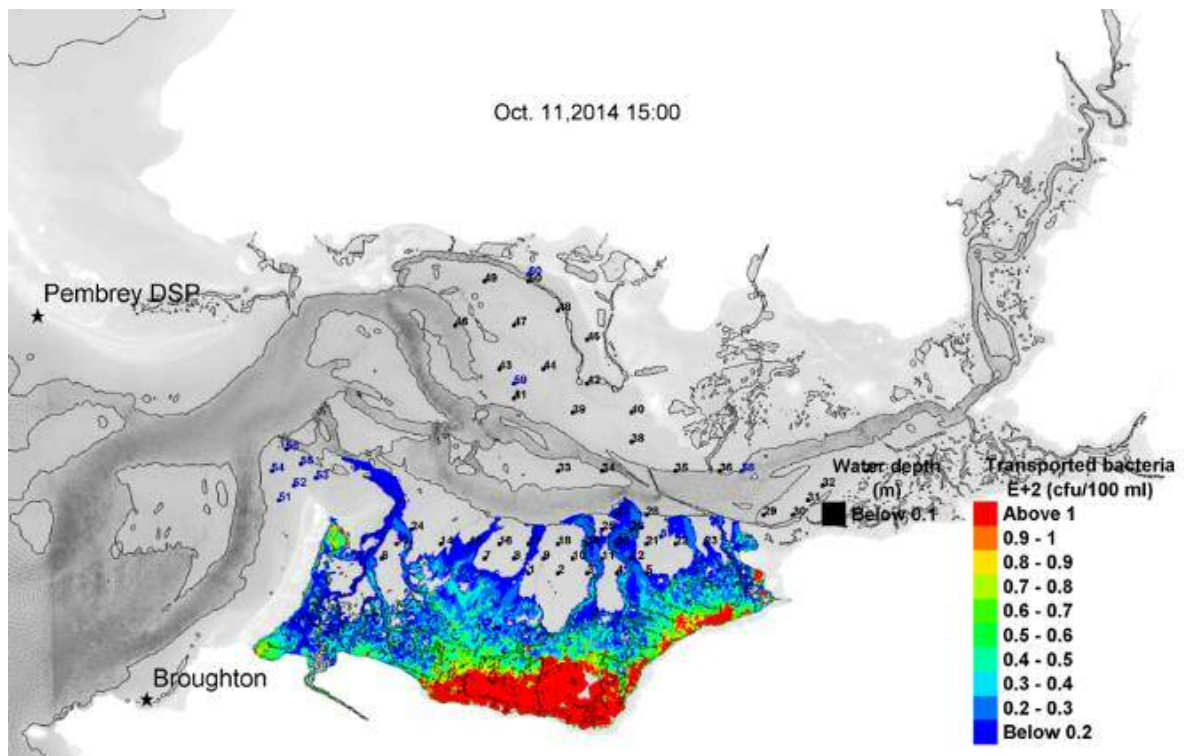
6.3.4 FIO transport and decay

6.3.4.1 Conservative mass

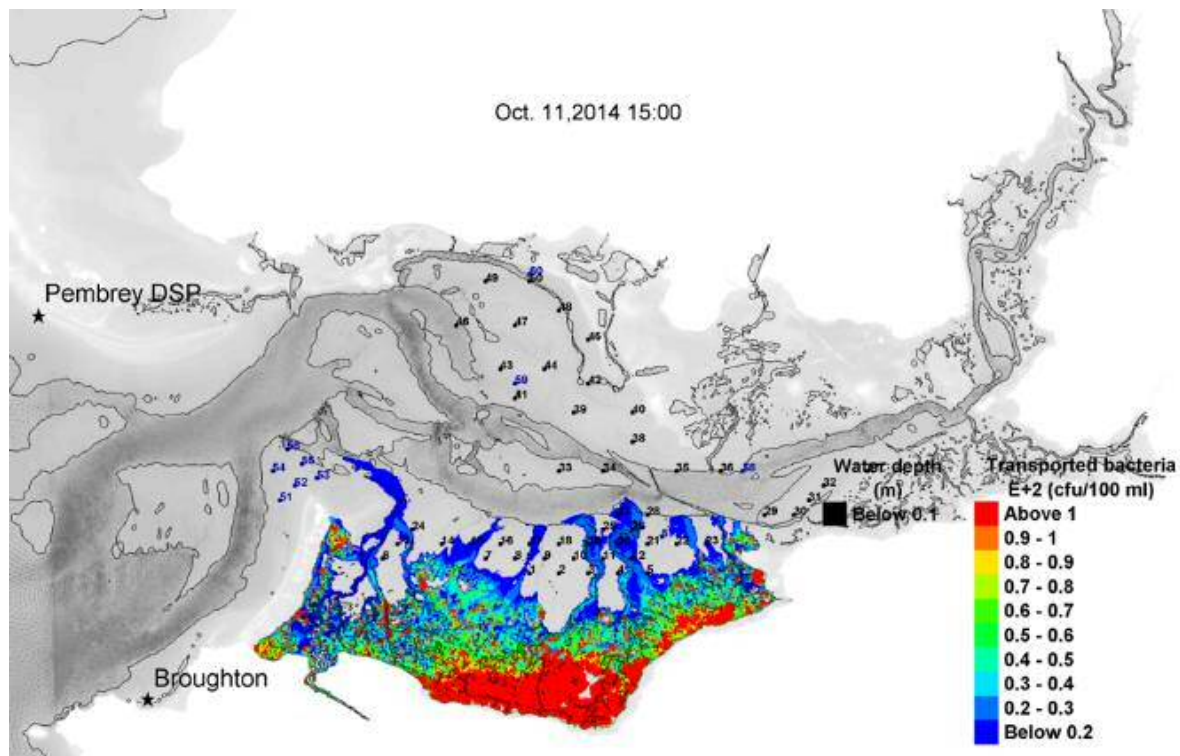
Results of the FIO transport as a conservative mass based on the B-S release-kinetic model are depicted in Figure 6.16. Their concentration gradients with different Δx across the Loughor Estuary were at 3 hours before high water (HW) during a spring tide. For the Δx equal or greater than 1×10^{-1} m, the FIO concentration above 1×10^2 cfu/100 ml was retained at the south of the grazing marshland within the area of 1.40 km^2 (11.62%). These retained and flushed out mass to the adjacent shellfish beds were at 2.03×10^{11} cfu (14.71%) and 1.17×10^{12} cfu (85.29%) respectively. For the Δx equal or greater than 1×10^{-2} m, the FIO concentration above 1×10^2 cfu/100 ml was retained at the south of the grazing marshland within the area of 2.80 km^2 (23.24%). These retained and flushed out mass to the adjacent shellfish beds were at 3.28×10^{11} cfu (22.08%) and 1.16×10^{12} cfu (77.92%) respectively. For the Δx equal or greater than 1×10^{-3} m, the FIOs concentration above 1×10^2 cfu/100 ml was retained at the south of the grazing marshland within the area of 5.08 km^2 (42.16%). These retained and flushed out mass to the adjacent shellfish beds were at 4.36×10^{11} cfu (27.52%) and 1.15×10^{12} cfu (72.48%) respectively. The distributions of the transported FIO in Figure 6.16 were based on the analysis from Table E.1 in the Appendix.



a) Releasing at of 1 10^{-1} m.



b) Releasing at of 1 10^{-2} m.



c) Releasing at 1×10^{-3} m.

Figure 6.16: Concentration gradients of the FIO transport as a conservative mass across the Loughor Estuary at HW -3 hours referred at Burry Port (i.e. 284.25-284.75 JD from 01/01/2014), that released at different 1×10^{-3} m based on the B-S release-kinetic model.

The distribution of FIO concentrations as a conservative mass based on the B-S release-kinetic model is depicted in Figure 6.17 as box plots at the top 10 of the impacted shellfish beds. Bed no. 23 was the most impacted site, with the mean concentration of 33.43 cfu/100 ml and the median concentration of 14.20 cfu/100 ml. Bed no. 20 was the least impacted site from the 10 listed beds, with the mean concentration of 10.78 cfu/100 ml and the median concentration of 5.74 cfu/100 ml. The inter-quartile range (IQR) was the highest at bed no. 15 with the value of 30.32 cfu/100 ml, and the lowest at bed no. 14 with the value of 10.11 cfu/100 ml. Readers are referred to Table E.5 in the Appendix for the distribution of FIO concentrations at the remaining shellfish beds.

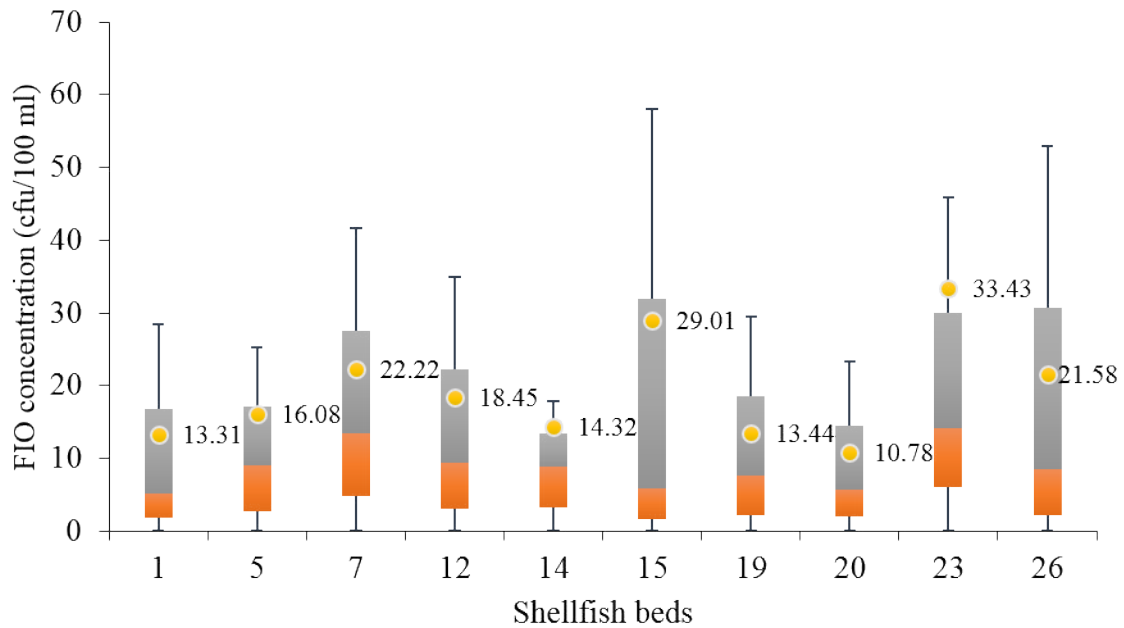


Figure 6.17: Box plots at 3 of the FIO concentrations distribution as a conservative mass at top 10 impacted shellfish beds, that released at different based on the B-S release-kinetic model.

Time series of the FIO concentration at shellfish bed no. 15 are depicted in Figure 6.18 as a 15 days simulation covering the neap and spring tidal cycles. The FIO was released as a conservative mass at different based on the B-S release-kinetic model. For the first three days during neap tides, the FIO was observed at the minimum concentration as the area was dried most of the time. The concentration was begun to increase from day fourth as the FIO was flushed out from the marshland during ebb tides. Higher FIO concentration was observed from of 1×10^{-3} m as compared to the deeper release. The concentration was continued to increase over 150 cfu/100 ml following the increase in water level during spring tides before was peaked over 400 cfu/100 ml during an ebb tide. Higher FIO concentration was observed from of 1×10^{-1} m as compared to the shallower release during this occurrence. The FIO concentration was then decreased below 50 cfu/100 ml during the subsequent spring tides before was reduced to the minimum during the following neap tides.

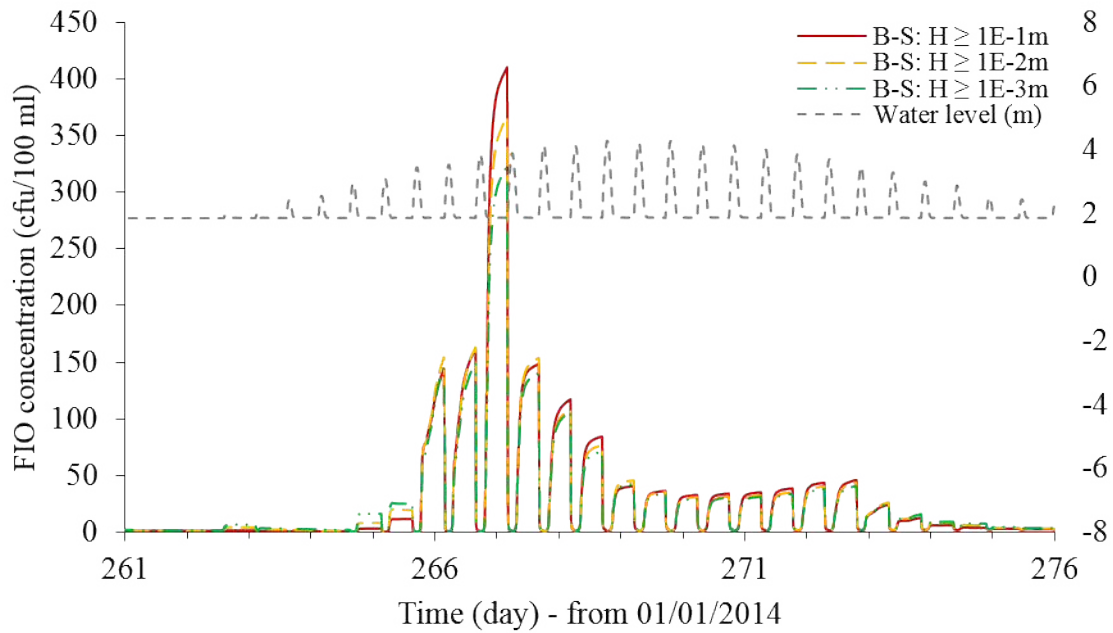
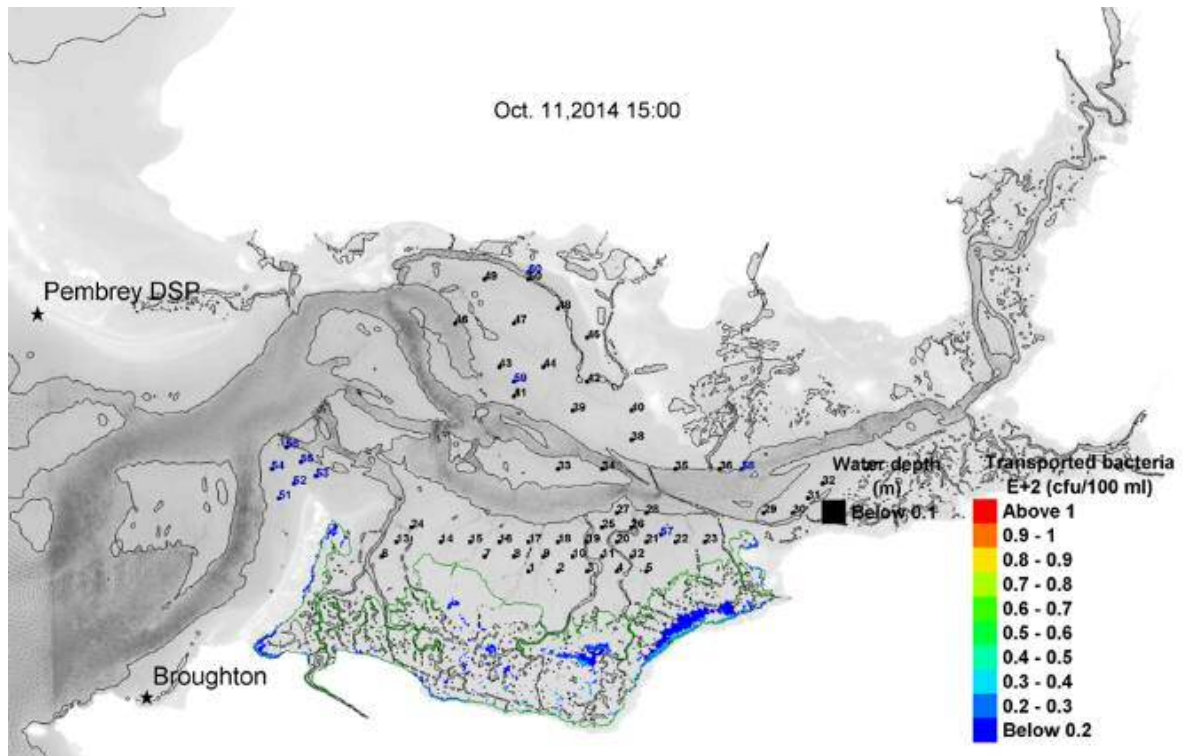


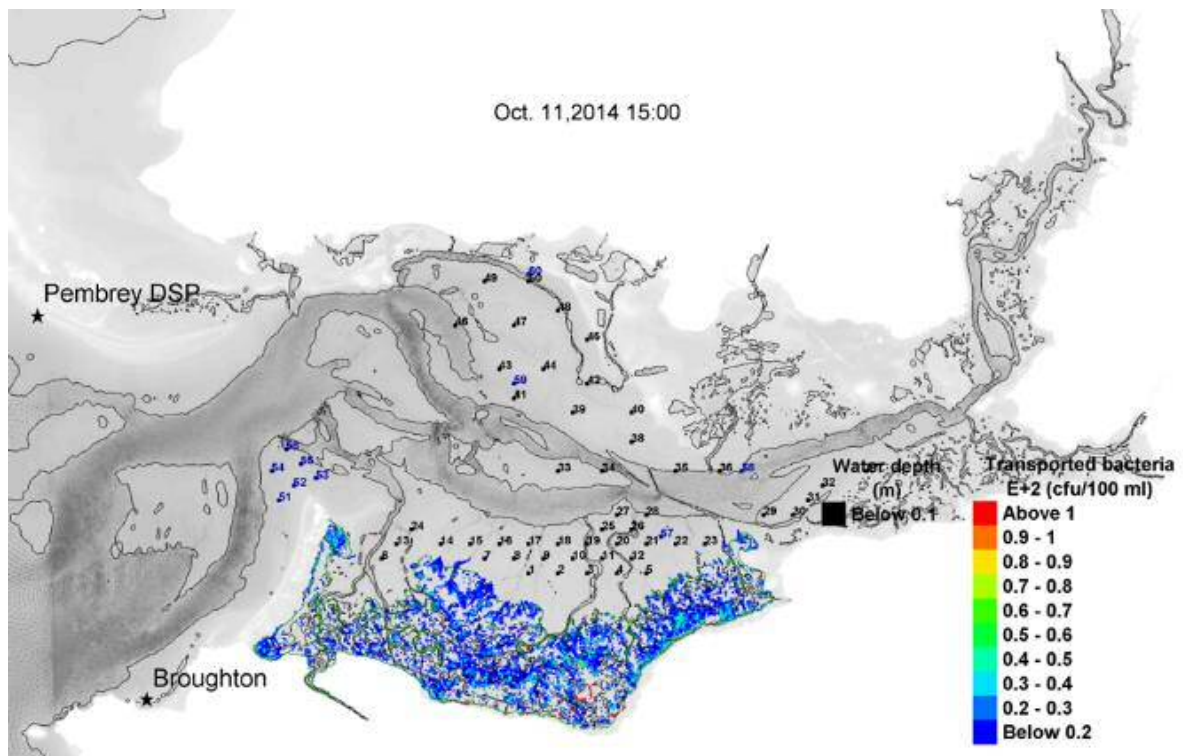
Figure 6.18: Time series of the FIO concentrations at shellfish bed no. 15, as a conservative mass and at different based on the B-S release-kinetic model.

6.3.4.2 Constant decay at $T_{90} = 14.9$ hours

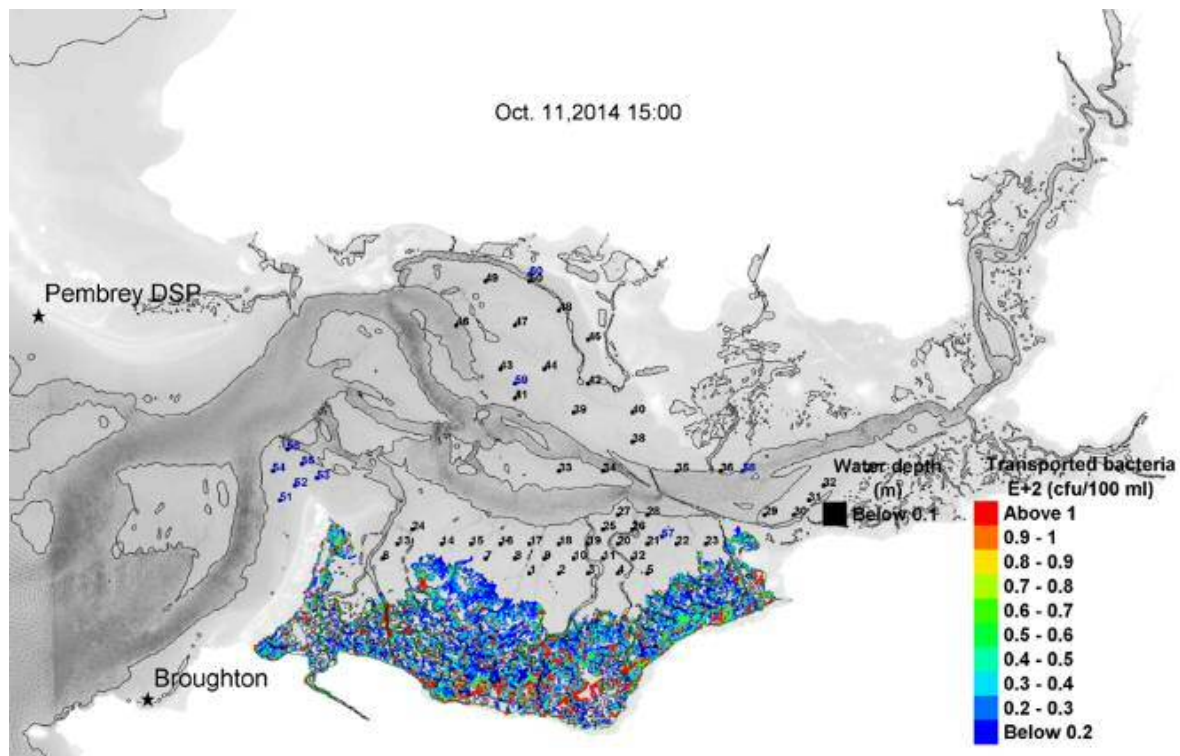
Results of the FIO transport with constant decay ($T_{90} = 14.9$ hours) based on the B-S release-kinetic model are depicted in Figure 6.19. Their concentration gradients with different across the Loughor Estuary were at 3 hours before high water (HW) during a spring tide. For the equal or greater than 1×10^{-1} m, the FIO concentration above 1×10^2 cfu/100 ml was retained at the south of the grazing marshland within the area of 4.30×10^{-6} km² (3.57 $\times 10^{-5}$ %). These retained and flushed out mass to the adjacent shellfish beds were at 1.45×10^{10} cfu (30.76%) and 3.26×10^{10} cfu (69.24%) respectively. For the equal or greater than 1×10^{-2} m, the FIO concentration above 1×10^2 cfu/100 ml was retained at the south of the grazing marshland within the area of 0.15 km² (1.24%). These retained and flushed out mass to the adjacent shellfish beds were at 3.17×10^{10} cfu (52.92%) and 2.82×10^{10} cfu (47.08%) respectively. For the equal or greater than 1×10^{-3} m, the FIO concentration above 1×10^2 cfu/100 ml was retained at the south of the grazing marshland within the area of 1.71 km² (14.19%). These retained and flushed out mass to the adjacent shellfish beds were at 9.27×10^{10} cfu (74.83%) and 3.12×10^{10} cfu (25.17%) respectively. The distributions of the transported FIO in Figure 6.19 were based on the analysis from Table E.2 in the Appendix.



a) Releasing at of 1 10^{-1} m.



b) Releasing at of 1 10^{-2} m.



c) Releasing at 1×10^{-3} m.

Figure 6.19: Concentration gradients of the FIO transport with constant decay ($T_{90} = 14.9$ hours) across the Loughor Estuary at HW -3 hours referred at Burry Port (i.e. 284.25-284.75 JD from 01/01/2014), that released at different based on the B-S release-kinetic model.

The distribution of the FIO concentrations with constant decay ($T_{90} = 14.9$ hours) based on the B-S release-kinetic model is depicted in Figure 6.20 as box plots at the top 10 of the impacted shellfish beds. Bed no. 15 was the most impacted sites, with the mean concentration of 5.60 cfu/100 ml, and the median concentration of 0.13 cfu/100 ml. Bed no. 20 was the least impacted site from the 10 listed beds, with the mean concentration of 0.92 cfu/100 ml, and the median concentration of 0.06 cfu/100 ml. The inter-quartile range (IQR) was the highest at bed no. 15 with the value of 5.44 cfu/100 ml, and the lowest at bed no. 20 with the value of 1.10 cfu/100 ml. Readers are referred to Table E.6 in the Appendix for the distribution of FIO concentrations at the remaining shellfish beds.

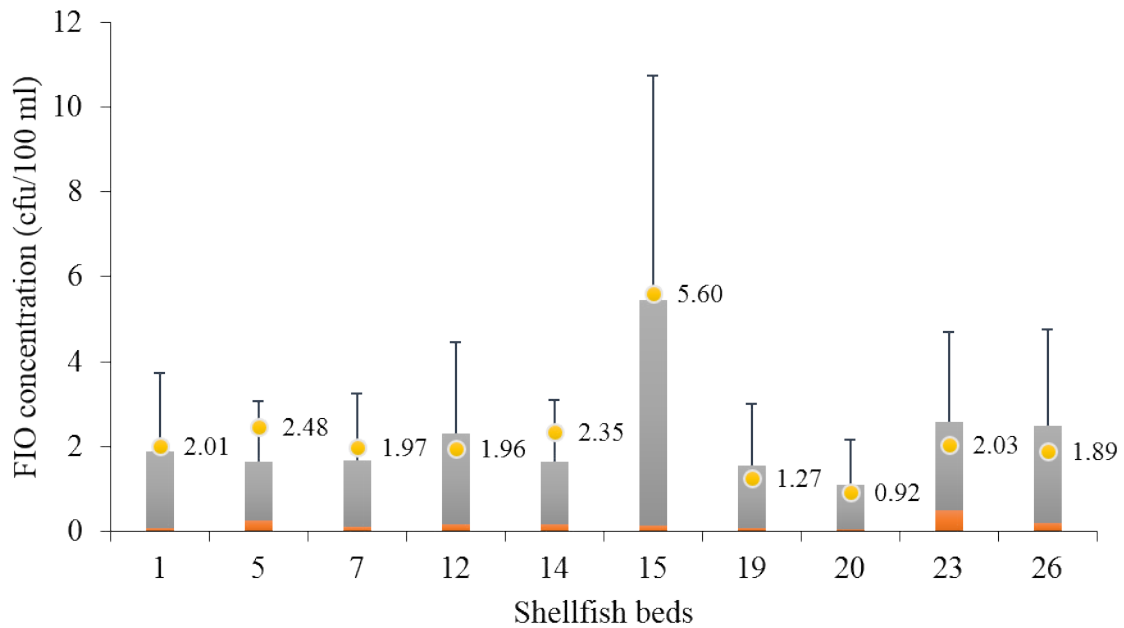


Figure 6.20: Box plots at 3 of the FIO concentrations distribution with constant decay ($T_{90} = 14.9$ hours) at top 10 impacted shellfish beds, that released at different based on the B-S release-kinetic model.

Time series of the FIO concentration at shellfish bed no. 15 again are depicted in Figure 6.21 as a 15 days simulation covering the neap and spring tidal cycles. The FIO was released with constant decay ($T_{90} = 14.9$ hours) at different based on the B-S release-kinetic model. For the first four days during neap tides, the FIO was observed at the minimum concentration same as in Figure 6.18. The concentration was begun to increase from day fifth at values below 50 cfu/100 ml following the increase in water level during spring tides before was peaked over 150 cfu/100 ml during an ebb tide. Higher FIO concentration was observed from of 1 10^{-1} m as compared to the shallower release and was reduced at the modelled decay rate after the peak. The FIO concentration was then decreased below 50 cfu/100 ml during the subsequent spring tides before was reduced to the minimum during the following neap tides.

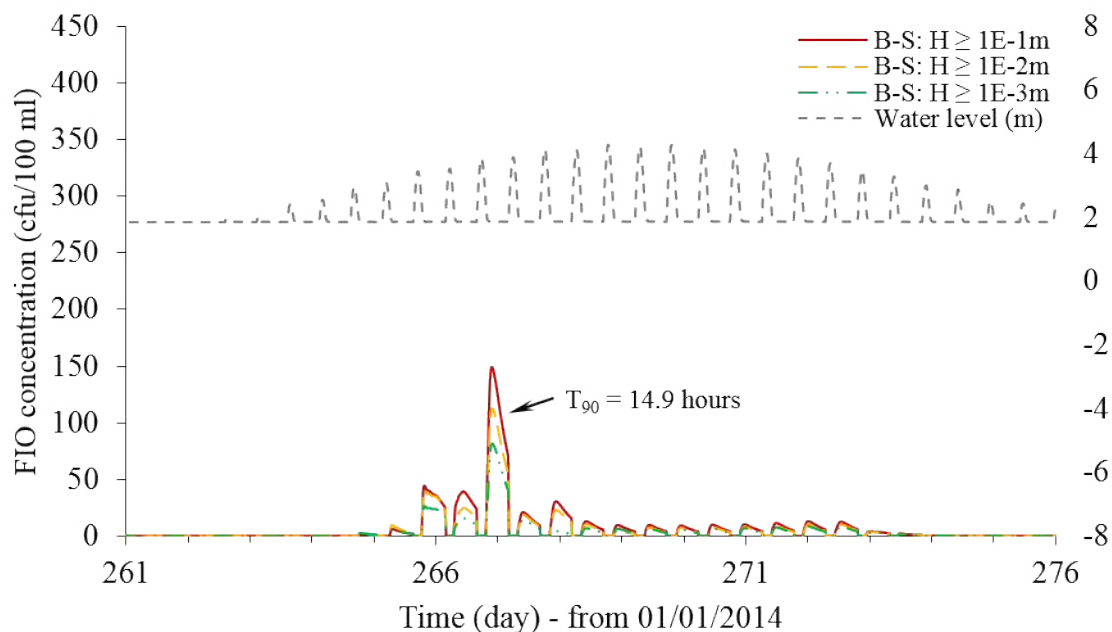
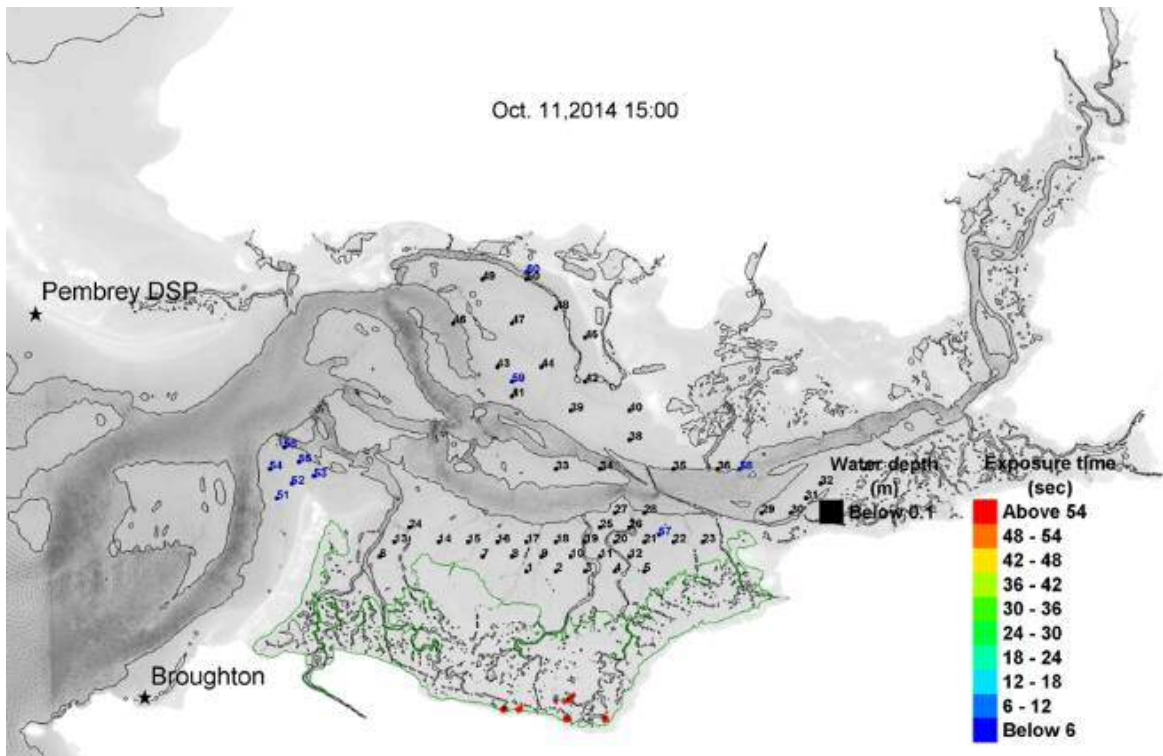


Figure 6.21: Time series of the FIO concentrations at shellfish bed no. 15, with constant decay ($T_{90} = 14.9$ hours) and at different based on the B-S release-kinetic model.

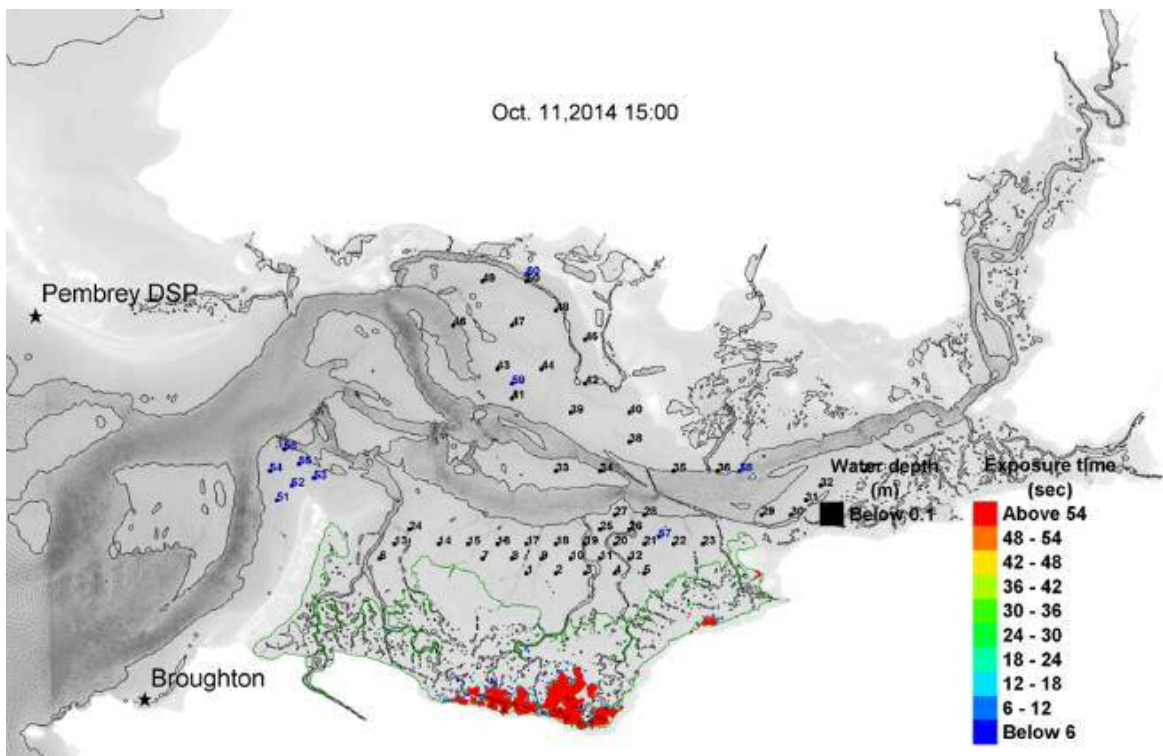
6.3.5 FIO exposure to shellfish

6.3.5.1 Conservative mass

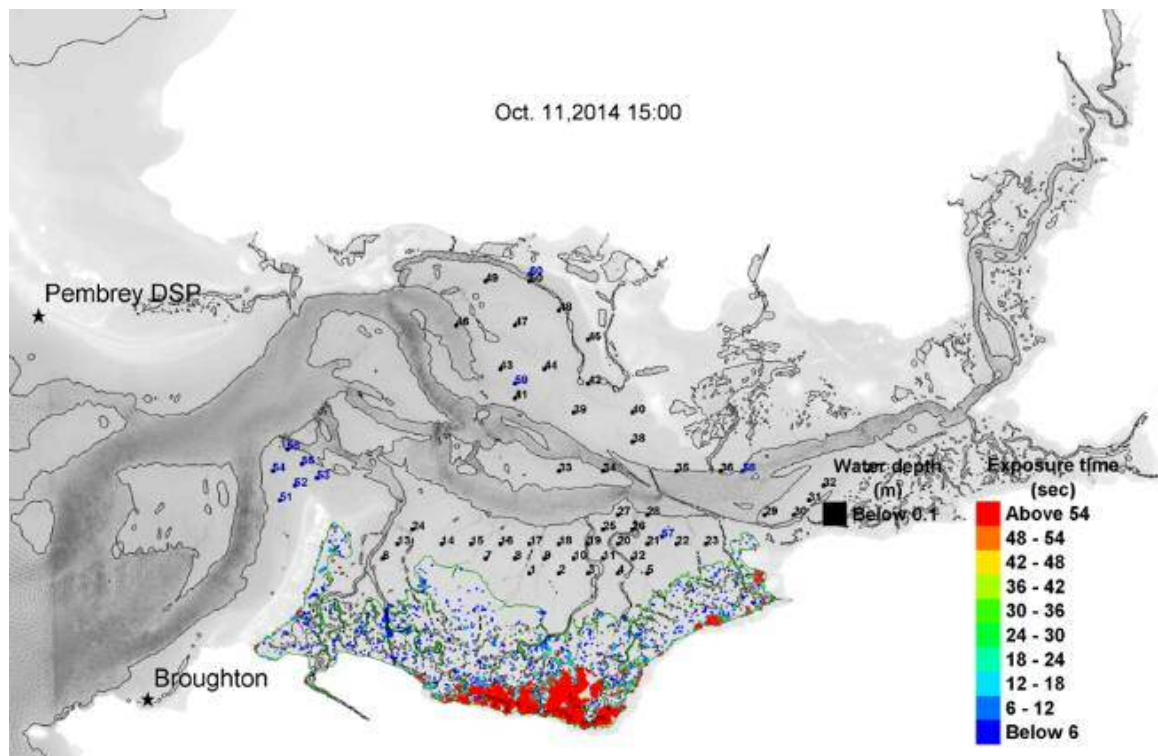
Exposure times of the FIO to shellfish fleshes across the Loughor Estuary as a result of the diffuse source releasing at different , are illustrated in Figure 6.22 at 3 hours before high water (HW) during a spring tide. The transported FIO was modelled as a conservative mass for this illustration. For the release at of 1×10^{-1} m, the exposure time above 54 seconds was minimally recorded within the area of 0.08 km^2 (0.66%) at the south of the grazing marshland. For the release at of 1×10^{-2} m and 1×10^{-3} m respectively, the exposure times above 54 seconds were moderately and severely recorded within the areas of 0.98 km^2 (8.17%) and 1.38 km^2 (11.42%) at the south of the grazing marshland.



a) Releasing at 10^{-1} m.



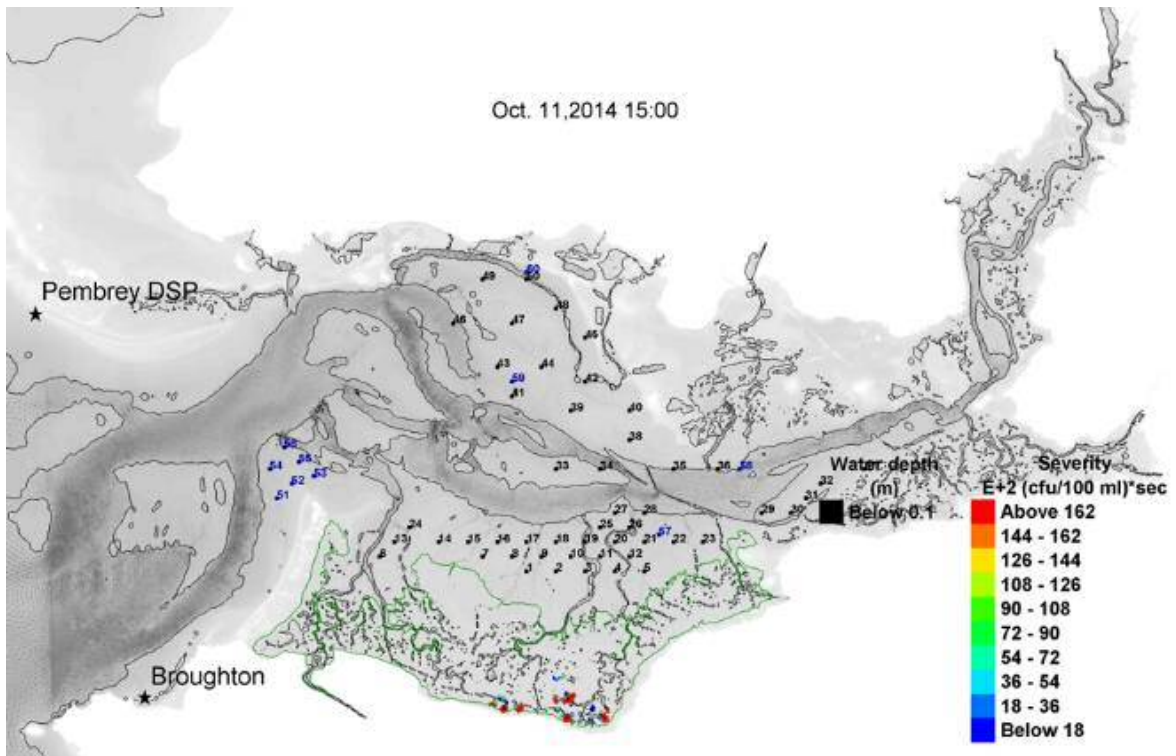
b) Releasing at 10^{-2} m.



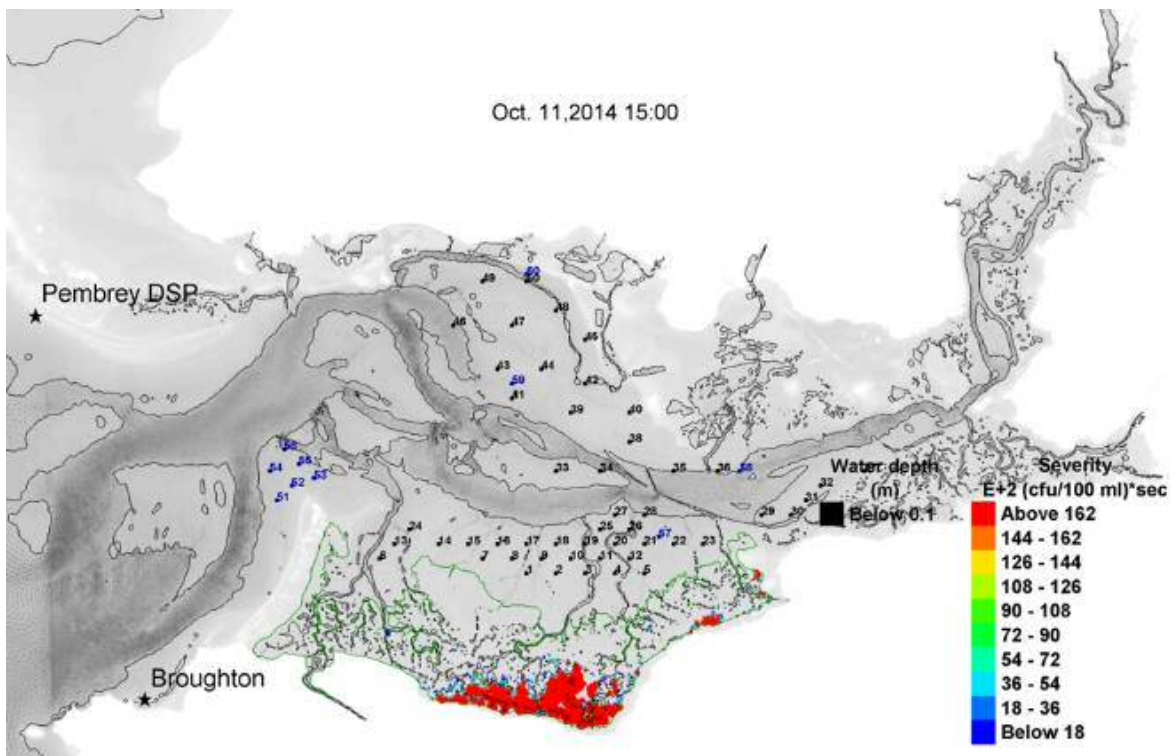
c) Releasing at 1×10^{-3} m.

Figure 6.22: Exposure time of FIO to shellfish at HW -3 hours referred at Burry Port (i.e. 284-284.5 JD from 01/01/2014), that released as a conservative mass at different 1×10^{-3} m based on the B-S release-kinetic model.

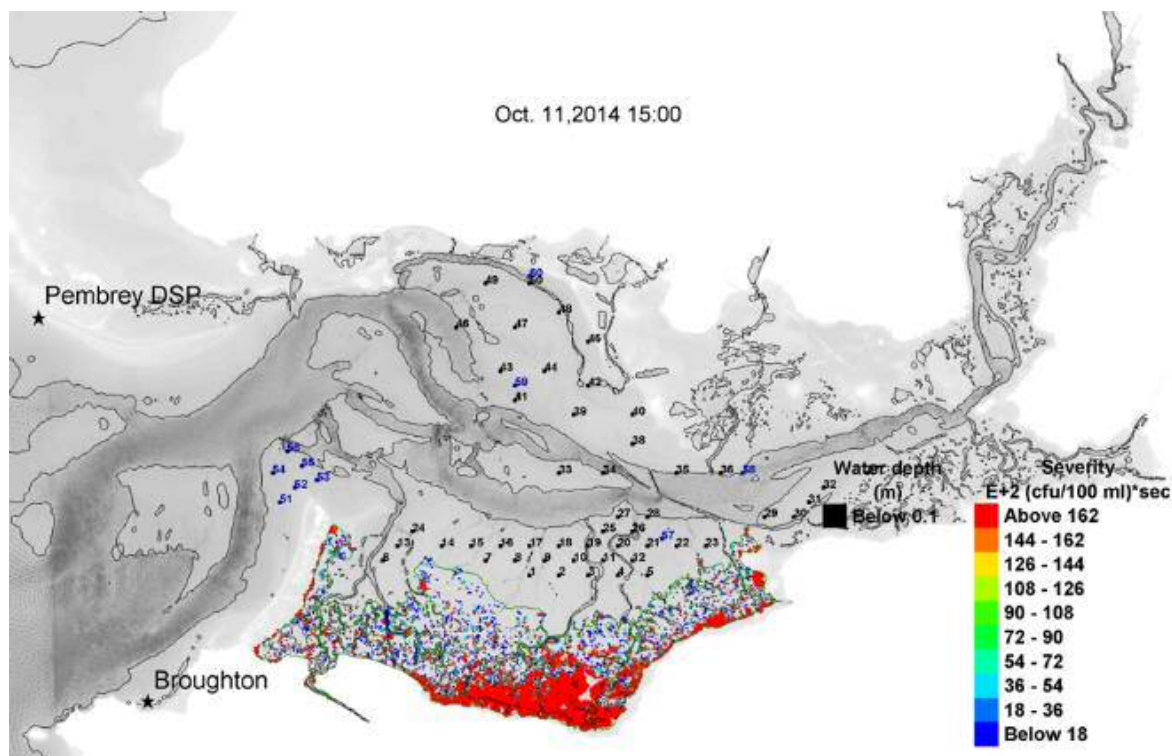
Exposure severities of the FIO to shellfish fleshes across the Loughor Estuary as a result of the diffuse source releasing at different 1×10^{-3} m, are illustrated in Figure 6.23 at 3 hours before high water (HW) during a spring tide. The transported FIO was modelled as a conservative mass for this illustration. For the release at 1×10^{-1} m, the exposure severity above 1.62×10^4 (cfu/100 ml)*sec was minimally recorded within the area of 0.11 km^2 (0.88%) at the south of the grazing marshland. For the release at 1×10^{-2} m and 1×10^{-3} m respectively, the exposure severities above 1.62×10^4 (cfu/100 ml)*sec were moderately and severely recorded within the areas of 1.42 km^2 (11.75%) and 3.06 km^2 (25.36%) at the south of the grazing marshland. The distributions of the shellfish exposure time and severity to FIO in Figures 6.22 and 6.23 were based on the analysis from Table E.3 in the Appendix.



a) Releasing at of 1 10^{-1} m.



b) Releasing at of 1 10^{-2} m.

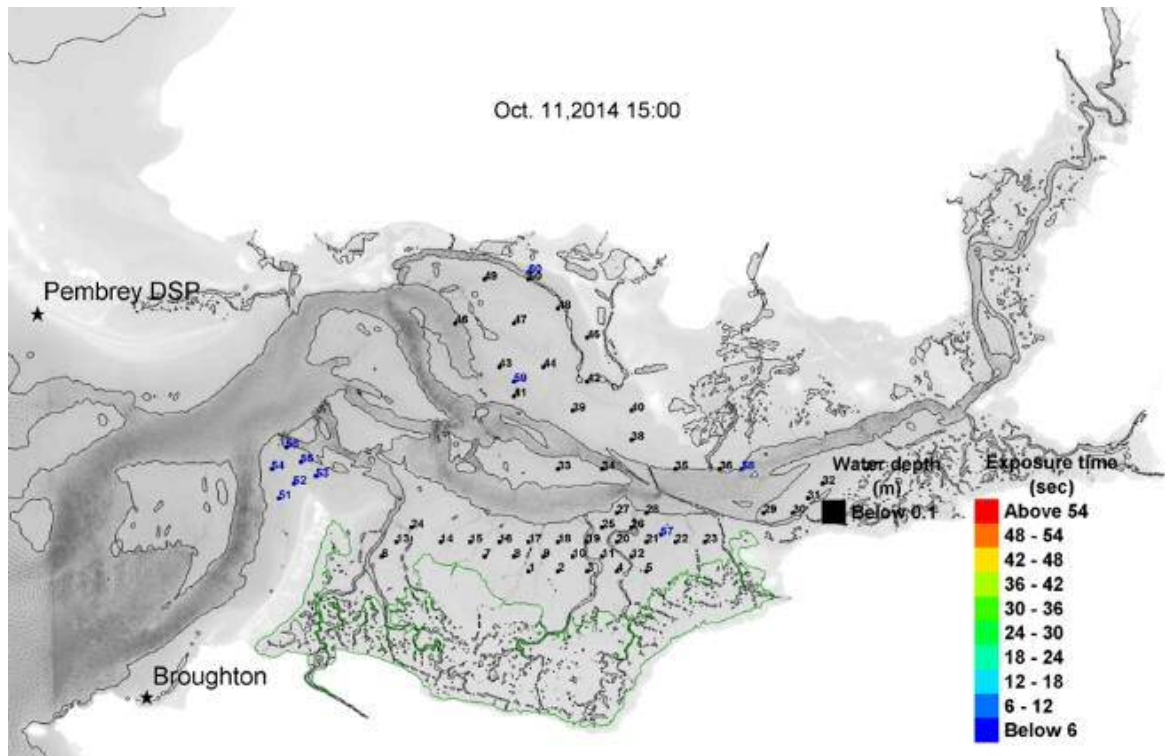


c) Releasing at 1×10^{-3} m.

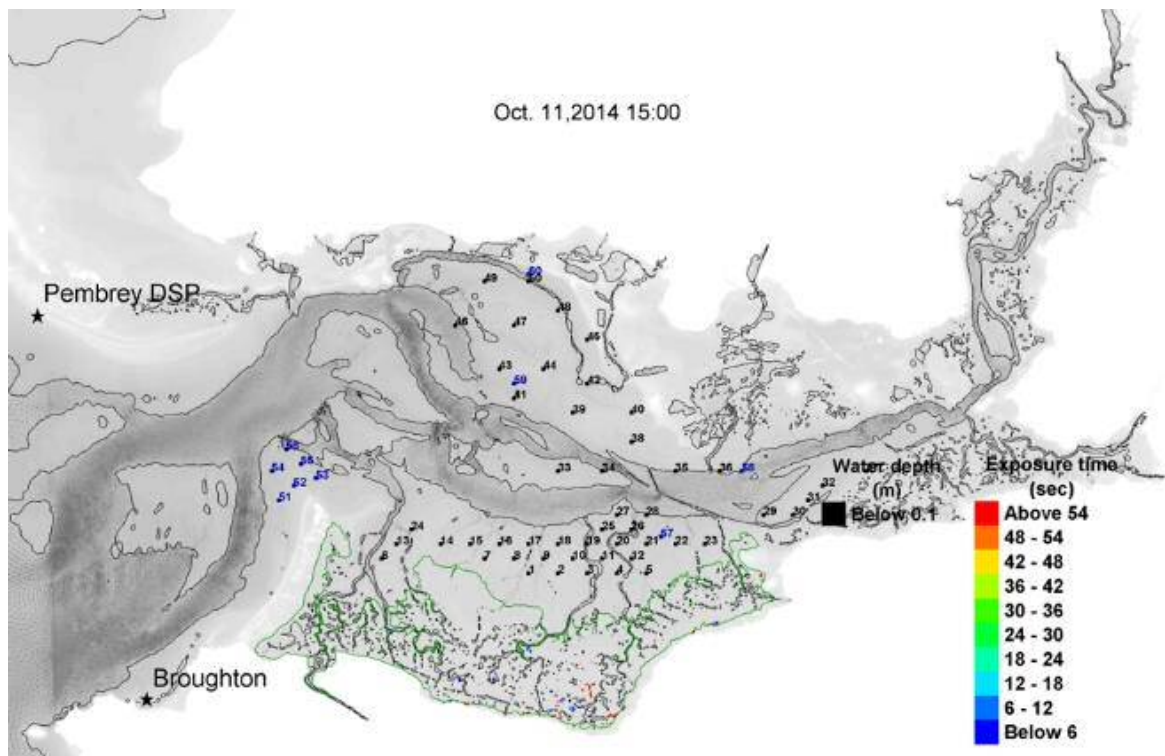
Figure 6.23: Exposure severity of FIO to shellfish at HW -3 hours referred at Burry Port (i.e. 284-284.5 JD from 01/01/2014), that released as a conservative mass at different 10^{-3} m based on the B-S release-kinetic model.

6.3.5.2 Constant decay at $T_{90} = 14.9$ hours

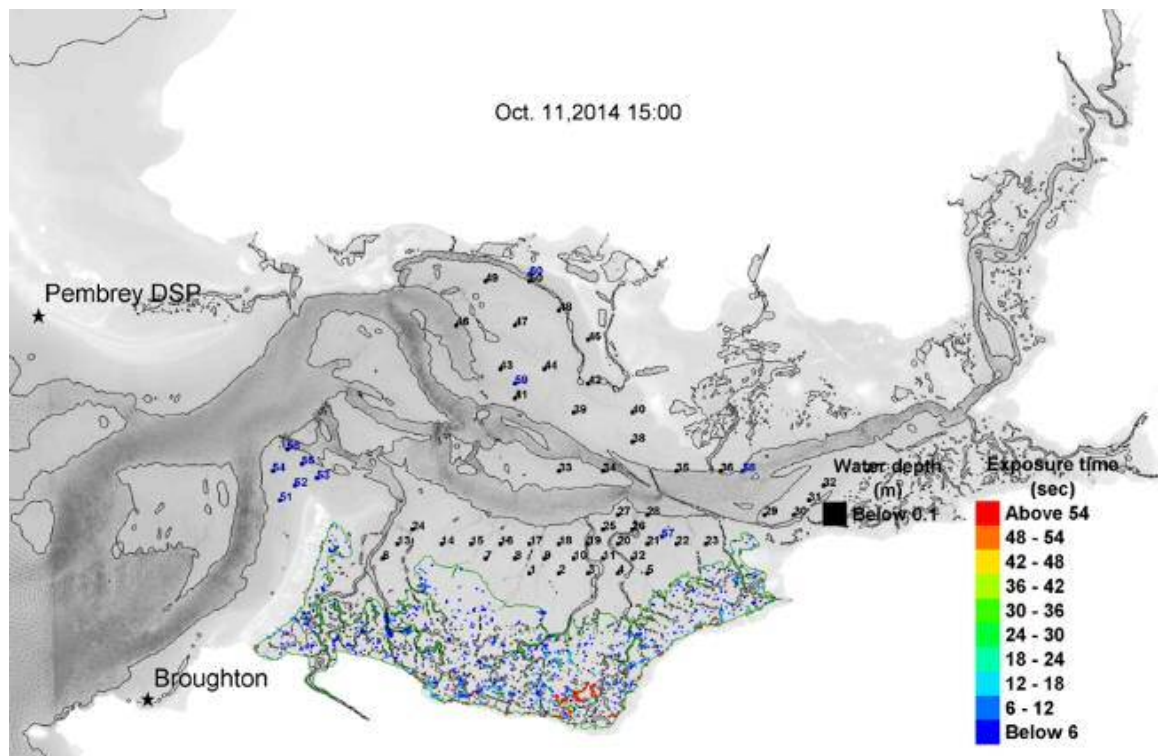
Exposure times of the FIO to shellfish fleshes across the Loughor Estuary as a result of the diffuse source releasing at different 10^{-3} m, are illustrated in Figure 6.24 at 3 hours before high water (HW) during a spring tide. The transported FIO was modelled with constant decay ($T_{90} = 14.9$ hours) for this illustration. For the release at 1×10^{-1} m, the exposure time above 54 seconds was not recorded within the area of the grazing marshland. For the release at 1×10^{-2} m and 1×10^{-3} m respectively, the exposure times above 54 seconds were minimally and moderately recorded within the areas of 0.05 km^2 (0.43%) and 0.22 km^2 (1.83%) at the south of the grazing marshland.



a) Releasing at of $1 \cdot 10^{-1}$ m.



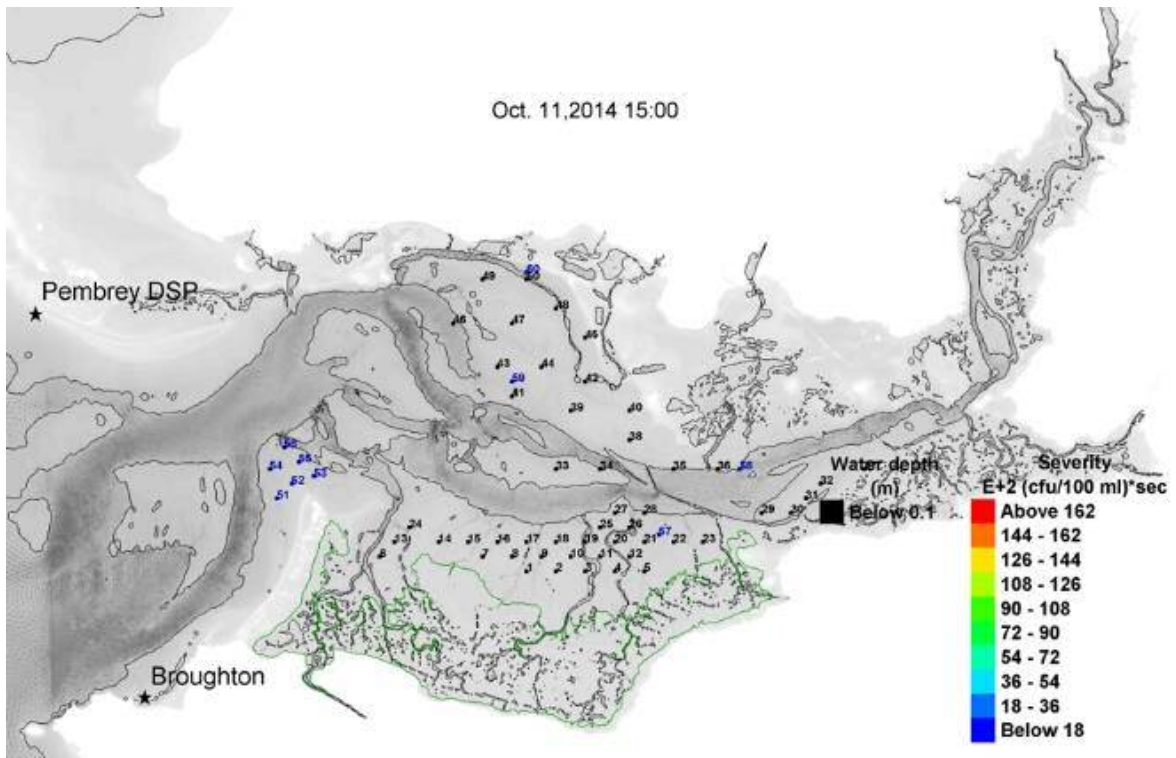
b) Releasing at of $1 \cdot 10^{-2}$ m.



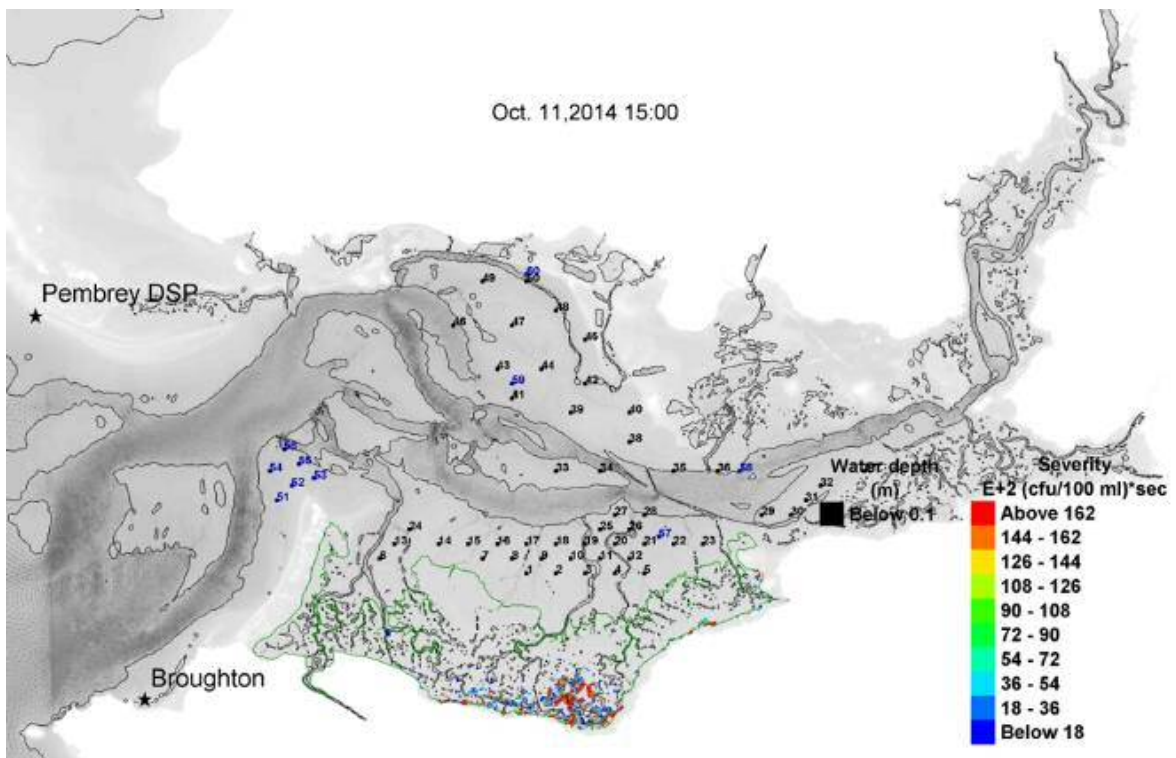
c) Releasing at 1×10^{-3} m.

Figure 6.24: Exposure time of FIO to shellfish at HW -3 hours referred at Burry Port (i.e. 284-284.5 JD from 01/01/2014), that released with constant decay ($T_{90} = 14.9$ hours) at different based on the B-S release-kinetic model.

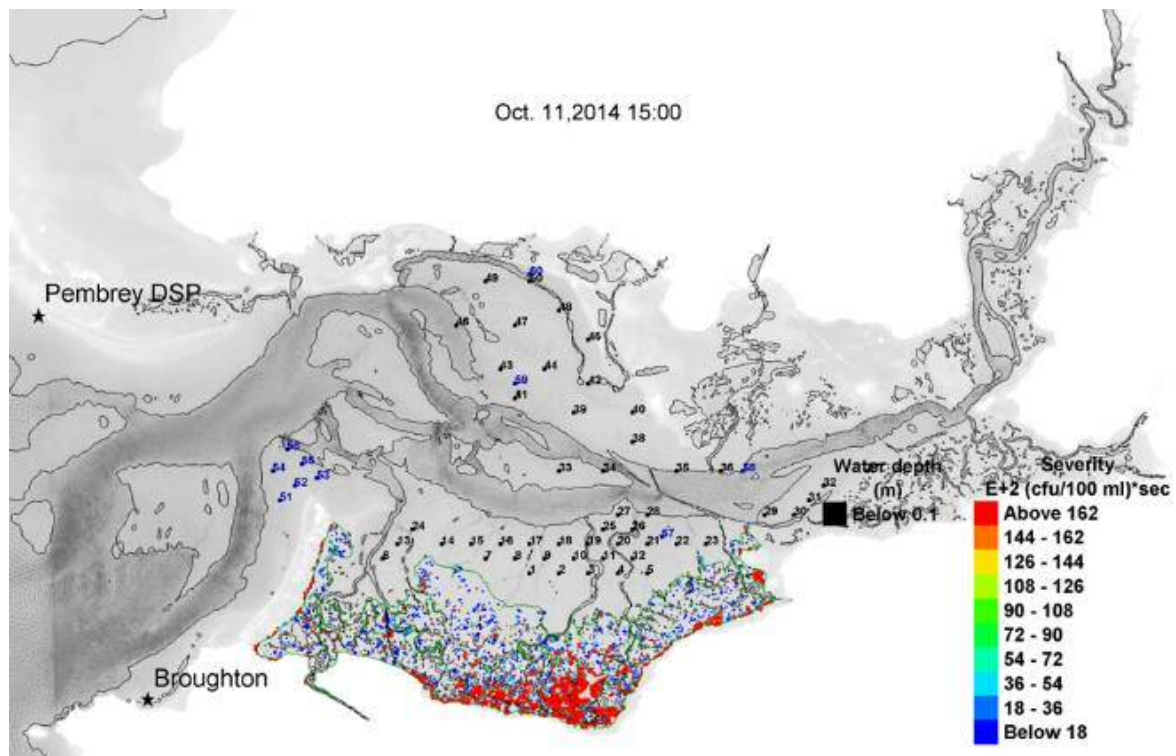
Exposure severities of the FIO to shellfish fleshes across the Loughor Estuary as a result of the diffuse source releasing at different , are illustrated in Figure 6.25 at 3 hours before high water (HW) during a spring tide. The transported FIO was modelled with constant decay ($T_{90} = 14.9$ hours) for this illustration. For the release at of 1×10^{-1} m, the exposure severity above 1.62×10^4 (cfu/100 ml)*sec was not recorded within the area of the grazing marshland. For the release at of 1×10^{-2} m and 1×10^{-3} m respectively, the exposure severities above 1.62×10^4 (cfu/100 ml)*sec were minimally and moderately recorded within the areas of 0.25 km^2 (2.09%) and 1.67 km^2 (13.87%) at the south of the grazing marshland. The distributions of the shellfish exposure time and severity to FIO in Figures 6.24 and 6.25 were based on the analysis from Table E.4 in the Appendix.



a) Releasing at of 1 10^{-1} m.



b) Releasing at of 1 10^{-2} m.



c) Releasing at 1×10^{-3} m.

Figure 6.25: Exposure severity of FIO to shellfish at HW -3 hours referred at Burry Port (i.e. 284-284.5 JD from 01/01/2014), that released with constant decay ($T_{90} = 14.9$ hours) at different based on the B-S release-kinetic model.

As the threshold concentration of FIO at 300 cfu/100 ml was applied for the calculation of the exposure time and severity (Section 6.6), zero exposures of FIO were recorded at the designated shellfish beds for both scenarios of conservative mass (see Figures 6.22 and 6.23) and constant decay (see Figures 6.24 and 6.25) as its concentration was below the threshold value (see Figures 6.16 and 6.19).

Over 72.48% of the conservative FIO mass that was flushed out into the estuary was considered high to result in a serious impact on the shellfish water compliance. Due to the dispersion process, the FIO concentration however was decreased much at tidal flats and deeper waters after being transported from the grazing marshland. Furthermore, the FIO mass that was transported through bathymetrically induced dispersion was retained much at the grazing marshland for every post-flooding events as compared to its flushed-out rate through tidal creeks. Higher values of the bottom roughness at the grazing marshland would even increase the retention capacity of the FIO mass within this area (see Figure 5.14). These are highlighting the significance of extending the modelling domain at intertidal floodplains of the Loughor

Estuary as stressed in the second objective, that influences the transport process and retention of FIO within this region.

The exchange of the surficial FIO loading from the grazing marshland based on the B-S release-kinetic model though was released in proportion beginning at 1×10^{-3} m, was successfully transferred the total build-up loading at 1×10^{-1} m that took less than 25 minutes (see Figure 6.7). After fully transferred, the earlier release at 1×10^{-3} m was transported the total FIO mass to the larger extent into the estuary (i.e. the case of conservative) as compared to the later release at 1×10^{-1} m during post-flooding (see Figure 6.16). These are highlighting the difference in water quality status after considering the realistic exchange of FIO loadings from the diffuse source as proposed in the fourth objective.

As for the case of the FIO transport with constant decay, the earlier release at 1×10^{-3} m was resulted in lower FIO concentration at the designated shellfish beds as compared to the later release at 1×10^{-1} m. This situation was due to a reason that the FIO mass with the earlier release was experiencing a longer period of decay as compared to the mass that was released later. The decay process with a constant rate of $T_{90} = 14.9$ hours that was based on the field experiment and the previous modelling work was considered as an appropriate modelling approach. A site-specific decay model can be developed based on the measured FIO concentration that was released at the grazing marshland (i.e. Site 101 – Great Pill) following the successive approach in the third objective.

The transport of FIO from different sources will have different impacts on the water quality at shellfish beds. The source near to shellfish beds will have a shorter transport timescale and will result in the arrival of higher FIO concentrations due to less dispersion and decay effects. The point source that releases intermittently during ebb tides will have a significant reduction in the FIO concentration at shellfish beds after experiencing higher dispersion effect during the transport. The diffuse source as compared to the point source, will have a higher FIO loading into the waterbody due to continuous release from a large area of grazing marshlands. Cumulative FIO loadings from both point and diffuse sources will have a significant impact on the water quality compliance at shellfish beds.

6.4 Summary

This chapter focused on modelling the transport and decay of FIO from the intertidal marshland as the diffuse source. Value of 3.33×10^5 cfu/m²/h that was quantified based on the literature search was applied as an idealised test case for modelling the deposition of FIO loading at the grazing marshland. The FIO that was accumulated during grazing activities was considered as a conservative mass with the decay effect during drying periods was assumed as much lower than the deposition rate. Comparisons in term of the mass balance that was based on the B-S release-kinetic model was made between different λ values, with the values between 1×10^{-2} to 1×10^{-3} m have overpredicted the balance at the node scale while underpredicted at the marshland scale for both scenarios of the conservative mass and the constant decay ($T_{90} = 14.9$ hours). The transport of the FIOs has resulted in the increase of the spreading area and the flush-out mass with the decrease in λ value for both scenarios, with site no. 26 was the most impacted shellfish bed. Zero exposure risk of the faecal contamination was recorded within the area of shellfish harvesting waters based on the threshold concentration of 300 cfu/100 ml as most of the FIOs mass from the diffuse source was retained at the south of the grazing marshland.

Chapter 7: Conclusion and recommendations

7.1 Conclusion

The research was conducted to improve the understanding of the processes experienced by the faecal indicator organisms (FIOs) while being transported in the estuarine environment, from different sources, and on their impacts to water quality at the sites of interest. Four research objectives were created to answer the main research question of “what processes are experienced by the FIOs while being transported in the estuarine environment” (Section 1.5).

The research was contributed to three major findings:

1. The understanding of the microbial behaviour in response to the complex estuarine environment. This understanding was not only based on the typical response from the environment, but also the understanding of the implicit response from the perspective of morphological characteristics of the microbial.
2. The representation of the tidal creek connectivity at the complex floodplain topography. This representation was not only done with the typical refinement around the feature of interest, but also was done with the sub-mesh scale design based on the hydraulic characteristic of floodplains.
3. The inclusion of the diffuse source for the transport model at the wetting and drying boundary. This inclusion was not only done with a simplified release assumption, but also was done with the integration to the release-kinetic model and was based on an active source.

7.1.1 Development and calibration of a hydrodynamic model for the SEBC waterbody

Prior to simulating the transport process of FIOs, the establishment of a hydrodynamic circulation model for the Severn Estuary and Bristol Channel (SEBC) was the first milestone in this research. The TELEMAC Modelling System was employed for its rigorous theoretical framework and flexibility in describing complex geometries through the unstructured mesh. A two-dimensional model domain was set up for the well-mixed SEBC waterbody. Tidal and stream forcings were specified at the open boundary for driving the primary circulation process. Based on the hydrodynamic calibration at several sites for the water level and the tidal current, the Manning’s n of 0.025 was found as an optimum value when compared to the measured

data. Therefore, future hydrodynamic models developed for this waterbody should be calibrated based on this bottom roughness value as for optimising the modelling effort.

7.1.2 Extension of the modelling domain at intertidal floodplains of the Loughor Estuary

To understand the influence of intertidal floodplains to the transport process of FIOs, the model domain was successfully extended to the floodplains of Carmarthen Bay, Loughor Estuary and Swansea Bay. Prior to the extension, the digital elevation model (DEM) was projected to the WGS 1984 UTM Zone 30N coordinate system for the integration with bathymetric data. The land-water boundary mask was successfully separated from the DEMs and the elevation of Liang et al. (2013) model was used to replace these gaps. The maximum buffer zone of 100 m was properly blended to the elevation difference at the transition between datasets of over 3.7 m. Therefore, the edge of the gap-fill data should be extended wide enough to minimise errors of the elevation difference during the integration between two datasets.

The extended model domain over the mean high water spring (MHWS) was successfully triangulated into a multi-scale resolution mesh with a better representation of the sub-mesh-scale features. Different resolution functions based on the bottom elevation over Loughor were assigned to the decomposed domain. Tidal creek networks with redistributed vertices were successfully extracted from the DEMs based on the steepest downslope flow direction. The sub-mesh-scale feature of creek networks was successfully represented by placing the mesh-nodes based on its vertices while optimising the computational cost based on the resolution functions at floodplains. Hydraulically connecting and blocking characteristics of the creek networks and training walls were improved by interpolating the elevation to their vertices based on three-dimensional polylines. Therefore, modelling the transport in the tidal creek-marsh system should consider designing the mesh-nodes with the sub-mesh-scale features in mind for improving the hydraulic conductivity. This is particularly important as the industrial and domestic wastes are frequently released into intertidal zones, either as point or diffuse source inputs (Bakar *et al.* 2019).

The spatial bottom roughness over Loughor was successfully parameterised based on principle terrain features of its intertidal floodplains. Prior to the parameterisation, the model domain was characterised into friction sub-domains of the subtidal channel, intertidal channel, tidal flat and marshland. Due to the unavailability of site-specific data, the Manning's n was estimated

based on the floodplain's global resistance factors and was conditioned into the uniform, minor, moderate and severe scenarios. The sensitivity analysis of the current circulation and transport process based on these roughness conditions was therefore conducted within this estuary. The site-specific data for parameterising the spatial bottom roughness at the intertidal floodplains was required for modelling an accurate transport process of FIOs in the future. This is especially important at marshland areas as the roughness of vegetative drag will increase with the increase in water depths.

The range of stream discharges into the Loughor Estuary were successfully estimated from the contributed catchments. Prior to the estimation, 25 sub-catchments and their stream networks were successfully delineated based on the derivation of runoff characteristics from the DEMs. Flow-duration percentiles of the ungauged stream discharges were calculated based on the statistic of 10 years discharge measurements around South West Wales. The developed LSR equations between discharges and areas were found as strongly correlated with the R^2 of 0.59 and above. This model therefore should be tested for a correct discharge boundary during a specific period prior to simulating the transport process of FIOs. It is because higher inflows from the catchments due to higher rainfall intensities will majorly influence the flushing process in the estuarine environment.

7.1.3 Modelling the transport and persistence of microbial tracers in the estuarine environment

Prior to modelling the transport process of FIOs, a release experiment of microbial tracers was conducted at the Loughor Estuary. Four release and five sampling sites were selected in and around this waterbody. The MS2 coliphage based on assessments of the tracer suitability was assigned at the furthest upstream site of Loughor Bridge for its highest titre concentration. The microbial tracers were introduced simultaneously each at the release sites and were sampled at the hourly interval for observing their concentration changes with time. The enumeration result of MS2 coliphage therefore was used for validating the transport and persistence model of microbial tracers in the Loughor Estuary.

Hydrodynamic processes were successfully validated at several sites to the measured data. The water level was correctly simulated at Burry Port, Llanelli and Lliw. The tidal current was significantly improved at site 1076H although insignificant changes in the water level were observed at nearby sites. These show a sensitive response of the tidal current to the mesh

refinement that has improved the elevation's variation at the floodplains (Cea and French 2012). The inundation extends and vertical features representation at floodplains respectively during flooding and drying were realistically simulated as a result of the mesh-nodes placement and the elevation interpolation based on vertices of the sub-mesh-scale features. The hydrodynamic dependence to the stream discharges along with the creek networks during drying was an indicator of the improvement in hydraulic conductivity within this tidal creek-marsh system. Therefore, designing the mesh-nodes with a better representation of the sub-mesh-scale features at the extension of intertidal floodplains should be considered for an improvement in the hydrodynamic simulation.

To understand the processes experienced by the FIOs while being transported, the sensitivity analysis on the microbial tracer diffusivity was successfully conducted within the Loughor waterbody. The transport of MS2 coliphage was modelled as the conservative mass assuming its high persistence in the marine environment. A decrease in the tracer diffusivity was observed with an increase in the mesh resolution for the transport simulation at two domains of the different refinement. A decrease in concentration gradients of the tracer was further observed with the increase in the assigned diffusivity value from 1×10^{-10} to 1×10^3 m²/s at an identical mesh resolution. Therefore, the mesh resolution should be scaled to the size of the eddy at a specific waterbody prior to the calibration of the diffusive transport. The constant viscosity is not suitable to be used with a multi-scale resolution mesh that scaled at the different range of eddy sizes. Two equations model that solves for the transport of turbulent energy and dissipation processes, i.e. k-epsilon model, should be used instead.

The sensitivity analysis on the bottom roughness was further conducted to the transport of the microbial tracer. Scenarios of the uniform, minor, moderate and severe floodplains roughness were simulated for the transport of MS2 coliphage. An increase in the tracer retention at the marshland was observed during low tides with the changes in roughness scenarios from minor to severe. The tracer concentration at the subtidal channel was further observed as less sensitive to the changes in roughness scenarios during high tides. Therefore, parameterisation of the spatial bottom roughness based on the site-specific data was necessary for estimating a correct distribution of the microbial tracer at intertidal floodplains while being transported. Furthermore, two consecutive analyses on the transport process were further indicated that MS2 coliphage was experiencing certain decay kinetics as the results were overpredicted the measured data.

To understand the processes experienced by the FIOs while being transported, the sensitivity analysis on the decay kinetics was successfully conducted to the microbial tracer in the estuarine waterbody. The decay process was modelled as the first-order degradation following Chick's Law (Chick 1910). The modelled concentrations were agreed to the measured data within the period of 12 hours and less when simulated at the constant decay rates either as the single T_{90} or the day-night T_{90s} . The two-stage (i.e. biphasic) degradation process was successfully modelled to inform that MS2 coliphage was experiencing the biphasic decay at the T_{90s} of 1 hour and between 50 to 125 hours for the labile and resistance groups respectively (Bakar *et al.* 2017). Therefore, modelling the transport of microbial tracers in the estuarine environment should consider the two-stage (i.e. biphasic) decay kinetic besides as the constant decay. This finding was further supported by the literature that microbial with different levels of persistence will be degraded at different rates (Charles *et al.* 2009) besides were experiencing mutation (Bucci *et al.* 2011). The transport of the microbial tracer should be further modelled as particles to investigate the hypothesis on the biphasic decay mechanisms (Bakar *et al.* 2018).

7.1.4 Modelling the transport and decay of FIOs from intertidal marshlands as the diffuse source

Prior to modelling the release process of FIOs, the model was successfully simulated its deposition at the grazing area. The FIOs loading from sheep was idealised as a product between the population density, manure rates and *E. coli* prevalence. The deposition at 3.33×10^5 cfu/m²/h was successfully modelled as a distributed source over the exposed area. This process was stopped at the time of the irrigation depth at modelling nodes was increased over 10 cm. The model therefore was actively simulated the deposition of FIOs as this process was benchmarked to the wetting and drying depths over the grazing area.

To understand the water quality impact of FIOs from a grazing marshland, the model was successfully simulated its releasing process into the water columns. The two-parametric Bradford-Schijven (B-S) model was successfully coupled for the release of FIOs besides was idealised as instantaneous flushing (IF) upon flooding. The B-S model with the threshold depth, between 1×10^{-2} to 1×10^{-4} m was overpredicted and underpredicted the mass balance at the node and the marshland scale respectively. The highest overprediction and

underprediction at RRE of 5.56% and 7.33% respectively for the scenario of conservative mass however were considered as the low range error. The wetting and drying process at the intertidal boundary therefore should be further understood prior to improve this error.

The processes of FIOs transport and decay from the diffuse source were successfully simulated in the estuarine water based on the B-S model. The moderate roughness was found as the most appropriate condition for the intertidal floodplains of Loughor Estuary (French 2003; Bilskie *et al.* 2015). The discharge boundary at 40% catchment inflows was empirically assigned based on the salinity transport condition during the tracer release experiment. The transport of FIOs was successfully modelled as the scenario of constant decay at the T_{90} of 14.9 hours (Kay *et al.* 2005; Bermúdez *et al.* 2014) besides as a conservative mass. The increase in the spreading area of FIOs and their flush-out mass was found with the decrease in _____ as for the case of conservative mass. The later released however was resulted in higher FIOs concentrations near tidal creeks and the adjacent marshland as for the case of decay. Therefore, _____ and T_{90} are two major parameters that control the transport and decay processes of FIOs from the diffuse source.

To understand the water quality impact of FIOs from a grazing marshland, the model was successfully simulated its exposure risk to the shellfish flesh. The accumulation and depuration of FIOs by filter-feeders were successfully idealized based on the ambient concentration relative to the threshold concentration of 300 cfu/100 ml (Kay *et al.* 2008). The risks of FIOs from ambient in term of the exposing time and its severity to the shellfish flesh were undetected even at any nearfield sampling station for both cases the conservative mass and decay. This was as expected due to the high retention of FIOs mass at the south of the grazing marshland for every post-flooding events. Therefore, higher FIOs deposition rates should be simulated based on the idealised value of 3.33×10^5 cfu/m²/h to observe the worst-case scenario.

7.2 Recommendations

Based on the advance in the representation of the tidal creek connectivity at the complex floodplain topography, the hydraulic conductivity of the tidal creek-marsh system shall be further evaluated. The information based on the microbial tracer experiment that was conducted

at the intertidal marshland should be applied for the model validation. The validated model should be served as a test case for modelling the transport of FIO as a diffuse source.

Based on the advance in the understanding of the microbial tracer behaviour in response to the complex estuarine environment, the transport of the microbial tracer should be further modelled as particles to investigate the hypothesis on the biphasic decay mechanisms. Accurate transport and decay model can be used to inform the WwTW managers for optimising the plant operation.

Based on the advance at the inclusion of the diffuse source for the transport model at the wetting and drying boundary, the model should be further improved for the conservation of mass. The decay model should be evaluated to represent more realistic conditions of the site. The improved model can be used for testing the impact of water quality from multiple sources.

References

- Adams, M.H. (1959). Bacteriophages. *Interscience Publishers*:1–592.
- Ahmadian, R., Falconer, R. and Lin, B. (2010). Hydro-environmental modelling of proposed Severn barrage, UK. *Proceedings of the Institution of Civil Engineers-Energy* **163**(3):107–117.
- Ahmadian, R., Falconer, R.A. and Bockelmann-Evans, B. (2014). Comparison of hydro-environmental impacts for ebb-only and two-way generation for a Severn Barrage. *Computers & Geosciences* **71**:11–19.
- Ahmadian, R., Olbert, A.I., Hartnett, M. and Falconer, R.A. (2014). Sea level rise in the Severn Estuary and Bristol Channel and impacts of a Severn Barrage. *Computers and Geosciences* **66**(5):94–105.
- Aldridge, B.N. and Garrett, J.M. (1973). Roughness coefficients for stream channels in Arizona. *USGS* **73**(3).
- Allen, J.R. (2000). Morphodynamics of Holocene salt marshes: a review sketch from the Atlantic and Southern North Sea coasts of Europe. *Quaternary Science Reviews* **19**(12):1155–1231.
- Almeida, C. and Soares, F. (2012). Microbiological monitoring of bivalves from the Ria Formosa Lagoon (south coast of Portugal): A 20 years of sanitary survey. *Marine Pollution Bulletin* **64**(2):252–262.
- Amin, M. and Flather, R.A. (1995). Investigation into the possibilities of using Bristol Channel models for tidal predictions. *Estuarine and Coastal Modeling*:41–52.
- Araújo, M.A.V.C., Mazzolari, A. and Trigo-Teixeira, A. (2011). Wave set-up in the modeling of storm surge at Viana do Castelo (Portugal). *Journal of Coastal Research* **64**:971.
- Arcement, G.J. and Schneider, V.R. (1989). Guide for selecting Manning's roughness coefficients for natural channels and flood plains. *U.S. Geological Survey Water-Supp*(Paper 2339):1–38.
- Atkinson, T.C. and Davis, P.M. (2000). Longitudinal dispersion in natural channels: 1. Experimental results from the River Severn, UK. *Hydrology and Earth System Sciences* **4**(3):345–353.
- Azinheira, D.L., Scott, D.T., Hession, W. and Hester, E.T. (2014). Comparison of effects of inset floodplains and hyporheic exchange induced by in stream structures on solute retention. *Water Resources Research* **50**(7):6168–6190.
- Bacopoulos, P., Parrish, D.M. and Hagen, S.C. (2011). Unstructured mesh assessment for tidal model of the South Atlantic Bight and its estuaries. *Journal of Hydraulic Research* **49**(4):487–

502.

Bakar, A.A., Ahmadian, R. and Falconer, R.A. (2017). Modelling the transport and decay processes of microbial tracers in a macro-tidal estuary. *Water Research* **123**:802–824.

Bakar, A.A., Ahmadian, R. and Falconer, R.A. (2018). Microbial tracer transport as particles with biphasic-decay. *Proceedings of the 5th IAHR Europe Congress*:171–172. doi: https://doi.org/10.3850/978-981-11-2731-1_359-cd.

Bakar, A.A., Ahmadian, R. and Falconer, R.A. (2019). The representation of tidal creek connectivity for a complex floodplain topography. *Proceedings of the 38th IAHR World Congress*:Submitted.

Barber, R.W. and Scott, L.J. (2000). Numerical modelling of tidal propagation in the Severn Estuary using a depth-adapted non-orthogonal grid. *Transactions on Ecology and the Environment*:126–36.

Bates, P.D. and Hervouet, J.M. (1999). A new method for moving–boundary hydrodynamic problems in shallow water. *Proceedings of the Royal Society of London A: Mathematical, Physical and Engineering Sciences* **455**(1988):3107–3128.

Bates, P.D., Marks, K.J. and Horritt, M.S. (2003). Optimal use of high resolution topographic data in flood inundation models. *Hydrological Processes* **17**(3):537–557.

Behrens, J. (1998). Atmospheric and ocean modeling with an adaptive finite element solver for the shallow-water equations. *Applied Numerical Mathematics* **26**(1–2):217–226.

Bermúdez, M., Ahmadian, R., Bockelmann-Evans, B., Cea, L. and Puertas, J. (2014). Sensitivity of an Escherichia Coli transport model to the decay rate in a coastal basin. *Proceedings of the 3rd IAHR Europe Congress*:1–10.

Bettencourt, F., Almeida, C., Santos, M.I., Pedroso, L. and Soares, F. (2013). Microbiological monitoring of *Ruditapes decussatus* from Ria Formosa Lagoon (South of Portugal). *Journal of Coastal Conservation* **17**(3):653–661.

Bicknell, B.R., Imhoff, J.C., Kittle Jr, J.L., Donigian Jr, A.S. and Johanson, R.C. (1996). Hydrological Simulation Program-Fortran: User’s manual for version 11. *USEPA*:1–755.

Bilgili, A., Smith, K.W. and Lynch, D.R. (2006). BatTri: A two-dimensional bathymetry-based unstructured triangular grid generator for finite element circulation modeling. *Computers & Geosciences* **32**(5):632–642.

Bilskie, M.V., Coggin, D., Hagen, S.C. and Medeiros, S.C. (2015). Terrain-driven unstructured mesh development through semi-automatic vertical feature extraction. *Advances in Water Resources* **86**:102–118.

Blain, C.A., Westerink, J.J. and Luetlich, R.A. (1998). Grid convergence studies for the

prediction of hurricane storm surge. *International Journal for Numerical Methods in Fluids* **26**(4):369–401.

Blanton, J.O., Garrett, A.J., Bollinger, J.S., Hayes, D.W., Koffman, L.D., Amft, J. and Moore, T. (2010). Transport and retention of a conservative tracer in an isolated creek–marsh system. *Estuarine, Coastal and Shelf Science* **87**(2):333–345.

Blaustein, R.A., Pachepsky, Y.A., Hill, R.L. and Shelton, D.R. (2015). Solid manure as a source of fecal indicator microorganisms: Release under simulated rainfall. *Environmental Science and Technology* **49**(13):7860–7869.

Blaustein, R.A., Pachepsky, Y.A., Shelton, D.R. and Hill, R.L. (2015). Release and removal of microorganisms from land-deposited animal waste and animal manures: A review of data and models. *Journal of environmental quality* **44**(5):1338–1354.

Bougeard, M., Le Saux, J.C., Pérenne, N., Baffaut, C., Robin, M. and Pommepey, M. (2011). Modeling of Escherichia coli fluxes on a catchment and the impact on coastal water and shellfish quality. *Journal of the American Water Resources Association* **47**(2):350–366.

Bowie, G.L., Mills, W.B., Porcella, D.B., Campbell, C.L., Pagenkopf, J.R., Rupp, G.L., ... Barnwell, T.O. (1985). Rates, constants, and kinetics formulations in surface water quality modeling. *U.S. Environmental Protection Agency*:1–455.

Bradford, S.A., Morales, V.L., Zhang, W., Harvey, R.W., Packman, A.I., Mohanram, A. and Welty, C. (2013). Transport and fate of microbial pathogens in agricultural settings. *Critical Reviews in Environmental Science and Technology* **43**(8):775–893.

Bradford, S.A. and Schijven, J. (2002). Release of Cryptosporidium and Giardia from dairy calf manure: impact of solution salinity. *Environmental Science and Technology* **36**(18):3916–3923.

Brauer, C.C., Teuling, A.J., Torfs, P.J.J.F. and Uijlenhoet, R. (2014). The Wageningen Lowland Runoff Simulator (WALRUS): a lumped rainfall–runoff model for catchments with shallow groundwater. *Geoscientific Model Development* **7**(5):2313–2332.

De Brauwere, A., Ouattara, N.K. and Servais, P. (2014). Modeling fecal indicator bacteria concentrations in natural surface waters: a review. *Critical Reviews in Environmental Science and Technology* **44**(21):2380–2453.

Brouwer, A.F., Eisenberg, M.C., Remais, J.V., Collender, P.A., Meza, R. and Eisenberg, J.N. (2017). Modeling biphasic environmental decay of pathogens and implications for risk analysis. *Environmental Science and Technology* **51**(4):2186–2196.

Bucci, V., Hoover, S. and Hellweger, F.L. (2012). Modeling adaptive mutation of enteric bacteria in surface water using agent-based methods. *Water, Air, & Soil Pollution* **223**(5):2035–

2049.

Bucci, V., Vulić, M., Ruan, X. and Hellweger, F.L. (2011). Population dynamics of *Escherichia coli* in surface water. *Journal of the American Water Resources Association* **47**(3):611–619.

Buczowski, B.J., Reid, J.A., Jenkins, C.J., Reid, J.M., Williams, S.J. and Flocks, J.G. (2006). USSEABED: Gulf of Mexico and Caribbean (Puerto Rico and US Virgin Islands) offshore surficial-sediment data release. *USGS*:1–50.

Bunya, S., Dietrich, J.C., Westerink, J.J., Ebersole, B.A., Smith, J.M., Atkinson, J.H., ... Cardone, V.J. (2010). A high-resolution coupled riverine flow, tide, wind, wind wave, and storm surge model for southern Louisiana and Mississippi. Part I: Model development and validation. *Monthly Weather Review* **138**(2):345–377.

Burchard, H. and Bolding, K. (2002). GETM: A general estuarine transport model - scientific documentation. *European Commission, Joint Research Centre, Institute for Environment and Sustainability*:1–157.

Burnham, K.P. and Anderson, D.R. (2003). Model selection and multimodel inference: a practical information-theoretic approach. *Springer Science & Business Media*.

Campos, C.J., Kershaw, S.R. and Lee, R.J. (2013). Environmental influences on faecal indicator organisms in coastal waters and their accumulation in bivalve shellfish. *Estuaries and Coasts* **36**(4):834–853.

Canann, S.A., Tristano, J.R. and Staten, M.L. (1998). An approach to combined Laplacian and optimization-based smoothing for triangular, quadrilateral, and quad-dominant meshes. *International Meshing Roundtable*:479–494.

Casas, A., Lane, S.N., Yu, D. and Benito, G. (2010). A method for parameterising roughness and topographic sub-grid scale effects in hydraulic modelling from LiDAR data. *Hydrology and Earth System Sciences* **14**(8):1567–1579.

Caviedes-Voullième, D., García-Navarro, P. and Murillo, J. (2012). Influence of mesh structure on 2D full shallow water equations and SCS Curve Number simulation of rainfall/runoff events. *Journal of Hydrology* **448–449**:39–59.

Cea, L. and French, J.R. (2012). Bathymetric error estimation for the calibration and validation of estuarine hydrodynamic models. *Estuarine, Coastal and Shelf Science* **100**:124–132.

Cerf, O. (1977). Tailing of survival curves of bacterial spores. *Journal of Applied Bacteriology* **42**(1):1–19.

Chan, Y.M., Thoe, W. and Lee, J.H. (2015). Field and laboratory studies of *Escherichia coli* decay rate in subtropical coastal water. *Journal of Hydro-environment Research* **9**(1):1–14.

Chapra, S.C. (2008). Surface water-quality modeling. :1–844.

- Charles, K.J., Shore, J., Sellwood, J., Laverick, M., Hart, A. and Pedley, S. (2009). Assessment of the stability of human viruses and coliphage in groundwater by PCR and infectivity methods. *Journal of applied microbiology* **106**(6):1827–1837.
- Chen, Z.T. and Guevara, J.A. (1987). Systematic selection of very important points (VIP) from digital terrain model for constructing triangular irregular networks. *Auto-carto* **8**:50–56.
- Chick, H. (1910). The process of disinfection by chemical agencies and hot water. *Epidemiology & Infection* **10**(2):237–286.
- Clements, K., Quilliam, R.S., Jones, D.L., Wilson, J. and Malham, S.K. (2015). Spatial and temporal heterogeneity of bacteria across an intertidal shellfish bed: implications for regulatory monitoring of faecal indicator organisms. *Science of the Total Environment* **506**:1–9.
- Coggin, D.W. (2008). *Lidar in Coastal Storm Surge Modeling: Modeling Linear Raised Features*. University of Central Florida.
- Connolly, J.P., Blumberg, A.F. and Quadrini, J.D. (1999). Modeling fate of pathogenic organisms in coastal waters of Oahu, Hawaii. *Journal of Environmental Engineering* **125**(5):398–406.
- Costabile, P. and Macchione, F. (2015). Enhancing river model set-up for 2-D dynamic flood modelling. *Environmental Modelling & Software* **67**:89–107.
- Council of the European Union (2000). Directive 2000/60/EC of the European Parliament and of the Council of 23 October 2000 establishing a framework for Community action in the field of water policy. *Official Journal of the European Communities* **L 327**:1–72.
- Council of the European Union (2004a). Corrigendum to Regulation (EC) No 853/2004 of the European Parliament and of the Council of 29 April 2004 laying down specific hygienic rules for food of animal origin. *Official Journal of the European Union* **L 226**:22–82.
- Council of the European Union (2004b). Regulation (EC) No 854/2004 of the European Parliament and of the Council of 29 April 2004 laying down specific rules for the organisation of official controls on products of animal origin intended for human consumption. *Official Journal of the European Union* **L 155**:206–321.
- Cowan, W.L. (1956). Estimating hydraulic roughness coefficients. *Agricultural Engineering* **37**(7):473–475.
- Crane, B.S. and Moore, J.A. (1986). Modeling enteric bacterial die-off: a review. *Water, Air, & Soil Pollution* **27**(3):411–439.
- Dabrowski, T., Doré, W.J., Lyons, K. and Nolan, G.D. (2014). Numerical modelling of blue mussel (*Mytilus edulis*) bacterial contamination. *Journal of Sea Research* **89**:52–63.
- Danielson, J.J., Poppenga, S.K., Brock, J.C., Evans, G.A., Tyler, D.J., Gesch, D.B., ... Barras,

- J.A. (2016). Topobathymetric elevation model development using a new methodology: Coastal national elevation database. *Journal of Coastal Research* **76**(SI):75–89.
- Dietrich, J.C., Tanaka, S., Westerink, J.J., Dawson, C.N., Luettich, R.A., Zijlema, M., ... Westerink, H.J. (2012). Performance of the unstructured-mesh, SWAN+ ADCIRC model in computing hurricane waves and surge. *Journal of Scientific Computing* **52**(2):468–497.
- Dorner, S.M., Huck, P.M. and Slawson, R.M. (2004). Estimating potential environmental loadings of *Cryptosporidium* spp. and *Campylobacter* spp. from livestock in the Grand River Watershed, Ontario, Canada. *Environmental Science & Technology* **38**(12):3370–3380.
- Drury, D.F. and Wheeler, D.C. (1982). Applications of a *Serratia marcescens* bacteriophage as a new microbial tracer of aqueous environments. *Journal of Applied Bacteriology* **53**(2):137–142.
- Dutka, B.J. and Kwan, K.K. (1980). Bacterial die-off and stream transport studies. *Water Research* **14**(7):909–915.
- Eakins, B.W. and Grothe, P.R. (2014). Challenges in building coastal digital elevation models. *Journal of Coastal Research* **30**(5):942–953.
- Easton, J.H., Gauthier, J.J., Lalor, M.M. and Pitt, R.E. (2005). Die-off of pathogenic *E. coli* O157:H7 in sewage contaminated waters. *Journal of the American Water Resources Association* **41**(5):1187–1193.
- Elliott, M., Burdon, D., Callaway, R., Franco, A., Hutchinson, T., Longshaw, M., ... Firmin, C. (2012). Burry inlet cockle mortalities investigation 2009–2011 (Technical report to the Environment Agency Wales). *Institute of Estuarine and Coastal Studies (University of Hull) YBB140-Tec(Final-2012):1–337*.
- Elliott, M., Burdon, D., Callaway, R., Franco, A., Hutchinson, T., Longshaw, M., ... Wither, A. (2012). *Burry Inlet Mortalities Investigation 2009-2011*. Hull, UK.
- Evans, G.P., Mollowney, B.M. and Spoel, N.C. (1990). Two-dimensional modelling of the Bristol Channel, UK. *Estuarine and Coastal Modeling*:331–340.
- Falconer, R.A., Lin, B., Kay, D. and Stapleton, C. (1998). Predicting coastal health risks using combined water quality and epidemiological models. In: V., B. and L.C., L. (eds.). *Hydroinformatics '98*. Rotterdam: A.A. Balkema, pp. 1213–1218.
- Falconer, R.A., Lin, B.L., Ahmadian, R. and Xia, J.Q. (2009). The Severn Barrage: hydroenvironmental impact assessment studies. *Proceedings of the 33rd IAHR World Congress*:2075–2082.
- FEMA (2014). Region II storm surge project—spatially varying nodal attribute parameters, federal emergency management agency. *Department of Homeland Security Technical Report*.

- Ferguson, C.M., Charles, K. and Deere, D.A. (2008). Quantification of microbial sources in drinking-water catchments. *Critical Reviews in Environmental Science and Technology* **39**(1):1–40.
- Field, D.A. (1988). Laplacian smoothing and Delaunay triangulations. *Communications in Applied Numerical Methods* **4**(6):709–712.
- Fischer-Antze, T., Stoesser, T., Bates, P. and Olsen, N.R.B. (2001). 3D numerical modelling of open-channel flow with submerged vegetation. *Journal of Hydraulic Research* **39**(3):303–310.
- De Floriani, L., Falcidieno, B., Nagy, G. and Pienovi, C. (1984). A hierarchical structure for surface approximation. *Computers & Graphics* **8**(2):183–193.
- Food and Agriculture Organization (2012). The state of world fisheries and aquaculture. *Agriculture Organization of the United Nations (Fisheries Department)* **3**:1–142.
- Foreman, M.G.G. (1984). A two-dimensional dispersion analysis of selected methods for solving the linearized shallow water equations. *Journal of Computational Physics* **56**(2):287–323.
- Francy, D.S. (2009). Use of predictive models and rapid methods to nowcast bacteria levels at coastal beaches. *Aquatic Ecosystem Health and Management* **12**(2):177–182.
- Freeman, T.G. (1991). Calculating catchment area with divergent flow based on a regular grid. *Computers & Geosciences* **17**(3):413–422.
- French, J.R. (2003). Airborne LiDAR in support of geomorphological and hydraulic modelling. *Earth Surface Processes and Landforms* **28**(3):321–335.
- French, J.R. and Clifford, N.J. (2000). Hydrodynamic modelling as a basis for explaining estuarine environmental dynamics: Some computational and methodological issues. *Hydrological Processes* **14**(11–12):2089–2108.
- French, R.H. (1985). Open-channel hydraulics.
- Gallegos, H.A., Schubert, J.E. and Sanders, B.F. (2009). Two-dimensional, high-resolution modeling of urban dam-break flooding: A case study of Baldwin Hills, California. *Advances in water resources* **32**(8):1323–1335.
- Gameson, A.L.H. (1974). Discharge of Sewage from Sea Outfalls. *Proceedings of an International Symposium at Church House, London*:1–455.
- Gao, G., Falconer, R.A. and Lin, B. (2011). Numerical modelling sediment-bacteria interaction processes in the Severn Estuary. *Journal of Water Resource and Protection* **3**(1):22–31.
- Geldreich, E.E. and Kenner, B.A. (1969). Concepts of fecal streptococci in stream pollution. *Water Pollution Control Federation*:336–352.

- Glover, R.S. (1984). The Bristol Channel—A case for special treatment. *Marine Pollution Bulletin* **15**(2):37–40.
- Goldscheider, N., Haller, L., Poté, J., Wildi, W. and Zopfi, J. (2007). Characterizing water circulation and contaminant transport in Lake Geneva using bacteriophage tracer experiments and limnological methods. *Environmental science & technology* **41**(15):5252–5258.
- Gooseff, M.N., Hall, R.O. and Tank, J.L. (2007). Relating transient storage to channel complexity in streams of varying land use in Jackson Hole, Wyoming. *Water Resources Research* **43**(1):1–10.
- Gorman, G.J., Piggott, M.D., Wells, M.R., Pain, C.C. and Allison, P.A. (2008). A systematic approach to unstructured mesh generation for ocean modelling using GMT and Terreno. *Computers & Geosciences* **34**(12):1721–1731.
- Grant, S.B., Sanders, B.F., Boehm, A.B., Redman, J.A., Kim, J.H., Mrše, R.D., ... Jones, B.H. (2001). Generation of enterococci bacteria in a coastal saltwater marsh and its impact on surf zone water quality. *Environmental Science and Technology* **35**(12):2407–2416.
- Greenberg, D.A., Dupont, F., Lyard, F.H., Lynch, D.R. and Werner, F.E. (2007). Resolution issues in numerical models of oceanic and coastal circulation. *Continental Shelf Research* **27**(9):1317–1343.
- Guber, A.K., Shelton, D.R., Pachepsky, Y.A., Sadeghi, A.M. and Sikora, L.J. (2006). Rainfall-induced release of fecal coliforms and other manure constituents: Comparison and modeling. *Applied and Environmental Microbiology* **72**(12):7531–7539.
- Hagen, S.C., Horstmann, O. and Bennett, R.J. (2002). An unstructured mesh generation algorithm for shallow water modeling. *International Journal of Computational Fluid Dynamics* **16**(2):83–91.
- Hagen, S.C. and Parrish, D.M. (2004a). Meshing requirements for tidal modeling in the western North Atlantic. *International Journal of Computational Fluid Dynamics* **18**(7):585–595.
- Hagen, S.C. and Parrish, D.M. (2004b). Unstructured mesh generation for the western North Atlantic tidal model domain. *Engineering with Computers* **20**(2):136–146.
- Hagen, S.C., Westerink, J.J. and Kolar, R.L. (2000). One-dimensional finite element grids based on a localized truncation error analysis. *International Journal for Numerical Methods in Fluids* **32**(2):241–261.
- Hagen, S.C., Westerink, J.J., Kolar, R.L. and Horstmann, O. (2001). Two-dimensional, unstructured mesh generation for tidal models. *International Journal for Numerical Methods in Fluids* **35**(6):669–686.
- Hagen, S.C., Zundel, A.K. and Kojima, S. (2006). Automatic, unstructured mesh generation

for tidal calculations in a large domain. *International Journal of Computational Fluid Dynamics* **20**(8):593–608.

Hall, B.R. and Freeman, G.E. (1994). Study of hydraulic roughness in wetland vegetation takes new look at Manning's n. *US Army Corps of Engineers Waterways Experiment Station, Wetlands Research Program Bulletin* **4**:1–4.

Hamrick, J.M. (1992). A three-dimensional environmental fluid dynamics computer code: Theoretical and computational aspects. *Applied Marine Science and Ocean Engineering* **317**:1–63.

Hannah, C.G. and Wright, D.G. (1995). Depth dependent analytical and numerical solutions for wind driven flow in the coastal ocean. *Quantitative Skill Assessment for Coastal Ocean Models*:125–152.

Harris, E.L., Falconer, R.A. and Lin, B. (2004). Modelling hydroenvironmental and health risk assessment parameters along the South Wales Coast. *Journal of Environmental Management* **73**(1):61–70.

Havelaar, A.H. and Hogeboom, W.M. (1984). A method for the enumeration of male specific bacteriophages in sewage. *Journal of Applied Bacteriology* **56**(3):439–447.

Hellweger, F.L. and Bucci, V. (2009). A bunch of tiny individuals: individual-based modeling for microbes. *Ecological Modelling* **220**(1):8–22.

Hellweger, F.L. and Masopust, P. (2008). Investigating the fate and transport of Escherichia coli in the Charles River, Boston, using high resolution observation and modeling. *Journal of the American Water Resources Association* **44**(2):509–522.

Hervouet, J.M. (2000). TELEMAC modelling system: an overview. *Hydrological Processes* **14**(13):2209–2210.

Hipsey, M.R., Antenucci, J.P. and Brookes, J.D. (2008). A generic, process based model of microbial pollution in aquatic systems. *Water Resources Research* **44**(7):1–26.

Hodges, B.R. (2015). Representing hydrodynamically important blocking features in coastal or riverine lidar topography. *Natural Hazards and Earth System Sciences* **15**(5):1011–1023.

Hoffmann, K.A. and Chiang, S.T. (1993). *Computational Fluid Dynamics for Engineers (Vol. 2)*. Engineering Education System.

Holden, N. (2004). LIDAR data: Technical note. *Environment Agency* **5**(3):1–16.

Holmgren, P. (1994). Multiple flow direction algorithms for runoff modelling in grid based elevation models: an empirical evaluation. *Hydrological Processes* **8**(4):327–334.

Homer, C.H., Fry, J.A. and Barnes, C.A. (2012). The national land cover database. *US*

Geological Survey Fact Sheet **3020**(4):1–4.

Horritt, M.S., Bates, P.D. and Mattinson, M.J. (2006). Effects of mesh resolution and topographic representation in 2D finite volume models of shallow water fluvial flow. *Journal of Hydrology* **329**:306–314.

Huang, G., Falconer, R.A., Boye, B.A. and Lin, B. (2015). Cloud to coast: Integrated assessment of environmental exposure, health impacts and risk perceptions of faecal organisms in coastal waters. *International Journal of River Basin Management* **13**(1):73–86.

Iwamoto, M., Ayers, T., Mahon, B.E. and Swerdlow, D.L. (2010). Epidemiology of seafood-associated infections in the United States. *Clinical Microbiology Reviews* **23**(2):399–411.

Jamieson, R., Gordon, R., Joy, D. and Lee, H. (2004). Assessing microbial pollution of rural surface waters: A review of current watershed scale modeling approaches. *Agricultural Water Management* **70**(1):1–17.

Jenson, S.K. and Domingue, J.O. (1988). Extracting topographic structure from digital elevation data for geographic information system analysis. *Photogrammetric Engineering and Remote Sensing* **54**(11):1593–1600.

Ji, Z.G. (2008). Hydrodynamics and water quality: modeling rivers, lakes, and estuaries. *John Wiley & Sons*:1–624.

Jones, N.L. and Richards, D.R. (1992). Mesh generation for estuarine flow modeling. *Journal of Waterway, Port, Coastal, and Ocean Engineering* **118**(6):599–614.

Kalyanapu, A.J., Burian, S.J. and McPherson, T.N. (2010). Effect of land use-based surface roughness on hydrologic model output. *Journal of Spatial Hydrology* **9**(2):51–71.

Käser, D., Graf, T., Cochand, F., McLaren, R., Therrien, R. and Brunner, P. (2014). Channel representation in physically based models coupling groundwater and surface water: pitfalls and how to avoid them. *Groundwater* **52**(6):827–836.

Kashefipour, S.M., Lin, B. and Falconer, R.A. (2006). Modelling the fate of faecal indicators in a coastal basin. *Water Research* **40**(7):1413–1425.

Katul, G., Wiberg, P., Albertson, J. and Hornberger, G. (2002). A mixing layer theory for flow resistance in shallow streams. *Water Resources Research* **38**(11):1–8.

Kay, D., Kershaw, S., Lee, R., Wyer, M.D., Watkins, J. and Francis, C. (2008). Results of field investigations into the impact of intermittent sewage discharges on the microbiological quality of wild mussels (*Mytilus edulis*) in a tidal estuary. *Water Research* **42**(12):3033–3046.

Kay, D., Stapleton, C.M., Wyer, M.D., McDonald, A.T., Crowther, J., Paul, N., ... Humphrey, N. (2005). Decay of intestinal enterococci concentrations in high-energy estuarine and coastal waters: towards real-time T90 values for modelling faecal indicators in recreational waters.

Water Research **39**(4):655–667.

Kim, B., Sanders, B.F., Schubert, J.E. and Famiglietti, J.S. (2014). Mesh type tradeoffs in 2D hydrodynamic modeling of flooding with a Godunov-based flow solver. *Advances in Water Resources* **68**:42–61.

Koppejan, H. (2000). Toelichting bij de vegetatiekartering Westerschelde 1998. *Rijkswaterstaat, Meetkundige Dienst*.

Lambrechts, J., Hanert, E., Deleersnijder, E., Bernard, P.E., Legat, V., Remacle, J.F. and Wolanski, E. (2008). A multi-scale model of the hydrodynamics of the whole Great Barrier Reef. *Estuarine, Coastal and Shelf Science* **79**(1):143–151.

Lawrence, D.S.L., Allen, J.R.L. and Havelock, G.M. (2004). Salt marsh morphodynamics: an investigation of tidal flows and marsh channel equilibrium. *Journal of Coastal Research* **20**(1):301–316.

Leclerc, H., Schwartzbrod, L. and Dei-Cas, E. (2002). Microbial agents associated with waterborne diseases. *Critical Reviews in Microbiology* **28**(4):371–409.

Lee, J. (1989). A drop heuristic conversion method for extracting irregular networks for digital elevation models. *Proceedings of GIS/LIS '89*:30–39.

Lees, D. (2000). Viruses and bivalve shellfish. *International Journal of Food Microbiology* **59**(1–2):81–116.

Legrand, S., Deleersnijder, É., Delhez, É. and Legat, V. (2007). Unstructured, anisotropic mesh generation for the Northwestern European continental shelf, the continental slope and the neighbouring ocean. *Continental Shelf Research* **27**(9):1344–1356.

Legrand, S., Deleersnijder, E., Hanert, E., Legat, V. and Wolanski, E. (2006). High-resolution, unstructured meshes for hydrodynamic models of the Great Barrier Reef, Australia. *Estuarine, Coastal and Shelf Science* **68**(1):36–46.

Lessard, P. and Beck, M.B. (1990). Operational water quality management: control of storm sewage at a wastewater treatment plant. *Research Journal of the Water Pollution Control Federation*:810–819.

Li, Z. and Hodges, B.R. (2018). Model instability and channel connectivity for 2D coastal marsh simulations. *Environmental Fluid Mechanics*:1–30.

Liang, D., Wang, X., Bockelmann-Evans, B.N. and Falconer, R.A. (2013). Study on nutrient distribution and interaction with sediments in a macro-tidal estuary. *Advances in Water Resources* **52**:207–220.

Liang, Q. (2011). A structured but non uniform Cartesian grid based model for the shallow water equations. *International Journal for Numerical Methods in Fluids* **66**(5):537–554.

- Liang, Q. and Borthwick, A.G. (2009). Adaptive quadtree simulation of shallow flows with wet–dry fronts over complex topography. *Computers & Fluids* **38**(2):221–234.
- Liang, Q., Du, G., Hall, J.W. and Borthwick, A.G. (2008). Flood inundation modeling with an adaptive quadtree grid shallow water equation solver. *Journal of Hydraulic Engineering* **134**(11):1603–1610.
- Limerinos, J.T. (1970). Determination of the Manning coefficient from measured bed roughness in natural channels. *U.S. Geological Survey Water-Supp*(Paper 1898-B):1–53.
- Liu, Y., Zhou, M., Zhao, S., Zhan, W., Yang, K. and Li, M. (2015). Automated extraction of tidal creeks from airborne laser altimetry data. *Journal of Hydrology* **527**:1006–1020.
- Loder, J.W. (1980). Topographic rectification of tidal currents on the sides of Georges Bank. *Journal of Physical Oceanography* **10**(9):1399–1416.
- Loewen, P.C. and Hengge-Aronis, R. (1994). The role of the sigma factor σ S (KatF) in bacterial global regulation. *Annual Reviews in Microbiology* **48**(1):53–80.
- Lohani, B. and Mason, D.C. (2001). Application of airborne scanning laser altimetry to the study of tidal channel geomorphology. *ISPRS Journal of Photogrammetry and Remote Sensing* **56**(2):100–120.
- Luetlich, R.A. and Westerink, J.J. (1995). Continental shelf scale convergence studies with a barotropic tidal model. *Quantitative Skill Assessment for Coastal Ocean Models*:349–371.
- Lynch, D.R., Ip, J.T., Naimie, C.E. and Werner, F.E. (1995). Convergence studies of tidally-rectified circulation on Georges Bank. *Coastal and Estuarine Studies*:153–174.
- Malham, S.K., Rajko-Nenow, P., Howlett, E., Tuson, K.E., Perkins, T.L., Pallett, D.W., ... McDonald, J.E. (2014). The interaction of human microbial pathogens, particulate material and nutrients in estuarine environments and their impacts on recreational and shellfish waters. *Environmental Science: Processes & Impacts* **16**(9):2145–2155.
- Malki, R. (2009). *The Influence of Saltmarsh Vegetation Canopies on Hydrodynamics in the Intertidal Zone*. Cardiff University.
- Manning, A.J., Langston, W.J. and Jonas, P.J.C. (2010). A review of sediment dynamics in the Severn Estuary: influence of flocculation. *Marine Pollution Bulletin* **61**(1–3):37–51.
- Marcus, W.A., Roberts, K., Harvey, L. and Tackman, G. (1992). An evaluation of methods for estimating Manning’s n in small mountain streams. *Mountain Research and Development*:227–239.
- Marks, K. and Bates, P. (2000). Integration of high resolution topographic data with floodplain flow models. *Hydrological Processes* **14**(11–12):2109–2122.
- Martin, Y., Troussellier, M. and Bonnefont, J.L. (1998). Adaptive responses of *E. coli* to

- marine environmental stresses: a modelling approach based on viability and dormancy concepts. *Oceanologica Acta* **21**(6):951–964.
- Martyr, R.C., Dietrich, J.C., Westerink, J.J., Kerr, P.C., Dawson, C., Smith, J.M., ... Roberts, H.J. (2012). Simulating hurricane storm surge in the lower Mississippi River under varying flow conditions. *Journal of Hydraulic Engineering* **139**(5):492–501.
- Mason, D.C., Scott, T.R. and Wang, H.J. (2006). Extraction of tidal channel networks from airborne scanning laser altimetry. *ISPRS Journal of Photogrammetry and Remote Sensing* **61**(2):67–83.
- Mazzolari, A., Trigo-Teixeira, A. and Araújo, M.A.V. (2013). A multi-criteria meshing method applied to a shallow water model. *Journal of Coastal Research* **65**(SI):1170–1175.
- Mazzolari, A., Trigo-Teixeira, A. and Araújo, M.A.V. (2015). Evaluation of different meshing criteria for areas exposed to flooding. *Computers & Fluids* **121**:81–91.
- McCuen, R.H. (1989). *Hydrologic Analysis and Design*. Englewood Cliffs, NJ: Prentice-Hall.
- Medeiros, S.C., Ali, T., Hagen, S.C. and Raiford, J.P. (2011). Development of a seamless topographic/bathymetric digital terrain model for Tampa Bay, Florida. *Photogrammetric Engineering and Remote Sensing* **77**(12):1249–1256.
- Medeiros, S.C., Hagen, S.C. and Weishampel, J.F. (2012). Comparison of floodplain surface roughness parameters derived from land cover data and field measurements. *Journal of Hydrology* **452**:139–149.
- Medema, G.J., Bahar, M. and Schets, F.M. (1997). Survival of *Cryptosporidium parvum*, *Escherichia coli*, faecal enterococci and *Clostridium perfringens* in river water: influence of temperature and autochthonous microorganisms. *Water Science and Technology* **35**(11–12):249–252.
- Morgan, N., Munro, D., Mollowney, B.M. and Linwood, P. (1995). Sewage dispersion in an estuary with distinct ebb and flood channels. *Environment international* **21**(2):123–130.
- Murdoch, N., Jonas, P.J.C., Falconer, R.A. and Lin, B. (2010). A modelling assessment of contaminant distributions in the Severn Estuary. *Marine Pollution Bulletin* **61**(1–3):124–131.
- Nightingale, P.D., Malin, G., Law, C.S., Watson, A.J., Liss, P.S., Liddicoat, M.I., ... Upstill-Goddard, R.C. (2000). In situ evaluation of air-sea gas exchange parameterizations using novel conservative and volatile tracers. *Global Biogeochemical Cycles* **14**(1):373–387.
- Noh, S.J., Lee, J.H., Lee, S., Kawaike, K. and Seo, D.J. (2018). Hyper-resolution 1D-2D urban flood modelling using LiDAR data and hybrid parallelization. *Environmental Modelling & Software* **103**:131–145.
- O’Callaghan, J.F. and Mark, D.M. (1984). The extraction of drainage networks from digital

- elevation data. *Computer vision, graphics, and image processing* **28**(3):323–344.
- Oden, J.T., Demkowicz, L., Rachowicz, W. and Westermann, T.A. (1990). A posteriori error analysis in finite elements: The element residual method for symmetrizable problems with applications to compressible Euler and Navier-Stokes equations. *Computer Methods in Applied Mechanics and Engineering* **82**(1–3):183–203.
- Olbert, A.I., Hartnett, M., Dabrowski, T. and Mikolajewicz, U. (2011). Long-term inter-annual variability of a cyclonic gyre in the western Irish Sea. *Continental Shelf Research* **31**(13):1343–1356.
- Owen, A. (1980). A three-dimensional model of the Bristol Channel. *Journal of Physical Oceanography* **10**(8):1290–1302.
- Owens, M. (1984). Severn Estuary - an appraisal of water quality. *Marine Pollution Bulletin* **15**(2):41–47.
- Parrish, D. (2007). *Target Element Sizes for Finite Element Tidal Models from a Domain-Wide, Localized Truncation Error Analysis Incorporating Bottom Stress and Coriolis Force*. University of Central Florida.
- Parrish, D.M. and Hagen, S.C. (2007). 2D unstructured mesh generation for oceanic and coastal tidal models from a localized truncation error analysis with complex derivatives. *International Journal of Computational Fluid Dynamics* **21**(7–8):277–296.
- Parrish, D.M. and Hagen, S.C. (2009). Incorporating spatially variable bottom stress and Coriolis force into 2D, a posteriori, unstructured mesh generation for shallow water models. *International Journal for Numerical Methods in Fluids* **60**(3):237–261.
- Passalacqua, P., Belmont, P. and Foufoula Georgiou, E. (2012). Automatic geomorphic feature extraction from lidar in flat and engineered landscapes. *Water Resources Research* **48**(3):1–18.
- Perkins, T.L., Perrow, K., Rajko-Nenow, P., Jago, C.F., Jones, D.L., Malham, S.K. and McDonald, J.E. (2016). Decay rates of faecal indicator bacteria from sewage and ovine faeces in brackish and freshwater microcosms with contrasting suspended particulate matter concentrations. *Science of the Total Environment* **572**:1645–1652.
- Petryk, S. and Bosmajian III, G. (1975). Analysis of flow through vegetation. *Journal of the Hydraulics Division* **101**(HY7):871–884.
- Petterson, S.R. and Ashbolt, N.J. (2001). Viral risks associated with wastewater reuse: modeling virus persistence on wastewater irrigated salad crops. *Water Science and Technology* **43**(12):23–26.
- Pike, E.B., Bufton, A.W.J. and Gould, D.J. (1969). The use of *Serratia indica* and *Bacillus subtilis* var. *niger* spores for tracing sewage dispersion in the sea. *Journal of Applied*

Bacteriology **32**(2):206–216.

Poggio, L. and Soille, P. (2012). Influence of pit removal methods on river network position. *Hydrological Processes* **26**(13):1984–1990.

Potasman, I., Paz, A. and Odeh, M. (2002). Infectious outbreaks associated with bivalve shellfish consumption: a worldwide perspective. *Clinical Infectious Diseases* **35**(8):921–928.

Le Provost, C., Genco, M.L. and Lyard, F. (1995). Modeling and predicting tides over the World Ocean. *Coastal and Estuarine Studies*:175–175.

Ralston, D.K. and Stacey, M.T. (2005). Longitudinal dispersion and lateral circulation in the intertidal zone. *Journal of Geophysical Research: Oceans* **110**:1–17.

Rapinel, S., Rossignol, N., Gore, O., Jambon, O., Bouger, G., Mansons, J. and Bonis, A. (2018). Daily monitoring of shallow and fine-grained water patterns in wet grasslands combining aerial LiDAR data and in situ piezometric measurements. *Sustainability* **10**(3):708.

Ree, W.O. and Crow, F.R. (1977). Friction factors for vegetated waterways of small slope. *Report ARS-S-151*:1–61.

Rinaldo, A., Fagherazzi, S., Lanzoni, S., Marani, M. and Dietrich, W.E. (1999). Tidal networks: 2. Watershed delineation and comparative network morphology. *Water Resources Research* **35**(12):3905–3917.

Riou, P., Le Saux, J.C., Dumas, F., Caprais, M.P., Le Guyader, S.F. and Pommepuy, M. (2007). Microbial impact of small tributaries on water and shellfish quality in shallow coastal areas. *Water Research* **41**(12):2774–2786.

Rippey, S.R. (1994). Infectious diseases associated with molluscan shellfish consumption. *Clinical Microbiology Reviews* **7**(4):419–425.

Risley, J.C., Stonewall, A. and Haluska, T.L. (2008). Estimating flow-duration and low-flow frequency statistics for unregulated streams in Oregon. *USGS*.

Rossi, P., Dörfliger, N., Kennedy, K., Müller, I. and Aragno, M. (1998). Bacteriophages as surface and ground water tracers. *Hydrology & Earth system sciences* **2**(1):101–110.

Runkel, R.L. (1998). One-dimensional transport with inflow and storage (OTIS): A solute transport model for streams and rivers. *USGS Water-Reso*.

Saito, T. and Toriwaki, J.I. (1994). New algorithms for euclidean distance transformation of an n-dimensional digitized picture with applications. *Pattern Recognition* **27**(11):1551–1565.

Saleh, F., Ramaswamy, V., Wang, Y., Georgas, N., Blumberg, A. and Pullen, J. (2017). A multi-scale ensemble-based framework for forecasting compound coastal-riverine flooding: The Hackensack-Passaic watershed and Newark Bay. *Advances in Water Resources* **110**:371–386.

- Sampath, A. and Shan, J. (2007). Building boundary tracing and regularization from airborne LiDAR point clouds. *Photogrammetric Engineering & Remote Sensing* **73**(7):805–812.
- Sanders, B.F., Arega, F. and Sutula, M. (2005). Modeling the dry-weather tidal cycling of fecal indicator bacteria in surface waters of an intertidal wetland. *Water Research* **39**(14):3394–3408.
- Schernewski, G., Fischer, E., Huttula, T., Jost, G. and Ras, M. (2012). Simulation tools to support bathing water quality management: Escherichia coli bacteria in a Baltic lagoon. *Journal of Coastal Conservation* **16**(4):473–488.
- Schnauder, I., Bockelmann-Evans, B. and Lin, B. (2007). Modelling faecal bacteria pathways in receiving waters. *Proceedings of the Institution of Civil Engineers-Maritime Engineering* **160**(4):143–154.
- Schubert, J.E. and Sanders, B.F. (2012). Building treatments for urban flood inundation models and implications for predictive skill and modeling efficiency. *Advances in Water Resources* **41**:49–64.
- Schubert, J.E., Sanders, B.F., Smith, M.J. and Wright, N.G. (2008). Unstructured mesh generation and landcover-based resistance for hydrodynamic modeling of urban flooding. *Advances in Water Resources* **31**(12):1603–1621.
- Sellin, R.H., Bryant, T.B. and Loveless, J.H. (2003). An improved method for roughening floodplains on physical river models. *Journal of Hydraulic Research* **41**(1):3–14.
- Shen, C., Phanikumar, M.S., Fong, T.T., Aslam, I., McElmurry, S.P., Molloy, S.L. and Rose, J.B. (2008). Evaluating bacteriophage P22 as a tracer in a complex surface water system: the Grand River, Michigan. *Environmental Science & Technology* **42**(7):2426–2431.
- Shen, J., Jia, J.J. and Sisson, G.M. (2006). Inverse estimation of nonpoint sources of fecal coliform for establishing allowable load for Wye River, Maryland. *Water Research* **40**(18):3333–3342.
- Shoemaker, L., Lahlou, M., Bryer, M., Kumar, D. and Kratt, K. (1997). Compendium of tools for watershed assessment and TMDL development. *USEPA*:1–244.
- Simpson, J.M., Santo Domingo, J.W. and Reasoner, D.J. (2002). Microbial source tracking: State of the science. *Environmental Science & Technology* **36**(24):5279–5288.
- Sinton, L.W., Finlay, R.K. and Lynch, P.A. (1999). Sunlight inactivation of fecal bacteriophages and bacteria in sewage-polluted seawater. *Applied and Environmental Microbiology* **65**(8):3605–3613.
- Standing Committee of Analysts (SCA) (2000). The microbiology of recreational and environmental waters: Methods for the examination of waters and associated materials.

Environment Agency:1–84.

Stapleton, C.M., Kay, D., Magill, S.H., Wyer, M.D., Davies, C., Watkins, J., ... Crowther, J. (2011). Quantitative microbial source apportionment as a tool in aiding the identification of microbial risk factors in shellfish harvesting waters: the Loch Etive case study. *Aquaculture Research* **42**(s1):1–20.

Stapleton, C.M., Wyer, M.D., Kay, D., Bradford, M., Humphrey, N., Wilkinson, J., ... Francis, C.A. (2007). Fate and transport of particles in estuaries - Volume IV: Numerical modelling for bathing water enterococci estimation in the Severn estuary. *Environment Agency Science Report SC000002*(SR4):1–138.

Steets, B.M. and Holden, P.A. (2003). A mechanistic model of runoff-associated fecal coliform fate and transport through a coastal lagoon. *Water Research* **37**(3):589–608.

Stephens, C.V. (1986). A three-dimensional model for tides and salinity in the Bristol Channel. *Continental Shelf Research* **6**(4):531–560.

Sterk, A., Schijven, J., de Roda Husman, A.M. and de Nijs, T. (2016). Effect of climate change on runoff of *Campylobacter* and *Cryptosporidium* from land to surface water. *Water Research* **95**:90–102.

Sullivan, J.C., Torres, R., Garrett, A., Blanton, J., Alexander, C., Robinson, M., ... Hayes, D. (2015). Complexity in salt marsh circulation for a semienclosed basin. *Journal of Geophysical Research: Earth Surface* **120**(10):1973–1989.

Symonds, A.M., Vijverberg, T., Post, S., van der Spek, B.J., Henrotte, J. and Sokolewicz, M. (2017). Comparison between Mike 21 FM, Delft3D and Delft3D FM flow models of Western Port Bay, Australia. *Coastal Engineering Proceedings* **1**(35):1–12.

Tarboton, D.G. (1997). A new method for the determination of flow directions and upslope areas in grid digital elevation models. *Water Resources Research* **33**(2):309–319.

Tarboton, D.G., Bras, R.L. and Rodriguez Iturbe, I. (1991). On the extraction of channel networks from digital elevation data. *Hydrological Processes* **5**(1):81–100.

Temmerman, S., Bouma, T.J., Govers, G., Wang, Z.B., De Vries, M.B. and Herman, P.M.J. (2005). Impact of vegetation on flow routing and sedimentation patterns: Three dimensional modeling for a tidal marsh. *Journal of Geophysical Research: Earth Surface* **110**(F04019):1–18.

Thomann, R.V. and Mueller, J.A. (1987). *Principles of Surface Water Quality Modeling and Control*. New York: Harper & Row.

Troussellier, M., Bonnefont, J.L., Courties, C., Derrien, A., Dupray, E., Gauthier, M., ... Pommepuy, M. (1998). Responses of enteric bacteria to environmental stresses in seawater.

Oceanologica Acta **21**(6):965–981.

Tsubaki, R. and Fujita, I. (2010). Unstructured grid generation using LiDAR data for urban flood inundation modelling. *Hydrological processes* **24**(11):1404–1420.

Uncles, R.J. (1981). A numerical simulation of the vertical and horizontal M2 tide in the Bristol Channel and comparisons with observed data. *Limnology and Oceanography* **26**(3):571–577.

Uncles, R.J. (1984). Hydrodynamics of the Bristol Channel. *Marine Pollution Bulletin* **15**(2):47–53.

US Department of Agriculture (1963). Guide for selecting roughness coefficient "n" values for channels.

Vadas, P.A., Kleinman, P.J.A. and Sharpley, A.N. (2004). A simple method to predict dissolved phosphorus in runoff from surface-applied manures. *Journal of Environmental Quality* **33**(2):749–756.

Wang, C.F., Hsu, M.H. and Kuo, A.Y. (2004). Residence time of the Danshuei River estuary, Taiwan. *Estuarine, Coastal and Shelf Science* **60**(3):381–393.

Wang, F. and Newkirk, R. (1988). A knowledge-based system for highway network extraction. *IEEE Transactions on Geoscience and Remote Sensing* **26**(5):525–531.

Weng, Q. and Quattrochi, D.A. (eds.) (2006). *Urban Remote Sensing*. CRC Press.

Westerink, J.J., Luettich, R.A., Feyen, J.C., Atkinson, J.H., Dawson, C., Roberts, H.J., ... Pourtaheri, H. (2008). A basin- to channel-scale unstructured grid hurricane storm surge model applied to southern Louisiana. *Monthly Weather Review* **136**(3):833–864.

Wilkinson, J., Jenkins, A., Wyer, M. and Kay, D. (1995). Modelling faecal coliform dynamics in streams and rivers. *Water Research* **29**(3):847–855.

Winterbourn, J.B., Clements, K., Lowther, J.A., Malham, S.K., McDonald, J.E. and Jones, D.L. (2016). Use of *Mytilus edulis* biosentinels to investigate spatial patterns of norovirus and faecal indicator organism contamination around coastal sewage discharges. *Water Research* **105**:241–250.

World Health Organization (2003). Guidelines for safe recreational water environments: Coastal and fresh waters (Vol. 1). **1**.

Wyer, M., Kay, D., Naylor, S., Thomas, S. and Fracchiolla, A. (2014). Loughor estuary microbial tracer study logistics: Field study outline. *Interreg 4A Smart Coasts and Sustainable Communities Project*:1–7.

Wyer, M.D., Kay, D., Watkins, J., Davies, C., Kay, C., Thomas, R., ... Moore, H. (2010). Evaluating short-term changes in recreational water quality during a hydrograph event using a combination of microbial tracers, environmental microbiology, microbial source tracking and

hydrological techniques: a case study in Southwest Wales, UK. *Water Research* **44**(16):4783–4795.

Xia, J., Falconer, R.A. and Lin, B. (2010a). Impact of different tidal renewable energy projects on the hydrodynamic processes in the Severn Estuary, UK. *Ocean Modelling* **32**(1–2):86–104.

Xia, J., Falconer, R.A. and Lin, B. (2010b). Hydrodynamic impact of a tidal barrage in the Severn Estuary, UK. *Renewable Energy* **35**(7):1455–1468.

Xu, M. and Chua, V.P. (2017). A numerical study on land-based pollutant transport in Singapore coastal waters with a coupled hydrologic-hydrodynamic model. *Journal of Hydro-environment Research* **14**:119–142.

Yang, L., Lin, B. and Falconer, R.A. (2008). Modelling enteric bacteria level in coastal and estuarine waters. *Proceedings of the Institution of Civil Engineers Engineering and Computational Mechanics* **161**(4):179–186.

Youell, M., Osborn, H., Stuart, T., Evans, S. and Llewellyn-Davies, R. (2013a). South West Area Shellfish Waters Investigation Project - (Shellfish) Waterbody Action Report Burry Inlet (North) November 2011 - March 2013. :1–39.

Youell, M., Osborn, H., Stuart, T., Evans, S. and Llewellyn-Davies, R. (2013b). South West Area Shellfish Waters Investigation Project - (Shellfish) Waterbody Action Report Burry Inlet (South) November 2011 - March 2013. :1–46.

National Research Council Canada (NRCC). Available at: www.nrc-cnrc.gc.ca.

British Oceanographic Data Centre (BODC). Available at: www.bodc.ac.uk.

Appendix A

A.1 Shellfish Water Directive (SWD) compliance studies at Loughor Estuary

Table A.1: Reason for failure (RFF) table for Burry Inlet (BI) North (Youell *et al.* 2013a).

Tier 1: Issue	Tier 2: Activity/source	Tier 3: Sector	Certainty Suspected, probable or confirmed	Which quality element?	Apportionment	Comment
Point source	Sewage discharge (intermittent)	Water industry	Probable	Flesh standard 'G' compliance	Moderate	Cross Hands and Cwm Tawel STW Emergency/Storm operation.
Point source	Sewage discharge (intermittent)	Water industry	Probable	Flesh standard 'G' compliance	Minor	Yard bridge CSO.
Point source	Sewage discharge (intermittent)	Water industry	Suspected	Flesh standard 'G' compliance	Minor	Assets in the lower Nant Dyfatty catchment, Pembrey STW Emergency Overflow and Kymer Canal assets.
Point source	Abandoned mine	Non-coal mining	Suspected	Flesh standard 'G' compliance	Minor	Discharge identified on the Afon Dulais.

Point source	Sewage discharge (continuous)	Water industry	Suspected	Flesh standard 'G' compliance	Moderate	Cross Hands and Cwm Tawel STW operation and loading from Llangenech STW.
Point source	Sewage discharge (intermittent)	Water industry	Suspected	Flesh standard 'G' compliance	Moderate	Issues with Burry port SPS Emergency/Storm overflow and Main Sewer Bursts.
Diffuse source	Agricultural and rural land management	Agricultural and rural land management	Probable	Flesh standard 'G' compliance	Moderate	Problematic tributaries identified in the Lliedi, Gwili and Dulais catchments.
Diffuse source	Sewage discharge (diffuse)	Urban	Suspected	Flesh standard 'G' compliance	Minor	Misconnection – several inputs identified on the lower urbanised stretch of the Lliedi and suspected throughout the wider Loughor catchment.
Point source	Unsewered domestic sewage	Other	Suspected	Flesh standard 'G' compliance	Minor	Approx. 160 domestic discharges in Loughor catchment.
Point source	Industrial discharge (EPR)	Industry	Suspected	Flesh standard 'G' compliance	Minor	Shellfish processing discharges. Greater localised impact on BI South but likely to impact BI North.

Diffuse source	Agricultural and rural land management	Agricultural and rural land management	Probable	Flesh standard 'G' compliance	Minor	Large area of historically grazed salt marsh on North Gower coast and to a lesser extent on South Carmarthenshire.
----------------	--	--	----------	-------------------------------	-------	--

Table A.2: Reason for failure (RFF) table for Burry Inlet (BI) South (Youell *et al.* 2013b).

Tier 1: Issue	Tier 2: Activity/source	Tier 3: Sector	Certainty Suspected, probable or confirmed	Which quality element?	Apportionment	Comment
Point source	Unsewered domestic sewage	Other	Suspected	Flesh standard 'G' compliance	Minor	Approx. 160 small-scale private domestic discharges throughout Loughor catchment.
Point source	Industrial discharge (EPR)	Industry	Suspected	Flesh standard 'G' compliance	Moderate	Several problematic shellfish processing discharges in Crofty/Penclawdd area.
Diffuse source	Agricultural and rural land management	Agricultural and rural land management	Probable	Flesh standard 'G' compliance	Moderate	Large area of historically grazed salt marsh on North Gower coast and to a lesser extent on South Carmarthenshire.

Point source	Sewage discharge (continuous)	Water industry	Suspected	Flesh standard 'G' compliance	Moderate	Garnswllt, Llanrhidian, Reynoldston and Llanmadoc STW.
Diffuse source	Agricultural and rural land management	Agricultural and rural land management	Probable	Flesh standard 'G' compliance	Moderate	Diffuse agricultural issues prevalent throughout the Lliw, Llan and Loughor catchments.
Diffuse source	Sewage discharge (diffuse)	Urban	Suspected	Flesh standard 'G' compliance	Minor	Misconnection – suspected throughout the BI South catchment.
Diffuse source	Sewage discharge (diffuse)	Urban	Probable	Flesh standard 'G' compliance	Minor	Penclawdd boat slip misconnection.
Point source	Sewage discharge (intermittent)	Water industry	Probable	Flesh standard 'G' compliance	Moderate	Numerous DCWW intermittent assets, specifically those identified in the Lliw/Llan catchments.
Point source	Sewage discharge (intermittent)	Private/trade	Suspected	Flesh standard 'G' compliance	Moderate	Llanrhidian Caravan Park final effluent.

Appendix B

B.1 Stream flows boundary condition

Table B.1: Details of the 29 inputs from rivers at upstream boundaries of the model domain (Stapleton *et al.* 2007).

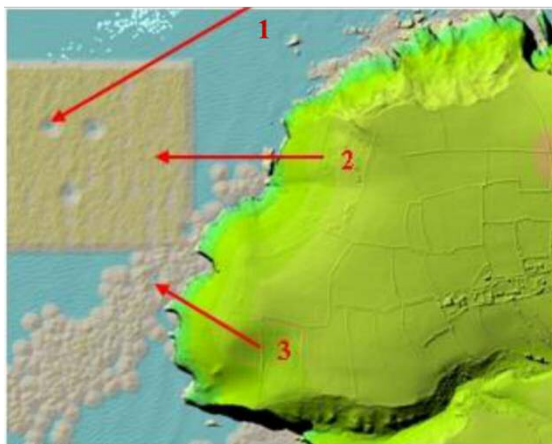
Catchment	OS grid (metres)		Coordinate		Mean annual discharge (m ³ /s)
	Easting	Northing	Longitude	Latitude	
1. Tawe	266598	191653	3°55'26"	51°36'20"	-
2. Nedd	271881	192432	3°55'26"	51°36'20"	-
3. Afan	274556	188667	3°48'28"	51°35'05"	4.97
4. Kenfig	277919	183473	3°45'35"	51°32'12"	-
5. Ogwr	286123	175787	3°38'50"	51°28'00"	-
6. Ely	318583	172672	3°09'20"	51°26'40"	4.43
7. Taff	318218	172672	3°09'20"	51°26'40"	22.42
8. Rhymney	322282	177474	3°07'20"	51°28'30"	6.02
9. Ebbw	331480	183805	2°58'30"	51°31'18"	7.29
10. Usk	331798	183633	2°58'30"	51°31'18"	19.56
11. Wye	354231	190223	-	-	73.96
12. Severn	381548	219350	-	-	75.03
13. Frome	375173	210497	-	-	1.53
14. Little Avon	366257	200314	-	-	1.28
15. Avon	350115	178583	2°43'20"	51°30'20"	18.38
16. Portbury Ditch	347817	177420	2°43'20"	51°30'20"	-
17. Land Yeo	338862	170310	2°52'40"	51°26'00"	0.27
18. Congresbury Yeo	336494	166748	2°55'30"	51°23'55"	0.54
19. Banwell	-	-	2°55'30"	51°23'55"	-
20. Axe	330852	158536	3°01'10"	51°13'20"	-
21. Brue	329428	147527	3°00'15"	51°13'20"	1.67
22. Parrett	329130	146844	3°00'15"	51°13'20"	0.98
23. Kilve Stream	314335	144453	3°13'50"	51°11'50"	-
24. Doniford Stream	309059	143213	3°18'15"	51°11'35"	0.98

25. Washford River	306997	143524	3°18'15"	51°11'35"	0.87
26. Pill River	302706	143520	3°23'25"	51°11'35"	-
27. Avill River	300883	144247	3°23'25"	51°11'35"	-
28. Aller-Horner Water	289210	148512	3°35'15"	51°13'58"	0.45
29. East-West Lyn	272291	149678	3°49'45"	51°14'20"	-

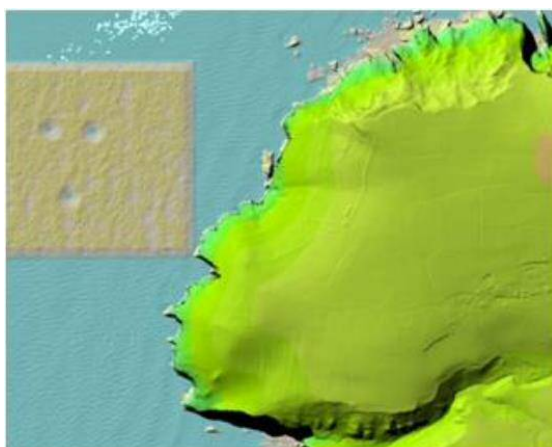
Appendix C

C.1 Lidar composite

The images below show features in the DSM and DTM, which may be present in coastal areas of the merged Lidar composite product. Concave spots (1) and convex spots (3) in coastal areas are the results of the feathering processes between different Lidar surveys. If there are gaps in the most recent dataset captured in the coverage over the sea, these gaps will be filled by pulling values from an older dataset. As the data will have been captured at different states of the tide, a feathering up or down of the Lidar surface at these points would be seen. Unexpected shapes over the sea (2) may also be seen, which are due to an older dataset having been used to fill gaps where no coverage exists in the more recent dataset. The older dataset in this example has been flown at a time of higher tidal levels.



a. DSM



b. DTM

Figure C.1: DSM and DTM at 2 m resolution.

C.2 DEM data processing

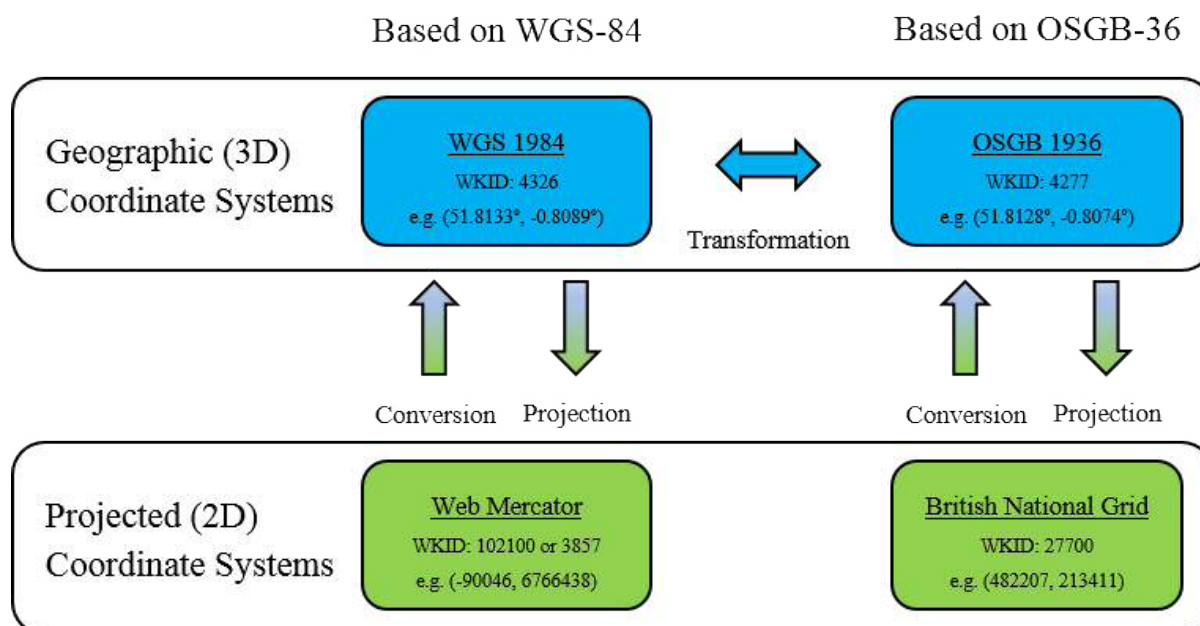


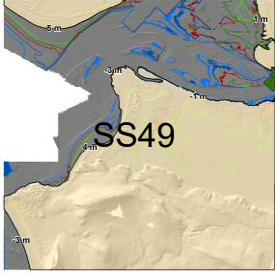
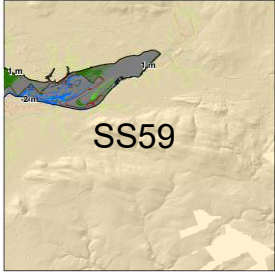


Figure C.2: Horizontal datum conversion.

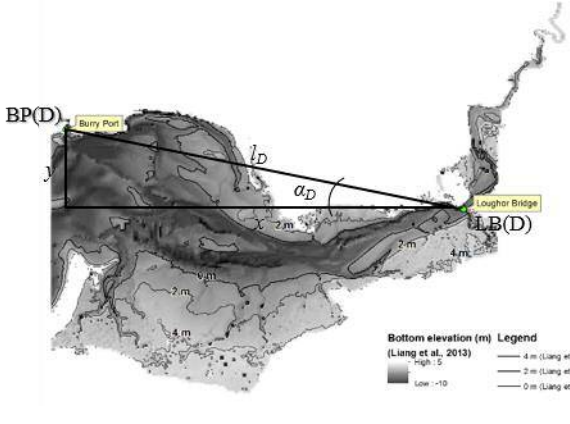
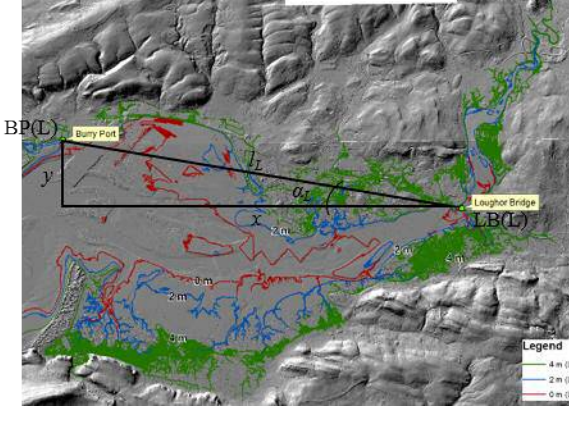
Table C.1: Data tiles for the area of Loughor Estuary* (i.e. SN40, SN50, SS49, SS59) with descriptions of the continuous-closed delineated boundary (i.e. thick-black lines).

Data tiles	Descriptions
 <p>SN40</p>	<p>For data tile SN40 at the north-west of Loughor Estuary, the lowest contour line at 0 m is used which just above the water surface at Pwll, elevated to 1 m at Llanelli to eliminate the higher water, and 2 m contour line is used at the east of Burry Port to consider the morphological changes.</p>
 <p>SN50</p>	<p>For data tile SN50 at north-east of Loughor Estuary, the lidar surveys flew at this area during low tides did not capture any water surfaces above 0 m, as the area is at the higher elevation and upstream to the estuarine lower tidal limit. The original edges of data tile are being used as the land boundary for this area.</p>

	<p>For data tile SS49 at the south-west of Loughor Estuary, the lowest contour line at -3 m is used to include the land extension at Rhossili and Whiteford Point and elevated up to 4 m at Llanmadoc and 5 m at Pembrey to consider the morphological changes. The 1 m contour line is used at Llanelli same as in SN40 to eliminate the higher water.</p>
	<p>For data tile SS59 at the south-east of Loughor Estuary, the lowest contour line at -2 m is used which just above the water surface at the east of Llanrhidian marsh and elevated to above 1 m contour to eliminate the higher water at downstream of Loughor Bridge until proximity of Llanelli.</p>

* descriptions of the continuous-closed delineated boundary for the area of Swansea Bay (i.e. SS68, SS78, SS69, SS79) were following the similar approach.

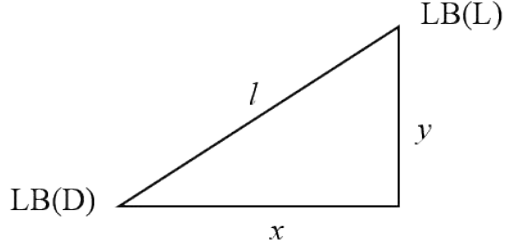
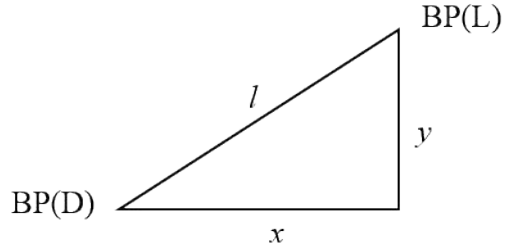
Table C.2: The calculation on horizontal datum projections for the Liang *et al.* (2013) elevation data that based at the reference point (i.e. Loughor Bridge) of Lidar DEM.

Liang <i>et al.</i> (2013)	Lidar DEM
	
<p>Loughor Bridge (12024.433, 5425.076) Burry Port (469.470, 7752.938)</p>	<p>Loughor Bridge (425125.365, 5724044.499) Burry Port (413524.756, 5726036.595)</p>
<p>$x = 12024.433 - 469.470 = 11554.963 \text{ m}$ $y = 7752.938 - 5425.076 = 2327.862 \text{ m}$ $\text{—————} = 11787.116 \text{ m}$</p>	<p>$x = 425125.365 - 413524.756 = 11600.609 \text{ m}$ $y = 5726036.595 - 5724044.499 = 2092.096 \text{ m}$ $\text{—————} = 11787.748 \text{ m}$</p>

$\tan \alpha_D = 2327.862/11554.963, \alpha_D = 11.39$ deg.	$\tan \alpha_L = 2092.096/11600.609, \alpha_L = 10.22$ deg.
--	--

From Table C.2, $l_L - l_D = 0.632$ m which is acceptable, and α_D greater than α_L at 1.17 deg.

Table C.3: The calculation of horizontal and vertical distances of two reference points (i.e. Loughor Bridge and Burry Port) between two elevation datasets (i.e. Liang *et al.* (2013) and Lidar DEM).

<p>1. Loughor Bridge</p> <p>$x = 425125.365 - 12024.433 = 413100.932$ m</p> <p>$y = 5724044.499 - 5425.076 = 5718619.423$ m</p>	
<p>2. Burry Port</p> <p>$x = 413524.756 - 469.470 = 413055.286$ m</p> <p>$y = 5726036.595 - 7752.938 = 5718283.657$ m</p>	

From Table C.3, horizontal (x) and vertical (y) distances of Loughor Bridge (LB) and Burry Port (BP) between the Liang *et al.* (2013) elevation data (D) and Lidar DEM data (L) are identical. Hence, horizontal datum projection is conducted by translating and rotating the Liang *et al.* (2013) elevation data based at the reference point (Loughor Bridge) of Lidar at $x = 413,100.932$ m and $y = 5,718,619.423$ m, and at angle 1.17 deg. respectively. The data is rotated using the rotation matrix as follows:

Eqn. C.1

Eqn. C.2

Eqn. C.3

The rotation on the Liang *et al.* (2013) elevation data could also be conducted by using the Data Management Toolbox of ArcGIS (i.e. data management tools; projections and transformations; raster; rotate).

C.3 Streams discharge estimation

Table C.4: The flow-duration percentiles calculated based on the 10 years mean daily streams discharge measured at 18 gauging stations at South West Wales (Source: National River Flow Archive).

Gauging stations	Catchment area (km ²)	10% flow (m ³ /s)	20% flow (m ³ /s)	30% flow (m ³ /s)	40% flow (m ³ /s)	50% flow (m ³ /s)	60% flow (m ³ /s)	70% flow (m ³ /s)	80% flow (m ³ /s)	90% flow (m ³ /s)
58002 - Neath at Resolven	190.90	1.06	1.66	2.30	3.04	4.02	5.82	8.99	13.85	23.18
58004 - Afan at Cwmafan	81.50	1.20	1.59	1.94	2.37	2.98	3.88	5.30	7.50	11.70
58006 - Mellte at Pontneddfechan	65.80	0.47	0.67	0.88	1.13	1.52	2.25	3.54	5.08	7.86
58008 - Dulais at Cilfrew	43.00	0.32	0.45	0.60	0.77	1.02	1.39	2.00	2.97	5.05
58010 - Hepste at Esgair Carnau	11.00	0.05	0.08	0.11	0.15	0.21	0.33	0.53	0.91	1.83
58012 - Afan at Marcroft Weir	87.80	1.14	1.55	1.93	2.41	3.03	3.96	5.36	7.63	12.04
59001 - Tawe at Ynystanglws	227.70	1.97	2.80	3.68	4.80	6.26	8.46	12.10	18.30	30.30
59002 - Loughor at Tir-y-Dail	46.40	0.42	0.57	0.73	0.93	1.17	1.52	2.06	2.96	4.94
60002 - Cothi at Felin Mynachdy	297.80	1.49	2.49	3.62	4.97	6.71	9.16	12.66	17.70	27.20
60003 - Taf at Clog-y-Fran	217.30	1.17	1.84	2.68	3.64	4.81	6.24	8.32	11.30	17.20
60004 - Dewi Fawr at Glasfryn Ford	36.70	0.19	0.30	0.45	0.61	0.81	1.09	1.49	2.02	3.06
60005 - Bran at Llandoverly	66.80	0.22	0.42	0.63	0.90	1.25	1.73	2.44	3.55	5.60
60006 - Gwili at Glangwili	129.50	0.69	1.12	1.64	2.25	2.98	4.01	5.46	7.72	11.90

60007 - Tywi at Dolau Hirion	231.80	2.76	3.31	3.83	4.53	5.68	7.63	10.40	14.60	22.70
60008 - Tywi at Ystradffin	89.80	1.17	1.94	2.57	2.73	2.84	3.08	3.92	6.12	8.15
60009 - Sawdde at Felin-y-Cwm	77.50	0.50	0.75	1.03	1.37	1.76	2.35	3.24	4.61	7.53
60012 - Twrch at Ddol Las	20.70	0.06	0.11	0.17	0.25	0.36	0.50	0.70	1.05	1.73
60013 - Cothi at Pont Ynys Brechfa	261.60	1.03	1.40	2.64	3.70	5.32	6.85	8.96	12.00	20.26

Table C.5: Estimates of the stream discharge statistics at the 25 ungauged stream outlets based on the developed LSR equations that referred to the sub-catchment areas.

Stream outlets	Catchment area (km ²)	10% flow (m ³ /s)	20% flow (m ³ /s)	30% flow (m ³ /s)	40% flow (m ³ /s)	50% flow (m ³ /s)	60% flow (m ³ /s)	70% flow (m ³ /s)	80% flow (m ³ /s)	90% flow (m ³ /s)
01 - Unnamed	1.77	0.17	0.26	0.28	0.28	0.26	0.31	0.47	0.82	1.24
02 - Unnamed	4.44	0.18	0.28	0.31	0.32	0.32	0.39	0.58	0.97	1.48
03 - Unnamed	1.25	0.16	0.25	0.27	0.27	0.25	0.29	0.45	0.79	1.19
04 - Dulas	7.75	0.20	0.31	0.35	0.38	0.39	0.49	0.72	1.16	1.79
05 - Unnamed	3.06	0.18	0.27	0.29	0.30	0.29	0.35	0.52	0.89	1.36
06 - Lleidi	19.47	0.27	0.41	0.50	0.57	0.66	0.84	1.20	1.85	2.88
07 - Dafen	8.97	0.21	0.32	0.37	0.40	0.42	0.52	0.77	1.23	1.90
08 - Unnamed	2.80	0.17	0.27	0.29	0.30	0.28	0.34	0.51	0.88	1.33
09 - Morlais	22.58	0.29	0.44	0.53	0.62	0.72	0.93	1.33	2.03	3.17

10 - Gwili	33.33	0.36	0.53	0.67	0.80	0.96	1.26	1.78	2.65	4.17
11 - Unnamed	3.98	0.18	0.28	0.31	0.32	0.31	0.37	0.56	0.94	1.44
12 - Loughor	142.22	1.01	1.46	2.01	2.60	3.39	4.53	6.29	8.99	14.28
13 - Unnamed	2.25	0.17	0.26	0.28	0.29	0.27	0.32	0.49	0.84	1.28
14 - Unnamed	5.29	0.19	0.29	0.32	0.34	0.34	0.41	0.62	1.02	1.56
15 - Dulais	9.92	0.22	0.33	0.38	0.42	0.44	0.55	0.81	1.29	1.99
16 - Unnamed	1.70	0.17	0.26	0.28	0.28	0.26	0.31	0.47	0.81	1.23
17 - Unnamed	1.43	0.17	0.25	0.27	0.28	0.25	0.30	0.46	0.80	1.20
18 - <u>Lliw</u>	33.75	0.36	0.53	0.67	0.81	0.97	1.27	1.79	2.68	4.21
19 - <u>Llan</u>	32.68	0.35	0.52	0.66	0.79	0.95	1.24	1.75	2.61	4.11
20 - Unnamed	6.46	0.20	0.30	0.34	0.36	0.37	0.45	0.66	1.09	1.67
21 - Unnamed	1.12	0.16	0.25	0.27	0.27	0.25	0.29	0.44	0.78	1.18
22 - Unnamed	1.84	0.17	0.26	0.28	0.28	0.26	0.31	0.47	0.82	1.24
23 - Unnamed	1.23	0.16	0.25	0.27	0.27	0.25	0.29	0.45	0.78	1.19
24 - Salthouse Pill	4.87	0.19	0.28	0.32	0.33	0.33	0.40	0.60	1.00	1.52
25 - Burry Pill	30.94	0.34	0.51	0.64	0.76	0.91	1.19	1.68	2.51	3.95

Appendix D

D.1 Microbial tracer release experiment

Table D.1: Details of tracer release sites.

Site	Name	Easting	Northing	Latitude	Longitude
101	Great Pill – Llanrhidian	247633	193098	51.616043	4.201725
201	Morlais River – Crofty	252686	194791	51.632592	4.129941
501	Loughor Bridge – A484	256107	198049	51.662752	4.081887
601	Afon Lliedi – North Dock	249932	199443	51.673662	4.171701

Table D.2: Details of marine/estuarine monitoring sites.

Site	Name	Easting	Northing	Latitude	Longitude
408	Rhossili DSP* (Hillend)	241125	190857	51.594101	4.295065
409	Broughton Bay	241875	193136	51.614787	4.285274
410	Burry Port slipway	244877	200068	51.677904	4.245026
411	Loughor Boat Club slip	256521	198272	51.664862	4.075997
412	Pembrey DSP*	240078	199784	51.674006	4.314246

* Designated sampling point

Table D.3(a): Microbial background concentrations at release sites (16th June 2014).

Site	Name	MS2 coliphage (pfu/ml)	S.marcescens phage (pfu/ml)	Ent. cloacae phage (cfu/ml)	Phi-X-174 coliphage (cfu/ml)
101	Great Pill – Llanrhidian (09:16 a.m.)	0	0	0	16
	Great Pill – Llanrhidian (09:58 a.m.)	0	0	0	3
201	Morlais River – Crofty (09:41 a.m.)	1	0	0	0
	Morlais River – Crofty (10:23 a.m.)	2	0	0	4

501	Loughor Bridge – A484 (10:50 a.m.)	1	0	0	3
	Loughor Bridge – A484 (11:41 a.m.)	0	0	0	4
601	Afon Lliedi – North Dock (11:14 a.m.)	39	0	0	17
	Afon Lliedi – North Dock (12:05 p.m.)	15	0	0	9

Table D.3(b): Microbial background concentrations at release sites (15th July 2014).

Site	Name	MS2 coliphage (pfu/ml)	S.marcescens phage (pfu/ml)	Ent. cloacae phage (cfu/ml)	Phi-X-174 coliphage (cfu/ml)
101	Great Pill – Llanrhidian (21:08 p.m.)	1	0	0	9
	Great Pill – Llanrhidian (21:22 p.m.)	0	0	0	7
201	Morlais River – Crofty (20:26 p.m.)	2	0	1	34
	Morlais River – Crofty (20:46 p.m.)	1	0	0	29
501	Loughor Bridge – A484 (18:31 p.m.)	7	0	0	17
	Loughor Bridge – A484 (19:22 p.m.)	1	0	0	37
601	Afon Lliedi – North Dock (18:56 p.m.)	1	0	0	7
	Afon Lliedi – North Dock (19:43 p.m.)	1	0	0	6

Table D.3(c): Microbial background concentrations at release sites (12th Aug 2014).

Site	Name	MS2 coliphage (pfu/ml)	S.marcescens phage (pfu/ml)	Ent. cloacae phage (cfu/ml)	Phi-X-174 coliphage (cfu/ml)
101	Great Pill – Llanrhidian (20:32 p.m.)	0	0	0	85
	Great Pill – Llanrhidian (21:03 p.m.)	0	0	0	50
201	Morlais River – Crofty (20:05 p.m.)	1	0	0	49
	Morlais River – Crofty (21:32 p.m.)	0	0	0	50
501	Loughor Bridge – A484 (18:20 p.m.)	3	0	0	29
	Loughor Bridge – A484 (19:04 p.m.)	0	0	0	6
601	Afon Lliedi – North Dock (18:42 p.m.)	1	0	0	7
	Afon Lliedi – North Dock (19:23 p.m.)	0	0	0	9

Table D.3(d): Microbial background concentrations at release sites (9th, pm times and 10th, am times Sept 2014).

Site	Name	MS2 coliphage (pfu/ml)	S.marcescens phage (pfu/ml)	Ent. cloacae phage (cfu/ml)	Phi-X-174 coliphage (cfu/ml)
101	Great Pill – Llanrhidian (08:35 a.m.)	0	0	0	6
201	Morlais River – Crofty (08:00 a.m.)	0	0	1	15
501	Loughor Bridge – A484 (20:30 p.m.)	1	0	0	2
601	Afon Lliedi – North Dock (19:23 p.m.)	1	0	0	0

Table D.4: Microbial background concentrations at sampling sites (9th, pm times and 10th, am times Sept 2014).

Site	Name	MS2 coliphage (pfu/ml)	S.marcescens phage (pfu/ml)	Ent. cloacae phage (cfu/ml)	Phi-X-174 coliphage (cfu/ml)
408	Rhossili DSP (Hillend) (10:20 a.m.)	0	0	0	0
409	Broughton Bay (09:30 a.m.)	0	0	0	1
410	Burry Port slipway (20:50 p.m.)	1	0	0	2
411	Loughor Boat Club slip (19:30 p.m.)	0	0	0	0
412	Pembrey DSP (19:00 p.m.)	0	0	0	0

D.2 Environmental data analysis

Table D.5: Statistical results from environmental data analysis.

Sampling location	Temperature (deg. Celsius)	Salinity (ppt)	Light extinction (m ⁻¹)	Water depth (m)	k _b (d ⁻¹)	k _i (d ⁻¹)	T _{90(d)} (hr)	T _{90(l)} (hr)
Rhossili DSP								
Max	16.2000	37.0000	8.9116	11.5886	1.1782	41.1116	54.6346	23.1238
3 rd Quartile	15.8000	36.6000	7.8003	10.1613	1.1395	25.5688	51.0247	10.9822
Median	15.4000	36.2000	7.0631	6.8876	1.1181	12.0106	49.4348	5.3480
1 st Quartile	15.1000	35.7750	6.5296	3.8478	1.0832	5.0362	48.5055	2.8701
Min	14.1000	34.2000	5.2803	2.5194	1.0117	1.3332	46.9112	1.7411
Mean	15.3585	36.0679	7.1322	7.0206	1.1122	15.8669	49.7566	8.5295
Broughton								
Max	16.0000	38.3000	46.2210	8.9997	1.1628	485.6864	60.9512	19.4080
3 rd Quartile	15.4000	36.3000	10.0365	7.4946	1.1070	72.4763	51.8359	8.1922
Median	15.2500	35.7000	8.0963	4.3040	1.0841	17.9225	50.9822	2.5931
1 st Quartile	14.8250	34.8000	6.8818	1.2966	1.0663	4.8133	49.9308	0.8999
Min	12.8000	32.0000	4.6895	0.0395	0.9068	1.1904	47.5337	0.1292
Mean	15.0940	35.5339	9.9140	4.4122	1.0833	90.4494	51.1025	5.4171
Loughor Boat Club								
Max	14.3000	30.6000	99.6270	5.5444	0.9425	49.4393	113.0171	36.9088

3 rd Quartile	13.7250	27.3000	39.2550	3.9190	0.8741	31.5063	102.5832	4.2540
Median	13.2000	17.1300	20.7435	1.5317	0.7187	16.6257	77.0888	3.1913
1 st Quartile	12.8000	3.4025	9.2499	0.6679	0.5388	12.5275	63.2309	1.7667
Min	11.6000	1.1200	5.1023	0.3376	0.4891	0.9449	58.6448	1.2579
Mean	13.1482	15.6786	25.3605	2.2709	0.7060	21.1651	83.1277	6.8555
Burry Port Harbour								
Max	15.2000	36.0000	33.9660	8.4866	1.0840	717.7444	61.9025	16.5957
3 rd Quartile	14.9000	35.3000	8.7694	6.9198	1.0594	143.2956	55.7779	6.1851
Median	14.7500	34.8000	7.3307	3.9498	1.0374	25.1290	53.2800	1.9652
1 st Quartile	14.3000	33.0750	6.3964	1.0059	0.9910	6.6699	52.1726	0.5124
Min	13.0000	23.9000	3.7413	0.0002	0.8929	2.2236	50.9866	0.0769
Mean	14.5167	33.9911	8.1370	4.0243	1.0218	133.8643	54.2347	4.5432
Pembrey DSP								
Max	15.2000	37.2000	14.6160	9.8610	1.0911	146.7067	62.8011	20.1964
3 rd Quartile	14.8000	35.9250	10.1333	8.3878	1.0655	50.9310	56.6606	7.5649
Median	14.3000	35.2000	6.7567	5.1523	1.0269	20.5261	53.8225	2.5612
1 st Quartile	13.9500	34.6000	5.7015	2.1260	0.9755	6.2886	51.8765	1.1964
Min	12.1000	31.8000	4.3166	0.8468	0.8801	1.7033	50.6573	0.3832
Mean	14.2429	35.0964	7.8558	5.2729	1.0187	39.3305	54.4116	5.9724

D.3 Sensitivity analysis on the transport of salinity

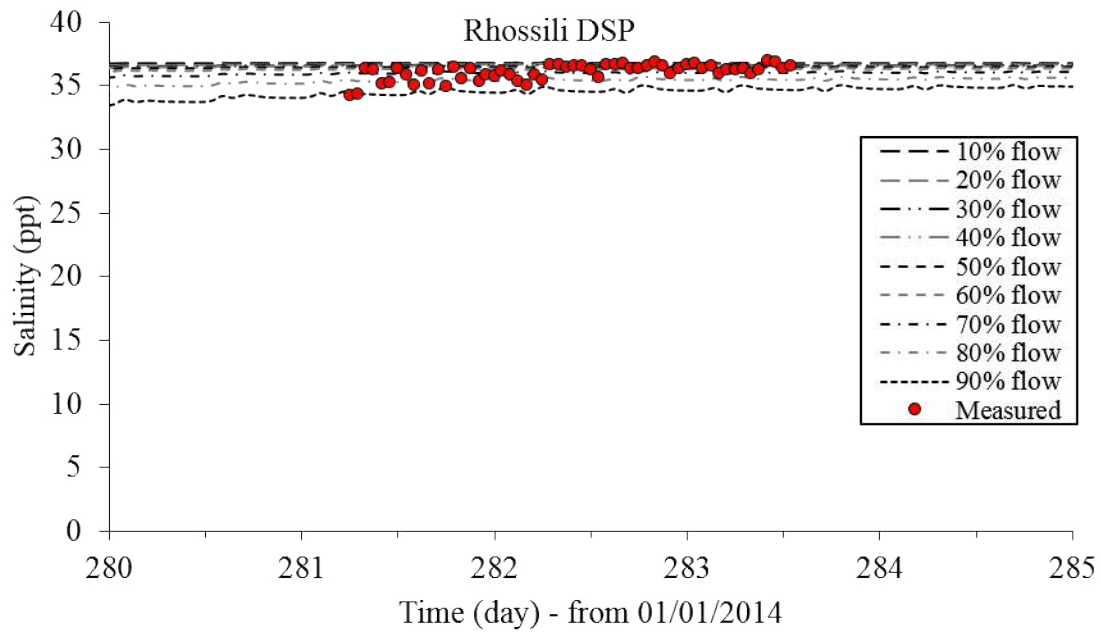


Figure D.1(a): Time series of the modelled salinity at Rhossili DSP as compared to the measured data with the range of catchment inflows between 10 to 90%.

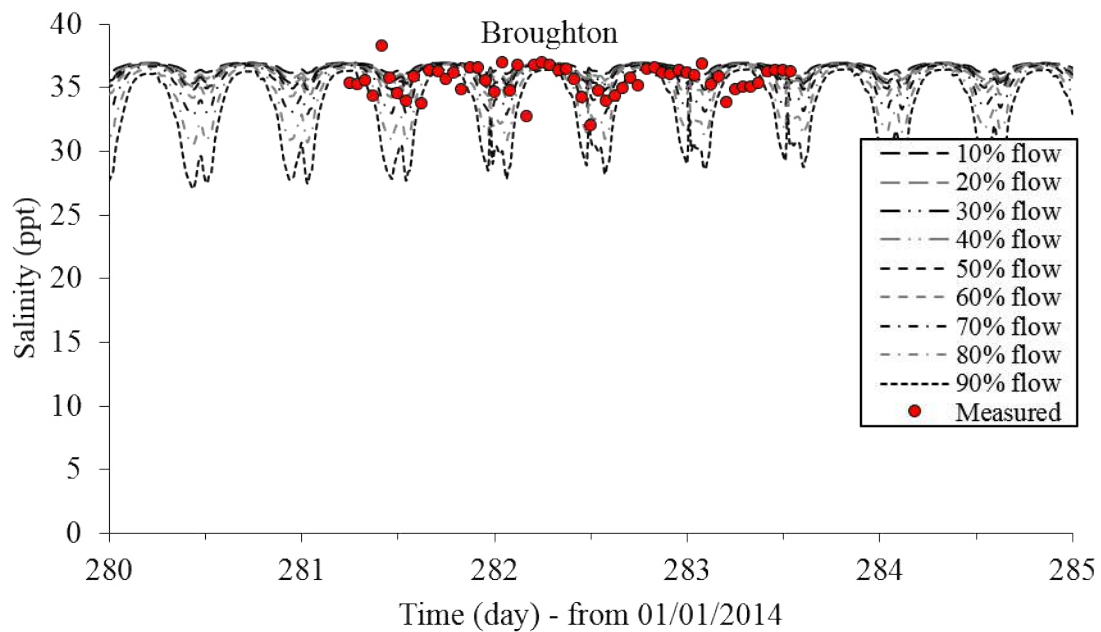


Figure D.1(b): Time series of the modelled salinity at Broughton as compared to the measured data with the range of catchment inflows between 10 to 90%.

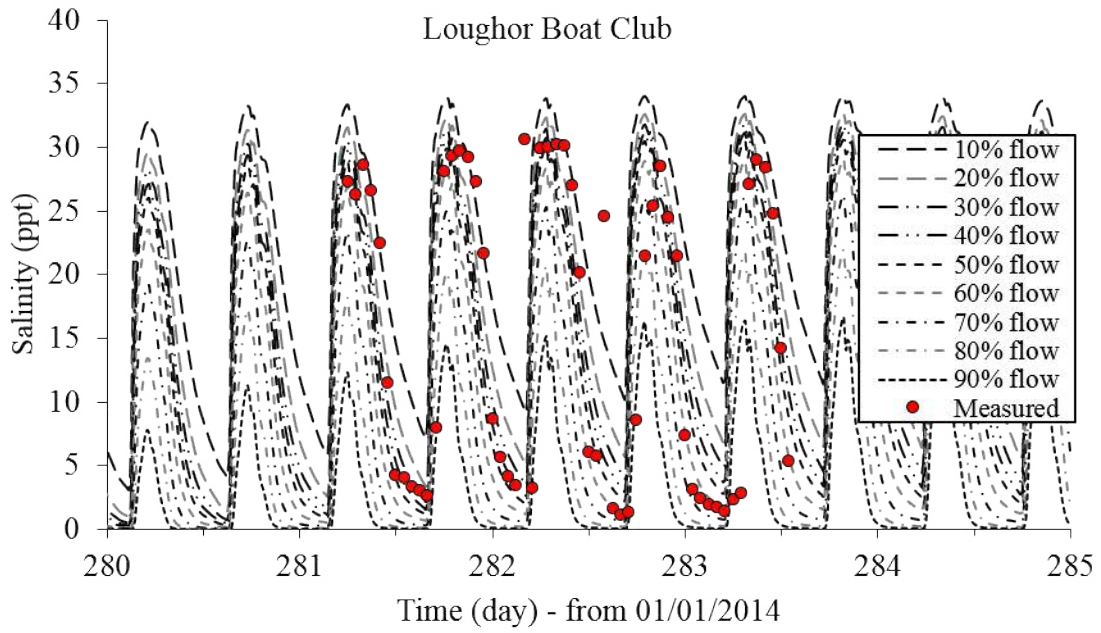


Figure D.1(c): Time series of the modelled salinity at Loughor Boat Club as compared to the measured data with the range of catchment inflows between 10 to 90%.

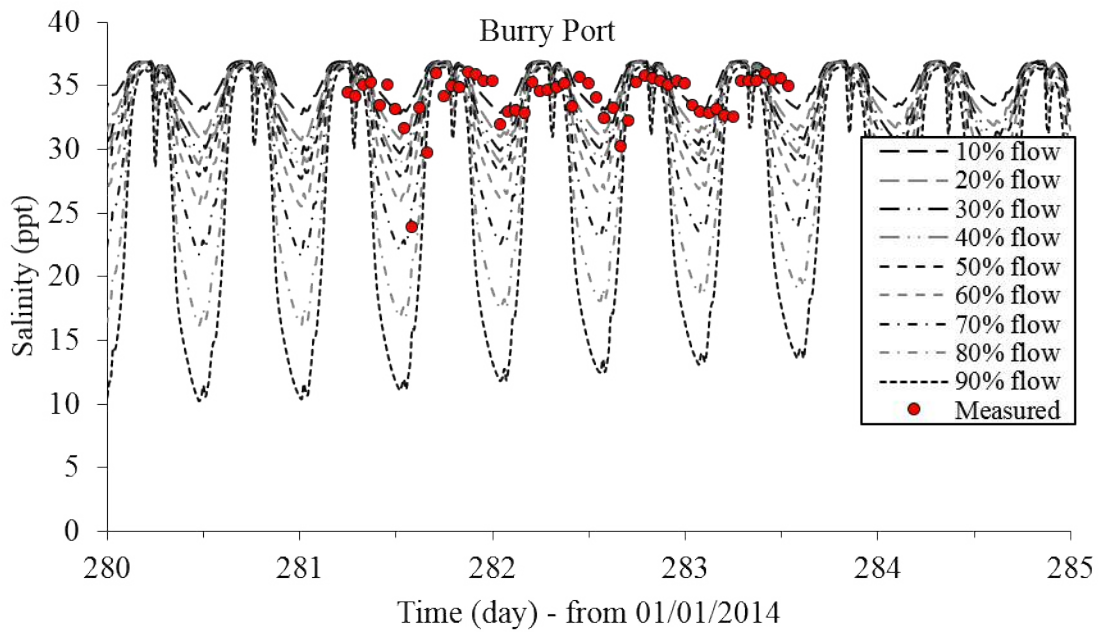


Figure D.1(d): Time series of the modelled salinity at Burry Port as compared to the measured data with the range of catchment inflows between 10 to 90%.

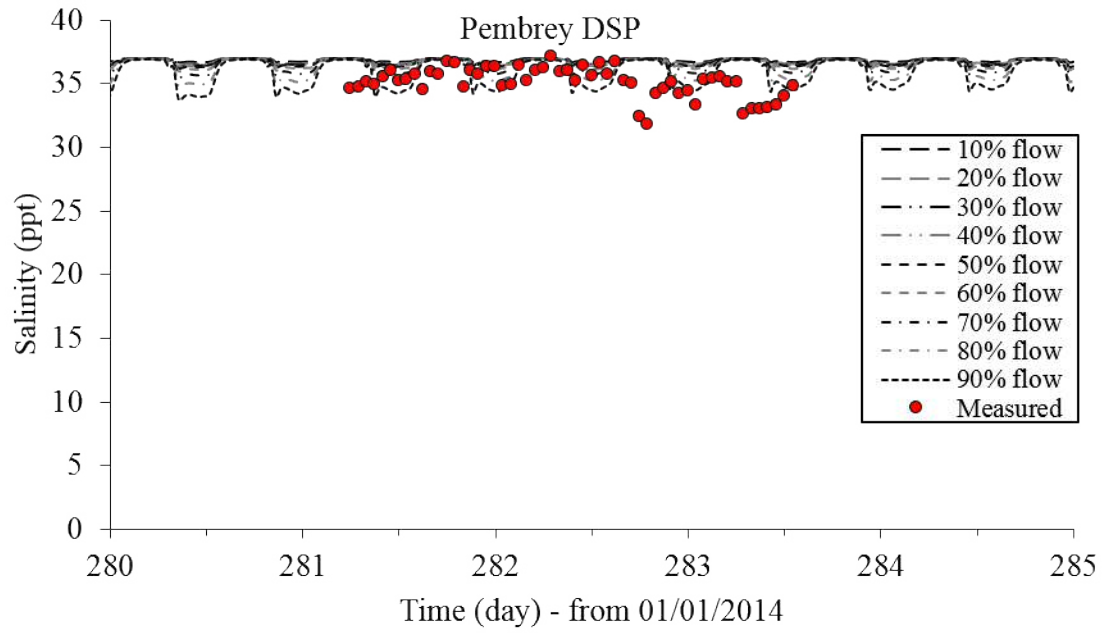


Figure D.1(e): Time series of the modelled salinity at Pembrey DSP as compared to the measured data with the range of catchment inflows between 10 to 90%.

Table D.6: Statistical results on the stream flows flushing sensitivity analysis to the salinity transport based from full tidal cycles.

Sampling location	10% flow	20% flow	30% flow	40% flow	50% flow	60% flow	70% flow	80% flow	90% flow
Rhossili DSP									
ME (ppt)	-0.7269	-0.6076	-0.5367	-0.4784	-0.4206	-0.2698	0.0479	0.6088	1.4602
MAE (ppt)	0.7440	0.6497	0.6047	0.5766	0.5516	0.5101	0.5370	0.7798	1.4755
RE (%)	2.0628	1.8013	1.6765	1.5986	1.5293	1.4142	1.4889	2.1620	4.0908
RMSE (ppt)	0.9796	0.8942	0.8472	0.8111	0.7780	0.7061	0.6480	0.8773	1.5821
RRE (%)	34.9844	31.9346	30.2573	28.9682	27.7848	25.2177	23.1426	31.3318	56.5045
Broughton									
ME (ppt)	-1.1104	-0.9152	-0.7991	-0.7037	-0.6091	-0.3688	0.1206	0.9538	2.1610
MAE (ppt)	1.2437	1.1574	1.1343	1.1242	1.1144	1.1071	1.3027	1.8435	2.7628
RE (%)	3.5000	3.2572	3.1920	3.1638	3.1361	3.1156	3.6661	5.1880	7.7751
RMSE (ppt)	1.6017	1.5029	1.4618	1.4389	1.4267	1.4407	1.6536	2.3710	3.6968
RRE (%)	25.4244	23.8550	23.2029	22.8404	22.6457	22.8690	26.2474	37.6352	58.6789
Loughor Boat Club									
ME (ppt)	-7.7100	-4.0004	-2.1075	-0.7239	0.5406	2.8059	5.8651	9.0686	11.7419
MAE (ppt)	8.9431	6.8616	6.3205	6.1665	6.3777	7.1125	8.9398	10.9030	12.5730
RE (%)	57.0402	43.7645	40.3128	39.3309	40.6776	45.3643	57.0194	69.5408	80.1925
RMSE (ppt)	11.8089	9.9763	9.5032	9.3912	9.4744	9.9908	11.3758	13.4826	15.6444
RRE (%)	40.0573	33.8408	32.2361	31.8561	32.1383	33.8902	38.5882	45.7348	53.0677
Burry Port Harbour									

ME (ppt)	-1.3482	-0.5402	-0.0772	0.2941	0.6518	1.5386	3.2087	5.7516	8.8096
MAE (ppt)	1.8392	1.9685	2.2349	2.4638	2.7249	3.3837	4.6610	6.8069	9.5801
RE (%)	5.4109	5.7911	6.5750	7.2483	8.0166	9.9545	13.7123	20.0255	28.1842
RMSE (ppt)	2.5082	2.5275	2.7299	2.9701	3.2555	4.0852	5.9016	8.8814	12.5145
RRE (%)	20.7287	20.8885	22.5613	24.5464	26.9052	33.7620	48.7734	73.4001	103.4260
Pembrey DSP									
ME (ppt)	-1.7688	-1.6968	-1.6588	-1.6276	-1.5999	-1.5180	-1.3457	-1.0685	-0.6917
MAE (ppt)	1.7763	1.7113	1.6778	1.6504	1.6287	1.5715	1.4615	1.3328	1.4064
RE (%)	5.0611	4.8761	4.7805	4.7024	4.6408	4.4777	4.1643	3.7975	4.0071
RMSE (ppt)	2.1425	2.0932	2.0677	2.0479	2.0311	1.9833	1.9007	1.8167	1.8112
RRE (%)	39.6766	38.7622	38.2913	37.9240	37.6133	36.7271	35.1984	33.6435	33.5404

D.4 Hydrodynamic validation at Swansea Bay

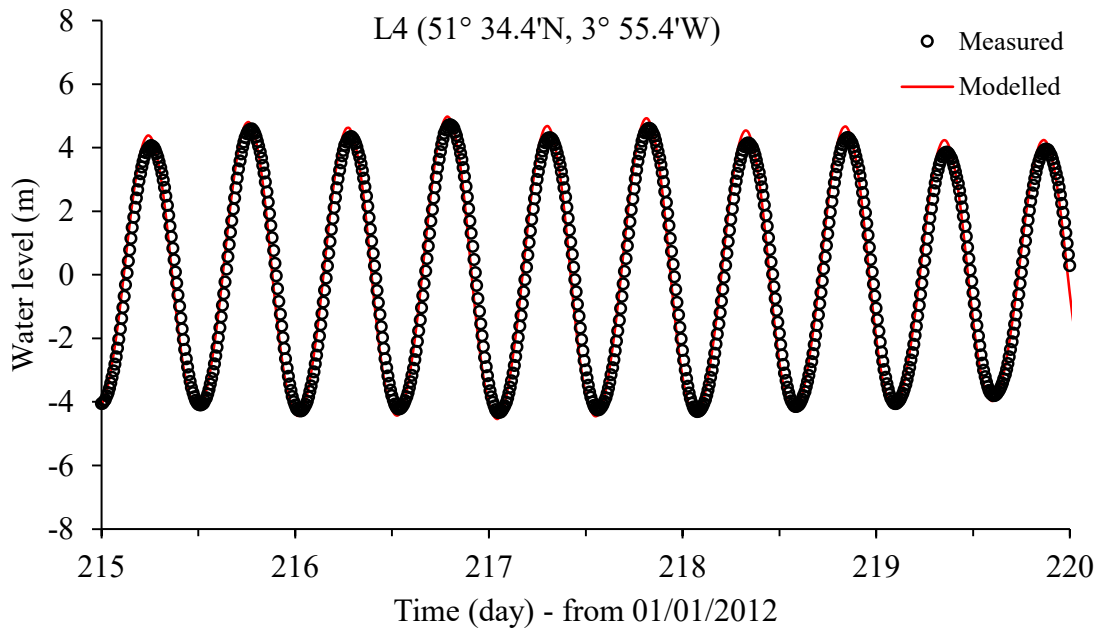


Figure D.2: Comparison of predicted water levels from the hydrodynamic model and measured data at station L4 of Swansea Bay.

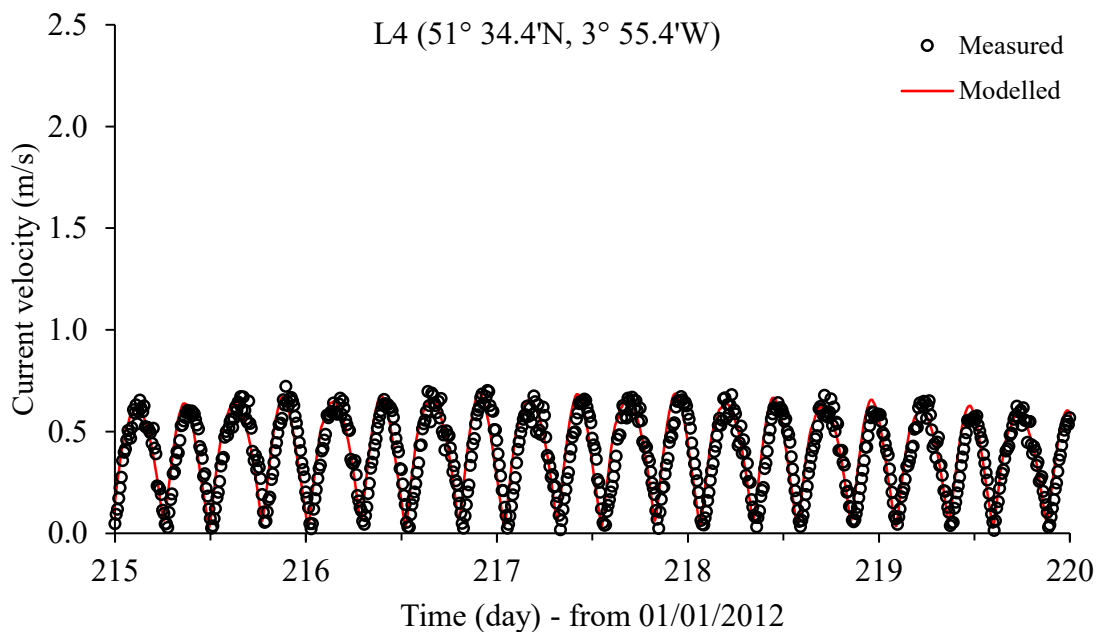


Figure D.3: Predicted current velocities from the hydrodynamic model and measured data at station L4 of Swansea Bay.

Appendix E

E.1 Spatial distribution analyses of FIO and its exposure to shellfish

Table E.1: FIO transport and decay – conservative mass.

Area	Mass
$H \geq 1E-1m$ Grazing marshland = 12.05 km ² FIOs concentration above 1E2 cfu/100ml = 1.40 km ² Total distributed FIOs = 14.76 km ²	$H \geq 1E-1m$ Retained within marshland = 2.03x10 ¹¹ cfu Flushed out from marshland = (1.38E12-2.03E11) = 1.1744x10 ¹² cfu
$H \geq 1E-2m$ Grazing marshland = 12.05 km ² FIOs concentration above 1E2 cfu/100ml = 2.80 km ² Total distributed FIOs = 16.74 km ²	$H \geq 1E-2m$ Retained within marshland = 3.28x10 ¹¹ cfu Flushed out from marshland = (1.49E12-3.28E11) = 1.1574x10 ¹² cfu
$H \geq 1E-3m$ Grazing marshland = 12.05 km ² FIOs concentration above 1E2 cfu/100ml = 5.08 km ² Total distributed FIOs = 17.18 km ²	$H \geq 1E-3m$ Retained within marshland = 4.36x10 ¹¹ cfu Flushed out from marshland = (1.59E12-4.36E11) = 1.1490x10 ¹² cfu

Table E.2: FIO transport and decay – constant decay at T90 = 14.9 hours.

Area	Mass
$H \geq 1E-1m$ Grazing marshland = 12.05 km ² FIOs concentration above 1E2 cfu/100ml = 4.30E-6 km ² Total distributed FIOs = 1.06 km ²	$H \geq 1E-1m$ Retained within marshland = 1.45x10 ¹⁰ cfu Flushed out from marshland = (4.71E10-1.45E10) = 3.2579x10 ¹⁰ cfu
$H \geq 1E-2m$ Grazing marshland = 12.05 km ² FIOs concentration above 1E2 cfu/100ml = 0.15 km ²	$H \geq 1E-2m$ Retained within marshland = 3.17x10 ¹⁰ cfu Flushed out from marshland = (5.99E10-3.17E10) = 2.8206x10 ¹⁰ cfu

Total distributed FIOs = 6.67 km ²	
H ≥ 1E-3m Grazing marshland = 12.05 km ² FIOs concentration above 1E2 cfu/100ml = 1.71 km ² Total distributed FIOs = 10.99 km ²	H ≥ 1E-3m Retained within marshland = 9.27x10 ¹⁰ cfu Flushed out from marshland = (1.24E11-9.27E10) = 3.1190x10 ¹⁰ cfu

Table E.3: Shellfish exposure to FIO – conservative mass.

Area (exposure time)	Area (exposure severity)
H ≥ 1E-1m Grazing marshland = 12.05 km ² FIOs exposure above 54 seconds = 0.08 km ²	H ≥ 1E-1m Grazing marshland = 12.05 km ² FIOs exposure above 1.62 x 10 ⁴ (cfu/100 ml)*sec = 0.11 km ²
H ≥ 1E-2m Grazing marshland = 12.05 km ² FIOs exposure above 54 seconds = 0.98 km ²	H ≥ 1E-2m Grazing marshland = 12.05 km ² FIOs exposure above 1.62 x 10 ⁴ (cfu/100 ml)*sec = 1.42 km ²
H ≥ 1E-3m Grazing marshland = 12.05 km ² FIOs exposure above 54 seconds = 1.38 km ²	H ≥ 1E-3m Grazing marshland = 12.05 km ² FIOs exposure above 1.62 x 10 ⁴ (cfu/100 ml)*sec = 3.06 km ²

Table E.4: Shellfish exposure time to FIO – constant decay at T90 = 14.9 hours.

Area (exposure time)	Area (exposure severity)
H ≥ 1E-1m Grazing marshland = 12.05 km ² FIOs exposure above 54 seconds = 0.00 km ²	H ≥ 1E-1m Grazing marshland = 12.05 km ² FIOs exposure above 1.62 x 10 ⁴ (cfu/100 ml)*sec = 0.00 km ²
H ≥ 1E-2m Grazing marshland = 12.05 km ² FIOs exposure above 54 seconds = 0.05 km ²	H ≥ 1E-2m Grazing marshland = 12.05 km ² FIOs exposure above 1.62 x 10 ⁴ (cfu/100 ml)*sec = 0.25 km ²
H ≥ 1E-3m	H ≥ 1E-3m

Grazing marshland = 12.05 km ² FIOs exposure above 54 seconds = 0.22 km ²	Grazing marshland = 12.05 km ² FIOs exposure above 1.62 x 10 ⁴ (cfu/100 ml)*sec = 1.67 km ²
--	---

E.2 Lumped statistics of temporal FIOs concentration at shellfish beds

Table E.5: Statistics of the FIO concentration as a conservative mass at 60 shellfish beds that released at different releasing depths based on the B-S release-kinetic model.

Shellfish beds	Min	1 st Quartile	Median	3 rd Quartile	Max	Mean
1	0.3701	1.7978	5.1361	16.8075	98.6560	13.3129
2	0.3866	2.1162	3.6061	4.8104	13.5270	3.4466
3	0.3993	1.9291	3.7251	5.1783	11.2690	3.7660
4	0.4009	1.6773	4.0162	7.0186	13.3270	4.8291
5	0.5494	2.7121	9.0405	17.1770	186.4000	16.0845
6	0.2166	1.7095	2.6028	3.2007	32.3360	2.6476
7	0.3482	4.7698	13.4230	27.6065	190.7200	22.2155
8	0.2819	1.4475	3.7308	6.4471	15.5520	4.4909
9	0.2823	2.0546	5.1082	10.1165	36.6350	7.3132
10	0.2962	1.4907	2.9760	4.1534	10.9250	2.8574
11	0.2993	1.6060	3.4860	6.3730	19.2590	4.2595
12	0.3512	3.1138	9.4899	22.2150	97.7290	18.4501
13	0.1485	1.5838	4.4173	12.6720	40.9960	8.1644
14	0.4649	3.3092	8.8699	13.4165	102.1600	14.3204
15	0.2770	1.6818	5.8170	31.9980	410.0200	29.0119
16	0.2462	1.3185	2.9830	5.5671	28.4160	3.6464
17	0.2573	1.6827	4.1509	10.1050	36.5530	7.5475
18	0.2545	1.2525	2.5503	3.8825	20.4380	2.6656
19	0.2633	2.2229	7.6072	18.5880	86.0980	13.4383
20	0.2757	2.0630	5.7405	14.5490	53.3970	10.7796
21	0.3468	1.6102	4.6473	8.3875	52.5510	5.9313
22	0.5066	1.8345	4.5349	8.3300	28.2010	5.7687
23	0.6425	6.1175	14.1970	30.0445	456.4800	33.4318
24	0.1312	1.3092	2.7112	4.2462	45.2840	3.7724

25	0.2469	1.5541	4.0887	10.1145	32.5810	7.0266
26	0.2908	2.2154	8.5455	30.7965	139.8500	21.5832
27	0.2749	1.6342	4.5279	13.0665	59.8570	10.2540
28	0.3471	1.4239	3.5084	7.0527	34.0370	4.9296
29	0.3449	1.1357	3.5521	4.8929	7.5247	3.2686
30	0.3929	1.1424	3.9075	5.1723	8.1861	3.4639
31	0.4700	1.0919	3.9763	5.2480	7.1949	3.5038
32	0.4009	1.0905	3.8541	5.1572	7.0242	3.4152
33	0.1980	0.8236	1.9688	3.4565	7.1692	2.1935
34	0.2063	0.8915	2.3474	4.1856	7.5618	2.5817
35	0.2916	0.9302	2.6027	3.9498	5.9073	2.5387
36	0.4148	1.0434	2.8770	4.1715	5.8060	2.6703
37	0.2875	0.8264	4.1916	5.0524	7.2569	3.2797
38	0.3997	0.9239	2.8795	3.8047	5.0283	2.4611
39	0.4797	0.8802	2.2044	3.3599	4.9557	2.1575
40	0.3847	0.7181	2.7113	3.6304	4.3176	2.2853
41	0.0674	0.6628	1.0622	3.3023	5.2997	1.8121
42	0.0060	0.4112	1.1149	2.2695	4.3971	1.4185
43	0.0530	0.6617	1.0625	3.3009	5.0029	1.8214
44	0.1164	0.7502	1.7826	3.5157	4.7960	2.0976
45	0.5060	0.6547	2.6827	3.4796	4.3613	2.2091
46	0.0226	0.4127	0.8844	3.1462	5.8297	1.6733
47	0.0704	0.6583	0.7800	2.0373	4.4888	1.3985
48	0.2238	0.6453	1.8276	3.3077	4.4967	1.9942
49	0.0440	0.5219	0.7314	2.6210	4.9338	1.4314
50	0.1113	0.6072	1.2888	3.0821	4.4749	1.7776
51	0.0648	0.2992	0.7745	1.3636	3.1349	0.8700
52	0.1299	0.3318	0.9345	1.3774	3.1311	0.9043
53	0.0993	0.4326	1.2394	1.6624	16.6210	1.3281
54	0.0249	0.2823	0.6745	2.0313	5.2750	1.2336
55	0.0553	0.3299	0.8028	1.6906	6.9838	1.0455
56	0.0277	0.2910	0.8731	3.0366	20.3440	2.6079

57	0.3843	1.5555	4.4486	7.7542	39.7590	5.3839
58	0.1547	0.9111	2.4209	3.8119	6.1545	2.4630
59	0.0741	0.6791	1.2354	3.3588	5.0991	1.9096
60	0.2079	0.6392	1.6000	3.1464	4.4203	1.8819

Table E.6: Statistics of the FIOs concentration with constant decay ($T_{90} = 14.9$ hours) at 60 shellfish beds that released at different releasing depths based on the B-S release-kinetic model.

Shellfish beds	Min	1 st Quartile	Median	3 rd Quartile	Max	Mean
1	0.0000	0.0013	0.0818	1.9045	52.0660	2.0122
2	0.0000	0.0017	0.0148	0.0326	1.2826	0.0277
3	0.0000	0.0023	0.0152	0.0687	2.1612	0.0550
4	0.0000	0.0032	0.0208	0.2315	4.4678	0.1850
5	0.0000	0.0071	0.2469	1.6581	92.9970	2.4770
6	0.0000	0.0041	0.0169	0.0453	3.5943	0.0522
7	0.0000	0.0014	0.1048	1.6836	47.7700	1.9739
8	0.0000	0.0011	0.0224	0.2298	4.3247	0.2041
9	0.0000	0.0015	0.0360	0.5756	13.5640	0.6225
10	0.0000	0.0012	0.0096	0.0235	1.0555	0.0208
11	0.0000	0.0020	0.0150	0.1605	8.8657	0.1690
12	0.0000	0.0160	0.1726	2.3220	38.8320	1.9601
13	0.0000	0.0058	0.0552	1.0479	17.2770	0.8455
14	0.0000	0.0015	0.1808	1.6416	57.8630	2.3535
15	0.0000	0.0016	0.1301	5.4449	149.0800	5.5997
16	0.0000	0.0012	0.0116	0.1438	4.2661	0.1082
17	0.0000	0.0013	0.0237	0.7254	18.6500	0.7377
18	0.0000	0.0011	0.0087	0.0194	2.9390	0.0255
19	0.0000	0.0049	0.0881	1.5544	21.3940	1.2676
20	0.0000	0.0068	0.0575	1.1098	19.7470	0.9216
21	0.0000	0.0025	0.0380	0.3688	12.5260	0.4434
22	0.0000	0.0000	0.0232	0.3987	13.8900	0.3088
23	0.0000	0.0189	0.5013	2.5969	46.5260	2.0300
24	0.0000	0.0034	0.0130	0.0407	23.4170	0.1915

25	0.0000	0.0037	0.0242	0.5900	11.5710	0.5059
26	0.0000	0.0058	0.2018	2.4842	31.9350	1.8942
27	0.0000	0.0031	0.0369	1.0610	17.9830	0.8529
28	0.0000	0.0031	0.0346	0.3419	7.7955	0.3271
29	0.0000	0.0027	0.0109	0.0242	0.5923	0.0220
30	0.0000	0.0025	0.0122	0.0272	0.8098	0.0241
31	0.0000	0.0019	0.0102	0.0248	0.4221	0.0209
32	0.0000	0.0028	0.0107	0.0248	0.3973	0.0213
33	0.0000	0.0001	0.0017	0.0062	0.4663	0.0076
34	0.0000	0.0002	0.0021	0.0088	0.5847	0.0091
35	0.0000	0.0001	0.0019	0.0065	0.1578	0.0055
36	0.0000	0.0001	0.0023	0.0053	0.1798	0.0048
37	0.0000	0.0000	0.0082	0.0219	0.5541	0.0186
38	0.0000	0.0000	0.0012	0.0034	0.0504	0.0027
39	0.0000	0.0000	0.0009	0.0026	0.0535	0.0022
40	0.0000	0.0000	0.0007	0.0020	0.0249	0.0016
41	0.0000	0.0000	0.0003	0.0022	0.0880	0.0020
42	0.0000	0.0000	0.0001	0.0008	0.0376	0.0012
43	0.0000	0.0000	0.0002	0.0019	0.0691	0.0018
44	0.0000	0.0000	0.0004	0.0023	0.0596	0.0018
45	0.0000	0.0000	0.0008	0.0029	0.0383	0.0021
46	0.0000	0.0000	0.0001	0.0032	0.1703	0.0033
47	0.0000	0.0000	0.0002	0.0005	0.0514	0.0006
48	0.0000	0.0000	0.0004	0.0018	0.0479	0.0015
49	0.0000	0.0000	0.0001	0.0009	0.0788	0.0012
50	0.0000	0.0000	0.0003	0.0015	0.0507	0.0014
51	0.0000	0.0000	0.0012	0.0043	0.2163	0.0044
52	0.0000	0.0001	0.0015	0.0043	0.2388	0.0043
53	0.0000	0.0002	0.0039	0.0122	2.7775	0.0232
54	0.0000	0.0000	0.0007	0.0397	1.1509	0.0411
55	0.0000	0.0001	0.0013	0.0223	0.7857	0.0171
56	0.0000	0.0000	0.0011	0.1083	4.0183	0.1719

57	0.0000	0.0024	0.0362	0.3752	19.1860	0.3365
58	0.0000	0.0001	0.0019	0.0068	0.2268	0.0061
59	0.0000	0.0000	0.0003	0.0026	0.0761	0.0020
60	0.0000	0.0000	0.0004	0.0016	0.0458	0.0015